Université Grenoble Alpes

THÈSE

Pour obtenir le grade de

DOCTEUR DE L'UNIVERSITE GRENOBLE ALPES

Spécialité : 2MGE : Matériaux, Méchanique, Génie civil, Electrochimie

Arrêté ministériel : 25 mai 2016

Présentée par

Shelby Rae TURNER

Thèse dirigée par **Marc DE BOISSIEU** et codirigée par **Stéphane PAILHÈS, Valentina GIORDANO, Frédéric BOURDAROT, et Helmut SCHOBER**

préparée au sein de **l'Institut Laue-Langevin**, au **Laboratoire des Science et Ingénierie des Matériaux et Procédés**, et à **l'Institut Lumière Matière**
dans **l'École Doctorale I-MEP2 - Ingénierie - Matériaux, Mécanique, Environnement, Energétique, Procédés, Production**

L'étude des temps de vie des phonons et des mécanismes de transport thermique dans les systèmes cristallins complexes et désordonnés par spectroscopie inélastique des neutrons et des rayons X

The investigation of phonon lifetime and thermal transport mechanisms in complex and disordered crystalline systems by means of inelastic neutron and X-ray spectroscopy

Thèse soutenue publiquement le **22 octobre 2021**,
devant le jury composé de :

Monsieur Olivier DELAIRE
Associate Professor, Duke University (Rapporteur)
Monsieur Matthieu LE TACON
Professeur des Universités, Karlsruhe Institute of Technology (Rapporteur)
Madame Virginie SIMONET
Directrice de recherche CNRS, Institut Néel (Examinatrice, Présidente du jury)
Madame Jelena SJAKSTE
Chargée de recherche CNRS, Laboratoire des Solides Irradiées (Examinatrice)
Monsieur Marc DE BOISSIEU
Directeur de recherche CNRS, Laboratoire des Science et Ingénierie des Matériaux et Procédés (Membre)
Monsieur Stéphane PAILHÈS
Chargé de recherche CNRS, Institut Lumière Matière (Membre)
Madame Valentina GIORDANO
Chargée de recherche CNRS, Institut Lumière Matière (Invitée)
Monsieur Frédéric BOURDAROT
Ingénieur chercheur, Institut de Recherche Interdisciplinaire de Grenoble (Invité)
Monsieur Helmut SCHOBER
Professeur, Université Grenoble Alpes et Institut Laue-Langevin (Invité)

Abstract

Interest in the engineering of thermal process mechanisms has grown significantly in recent years, particularly for applications involving thermal functionalization of a material for use as a thermal barrier, thermoelectric converter, thermal diode, etc., which requires the control of thermal conductivity. The thermal manipulation and design of a material in turn requires knowledge of the fundamental transport properties of the elementary heat carrier particle, the phonon.

This is easier said than done, however, since models that would allow us to comprehend heat transport in complex materials are still under development, and because we lack systematic energy and temperature dependencies of experimentally measured phonon dispersions and lifetimes on a wide range of materials. This presents a barrier to our understanding of more complex and disordered systems, which are typically the ones needed to produce the thermal conductivity spectrum for the applications listed above. With the introduction of the many more atoms per unit cell and/or the disorder, we must now connect the dots between the effects of increasing structural complexity and defects on the phonon spectrum, and, ultimately, on thermal conductivity.

Within the context of overcoming these challenges, I present the phonon spectra in three families of materials that exhibit different types of structural disorder and complexity. These contributions include the inorganic type-I clathrate $Ba_{7.81}Ge_{40.67}Au_{5.33}$, defined by its cage structure and many atoms per unit cell; the equimolar high-entropy alloy FeCoCrMnNi, represented by a simple and averaged monatomic FCC unit cell with significant chemical disorder; and cubic Yttria-Stabilized Zirconia, characterized by an extended and correlated defect structure brought on by the inclusion of oxygen vacancies. Towards this end, I have experimentally measured their phonon dispersions, lifetimes, and mean free paths using inelastic neutron and X-ray scattering techniques found at large-scale facilities.

My results confirm the use of the *ab-initio* self-consistent phonon method calculations for clathrates, emphasizing the importance of quartic anharmonic terms in our understanding of both the hardening of the lowest-lying optical branch with increasing temperature, and in the reproduction of the weak temperature dependence of the lattice thermal conductivity. The FeCoCrMnNi alloy study establishes the lattice dynamics of a random five-element alloy, demonstrating that the factor limiting phonon lifetimes is associated to force-constant fluctuations. Finally, I revisit the lattice dynamics of cubic Yttria-Stabilized Zirconia with higher resolution measurements, bringing new insight into the acoustic-optic interaction within the phonon spectrum, and to the linewidth broadening that results from the extended defect structure in this material.

Through each of my case studies, I provide the energy dependence of a specific type of phonon scattering mechanism. Then, by methodically detailing these features in each system, we can work upwards from their microscopic phonon properties to their macroscopic material properties, bringing us one step closer to understanding heat transport in complex and disordered crystalline systems.

Keywords: lattice dynamics, phonon lifetime, clathrates, high-entropy alloys, yttria-stabilized zirconia, inelastic neutron and X-ray scattering

Résumé

L'intérêt pour le développement et l'ingénierie des systèmes cristallins pour les applications thermiques s'est fortement accru ces dernières années notamment pour des applications nécessitant la fonctionnalisation de la thermique des matériaux à utiliser comme barrière thermique, convertisseur thermoélectrique, diode thermique etc. qui nécessitent le contrôle de la conductivité thermique. Le contrôle et design de la thermique d'un matériau nécessite de connaître les propriétés fondamentales de transport des porteurs élémentaires de la chaleur, les phonons.

C'est plus facile à dire qu'à faire, cependant, car des modèles qui nous permettraient de comprendre le transport de chaleur dans ces matériaux complexes sont encore en cours de développement. De plus, nous manquons d'études expérimentales systématiques sur une large gamme de matériaux des dépendances en énergie et en température des dispersions et des temps de vie des phonons. Cela représente un obstacle à notre compréhension des systèmes plus complexes et désordonnés, qui sont généralement ceux nécessaires pour produire le spectre de conductivité thermique pour les applications mentionnées ci-dessus. Avec l'introduction d'un grand nombre d'atomes dans la maille élémentaire et/ou du désordre, nous devons maintenant faire le lien entre les effets de l'augmentation de la complexité structurale et des défauts sur le spectre des phonons, et, finalement, sur la conductivité thermique.

Pour cela, je présente les spectres de phonons dans trois familles de matériaux qui présentent différents types de désordre structurel et de complexité. Ces contributions comprennent le clathrate inorganique de type-I $Ba_{7.81}Ge_{40.67}Au_{5.33}$, défini par sa structure en cage et de nombreux atomes par maille élémentaire ; l'alliage à haute entropie équimolaire FeCoCrMnNi, décrit par un réseau FCC moyen mono-atomique avec un désordre chimique important ; et la zircone cubique stabilisée par l'yttria, caractérisée par un désordre étendu et corrélé, provoqué par l'inclusion de lacunes d'oxygène. À cette fin, j'ai mesuré expérimentalement les dispersions, temps de vie et libres parcours moyens des phonons en utilisant des techniques de diffusion inélastique des neutrons et des rayons X disponibles dans des très grandes infrastructures de recherche.

Mes résultats confirment les calculs théoriques *ab initio* avec une approche self-consistante pour les clathrates, soulignant l'importance des termes anharmoniques quartiques qui déterminent le durcissement de la branche optique de plus basse énergie quand la température croît, ainsi que une faible dépendance en température de la conductivité thermique. L'étude de l'alliage FeCoCrMnNi établit la dynamique de réseau d'un alliage aléatoire à cinq éléments et démontre que le facteur limitant le temps de vie des phonons est associé aux fluctuations des constantes de force. Enfin, je revisite la dynamique de la zircone cubique stabilisée par l'yttria avec des mesures à plus haute résolution, apportant un nouvel aperçu sur l'interaction acoustique-optique dans le spectre des phonons et je montre que leur temps de vie résulte de la structure étendue des défauts dans ce matériau.

A travers chacune de mes études de cas, je fournis la dépendance en énergie d'un type spécifique de mécanisme de diffusion de phonons. Ensuite, en détaillant méthodiquement ces caractéristiques dans chaque système, nous pouvons passer des propriétés microscopiques des phonons aux propriétés macroscopiques des matériaux, nous rapprochant ainsi de la compréhension du transport de chaleur dans les systèmes cristallins complexes et désordonnés.

Mots clés: dynamique de réseau, temps de vie des phonons, clathrates, alliages à haute entropie, zircone stabilisée par l'yttria et diffusion inélastique des neutrons et des rayons X

Acknowledgments

It is with great pleasure that I reflect on the many wonderful people and organizations that I have been involved with throughout this experience of completing a thesis project. In order to complete my thesis work, I have been granted financial support from the Institut Max von Laue-Paul Langevin (ILL) and the International Strategic Partnership (ISP) program of the Université Grenoble Alpes (UGA) Initiative of Excellence (IDEX). My Ph.D. program requirements have been set and tracked by the Ingénierie - Matériaux, Mécanique, Environnement, Energétique, Procédés, Production (I-MEP2) doctoral school at UGA. My affiliate laboratory groups include the Spectroscopy Group at the ILL, the Physics of Metals (PM) Group at the Laboratoire de Science et Ingénierie des Matériaux et Procédés (SIMaP), and the Nanomaterials for Energy Group at the Institut Lumière Matière (ILM).

I would like to recognize the referees of the jury for my thesis defense, Dr. Olivier Delaire, Associate Professor at the Mechanical Engineering and Materials Science Department of Duke University, and Dr. Matthieu Le Tacon, University Professor at the Karlsruhe Institute of Technology's Institute for Quantum Materials and Technologies; and as well the members of the jury, Dr. Virginie Simonet, Directrice de Recherche CNRS in the Magnétisme et Supraconductivité Group at the Institut Néel, and Dr. Jelena Sjakste, Chargée de Recherche CNRS at the Laboratoire des Solides Irradiées, Ecole Polytechnique. I consider it a great honor that you have agreed to read and judge my work.

To my supervisors, Marc de Boissieu, Stéphane Pailhès, Valentina Giordano, Frédéric Bourdarot, and Helmut Schober: it has been an absolute joy to work with you and learn from you. I have been lucky enough to have THE all-star, A+, can't-be-beat supervising team put together specifically for my thesis project, and I will fully admit that I have been spoiled by this. I have never met a group so passionate about science and discovery, and these qualities were contagious right from the start. Thank you for your patience, your teachings, and your kindness. You have set the bar for my future bosses impossibly high!

I am so proud to have worked at the ILL for these past three years. The friendly working environment and culture stand out to me as much as the incredible output of science, and I want to especially thank the Spectroscopy Group beamline scientists and technicians for being so welcoming and helpful. To Jacques Ollivier specifically, thank you for answering my endless questions about TOF data collection and interpretation over the years. As you already know, I consider you to be my sixth supervisor.

To the PM Group at SIMaP and the Nanomaterials for Energy Group at the ILM, I am very fortunate to have been given access to not one, not two, but three affiliate labs during my time as a Ph.D. student. I am so glad that I got to take advantage of this overwhelming range of expertise.

To my Comité de Suivi Individuel for the first and second years of my Ph.D. program, Olivier Bourgeois from the Institut Néel and Philippe Bourges from the Laboratoire Léon Brillouin (LLB), thank you for reading my yearly reports and participating in discussions on my progress. Your evaluations and opinions provided much-needed checkpoints throughout these past three years and I am grateful for the encouragements you gave me.

Thank you to Yuri Grin and Michael Baitinger from the Max-Planck-Institut für chemische Physik fester Stoffe, Michael Feuerbacher from the Peter Grünberg Institut, Kheirreddine Lebbou from the ILM, and Abdelmjid Benayad from the Centre de recherche sur les Ions, les MAtériaux et la Photonique (CIMAP) who provided the samples that I used for my experiments. These are collaborations that I value deeply.

Much of my training on inelastic neutron scattering instrumentation took place at the LLB during my first year. Therefore, to the Triple-Axis Group at the LLB, especially Yvan Sidis, Philippe Bourges, Sylvain Petit, and John-Paul Castellan, thank you for trusting me with your spectrometers. This group is truly one-of-a-kind, and I am grateful to have been along for the ride. Even though I did not have the fortune of meeting him in person before his retirement, I would also like to thank Bernard Hennion for his development of the 'AFITV' fitting tool. This program has been invaluable to my Ph.D.

Thank you to Thomas Keller from the Forschungs-Neutronenquelle Heinz Maier-Leibnitz (FRM-II) for your guidance and instruction during my NRSE experiment. You were so willing to share your amazing expertise of this revolutionary technique, and this left quite an impression on me.

To Alexei Bosak from the European Synchrotron Radiation Facility (ESRF), thank you for teaching me about IXS and IXS sample preparation. The care you take with your beamline shows, and I am grateful to have had such a professional introduction to this technique.

The publication on clathrates would not have been possible without Holger Euchner from the Helmholtz Institute Ulm for Electrochemical Energy Storage. Thank you for your availability, expertise, and calculations.

Thank you as well to Terumasa Tadano from the National Institute for Materials Science, Japan. Our discussions with you led me to have a much better understanding of your self-consistent phonon method, and I look forward to reading about this method being applied to many more materials in the future.

To Christophe Candolfi and Bertrand Lenoir from the Institut Jean Lamour at the Université de Lorraine, Petr Levinský and Jiří Hejtmánek from the Institute of Physics at the Czech Academy of Sciences, and Christian Carbogno from the Fritz-Haber-Institut der Max-Planck-Gesellschaft, thank you for your ongoing collaborations on the Yttria-Stabilized Zirconia project which include thermal conductivity measurements and *ab-initio* calculations.

Many of the collaborations listed above were made possible through the European Integrated Center for the Development of New Metallic Alloys and Compounds (E-CMetAC). This organization, along with the Groupement d'Intérêt Scientifique en Thermoélectricité (GIS-TE), have provided me with a very dynamic and interactive networking environment throughout my time as a Ph.D. student.

To the Ph.D. student family that I've made at the ILL, y'all rock. There is a very special type of bonding that takes place over shared experiences in a Ph.D. program, and I am so fortunate to have gone through it with this crew. Much love especially to Madeleine and Daniela, who showed me the importance of good girlfriends and good pancakes.

Finally, thank you to my family for supporting me going on this wild adventure of graduate school in France. Thank you for believing in me, encouraging me, and cheering me on. This achievement is as much yours as it is mine.

Table of Contents

General Introduction

There has been a great push in recent years towards utilizing more renewable and sustainable energy sources as mankind begins to understand the full impact that it has had, and continues to have, on its environment. Energy consumption in our society is ever-increasing, and the U.S. Energy Information Administration predicted in their recent International Energy Outlook presentation that, between the years 2012 and 2040, there will be a 48% increase in the consumption of energy worldwide. This problem is global, which is why scientists, researchers, engineers, politicians, and activists alike are all joining together to work on this issue.

There are many green energy solutions, each in various stages of development and production, and they are the key to expanding and diversifying our energy resources. One of these potential solutions is thermoelectricity, which is the conversion of heat into electricity [1, 2]. The history of thermoelectricity involves famous, household names within the scientific community such as Thomas Seebeck, Jean Charles Athanase Peltier, and William Thomson, and the credit to the first thermoelectric generator (TEG) goes to Abram Fedorovich Ioffe in 1948 [3, 4]. Unfortunately, however, there was a slight dip in interest just after the discovery of TEGs since their efficiencies were low, and therefore the lack of practicality of such devices as replacements for current methods halted the momentum of this work. Fast forward to the Space Race, and TEGs were once again starting to be recognized for their reliability and longevity in environmental conditions that were either extreme or did not allow for frequent maintenance, such as in space, which helped create new niche markets for TEGs [5].

Now, with the renewed push for more environmentally-friendly products and production methods, TEGs have begun to find additional markets, from power generation for sensors, biosensors, and microelectronics, to heat loss recovery, and even sonic filtration [6–10]. One of the now more classic examples are TEGs that are being designed to convert the excess heat from a gasoline combustion engine into electricity for a more "green" vehicle [5], and, in general, the scalability, low maintenance requirements, and reliability of TEGs make them ideal solutions to many of our current energy concerns.

There is much potential for TEGs in particular around the application of heat loss, both within the transportation industry but in all energy production facilities as well. For context, Lawrence Livermore National Laboratory and the USA's Department of Energy reported in their annual energy flow chart for 2020 that approximately two-thirds of the energy produced for consumption ends up as "rejected energy," otherwise known as heat lost in the process of creating energy. TEGs offer the potential to convert this excess heat back into electricity, and to reduce the waste that occurs during this processing.

As for the materials that are being used as TEGs, those that are currently on the market are typically made of toxic or otherwise harmful compounds such as bismuth and lead telluride. Now, however, materials such as clathrates, skutterudites, tetrahedrites, half-Heusler alloys, calcium and strontium oxides, and organic TEGs are proving to be both more environmentally-friendly and perhaps more efficient in their heat to electricity conversion, and will hopefully replace some of the more toxic TEGs that are currently on the market in the future [5]. The need for thermoelectric devices is growing, and the practicality and usefulness of such research

will surely aid mankind's inevitable transition to greener energy in the years to come.

Even though this new generation of materials shows great potential for improved and diversified thermoelectric devices, they present new challenges in our understanding of heat propagation in materials. Their unique and complex structural characteristics go beyond the models that we currently have in place, and their microscopic properties often test the limits of our highest resolution experimental methods as well. Over recent decades, therefore, scientific research has begun to address this need for understanding heat propagation in what I will term "non-simple systems" throughout this thesis.

While the macroscopic properties and application-specific outcomes for many such complex and disordered materials are largely known, the microscopic mechanisms behind their intriguing and sometimes mysterious thermal transport properties have been the subject of many continued studies, and for this we turn to the study of the quasiparticle responsible for heat propagation: the phonon. So much interest revolves around microscopic thermal transport, in fact, that distinct research communities have formed around the study of such properties in glasses, aperiodic crystals, complex metallic alloys, and other crystalline systems with complex atomic structures and many atoms per unit cell. Experimentally, the crystalline system communities have focused largely on phonon dispersions, phonon linewidths, and thermodynamic properties such as the phononic density of states of simple crystalline phases, intermetallics, and quasicrystals. The glasses community, on the other hand, has concentrated primarily on phonon group velocities, phonon linewidth broadening, and the relation of this broadening to the excess of vibrational states known as the Boson peak.

In terms of theory, until now solid state physics and materials science has been based largely on theories and models that have been derived for simple crystalline materials with only a few atoms per unit cell. The recent advancement and progress of *ab-initio* theory and the availability of more realistic interatomic-level Hamiltonians has given rise to the study of systems with increasing complexity, and, in particular, is beginning to uncover the links between crystalline structure, phonon lifetimes, and macroscopic thermal transport. For instance, theoreticians have proven that the incorporation of disorder and/or anharmonicity due to three-phonon scattering processes can help us understand heat propagation in rock-salt thermoelectric compounds, Ag-based conductors, quasicrystals, clathrates, oxides, glasses, and semiconductors in general.

There exists a certain disconnect, however, in how we use these results to comprehensively and systematically study the specific phononic behaviors brought about by complexity in non-simple systems in a way in which we can then use all of that information to draw global conclusions about phonons in complex and disordered systems and their impact on thermal conductivity. In other words, these studies are what will allow us to link the micro and macroscopic properties of such materials, and, for the moment, many questions globally remain unanswered.

To these studies and others I add my thesis work as a contribution to the overall story of thermal transport in complex and disordered crystalline systems. My thesis takes four seemingly very different materials and shows how, by uncovering their particular phonon behaviors and scattering processes, we can understand macroscopic material properties such as thermal conductivity, heat capacity, and Grüneisen parameter. Furthermore, and more importantly, my work pushes our global understanding of heat transport in complex and disordered systems. I show how we must understand heat transport by building up from properties of the phonon. By experimentally uncovering the particular scattering behaviors of each of my materials, I methodically show that complexity brings about certain comparisons that can be made across a large range of disordered, non-simple systems. By publishing this work, I have probed different aspects of complexity and disorder with the systems that I have studied, and I bring us closer not only to a unified understanding of heat propagation in such materials, but, more globally, to the commercialization of novel thermally engineered materials.

This thesis is divided into the following chapters: In Chapter 1, I will further define complexity as it pertains to crystalline systems and introduce my four systems of interest that each serve as case study examples of structural complexity in disordered crystalline systems. I will then explain the reasoning behind choosing these systems by giving context to the global and state-of-the-art investigations occurring on complexity that have already been published within the community.

Chapter 2 then provides the reader with the tools and language to discuss heat transport in disordered and complex systems through the current macro and microscopic theoretical understanding, focusing on properties of the phonon. Chapter 3 details the experimental methods used to measure phonon properties, focusing exclusively on techniques found at large-scale facilities, namely inelastic neutron and X-ray scattering. Chapter 4 introduces each of my published (and future published) works, which should be viewed as case studies, linked under the umbrella of studying complexity and disorder in crystalline systems. Those articles include:

- **Impact of temperature and mode polarization on the acoustic phonon range in complex crystalline phases: A case study on intermetallic clathrates**
  Shelby R. Turner, Stéphane Pailhès, Frédéric Bourdarot, Jacques Ollivier, Stéphane Raymond, Thomas Keller, Yvan Sidis, John-Paul Castellan, Pierre-François Lory, Holger Euchner, Michael Baitinger, Yuri Grin, Helmut Schober, Marc de Boissieu, Valentina M. Giordano
  State of the article: Phys. Rev. Research **3**, 013021 (2021).

- **Phonon behavior in a random solid solution: A lattice dynamics study on the high-entropy alloy FeCoCrMnNi**
  Shelby R. Turner, Stéphane Pailhès, Frédéric Bourdarot, Jacques Ollivier, Yvan Sidis, John-Paul Castellan, Jean-Marc Zanotti, Quentin Berrod, Florence Porcher, Alexei Bosak, Michael Feuerbacher, Helmut Schober, Marc de Boissieu, Valentina M. Giordano
  State of the article: submitted to an international peer-reviewed journal for review.

- **Revisiting the Lattice Dynamics of Cubic Yttria-Stabilized Zirconia**
  Shelby R. Turner, Stéphane Pailhès, Leila Ben Mahfoud, Christian Carbogno, Marc de Boissieu, Frédéric Bourdarot, Helmut Schober, Yvan Sidis, John-Paul Castellan, Andrea Piovano, Alexandre Ivanov, Valentina M. Giordano
  State of the article: manuscript.

Finally, I will provide some conclusions and thoughts on how my thesis work advances our knowledge not only on complexity but also on heat transport in crystalline systems. As the articles listed above represent the bulk of my Ph.D. work, their text and figures will be referenced throughout the following thesis chapters. The articles themselves have been integrated into Chapter 4 for the reader's convenience.

CHAPTER 1

Heat Propagation in Complex and Disordered Systems

The increasing demand for green energy methods and technologies is driving research communities to develop new and innovative ways to meet these needs [10, 11], giving renewed attention to thermoelectricity. Thermal design of materials has taken center stage for applications such as thermoelectric converters, thermal diodes, thermal barriers, etc. This is also the reason that heat transport is often discussed in the context of thermoelectric materials. Much is already understood about the macroscopic properties, such as thermal and electrical conductivity, of the materials that are currently on the market. However, if we want to look beyond what is already commercially available, next-generation thermal devices require a deeper level of understanding.

1.1 Optimization of the dimensionless figure of merit

Customizing or tuning the properties of a thermoelectric device requires optimization of the dimensionless figure of merit, ZT. A derivation of ZT through the use of a basic thermoelectric generator can be found in the Appendix A. In general, a large Seebeck coefficient, S, and electrical conductivity σ, and a small thermal conductivity, κ, help raise ZT towards the Carnot, or maximum, efficiency for a given temperature range of T [1], as shown in eq. 1.1.

$$ZT = \frac{S^2\sigma}{\kappa}T \tag{1.1}$$

Fig. 1.1 summarizes the temperature dependence of ZT for materials that are currently the focus of thermoelectric applications. At the time of writing, the highest ZT coefficient of these sets of materials is $\sim$2.

G. A. Slack famously developed the Phonon Glass Electron Crystal (PGEC) concept in the 1990s [12] as a way of suggesting several directions that the scientific community should take in order to engineer better thermoelectric materials with a higher ZT. As the name suggests, a PGEC should exhibit glasslike thermal conductivity and crystalline or semiconductor-level electrical conductivity in order to maximize the effects on the ZT coefficient. As we will discuss later in this chapter, the term *glasslike* refers to the signature plateau and temperature independence of the thermal conductivity in glasses, and therefore for PGECs it represents the need to find semiconducting materials that replicate this behavior.

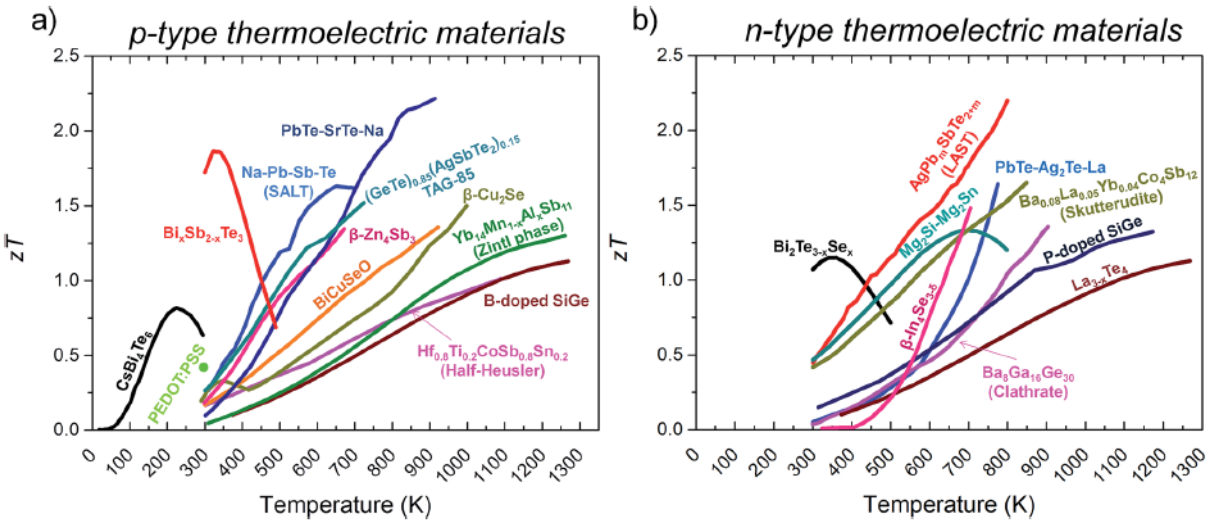

Figure 1.1: Temperature dependence of the figure of merit, *ZT. A sampling of (a) p-type and (b) n-type materials that exhibit a promising figure of merit, ZT, are plotted with temperature. Current state-of-the-art materials exhibit a maximum of $ZT \sim 2$. Notable materials that will be referred to in this thesis are Bi_2Te_3 and Sb_2Te_3 based materials, skutterudites, and clathrates. Figure comes directly from Ref. [13].*

There are therefore two main methods of optimizing ZT for a given material that have developed especially since the debut of Slack's PGEC concept: maximizing the thermoelectric power factor, $S^2\sigma$, and minimizing κ [14, 15]. The first school of thought towards maximization of $S^2\sigma$ is centered around PbTe, Bi_2Te_3, and Sb_2Te_3 based materials [16–18], as these have been proven to have a high ZT coefficient, even up to 1.8 [19], and therefore provide a starting place for further enhancement or materials engineering. They have been termed as benchmark thermoelectric materials for this reason. Research has shown that the ZT coefficient of these materials can be increased by focusing on engineering charge carrier concentration [20, 21] and/or blocking minority charge carriers [22], and by band convergence of the valence or conduction bands [19].

The second main school of thought for the optimization of ZT is to concentrate on limiting κ in the material [23, 24], and materials such as clathrates and skutterudites [25–30] with ZT~$1.35 - 1.7$ [13] fit into this category. Thermal conductivity, κ, is made up of two components: electronic, κ_{elect}, and lattice, κ_L, thermal conductivity. As a first approximation, the electronic component of thermal conductivity can be described by the Wiedemann-Franz-Lorenz Law, shown in eq. 1.2, which depends on σ, and where $L(T)$ is the Lorenz number, and T is temperature [30].

$$\kappa_{\text{elect}} = LT\sigma \tag{1.2}$$

There is an important implication associated to the κ_{elect} formula, which is that it depends on σ, which is also found in the numerator of the equation for ZT. This means that electrical and thermal conductivities can never be truly decoupled. Rather, we must search for a material that is dominated by the lattice component of thermal conductivity in order to decrease the influence of σ on κ.

The lattice component of thermal conductivity, on the other hand, depends on the heat capacity of the material, C_V, and on the group velocities, v_g, and the lifetimes, τ, of the phonons in the material, and is integrated across the full energy range [24].

$$\kappa_L = \frac{1}{3}\int_0^{\omega_{max}} C_V(\omega,T)v_g^2(\omega)\tau(\omega,T)\ d\omega \tag{1.3}$$

The lattice component is therefore dependent upon properties of the quasiparticle responsible for heat transport, the phonon. Chapter 2 will delve into phonon theory and detail the relevant phonon parameters that we concentrate on measuring and simulating in order to understand thermal transport properties in complex and disordered systems. However, in order to introduce the four systems relevant to my Ph.D. work in the following sections of this chapter, I will give a brief introduction here based on the components of eq. 1.3.

The phonon, or the quantized form of a lattice vibration, is a collective traveling plane wave that has a distinct wavevector $\mathbf{q}$, vibrational frequency ω, and polarization $\boldsymbol{\xi}$ [31]. Together, phonons form a dispersion relation, $\omega(q)$, within a given energy spectrum (usually in the tens of meV range). The group velocity in eq. 1.3 is therefore the local slope of the dispersion relation, $v_g(\omega) = \frac{\partial\omega}{\partial q}$, in a given direction.

Continuing with definitions for the terms given in eq. 1.3, heat capacity is defined as the amount of energy required to change the temperature of a material by one degree Kelvin. Group velocity and heat capacity are determined by the phonon dispersions and Bose-Einstein statistics, which in turn are needed to calculate all thermodynamic phonon properties. Thermodynamic properties out of equilibrium, however, require the energy and temperature dependence of phonon lifetime, $\tau(\omega, T)$. Phonon lifetime is the amount of time phonons propagate through a lattice before being scattered. It therefore defines the thermal resistance of a given material, and is dependent upon the chemical structure of said material.

Phonon lifetime and phonon scattering processes will remain a theme throughout this thesis, as we must first understand how microscopic heat transport is either successfully conducted or limited in a given material if we are to understand how we can manipulate or tune the κ_L value for an overall improved ZT coefficient. Towards this end, P. G. Klemens and J. Callaway derived simplified equations for the temperature and energy dependencies of the common types of phonon scattering mechanisms for crystalline systems in the 1950s [32, 33], which were then added onto by W. A. Kamitakahara and B. N. Brockhouse in the 1970s [34]. When working in the microscale, we must consider what can scatter a phonon, and these potential mechanisms usually come from the interactions of a phonon with other phonon(s), with other particles such as electrons, with a defect in the crystal, with a grain boundary in the material, and/or from the mass and force-constant fluctuations in the lattice.

Assuming that all of the above mentioned scattering processes are independent of one another, the total phonon lifetime can be calculated using the Matthiessen rule, as seen in eq. 1.4, where A is the concentration of defects in the material, B is a constant that depends on the Debye temperature (see Section 2.2) of the material, v_s is the sound velocity, L is the length between boundaries in the material or sample, V is the volume of the unit cell, and $g(\omega)$ is the vibrational density of states. The τ_M^{-1} and τ_{FC}^{-1} terms also include summations based on the fractional contribution of atom type i in the unit cell, its mass m_i and force constant F_i, and the average mass $\overline{m}$ and force constant $\overline{F}$ in the unit cell.

$$\begin{aligned}\tau_{tot}^{-1} &= \tau_d^{-1} + \tau_U^{-1} + \tau_b^{-1} + \tau_{e-ph}^{-1} + \tau_M^{-1} + \tau_{FC}^{-1} \\ &= A\omega^4 + B(T)T\omega^2 + v_s/L + C\frac{\lambda\langle\omega^2\rangle}{T} \\ &+ \frac{\pi V\omega^2 g(\omega)}{6}\sum_i f_i\left(\frac{\overline{m} - m_i}{\overline{m}}\right)^2 + \frac{\pi V\omega^2 g(\omega)}{3}\sum_i f_i\left(\frac{\overline{F} - F_i}{\overline{F}}\right)^2\end{aligned} \tag{1.4}$$

Relaxation time of Umklapp (τ_U), point defect (τ_d) processes are energy ($\hbar\omega$) dependent, and Umklapp processes are also temperature (T) dependent. Relaxation time of grain boundaries (τ_b) depends on the grain size and is therefore related to the microstructure of the material. The formula for electron-phonon coupling relaxation time (τ_{e-ph}) depends on the second moment of Eliashberg's spectral function [35], $\lambda\langle\omega^2\rangle$, as seen in eq. 1.4, and on the constant C, but the use

of T in the function varies slightly with application. For many years, the two-temperature model (TTM) was used, which describes two main temperature ranges, the electron temperature (T_e) and lattice temperature (T_l) [36–38]. The key assumption in this model is that $\tau_{e-ph} >> \tau_{e-e}$, where τ_{e-e} are electron-electron relaxation times. In this case, $T = T_e$. For regions where it cannot be assumed that $\tau_{e-ph} >> \tau_{e-e}$, $T = T_l$ [39]. Finally, the relaxation times for mass (τ_M^{-1}) and force constant (τ_{FC}^{-1}) disorder can be used when there is a random distribution of atoms in the lattice. We will keep these in mind for Section 1.3.4, in which a random solid solution alloy is discussed.

The temperature dependence of the majority of these scattering mechanisms are plotted against thermal conductivity for a typical crystalline solid in Fig. 1.2. As seen in the figure, phonon scattering by grain boundaries, electron coupling, and impurities (point defects) dominate at low temperature while phonon-phonon scattering takes precedence at higher temperature. At low temperature, the thermal conductivity is expected to vary with T^3 due to the fact that the heat capacity has a T^3 dependence at low temperature, and close to a temperature of zero the heat capacity term of thermal conductivity dominates. This is also called the specific heat effect [31, 40]. Next, the peak in thermal conductivity, often called the Umklapp peak, comes from the dominance of Umklapp, or phonon-phonon, scattering processes, along with the contribution of phonon-impurity scattering. Finally, the $1/T$ dependence typical of crystals at high temperature comes from the Slack relation that says that high temperature thermal conductivity is dominated by three-phonon scattering processes [40, 41].

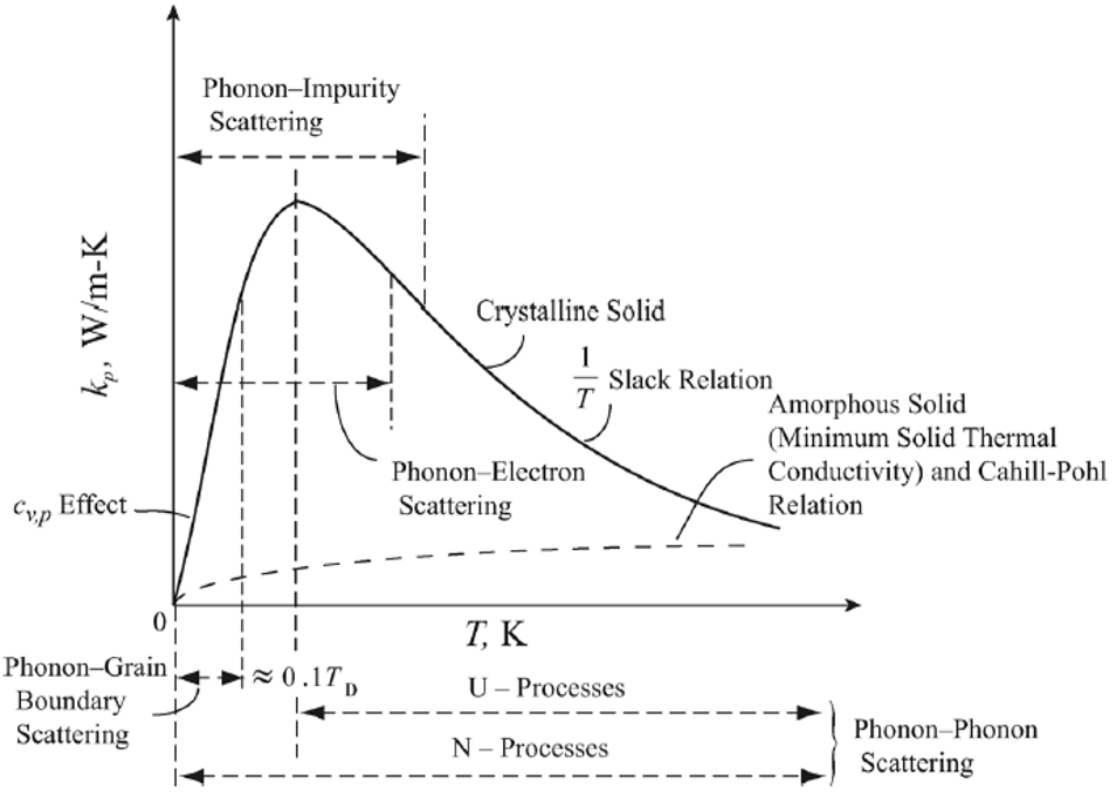

Figure 1.2: Temperature dependence of phonon scattering processes within thermal conductivity. *The regions of importance for the phonon scattering mechanisms discussed in eq. 1.4 are depicted for the thermal conductivity of a typical crystalline solid. Figure comes directly from Ref. [40].*

As we will see in Fig. 1.3 of Section 1.3, the complex and disordered materials that are the subject of my thesis tend to stray from these particular signatures of crystalline thermal

conductivity, namely the Umklapp peak at low temperature and $1/T$ dependence at high temperature. This points towards enhanced phonon scattering mechanisms that further limit the thermal conductivity in these systems.

While these equations for the major phonon scattering mechanisms in crystals provide a guide, they rarely are able to perfectly demonstrate the full, complete description of phonon scattering processes in non-simple systems. In fact Klemens clearly defines the range of expected operation for these formulas as being limited to monatomic and diatomic lattice systems. I reiterate from the General Introduction chapter of this thesis that we lack enough systematic experimental data to draw such general conclusions for more complex and disordered systems, especially when more than one type of phonon scattering mechanism is usually at play. The remaining sections of this chapter will focus on systems which have complex or otherwise disordered chemical structures that limit phonon propagation, and specifically the four specific systems that were studied during my Ph.D. work.

1.2 Defining Complexity

For clarity and consistency within this thesis, I will attempt to define complexity and disorder as they pertain to crystalline systems. These will be by no means exhaustive definitions, but they are merely meant to provide context and set the stage for the discussions proposed in the later text. I will purposefully try to keep these definitions as general and broad as possible, knowing that these terms are open to different interpretations within the scientific community.

One of the more straightforward ways to define structural complexity in the case of periodic crystals is to categorize it by the number of atoms per unit cell. If we consider the nearest-neighbor atomic interactions in a 1D chain of atoms which has alternating atoms of different mass, we know this to cause two phonon branches, one acoustic and one optic, with a gap in between the two branches [31] (see Section 2.1 for an example). As we add more atoms per unit cell and expand to a 3D model, we add more optical branches and decrease the size of the gaps between the branches. This effectively compresses the acoustic regime responsible for the heat-carrying phonons. With this overly simplified explanation, we can begin to see how we can impact lattice thermal conductivity simply by increasing the number of atoms per unit cell.

To this hand-waving explanation I add one for structurally complex systems. If we imagine the extreme case of N = 50+ atoms per unit cell, we not only compress the acoustic regime, but the rest of the available phase space is then taken up with N-1 optical branches with little gap in between each branch. With so many flattened, closely-packed branches, we expect phonon-phonon scattering mechanisms to become more relevant. This is the method behind the study of skutterudites, tetrahedrites, and clathrates as thermoelectric materials. (This will be discussed in more detail in Section 1.3.3.) Yet another extreme case is that of aperiodic crystals such as quasicrystals, which have an infinite number of atoms per unit cell while still maintaining long-range order [42]. They too have a succession of dispersionless and broad optical-like branches.

A large number of atoms per unit cell is therefore one form of structural complexity. I will also attempt to explain structural complexity through the possible "ingredients" of complexity that we see in different types of crystalline systems. Having many atoms per unit cell is one form of complexity not only because there are many branches packed closely together that create a continuum of optical branches, but also because atoms of different masses within the system may contribute unevenly both in phase and momentum space. In other words, moving from a one-element system to a multi-element system creates complexity.

Other sources of complexity include making atomic substitutions, inducing vacancies, and otherwise doping a structure. Furthermore, these sources can cause structural and chemical disorder in the form(s) of lattice distortions, strain, or chemical short-range ordering. Lattice

distortions and strain can cause certain atoms to be displaced from their equilibrium position, disrupting the ability of lattice vibrations to propagate, while chemical short-range ordering can be responsible for changing the local atomic environment, even if the global chemical and crystallographic structure is maintained. We must furthermore consider the local, microscopic disorder caused by chemical short-range ordering since it plays a role in how the lattice vibrations cope in this local environment, which also changes with the wavelength of the lattice vibration in consideration.

These sources of complexity impact the phononic momentum phase space and also change the way that phonons are scattered in a material, defining the scattering processes of said system. Looking again at the phonon lifetime formulas in eq. 1.4, vacancy or impurity scattering, grain boundary scattering, and electron-phonon scattering are all possible phonon scattering mechanisms that are usually considered in non-simple crystalline systems. Furthermore, having many atoms per unit cell increases the number of phonon branches in the optical phonon region, and this is then often associated with the Umklapp phonon-phonon scattering mechanism since there are more phonons available for phonon-phonon scattering interactions. More globally, we must also assume that when multiple phonon scattering processes exist, they add to the overall temperature and momentum dependence of phonon scattering in perhaps unconventional ways.

My Ph.D work is focused on isolating the effects that different types of complexity have on phonon lifetime. The goals are two-fold: (1) we need to increase the available experimentally-measured phonon lifetime data on all types of systems (simple, non-simple, and complex) in order to track patterns and draw conclusions on how specific phonon scattering mechanisms influence thermal conductivity, and (2) we need to complement these experiments with sufficient atomistic models that can explain these experimental findings. However, there are current limitations, both experimentally and theoretically, to these tasks. In Section 1.4, I provide this state-of-the-art, and enumerate the directions experimentalists and theoreticians are taking to overcome current limitations. First however, in Section 1.3, I would like to elaborate on the different families of systems that can exhibit forms of complexity, and, in particular, introduce the four systems that will be the focus of this thesis work.

1.3 Case Studies for the Effect of Structural Complexity on Phonon Behavior

As mentioned in the General Introduction of this thesis, there has been particular interest in recent decades on the heat propagation in glasses, aperiodic crystals, and complex metallic alloys, as these materials pose both unknowns in terms of their microscopic thermal transport mechanisms and have the potential for thermal-related applications.

As shown in Fig. 1.2, crystalline materials usually have a large peak in thermal conductivity centered around 10 K known as the Umklapp peak, which is associated with the multiphonon scattering mechanism. They are also characterized by a vibrational density of states that generally follows the Debye model, or an energy squared dependence [31]. Glasses, on the other hand, have a plateau in this same region of thermal conductivity, which can be understood in terms of a strong phonon lifetime reduction at energies of a few meV [43]. It was also observed in glasses, however, that there is often a peak that appears in the vibrational density of states, normalized by the Debye law, at these energies as well, emphasizing a strict departure from the Debye model prediction [44, 45] (see Section 2.2 for explanation of the Debye relation). This peak became widely known as the Boson peak.

The nature of the Boson peak found in glasses has since been a central debate within the glasses community, as it represents an anomaly and excess in the expected number of vibrational states [46]. Chumakov *et al.* [47] were able show experimental evidence that there was a

correlation between the van Hove singularity in the transverse acoustic phonon branch in crystals and the location of the Boson peak in glasses, which was a concept previously proposed by Taraskin *et al.* [48]. They found that the Boson peak of a $Na_2FeSi_3O_{8.5}$ glass corresponded to the energy of the flattening of the transverse acoustic phonon branch in the polycrystalline version $NaFeSi_2O_6$. This has continued to spark much debate within the community, and in particular has attracted scientists from other communities for disordered systems to contribute towards this particular explanation and to "demystifying" the Boson peak in glasses [46, 49–53]. At the time of writing, the conversation is still hotly debated, but, globally, has turned towards the importance of the inclusion of disorder in explaining such phenomena [54–56], once again circling back to the study of complexity for thermal transport.

This prompted the use of the term "glasslike" within the complex crystalline systems communities, as this plateau in the thermal conductivity of glasses exemplified the target of tuning PGEC crystalline systems into having a low and temperature-independent lattice thermal conductivity. There is the idea that, on the spectrum between completely harmonic crystals and completely disordered glasses, there exist anharmonic crystals and harmonic glasses, which contain certain properties or characteristics from the opposing side of the spectrum, respectively. Such is the case for type-I clathrates, which have a large temperature-independent region of thermal conductivity [30]. This term, *glasslike*, comes from the likeness of this temperature-independent region of thermal conductivity to glasses, and has promoted cross-communication between these respective communities as we search for a unified explanation of thermal transport that functions for both glasses and crystals. However, separating the impacts of anharmonicity, lattice substitutions, and the guest/host cage structure of such systems has proven to be quite the challenge for the community [25–30]. I will detail the main conclusions that the community has been able to draw up to the moment of writing this thesis in Section 1.3.3, and then further elaborate on the topic with my newly published work on the type-I clathrate $Ba_{7.81}Ge_{40.67}Au_{5.33}$ [57].

Glasslike thermal conductivity is not limited to PGECs alone, however. In fact, in order to tackle complex crystalline systems, we should also analyze the disorder-induced glasslike thermal conductivity of simpler systems. In the effort to understand complexity from all angles, therefore, I entreat the reader to also allow me to reference other systems such as Barium Fluoride with Lanthanum substitutions (Section 1.3.1) and Yttria-Stabilized Zirconia (Section 1.3.2), which also have glasslike thermal conductivity behaviors. In these cases, the complexity comes from substitutions made to the lattice and the resulting chemical short-range ordering. These systems are of particular interest because they allow us to distort the original simple systems, Barium Fluoride and Zirconia, and study the resulting complexity and glasslike thermal conductivity which is dominated by chemical short-range ordering. By analyzing the impact of complexity firstly on simple systems that have been strategically distorted, we can then attempt to build up to an understanding of systems such as clathrates.

Yet another lens with which we can view the types of complexity is by analyzing systems that fall along the spectrum between a perfectly ordered crystalline structure and a completely disordered glass. The logic follows that if we want to induce glasslike properties onto crystalline systems, we need to choose crystalline systems that imitate the types of disorder seen in glasses. For example, high-entropy alloys (HEAs) are a subcategory of alloys that are considered to be random solid solutions. They have no one principle element, and instead have an equimolar, random distribution of four or more elements. This brings in to question the validity of Bloch's theorem, and what, if any, phonon propagation would be allowed in such a system. HEAs provide a plethora of potential study groups, with potential complexities ranging from atomic size and mass differences, to chemical short-range ordering, and force-constant fluctuations. By choosing elements for an HEA that can help bring out or isolate one of these types of complexity,

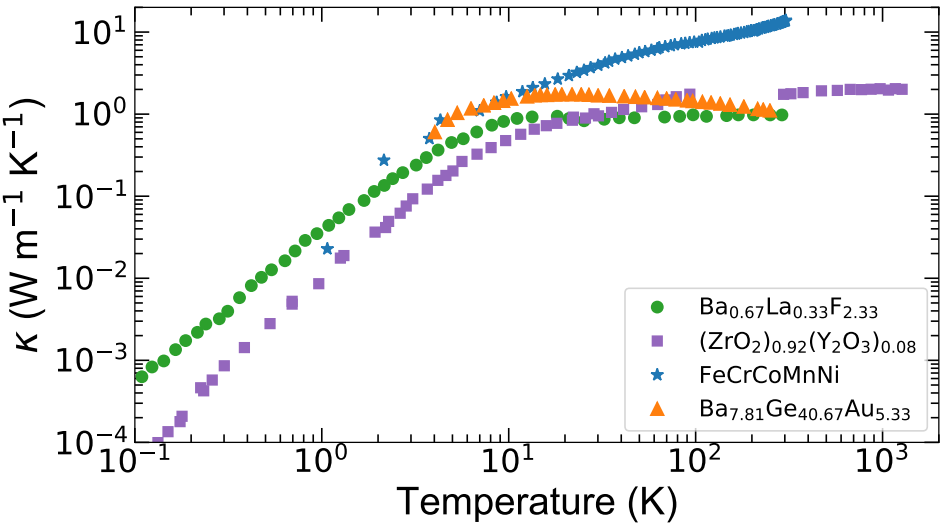

Figure 1.3: Thermal conductivities of the four materials of interest. *The thermal conductivities for each of my four materials of interest are plotted, including the high-entropy alloy FeCoCrMnNi (blue stars) [58], the type-I clathrate $Ba_{7.81}Ge_{40.67}Au_{5.33}$ (orange triangles) [27], $Ba_{0.67}La_{0.33}F_{2.33}$ (green circles) [59], and $(ZrO_2)_{0.92}(Y_2O_3)_{0.08}$ (purple squares), also called Yttria-Stabilized Zirconia. The Yttria-Stabilized Zirconia represents the combined data of Schlichting et al. [60] and Ackerman et al. [61], both of which used samples with 8 mol% Yttria.*

we can cocktail our own specific complexity study and begin to engineer properties of glasses onto crystals (Section 1.3.4).

To this end, I have chosen these four materials that each have specific types of complexity that contribute to their unique thermal conductivities. In the following subsections, I will briefly describe each material that I have worked on and give the context for studying each system, particularly emphasizing how their κ dependencies can be manipulated or engineered through an understanding of the disorder and phonon scattering mechanisms at play in each case. With this method in mind, I have probed different aspects of complexity and disorder within the systems studied, bringing us as a scientific community closer to a unified understanding of heat propagation and thermal transport in complex and disordered crystalline systems.

The thermal conductivities of my systems have also been plotted together in Fig. 1.3 for reference. The $Ba_{7.81}Ge_{40.67}Au_{5.33}$ [27], $Ba_{0.67}La_{0.33}F_{2.33}$ [59], and Yttria-Stabilized Zirconia [60, 61] all show large temperature-independent regions of thermal conductivity close to 1 $Wm^{-1}K^{-1}$. FeCoCrMnNi [58], on the other hand, being a concentrated metallic alloy, has an electronic component of thermal conductivity that is considerably higher than those of the other three systems, which accounts for the near-linear increase in thermal conductivity at higher temperatures.

1.3.1 Lanthanum-doped Barium Fluoride

In order to understand how we can manipulate the glasslike thermal conductivity behavior that is seen in complex crystalline systems such as clathrates, it is useful to also study doped fluorides, in which this glasslike behavior is also present. Heat transport in amorphous solids has been a topic of discussion for decades [43, 62, 63]. In this particular example, random La substitutions for Ba atoms are made in the fluoride BaF_2, following the chemical equation $(BaF_2)_{1-x}(LaF_3)_x$ [64, 65], as seen in Fig. 1.4. This causes an excess interstitial F^{-1} for every La^{3+} that replaces a Ba^{2+} on the lattice [63]. As detailed by Andersen *et al.* [62], when substantial amounts of substitutions have been made, such as when $x = 0.33$, the thermal conductivity

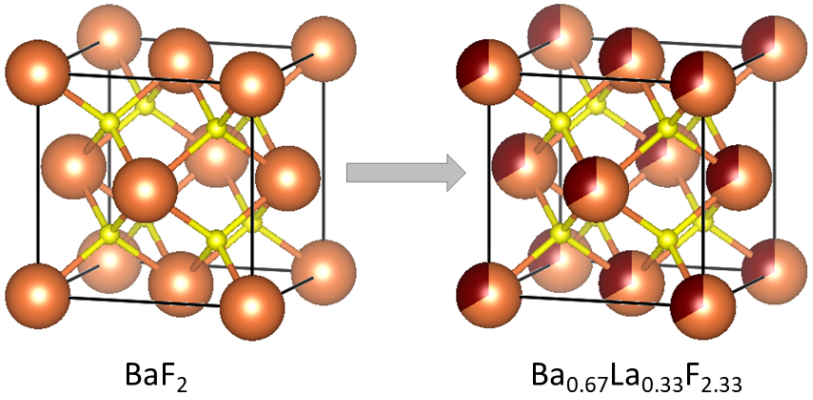

Figure 1.4: Crystallographic structure of $Ba_{0.67}La_{0.33}F_{2.33}$. *On the left, the pure BaF_2 structure is presented, with F (yellow) and Ba atoms (orange) forming an FCC structure with a lattice parameter of 6.20 Å. On the right, a symbolic representation of random La substitutions (brown) being made to the lattice, following the formula $(BaF_2)_{1-x}(LaF_3)_x$ for x=0.33, with a lattice parameter of 6.09 Å. Further information about the placement of the resulting F interstitials can be found in Andersen et al. [62] and Cahill and Pohl [63].*

drops from 10 $Wm^{-1}K^{-1}$ to 1 $Wm^{-1}K^{-1}$ at room temperature. This phenomenon is, in fact, common to Yttria-Stabilized Zirconia, another fluorite structured crystal that will be discussed in Section 1.3.2, as well as other similarly disordered solids [59].

In the case of $Ba_{0.67}La_{0.33}F_{2.33}$, the substitutions cause inherent changes to the 222 clusters found in the pure BaF_2 form. While the 222 clusters in pure BaF_2 are due to vacancies, in $Ba_{0.67}La_{0.33}F_{2.33}$ the clusters are associated with the charge balance that occurs between F interstitial and La substitutional atoms [66]. This seems to balance the clusters, stabilizing them and making them order themselves and form aggregates.

Therefore, these atomic replacements in going from the pure BaF_2 lattice to $Ba_{0.67}La_{0.33}F_{2.33}$ manifest themselves as aggregates of these clusters, a type of chemical short range ordering on the lattice. The $Ba_{0.67}La_{0.33}F_{2.33}$ structure is therefore markedly different, and distorted, from the pure one. This, in turn, is thought to be at the root of the glasslike thermal conductivity of $Ba_{0.67}La_{0.33}F_{2.33}$. This defect structure manifests itself in the diffraction pattern of the material by the occurrence of broad and intense elastic diffuse scattering [62]. In terms of the effect on phonon behavior, it is a signature that the Bloch theorem is no longer completely valid, and it causes additional phonon broadening and/or weakening for phonons dispersing from Bragg peaks near these satellites (Turner *et al.*, unpublished).

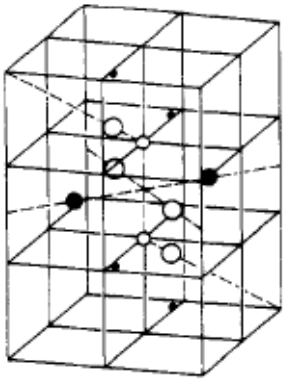

Figure 1.5: Example of a 222 Cluster in $(BaF_2)_{1-x}(LaF_3)_x$. *A Ba^{2+} site (empty circle) get replaced by La^{3+} (large black circle) according to the amount of substitutions defined by x in the chemical formula $(BaF_2)_{1-x}(LaF_3)_x$, and this results in an excess interstitial F^{-1} (small black circle), forming the particular pattern known as the 222 cluster [66]. Figure has been taken directly from Ref. [62].*

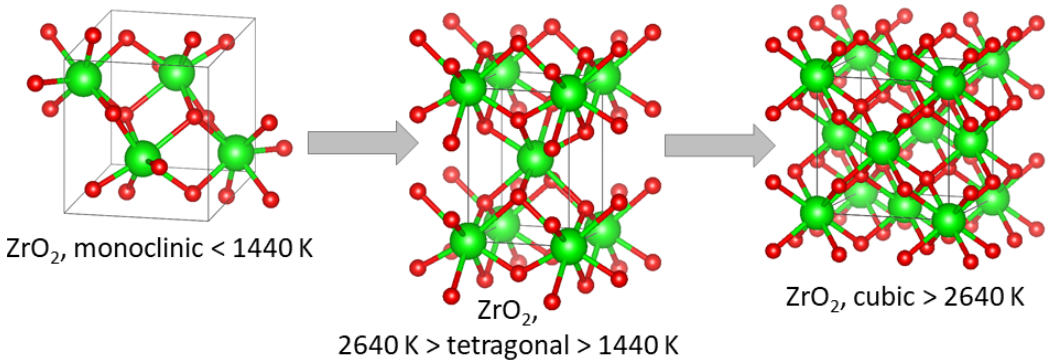

Figure 1.6: Crystallographic structures of Zirconia. *From left to right and by increasing temperature: ZrO_2 is monoclinic at room temperature, tetragonal between temperatures of 1440 and 2640 K, and cubic (FCC) above 2640 K. Zr atoms are represented in green and O atoms in red.*

1.3.2 Yttria-Stabilized Zirconia

Zirconia is a ceramic material of great interest for applications such as electrochemical cells, catalytic converters, and thermal barrier coatings. It is often used in high temperature situations due to its high fracture toughness, stability, and low thermal conductivity [67, 68]. These properties can be improved upon with the doping of rare-earth elements such as Mg or Ca, or with Yttria, Y_2O_3 [69] (chemical structure given in Fig. **??**). Pure Zirconia is monoclinic at room temperature, and becomes tetragonal at 1440 K, and then cubic at 2640 K, as seen in Fig. 1.6. However, doping with rare-earth elements stabilizes the cubic phase at room temperature. Particularly with the doping of Yttria as well, the thermal conductivity becomes glasslike, and applications focus on thermal barrier coatings and ion conductors in solid oxide fuel cells [70, 71]. More than 4 mol.% Yttria forces the cubic structure to stabilize at room temperature through oxygen vacancies that form due to the mismatch in charge between Zr and Y ions, giving this chemically disordered system the name Yttria-Stabilized Zirconia (YSZ) [72]. These oxygen vacancies are the key to the glasslike thermal conductivity of Yttria-Stabilized Zirconia, since they act as an extended defect structure and scatter phonons [67, 73].

These oxygen vacancies are created in order to maintain the overall charge balance of the lattice when one Y^{3+} ion replaces two Zr^{4+} ions [72]. The lattice balances itself according to the following equation, where charge balance is determined by the original ZrO_2 lattice: $Y_2O_3 \rightarrow 2Y'_{Zr} + V_O^{\cdot\cdot} + 3O_O^x$. For every two Y^{3+} ions that enter the lattice on Zr^{4+} sites, two Zr^{4+} ions are replaced (Y'_{Zr}). Additionally, there are 3 O^{2-} ions (O_O^x). This imbalance in charge between Zr and Y, however, causes an oxygen vacancy, $V_O^{\cdot\cdot}$ [67, 69].

Interestingly, it appears that there is a certain molar concentration of Yttria that creates a minimum of thermal conductivity for a temperature range of 300-800 K, after which point the thermal conductivity begins to increase again for higher doping concentrations. That point falls at 10 mol.% Yttria doping [73]. The idea proposed by Welberry *et al.* [74–76] and then further developed by Goff *et al.* [77] is that below 10 mol.% Yttria doping, the oxygen vacancies form divacancy clusters that are rather isolated from one another. As the name implies, a divacancy cluster is a $V_O^{\cdot\cdot} \rightarrow Zr^{4+} \rightarrow V_O^{\cdot\cdot}$ pattern that forms. Above this Yttria concentration, however, the oxygen vacancy clusters form into aggregates that order themselves, creating a local periodic field. It is within this change in defect structure that the distinction in thermal conductivity lies. It should be noted as well that, although the divacancy clusters with 10 mol.% Yttria concentration are labeled as isolated defects, we cannot consider them as producing a "textbook" point defect phonon scattering mechanism. The exact vacancy placements on the lattice, even at low Yttria concentrations, should be considered as chemical short-range ordering, which then

induces significant lattice distortions and gives rise to intense diffuse scattering corresponding to defects extended onto several atomic distances, the characteristics and sizes of which have been extensively documented by Welberry *et al.* [74–76] and Goff *et al.* [77].

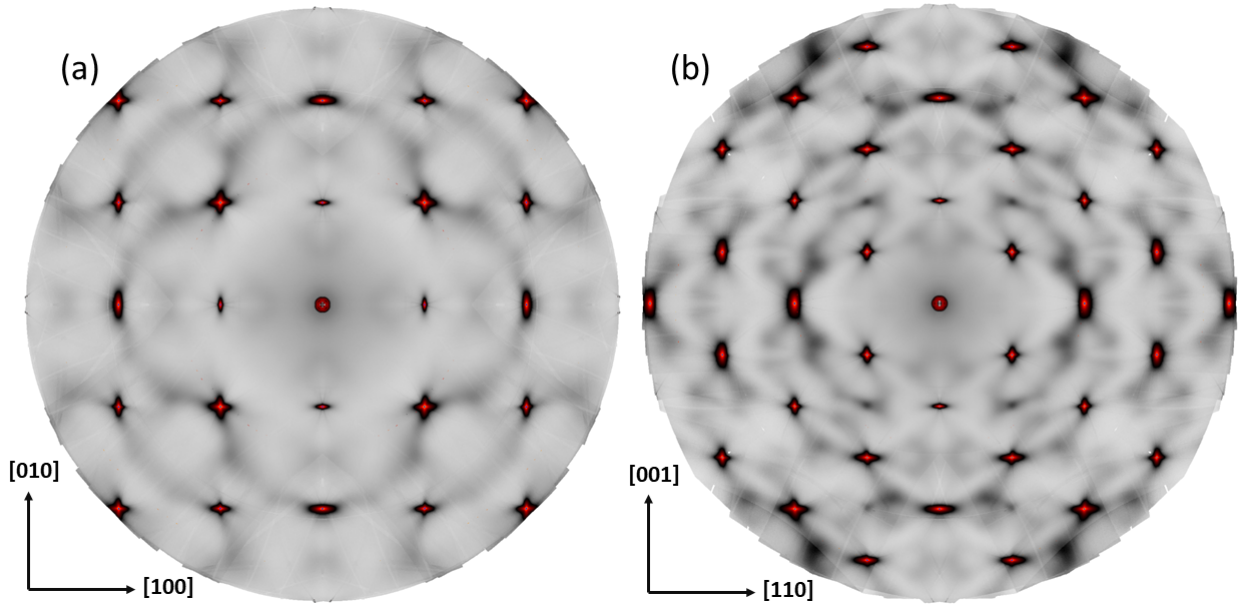

Figure 1.8: Thermal diffuse scattering in Yttria-Stabilized Zirconia. *The experimentally-measured diffuse scattering for $(ZrO_2)_{1-x}(Y_2O_3)_x$ containing 9.5 mol.% Y_2O_3 at 300 K have been plotted for the scattering plane [100][010] in (a) and [110][001] in (b) using the diffractometer on the ID28 beamline at the ESRF, an incoming wavelength of $\lambda = 0.697$ Å, and a typical beam size of about 40 µm FWHM. A 360° rotation with a step size of 0.25° was achieved using the PILATUS3 1M detector in shutterless mode, which was placed 244 mm away from the sample with elevations of both 19° and 48° above horizontal. CrysAlis software (Rigaku Oxford Diffraction) was used to refine the experimental geometry and orientation matrix, and locally developed software was used for high-resolution 2D reconstructions. Data are represented in a mixed lin-log scale using Albula by Dectris.*

An example of such diffuse scattering is shown in Fig. 1.8 for $(ZrO_2)_{1-x}(Y_2O_3)_x$ with a 9.5 mol.% Y_2O_3 concentration. The [100][010] scattering plane shown in (a) contains an arc pattern that appears more intense near the (400) Bragg peak series. In the [110][001] scattering plane shown in (b), however, the diffuse scattering creates quite a complex pattern that varies much more with direction and **Q**, noting as well that the sizes, shapes, and intensities of the diffuse satellites vary greatly. It is easy to see the reflected disorder of this system with these maps as they indicate that there is intense diffuse scattering that appears in every high-symmetry direction.

Coming back to this idea of isolated defects that turn into a form of chemical short-range ordering dependent upon the level of doping: it is supported by the derivation given by Févre *et al.* [73], in which the distance between two oxygen vacancies (d) can be related to the molar concentration of Yttria (x) and the lattice parameter of Yttria-Stabilized Zirconia (a=5.16 Å):

$$d = \frac{a}{2}\left[\frac{x}{2(1+x)}\right]^{-1/3} \tag{1.5}$$

Following this equation, the distance between oxygen vacancies is $1.5a$ for 10 mol.% Yttria-Stabilized Zirconia, but it quickly drops inverse-exponentially. As molar concentration of Yttria increases and the oxygen vacancy clusters begin to order themselves into aggregates, the isolated defect scattering mechanism will give way to a dependency related to the ordering of the vacancy

aggregates, causing the thermal conductivity to slightly increase. Goff *et al.* [77] confirmed that the oxygen vacancies order themselves differently according to Yttria concentration, and Cousland *et al.* [72] further defined that the oxygen vacancies align along the [111] direction for Yttria concentration of 9 mol.%, and form an O $\rightarrow V_{\mathrm{O}}^{\cdot\cdot} \rightarrow \mathrm{Zr}^{4+}$ pattern along the [112] direction (a slightly modified ordering opposed to that of Goff *et al.* [77]). Naturally, there were extensive lattice dynamics studies [72, 78–80] being contributed in parallel to this story line which gave information about how phonons were affected by this defect structure. In my unpublished manuscript, Turner *et al.* [81], we provide new insight into the evidence of disorder-induced low-lying optical phonon branches for the same 9.5 mol.% Y_2O_3 concentration sample whose diffuse scattering patterns are shown in Fig. 1.8.

1.3.3 Type-I Clathrates

As was introduced in Section 1.2, clathrates and other systems with many atoms per unit cell fall into the category of Slack's PGECs. A wide range of publications have also shown us that these materials are extremely customizable in terms of affecting κ_L and the Seebeck coefficient [30]. For instance, Suekuni *et al.* [82] have shown that changing the Ge content in $\mathrm{Sr_8Ga_{16}Si_{30-x}Ge_x}$ alters the size of the cages, which in turn lowers and flattens κ_L. Ye *et al.* [83] as well were able to produce *n*- and *p*-type samples, with both positive and negative Seebeck coefficients, and crystal-like and glasslike lattice thermal conductivities simply by changing the amount of Au substitutions to the clathrate series $\mathrm{Ba_8Au_xGa_{16-3x}Ge_{30-2x}}$. Such publications are perfect examples of how we can engineer complexity and disorder onto materials in order to manipulate thermal conductivity.

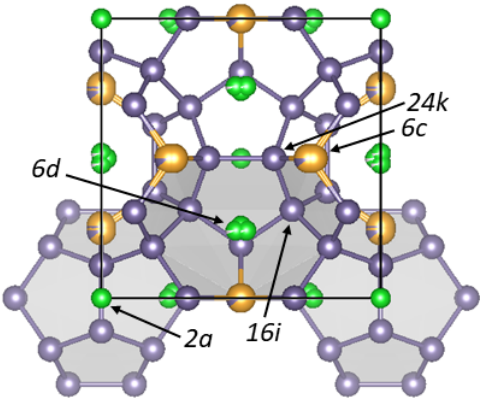

Figure 1.9: Crystallographic structure of the type-I clathrate $Ba_{7.81}Ge_{40.67}Au_{5.33}$. *Cages are formed by Ge atoms (light grey) with Au substitutions (gold) such that the cages are slightly distorted or compacted. Ba atoms (green) near the center of the cages have a slight off-centering due to the number and placement of the Au substitutions on the cage. Despite the complex structure, type-I clathrates form simple cubic structures with a lattice parameter of 10.8 Å. Figure has been taken directly from Fig. 1(a) in Turner et al. [57].*

Type-I clathrates specifically have a cage structure in which a host network of atoms surrounds a guest atom at the center of each cage. They consist of 2 dodecahedrons and 6 tetrakaidecahedrons per unit cell [84]. The cages of clathrates have an electrical conductivity on the level of a highly-doped semiconductor, while the atoms at the cage centers remain only loosely bonded to the cage, which disrupts the propagation of phonons, allowing clathrates to maintain a low and almost temperature-independent thermal conductivity.

In the case of the clathrate chosen for my Ph.D work, $\mathrm{Ba_{7.81}Ge_{40.67}Au_{5.33}}$, the Germanium cage maintains the electrical conductivity of a highly-doped semiconductor, while the Barium "rattler" atom disrupts the phonon propagation and therefore thermal conductivity. The rattler atom causes low-lying optical modes to cut off the acoustic phonon dispersion, limiting the available phase space for propagating, heat-carrying acoustic phonons. Since this is such a defining characteristic in the lattice thermal conductivity of clathrates, we can actually rewrite eq 1.3 as the following [57], where $E_1^{\nu}(T)$ marks the energy of the first optical mode, i.e. the cut off of the acoustic phonon regime. (The $\rho^{\nu}(\omega_{\mathbf{q}})$ term refers to the mode-specific phononic

density of states, and will be defined in Section 2.2.)

$$\kappa_L^{ac}(T) = \sum_{\nu} \int_0^{E_1^{\nu}(T)} \kappa_L^{ac,\nu}(\omega_{\mathbf{q}}) \rho^{\nu}(\omega_{\mathbf{q}}) d\omega \tag{1.6}$$

This, along with the anharmonicity of the system due to atomic substitutions and a flattening of the cage structure, control the temperature independent regime of thermal conductivity (50-300 K [27]). Even though the optical branches do not participate in heat transport, the presence of a large number of optical branches leads to a very large energy and momentum phase space for the three-phonon scattering mechanism, thus impacting κ_L [85].

In order to design a clathrate for the purpose of using it as a thermoelectric material, the clathrate must be semiconducting. This is done by making transition metal substitutions that follow the general formula $Ba_8TM_xGe_{46-x}$, for Ge-based clathrates. This formula comes from the Zintl-Klemm Rule, which ensures that the clathrate will be both semiconducting and chemically stable [86, 87]. This is a rule generalized for the entire class of so-called "Zintl materials," not just clathrates, that says that electropositive atoms should provide electrons to the electronegative atoms in order to balance the charge of the material [1, 88].

For clathrates, that means that the total charge of the guest atoms should balance the total charge of the substitution atoms. Inserting guest atoms to the center of the cage structure is much like inserting an ion into an otherwise inert system. The transition metal substitutions must be made to balance the charge of these ions. Predictions about stable type-I clathrates and elements that contribute to creating those stable clathrates have been established in literature [87]. Additionally, it is known that these substitutions prefer to fill the *6c* sites in the host lattice [89] (see Fig. 1.9 and explanation in the following paragraphs). A preference for other sites over *6c* is unlikely to occur since this requires more energy, and it leads to a less optimal configuration of the cage [90].

Therefore, for $Ba_{7.81}Ge_{40.67}Au_{5.33}$, the number of Au substitutions for Ge lattice atoms must balance the charge of the 8 Ba atoms, which have a total charge of +16. The charges of different transition metals are given as nominal charges, Δq, where Δq is the difference between the valence electrons of the transition metal and of Ge. In other words, moving left across the Periodic Table of Elements away from Ge, one is subtracted from Δq with each passing column, i.e. Au is three columns away from Ge, giving $\Delta q = -3$. Therefore, 6 Au substitutions can be made, giving the formula $Ba_8Ge_{40}Au_6$ [91]. However, it was found that $Ba_8Ge_{40}Au_6$ produced a metallic behavior [91, 92]. This was corrected by Zhang *et al.* [84], who proved that a semiconducting behavior could be engineered by inducing vacancies and applying the formula $Ba_8Au_xGe_{46-x-y}\square_y$, resulting in the final form of $Ba_{7.81}Ge_{40.67}Au_{5.33}$.

The chemical structure of $Ba_{7.81}Ge_{40.67}Au_{5.33}$ is given in Fig. 1.9. The host atoms occupy Wyckoff sites *6c*, *24k*, and *16i*, while the guest atoms are located at the *2a* and *6d* sites, accounting for 54 atoms per unit cell, all contained into a simple cubic lattice structure (a = 10.8 Å), space group $Pm\bar{3}n$ [27, 83, 84, 92]. As seen in Fig. 1(d)-(f) of Lory *et al.* [27], the number and placement of the Au substitutions onto the Ge cage determines the slight off-centering of the caged Ba atom at the center. In $Ba_{7.81}Ge_{40.67}Au_{5.33}$, there are opportunities for 1, 2, or 3 substitutions on a given cage, each resulting in a different local off-centering, which in turn result in the off-centered, four-fold-hollow-site motions of the Ba atoms in the tetrakaidecahedral cages [27]. On the macroscale, however, there is no ordering to these substitutions, meaning that the average crystal symmetry is still preserved, and that these types of off-centering should be considered more as point defects than as a kind of short-range ordering [27]. This off-centering is small in comparison to the size of the cage, but has a very large impact on the properties of clathrates [85].

In terms of the phonon scattering mechanisms mentioned above, the structural complexity in

clathrates comes from their cage structure and 54 atoms per unit cell. Then, $Ba_{7.81}Ge_{40.67}Au_{5.33}$ has additional chemical disorder due to Au substitutions that are made on the *6c* site of the cages [84] and the vacancies that are engineered according to the formula $Ba_8Au_xGe_{46-x-y}\square_y$. Finally, we must also consider anharmonicity, due to the large amount of phonon-phonon scattering that takes place in this system. Specifically for this third concern, the recent use of the self-consistent phonon (SCP) method by Tadano and Tsuneyuki [93] led to a more accurate calculation of anharmonicity in clathrates. This novel theoretical method will be discussed in more detail in Section 1.4.1. However, for now I reflect on the fact that this SCP method has provided improved results for a wide range of complex systems that require special attention given to anharmonicity [94–99], and that my recent results [57] confirm that the amount of quartic anharmonicity attributed to clathrates by the SCP method matches experimental findings. This conversation between theoreticians and experimentalists provides necessary checkpoints when introducing novel theoretical methods, and promotes the inclusion of different communities that see the potential for use of, for example, the SCP method in explaining their systems of interest.

1.3.4 High-Entropy Alloys

High Entropy Alloys (HEAs) are equimolar alloys containing four or more elements that are evenly dispersed in the lattice, also known as single-phase random solid solutions. They are attributed to the publications of Yeh *et al.* [100] and Cantor *et al.* [101] in 2004, and have drawn a significant amount of research interest since their discovery. As opposed to simple alloys, HEAs have no single principle element, and it is believed that this high entropy mixing of many elements is the reason that HEAs have improved mechanical strength, high-temperature capabilities, and many other unique characteristics. The selection of certain combinations of elements has led to applications in corrosion resistance, superconductivity, and even in hydrogen storage [102–105]. They are also often compared to bulk metallic glasses (BMGs), although they are principally different, with HEAs having long-range order and BMGs, being amorphous alloys, having no long-range order. (A detailed comparison between HEAs and BMGs is given in my submitted work, Turner *et al.* [106]).

The strict definition of what constitutes an HEA is still under debate within the community. However, in order to ensure that a random solid solution is actually the preferred formation of the system, also preferable over the formation of a bulk metallic glass or intermetallic compound, we look to the Hume-Rothery rule, which says that (1) the amount of mixing enthalpy and (2) the atomic size differences involved in a given alloy determine the outcome of a solid solution [107, 108]. From thermodynamics,

$$\Delta G_{\text{mix}} = \Delta H_{\text{mix}} - T\Delta S_{\text{mix}}. \tag{1.7}$$

In other words, at the phase formation stage, all elements are mixed at temperature T, and the entropy of mixing, ΔS_{mix}, is subtracted from the enthalpy of mixing, ΔH_{mix}, to obtain the Gibbs free energy of mixing, ΔG_{mix}.

As their name suggests, HEAs are made possible due to their high amount of entropy. In order to encourage the formation of a random solid solution, the mixing entropy needs to be large enough to counteract the want for the system to form either a compound due to negative mixing enthalpy, or a segregated state due to positive mixing enthalpy [109]. For HEAs, that mixing enthalpy is defined as [110–112]

$$\Delta H_{\text{mix}} = \sum_{i=1, i\neq j}^{n} 4\Delta H_{ij}^{\text{mix}} c_i c_j, \tag{1.8}$$

where, for n elements, ΔH_{mix} is the sum of the molar ratios c_i and c_j multiplied by the mixing enthalpy for each interaction of elements i and j.

There are usually four types of entropy at play, namely configurational, vibrational, magnetic dipole, and electronic randomness, but the mixing entropy of HEAs is almost completely due to configurational entropy. Configurational mixing entropy, S_{conf}, can be defined from Boltzmann's equation for thermodynamic entropy, where k_B is Boltzmann's constant, and w is the number of ways that the energy of the system can be distributed among the particles of a gas, or, in this case, among the atoms of the lattice:

$$\Delta S_{\text{conf}} = k_B \ln w. \tag{1.9}$$

By relating k_B to the gas constant, R, eq. 1.9 can be rewritten as

$$\Delta S_{\text{conf}} = -R \sum_{i=1}^{n} X_i \ln X_i, \tag{1.10}$$

where there are n components in the system, each with a mole fraction X_i. As stated before, HEAs are equimolar materials by definition, and therefore the equation can be reduced to

$$\Delta S_{\text{conf}}/mol = -R \ln n, \tag{1.11}$$

where S_{conf} per mole is dependent only on the gas constant and the number of elements in the system. An equimolar system with $n = 5$ elements, for instance, has a $\Delta S_{\text{conf}}/mol = 1.61$R. In practice, it is accepted that $\Delta S_{conf}/mol \geq 1.5$R is typically enough mixing entropy to overcome formation enthalpies of intermetallic compounds and cause a random solid solution to form within a given temperature range in a metastable state. The random alloy will be stable as long as prolonged exposure to high temperature does not promote atomic diffusion and, by consequence, phase segregation.

As for the second criteria, the atomic size differences, we look to the parameter Delta, δ [107, 108]

$$\delta = \sqrt{\sum_{i=1}^{n} c_i \left(\frac{1 - r_i}{\left(\sum_{i=1}^{n} c_i r_i \right)} \right)^2}, \tag{1.12}$$

which also depends on parameters listed above, in addition to the average atomic radius, $\bar{r} = \sum_{i=1}^{n} c_i r_i$, averaged from each atomic radius r_i for elements n.

These two parameters, ΔH_{mix} and δ, determine the chance that a solid solution is formed over the chance of a BMG or intermetallic phase. In general, a higher ΔH_{mix} and lower δ than those of BMGs are needed to ensure a solid solution (see Fig. 2 from Ref. [107] and Fig. 1 from Ref. [113]).

Once we have ensured a solid solution, we can also predict whether the HEA will form an FCC or BCC structure. Once again, in general, FCC HEAs have a higher ΔH_{mix} and lower δ than those of BCC HEAs (see Fig. 2.5 from Ref. [109]). In addition, elements Ni, Mn, Cu, and N tend to force an FCC phase, while elements Cr, Mo, Si, and Nb tend towards a BCC phase [108, 114]. Further methods by Guo *et al.* [115] exist that integrate the density of states of valence band electrons, predicting that a value less than 6.8 gives a BCC structure, while a value above 8 gives FCC. Finally, He *et al.* [110] were able to experimentally prove that simply by changing the amount of Al concentration, they were able to move the base HEA FeCoCrMnNi, originally an FCC structure, to a BCC structure. I also note that, at the time of writing, HCP-structure HEAs are currently in development (private communication with M. Feuerbacher).

From a lattice dynamics perspective, HEAs pose an interesting question as they are completely chemically disordered systems, as seen in Fig. 1.10, meaning that Bloch's theorem no

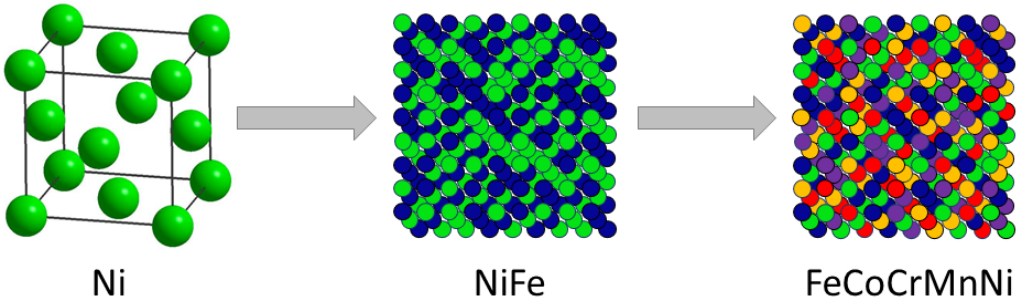

Figure 1.10: The evolution of reaching the crystallographic structure of FeCoCrMnNi. *In order to grasp the idea of a random solid solution, such as the high-entropy alloy (HEA) FeCoCrMnNi, we start with the FCC structure of pure Ni. The evolution of Ni, to equimolar NiFe, to equimolar FeCoCrMnNi provides a visual representation of the disorder produced by forming an HEA. Despite the lattice distortions and strain caused by creating a five-element HEA, all three structures shown maintain an FCC lattice with a lattice parameter of 3.6 Å.*

longer holds since there is no translational symmetry [116, 117]. Determining if and how phonons propagate in such a system could help us understand the influence of extreme disorder on long-range ordered crystals. Indeed, by forcing 5 or more elements into this random solid solution, it is thought to cause local lattice strain, since the lattice is trying to compensate for the many different-sized atoms that are randomly assorted in the system [108, 118, 119]. Furthermore, according to the combination of elements proposed, atomic size difference, mass difference, force-constant fluctuations, and chemical/magnetic short-range ordering are all possible types of disorder that can play roles in HEAs. All of this chemical disorder should make itself known in the phonon behavior of these materials.

The phononic density of states have been experimentally measured for a series of HEAs by Lucas *et al.* [120, 121], proving that there is still long-range ordering and an overall crystalline lattice structure with propagating phonons. My submitted work on the Cantor-Wu HEA FeCoCrMnNi, however, marks the first complete lattice dynamics study of a five-element HEA. This article provides a first look at the phonon dispersions and intrinsic linewidths of FeCoCrMnNi, and puts the results in the context of other highly disordered crystals.

1.4 The Study of Complexity within the Research Community

The above sections displayed the way that I am applying the definition of complexity from Section 1.2 to actual categories of materials. I will now try to globally summarize the current methods that the scientific community is using to model (Section 1.4.1) and measure (Section 1.4.2) different types of complexity and disorder. These methods all track the ongoing story of having a unified explanation of thermal transport for complex and disordered systems.

1.4.1 Theoretical Contributions

One of the driving forces right now in the story of unified heat transport in complex and disordered systems is the struggle to explain the deviation from $1/T$ at higher temperature in the lattice thermal conductivity of many such systems [27, 85, 96–98, 122]. As shown at higher temperatures in Fig. 1.3, a glasslike thermal conductivity plateaus and remains temperature independent, rather than following the expected $1/T$ decay. The distinction lies in the disorder of these types of systems, and calculations that use ordered model structures, even ones that incorporate three-phonon scattering processes, cannot fully replicate this behavior. Therefore, two key avenues of interest for theoreticians at the moment are to (1) incorporate disorder into

their models for better matching with experimental results and (2) move beyond the harmonic and quasiharmonic approximations to anharmonic perturbation theory in order to explain certain important anharmonic effects in these materials.

To elaborate on the inclusion of disorder, a pertinent example is that which was done for the quasicrystal approximant o-$Al_{13}Co_4$ [122]. The authors found that by randomly removing several Al atoms from the generated supercell in order to simulate vacancies, the model with vacancies had a lower minimum-energy atomic configuration than the ordered model. This disordered model then provided a better match to the experimental phonon dispersions, confirming the significance of using a model that includes a representation of the disorder in the system.

From recent studies like these, we could say that we have in fact barely scratched the surface when it comes to treating complexity and disorder through current theoretical means. While major breakthroughs are directing us towards possible solutions, we still globally lack a large enough library of case studies to accurately predict the methods needed for treating new and emerging systems. However, the promotion of the use of disordered structure models for complex and disordered systems will lead us to being able to decouple the effects of local chemical disorder, polarization mixing/dependence, and other significant components of disorder.

As for the second key avenue of interest, i.e. moving towards the consideration of anharmonic effects in such systems through the use of anharmonic perturbation theory, I will refer to the example of type-I clathrates. As another route to treating the deviation from the typical $1/T$ behavior at higher temperature, *ab initio* calculations for the type-I clathrate $Ba_8Ge_{30}Ga_{16}$ using the self-consistent phonon (SCP) method were published in 2018 [93]. These calculations are based on the ideas that not only must we include the quartic anharmonicity term to the Hamiltonian, but also that these anharmonicity terms are significant enough to be treated non-perturbatively. (These concepts will be further defined in Chapter 3, Section 2.3.1.2.) This use of the SCP method brought about a closer alignment to experimental lattice thermal conductivity for $Ba_8Ge_{30}Ga_{16}$, particularly between 10-300 K. This method has also been tested for other complex and disordered crystals with strong anharmonicity, with encouraging results [94–98, 123, 124]. Current SCP method calculations, such as those for $Ba_8Ge_{30}Ga_{16}$, also neglect important parameters such as polarization mixing, which the community agrees plays quite an important role in complex systems [125–129]. Therefore, there are still significant challenges to overcome, given that these additional considerations are often computationally expensive.

Lastly in the story of a unified understanding of heat transport in complex and disordered systems, I would like to reference the works of Simoncelli *et al.* [130] and Isaeva *et al.* [131]. In recent years, theoreticians have attempted to bridge the gap between the main theoretical methods used for thermal transport in glasses and crystals, namely the Allen-Feldman [132] and Peierls-Boltzmann [133] theories, respectively. Ideally, these methodologies would converge, allowing us to have one explanation for heat propagation in all solids, but disordered, anharmonic crystals and harmonic glasses, in particular, lie in somewhat of a gray area in which neither of the current two theoretical methods can fully explain. Though they use fundamentally different approaches, the work of these two research groups represents a new age of theories that will fill the gaps in the previous theoretical methods, some of which are now almost a century old. I emphasize that it is equally important to question and redefine, if necessary, the major equations and definitions of heat transport, at both the levels of phonon lifetime and κ, as it is to develop more sophisticated methods for calculating local atomic disorder and complexity.

1.4.2 Experimental Contributions

One of the main challenges for experimentalists is the collection of experimental phonon lifetime data. We are lacking lifetime measurements of almost all types of systems, both simple and complex. The difficulties remain that not only do we need to have access to phonon dispersions

and lifetimes at THz-range frequencies, but we also need them in a wide range of momentum. This makes X-ray and neutron scattering techniques the techniques of choice, however this already limits data collection sources to the few synchrotrons and nuclear reactor facilities that currently exist in the world for science. (For more information see Chapter 3.)

Many phonon lifetimes are or could be within the instrumental resolution of state-of-the-art X-ray and neutron scattering techniques, and while we are step-by-step beginning to understand the mysteries behind glasslike thermal conductivity in complex systems through these studies focused on intrinsic phonon lifetimes, the scientific community also needs to make a deep-dive into the study of intrinsic lifetimes of simple systems as well, in order to have proper comparisons. This is the only way that we will uncover the bridge between simple and complex systems. To give an example, in my recently submitted work Turner *et al.* [106], we have published the first experimentally measured intrinsic phonon linewidths for an HEA. While we are able to make experimental and theoretical comparisons to other binary and ternary alloys [134], we could not, to the best of our knowledge, find experimentally measured elemental linewidths, such as for Cr or Ni. This is critical if we are to truly follow the disorder induced in going from a single element to a five-element random solid solution alloy.

To give another example, experimental intrinsic phonon lifetime measurements for clathrates are beyond almost all state-of-the-art inelastic neutron and X-ray scattering techniques, making it difficult to see the trends of this parameter with momentum and temperature in this material, and therefore its direct influence on κ_L. However, the recent publication by P.-F. Lory and co-authors [27] used the Neutron Resonance Spin Echo (NRSE) technique (see Section 3.1.9) to prove that acoustic phonons in clathrates have remarkably long lifetimes, traveling even 100x the length of the unit cell. This is in conflict with the previously held theory that it was the anharmonic vibrations of the guest atoms that caused short-lived phonons and therefore limited the overall lattice thermal conductivity. While this was a tremendous step forward in our understanding of heat propagation in clathrates, a much larger data collection is needed in order to understand temperature and energy dependencies of phonon lifetime.

Experimental limitations to neutron- and X-ray-based phonon measurements aside, there can also be limitations in synthesis techniques. Neutron-based phonon measurements require quite large crystals ($\sim$1 cm^3), and both neutron and X-ray techniques depend on having extremely high quality single crystals with small mosaic spreads for maintaining a high resolution and easy alignment of the sample. Certain elements are also too absorbing to be measured with neutrons, or too light to be measured by X-rays (see Chapter 3). For example, coming back to the study of HEAs once again, large single crystal growth of an HEA by Bridgman technique was reported by Feuerbacher *et al.* [135] in 2016, and this has since opened the door for neutron-based studies that allow us to measure phonons, such as in my submitted work, Turner *et al.* [106]. As well for the NRSE measurements mentioned above, these were only made possible due to the excellent crystal quality and small sample mosaic. However, the perfection of synthesis techniques for such complex systems remains a difficult task, and if we as a research community are to push for the use of these novel materials in real-life applications, we first need to meet this essential proof-of-concept step by successfully synthesizing them.

CHAPTER 2

The Theory of Lattice Dynamics in Complex Crystals

In order to understand macroscopic thermal properties such as heat capacity and thermal conductivity of a semiconductor or dielectric material, the microscopic lattice properties must first be considered. Macroscopically, we think of a crystal as a solid, while microscopically we know that this solid is actually made up of a large number of atoms, typically on the order of Avogadro's number (10^{23}), that are strung together by chemical bonds to form a lattice structure. The vibrations of these 10^{23} atoms are described by a set of plane waves, which correspond to specific quantized states in quantum mechanics. Each state, therefore, is a channel through which heat is transported in a given material.

In order to describe phonons, or these quantized lattice vibrations, we must attempt to define these vibrational waves in a way that reflects the crystal structure and unit cell of a given system. A common analogy which will be expanded upon throughout this chapter is to think of a lattice structure as a 3D set of atoms that are bonded by springs, such that the interactions can be considered by Hooke's Law with a plane wave solution [31], which then allows us to relate the individual displacement of each atom to the force being acted upon on that given atom [136–138]. Hooke's Law states that the force used to stretch a spring is related to the distance the spring is stretched multiplied by the elastic spring constant.

This chapter will detail the harmonic oscillations of atoms at both 1D and 3D scales (Section 2.1). I will then use this foundation to discuss phonon properties in and outside of equilibrium (Section 2.2). Finally, I will provide examples of how these concepts are used to model complex and disordered crystalline systems, and in particular anharmonicity, using molecular dynamics and density functional theory simulations (Section 2.3).

2.1 Lattice Dynamics in the Harmonic Approximation

We can first consider that the atoms in a crystalline material oscillate about their equilibrium points due to the thermal energy in the system. The total potential energy would therefore be the sum of the potential energy of each atom at equilibrium, and the potential energy due to each atom's small displacement from equilibrium.

Under the adiabatic approximation [139], we can assume that the total energy of such a lattice can be described by the kinetic and potential energies of ions found in the nuclei and

their valance electrons. We will concern ourselves, however, only with the kinetic energy of the crystal as a whole, and of the potential energy of all ionic displacements from equilibrium within that crystal. In other words, we neglect the impact of the dynamics of electrons. This assumption comes from the fact that electrons are said to follow the slower motions of the much heavier ions (as viewed from the electron's point of view) in a way that is progressive and gradual, or adiabatic. This means that the dynamics can be reduced to a system of ions that are connected by an effective ion-ion pair potential [136].

The potential energy can be written as a Taylor expansion series [140, 141], and, within the harmonic approximation, these potential energies of displacements can be defined with Hooke's law in which the chemical bonds between the atoms act as springs [136, 137].

$$E = E_0 + \sum_n \frac{1}{n!} \frac{\partial^n E}{\partial u^n} \sum_s (u_s - u_{s+1})^n \tag{2.1}$$

The E_0 term is the total energy when the system is at rest, n is a non-zero positive integer, and s represents the location of a reference atom. The displacements of the atoms, $u_s, u_{s+1}, ...$, are then defined by the masses of the atoms and the spring constants of the chemical bonds. The $n = 1$ term cancels out since the first derivative of E is zero, or, in other words, because the forces compensate at equilibrium.

In the harmonic approximation, we only include elements of the Taylor expansion series through $n = 2$, and therefore eq. 2.1 becomes

$$E = E_0 + \frac{1}{2} \frac{\partial^2 E}{\partial u^2} \sum_s (u_s - u_{s+1})^2 \tag{2.2}$$

As the name suggests, each atom acts as a harmonic oscillator. For the moment we will put aside elements that include the higher-order terms such as $n = 3$ and $n = 4$, and we will return to this topic in Section 2.3, as these pertain to anharmonic motions of atoms. As one might suppose, however, these terms have proven relevant to the explanations of the motions of atoms in complex and disordered systems such as the ones discussed in this thesis.

Through the use of sophisticated computer programming techniques developed within the last decade or two, the harmonic approximation can now be calculated quite successfully, accurately, and quickly for many materials. Although this was not the direct topic of this thesis work, a brief overview of these developments will be given in Section 2.3. We will first, however, spend time on a simplified harmonic approximation model represented by a linear chain of atoms in order to present the relevant concepts and set the stage for this discussion. This model will then be compared to experimental results measured during my thesis work in order to provide evidence that we can still gain significant information on complex and disordered systems from the use of only the harmonic approximation.

Many derivations for the dispersion relation solutions to monatomic and diatomic linear chains of atoms exist in literature [31, 136, 140, 142]. Therefore, I prefer to focus on a more relevant example, namely one that represents the type-I clathrate cage and caged atom system. This derivation will follow similar derivations for cage structures that can be found in Refs. [24, 142], and in the Supplementary Material of Ref. [25], the latter of which contains a specific derivation for the type-I clathrate $Ba_8Ga_{16}Ge_{30}$. More advanced versions of this concept have also been developed by N. Nakayama, Y. Liu, and co-authors [125, 143], proving that this simple approach has merit.

2.1.1 A simplified linear chain of atoms model for clathrates

Recalling from Section 1.3.3 that, structurally, clathrates have cages made of host atoms with guest atoms at the center of the cages, the motions of atoms in a clathrate system can be

described with the simplified model sketched in Fig. 2.1 in which two host atoms (black circles) are bonded together and a guest atom (empty circle) is bonded to each of those two host atoms. The host atoms and the guest atom have masses of M_1 and M_2, respectively. The elastic spring constant between the two host atoms is denoted as K_1, and those between the guest atom and a host atom are K_2. The distance between two host atoms is defined as a. We will come back to the importance of a, or the lattice parameter, for the 3D lattice throughout this chapter. For this simplified 1D model, however, it represents the distance taken up by one unit, or cell, and we assume that Fig. 2.1 is repeated many times in order to create a chain, with a representing the minimum distance at which we can find the next repeated cell.

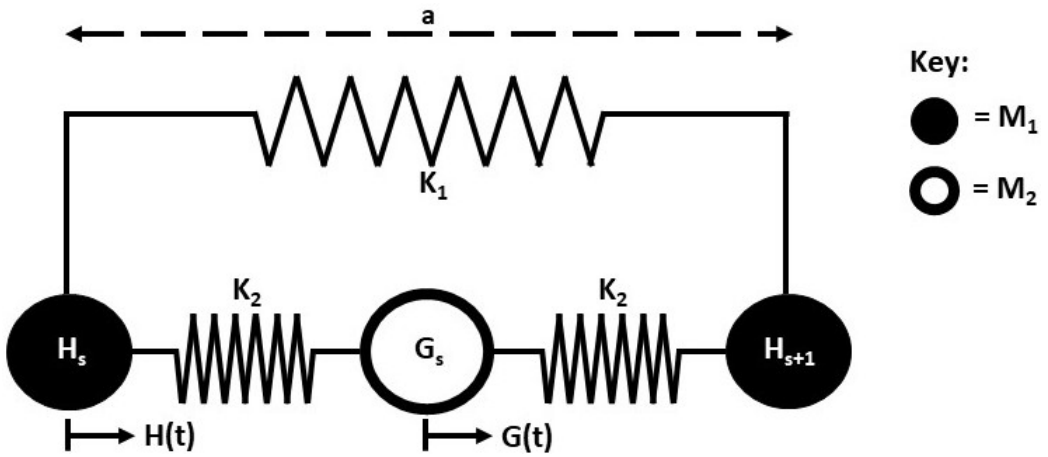

Figure 2.1: Linear Chain of Atoms Model for Clathrates. *The host-host and guest-host interactions within a clathrate cage are described with the given schematic. Host atoms (black circles) have mass M_1 and the guest atom (white circle) has mass M_2. The elastic spring constant between two host atoms is K_1, and between a guest and a host atom is K_2. The atoms are labeled with s and $s+1$ in order to distinguish between the naming of individual atoms. The distance between two host atoms is the lattice parameter a ($\sim$10.8 Å for type-I clathrates [144]). $H(t)$ and $G(t)$ represent the time-dependent displacements of the host and guest atoms, respectively, from their equilibrium positions.*

With this configuration, both the interactions of the lattice network (host-host) and the interaction between the guest and host atoms (guest-host) are described. The interaction between two guest atoms (guest-guest) will be ignored in this model, however, because we will only analyze the nearest-neighbor atomic interactions. Furthermore, as a first approximation, the guest atom subsystem can be considered as a network of independent atoms only loosely bonded to their host atom cages, making them act as independent harmonic oscillators like those described in the Einstein model [31].

With these concepts in mind, the two equations of motion that describe the linear chain of atoms in Fig. 2.1 can be written in terms of the nearest-neighbor interactions and Hooke's Law. The force on a given atom is the force due to the interaction with the atom on its right, subtracted by the force due to the interaction with the atom on its left. In the following two equations, we describe the interactions on host atom H_s as F_H and the interactions on guest atom G_s as F_G. For the host atom H_s, it is necessary to consider the interactions with the guest atom on either side, separated by a spring with K_2, and and interactions with the host atom on

either side, separated by a spring with K_1.

$$F_H = K_1\Big[H_{s+1}(t) - H_s(t)\Big] - K_1\Big[H_s(t) - H_{s-1}(t)\Big] + K_2\Big[G_s(t) - H_s(t)\Big] - K_2\Big[H_s(t) - G_{s-1}(t)\Big]$$

$$F_G = K_2\Big[H_{s+1}(t) - G_s(t)\Big] - K_2\Big[G_s(t) - H_{s+1}(t)\Big] \tag{2.3}$$

The equations of motion, F_H and F_G, are equal to $M_1\frac{d^2H(t)}{dt^2}$ and $M_2\frac{d^2G(t)}{dt^2}$. Using this relation and simplifying, we have the following. At this point I will also remark that eq. 2.4 reduces to the monatomic linear chain of atoms when $K_2 \ll K_1$, or to the diatomic linear chain of atoms when $K_1 \ll K_2$.

$$M_1\frac{d^2H(t)}{dt^2} = K_1\Big[H_{s-1} + H_{s+1} - 2H_s\Big] + K_2\Big[G_{s-1} + G_s - 2H_s\Big]$$

$$M_2\frac{d^2G(t)}{dt^2} = K_2\Big[H_s + H_{s+1} - 2G_s\Big] \tag{2.4}$$

We can consider that the displacements in Fig. 2.1 can be described by the solution to a plane wave, such as those given in eq. 2.5. These equations quantify the wave and its complex conjugate. $H(t)$ and $G(t)$ refer to these two solutions, where $H(t)$ refers to the solution for host atoms, and $G(t)$ refers to the solution for guest atoms. The amplitudes of motion are given the variable names A_1 and A_2 for host atoms and guest atoms, respectively. The letter s refers to the position of any given atom relative to the equilibrium position of the reference atoms, H_s and G_s. Finally, q refers to the wave-vector, t refers to time, and ω refers to the vibrational frequency of the propagating wave.

$$H(t) = A_1\Big[cos(qsa - \omega t) + i\ sin(qsa - \omega t)\Big] + \text{ c.c. } = A_1e^{i(qsa-\omega t)} + \text{ c.c.}$$

$$G(t) = A_2\Big[cos(qsa - \omega t) + i\ sin(qsa - \omega t)\Big] + \text{ c.c. } = A_2e^{i(qsa-\omega t)} + \text{ c.c.} \tag{2.5}$$

The system of equations of motion from Eq. 2.4 becomes:

$$\begin{cases} M_1\omega^2A_1 = 4K_1A_1\sin^2\left(\frac{1}{2}qa\right) - K_2A_2\Big(1 + e^{-iqa}\Big) + 2K_2A_1 \\ \\ M_2\omega^2A_2 = -K_2A_1\Big(1 + e^{iqa}\Big) + 2K_2A_2 \end{cases} \tag{2.6}$$

Next we define the Dynamical Matrix of the equations of motion, $\mathbf{D}$, and $\boldsymbol{\xi}$ as the polarization vector matrix of the waves. Together these can be related to the equations of motion, as shown in eq. 2.7. Note that the polarization vector includes the two amplitudes, A_1 and A_2. We will return to the importance of the polarization vector in Section 2.1.2.

$$w^2\boldsymbol{\xi} = \mathbf{D}\boldsymbol{\xi}, \text{ where } \boldsymbol{\xi} = \begin{bmatrix} \sqrt{M_1}A_1 \\ \\ \sqrt{M_2}A_2 \end{bmatrix} \tag{2.7}$$

The Dynamical Matrix, therefore, is written as follows:

$$\mathbf{D} = \begin{bmatrix} \frac{4K_1}{M_1}\sin^2\left(\frac{1}{2}qa\right) + \frac{2K_2}{M_1} & \frac{-K_2}{\sqrt{M_1M_2}}\Big(1 + e^{-iqa}\Big) \\ \\ \frac{-K_2}{\sqrt{M_1M_2}}\Big(1 + e^{iqa}\Big) & \frac{2K_2}{M_2} \end{bmatrix} \tag{2.8}$$

In order to solve the system of equations in eq. 2.7, we set the determinant equal to zero and diagonalize the Dynamical Matrix in order to obtain the eigenvalues:

$$\left|\mathbf{D} - \omega^2 \mathbf{1}\right| = 0 \tag{2.9}$$

The two solutions can be written in terms of the matrix $\mathbf{D}$ positions D_{11}, D_{12}, D_{21}, and D_{22}:

$$\omega^2 = \frac{D_{11} + D_{22} \pm \sqrt{(D_{11} + D_{22})^2 - 4(-D_{12}D_{21} + D_{11}D_{22})}}{2} \tag{2.10}$$

The dispersion relation is then written as the following[1]:

$$\omega^2 = K_2 \frac{M_1 + M_2}{M_1 M_2} + \frac{2K_1}{M_1} \sin^2\left(\frac{1}{2}qa\right) \pm \frac{1}{M_1 M_2} \times$$

$$\sqrt{\left(K_2(M_1 + M_2) + 2K_1 M_2 \sin^2\left(\frac{1}{2}qa\right)\right)^2 - M_1 M_2 \left(2K_2^2 - 2K_2^2 \cos(qa) + 8K_1 K_2 \sin^2\left(\frac{1}{2}qa\right)\right)} \tag{2.11}$$

2.1.1.1 Dispersion Relation from the Linear Chain of Atoms Model for Clathrates

We can take the two solutions to eq. 2.11 and plot them in order to view change with wavevector, q, of the vibrational frequency, ω, of the waves, as shown in Fig. 2.2. The following paragraphs will detail the fit that was made to actual ω dependencies for the type-I clathrate $Ba_{7.81}Ge_{40.67}Au_{5.33}$, which was introduced in Section 1.3.3. Therefore, the experimentally-measured, longitudinally-polarized phonon dispersion at 300 K for $Ba_{7.81}Ge_{40.67}Au_{5.33}$ has also been plotted in the figure for comparison alongside the linear chain of atoms model for reference.

The two solutions to our linear chain of atoms model in eq. 2.11 form the two types of phonon modes: acoustic and optical phonon modes. There is meaning in these two definitions in that acoustic modes refer to traveling waves in which all atoms are moving *in phase* with each other, otherwise known as a sound wave, while optical modes refer to *out of phase* motions of the linear chain [141]. I would like to take a moment to emphasize the importance of these definitions as this is the most trivial way to understand one of the main themes of this thesis: the phonons that are responsible for transporting heat in solids are the acoustic phonons, since these phonon modes displace the center of mass of each unit cell and therefore cause the sound wave to travel or disperse across multiple unit cells and through the lattice. Briefly recalling the formula for κ_L (eq. 1.3), an acoustic phonon with a given energy and velocity will carry some unit of heat through the lattice for a given distance before being scattered. Therefore, in the case of minimizing κ_L for the optimization of the ZT coefficient, these are the phonons that must be scattered quickly in order to limit the propagation of heat.

Optical phonon modes, on the other hand, do not displace the center of mass of the unit cell, and therefore stay centered at a given energy with zero velocity. They cannot, therefore, contribute to the propagative component of κ_L. They do, however, contribute to the heat capacity, which will be discussed in Section 2.2. (Note that there can be exceptions to this rule in some extreme situations in which there are highly dispersive optical phonon modes, and/or an interaction between acoustic and optical modes. In these cases the optical phonons could contribute in some way to the propagative component of thermal conductivity.)

[1] This formula includes a correction to an error in the Ref. [142] version of this derivation.

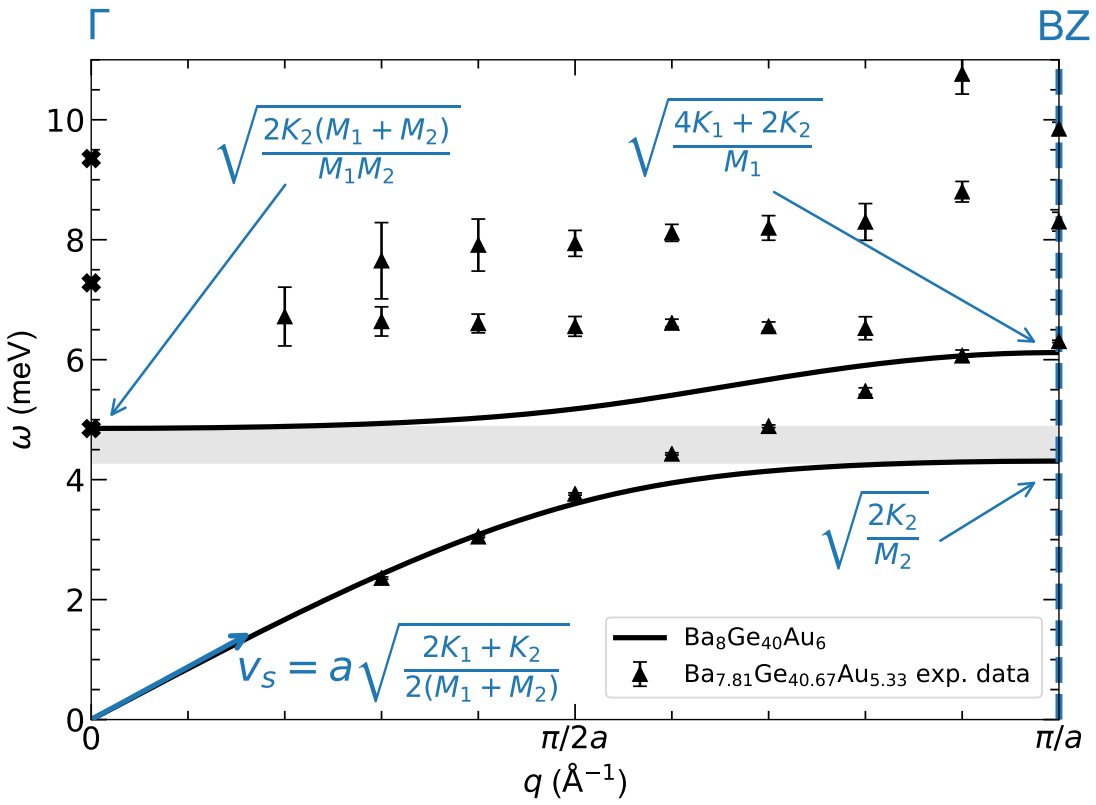

Figure 2.2: Dispersion relation for the clathrate linear chain of atoms model. *This dispersion relation, or vibrational frequency ω vs wave-vector q, has been derived from a linear chain of atoms model for a 1D clathrate system (see text). The model (solid black line) is compared to experimental data for the type-I clathrate $Ba_{7.81}Ge_{40.67}Au_{5.33}$ (black triangles and crosses) taken at 300 K [57]. The center of the Brillouin zone is marked as the Γ point and the end is marked by a dashed blue line at π/a. The sound velocity, v_s, is 26 meV.Å. The gap of 0.54 meV between the acoustic and optical branches that is calculated using the linear chain of atoms model is shaded in gray.*

Now looking again at Fig. 2.2, acoustic phonon modes form dispersive branches that are defined by having $\omega = 0$ at $q = 0$, followed by a linear dependence in ω at low q, and therefore this mode is the lower frequency mode of the two shown in Fig. 2.2. That linear dependence of the slope is called the sound velocity. This can be found by considering the group velocity, $v_g(\omega) = \frac{\partial\omega}{\partial q}$, at the acoustic limit when q goes to zero, or $\left(\frac{d\omega}{dq}\right)_{q\to 0}$:

$$v_s = \left(\frac{d\omega}{dq}\right)_{q\to 0} = a\sqrt{\frac{2K_1+K_2}{2(M_1+M_2)}} \tag{2.12}$$

The sound velocity based on this 1D linear chain of atoms model is 26 meV.Å, or 3,926 m/s. As we have fit this model to experimental data for the type-I clathrate $Ba_{7.81}Ge_{40.67}Au_{5.33}$, this is also the value found in Turner *et al.* [57]. The third defining characteristic of the acoustic mode is that there is a bending of the mode that occurs at higher q, leading to a decrease in $v_g(\omega)$, until the moment that $v_g(\omega) = 0$ at $q = \pi/a$. This is known as the van Hove singularity, and we will return to this concept in Section 2.2. Optical phonon modes, on the other hand, form almost non-dispersive branches that stay centered at or near a given non-zero energy, and they too have $v_g(\omega) = 0$ at $q = \pi/a$. This mode is the higher frequency mode of the two shown in the figure.

These behaviors are repeated for a selection of reciprocal space that contains all of the useful information, otherwise known as the first Brillouin zone, and is defined by $q = -\pi/a$ to $q = \pi/a$ [140]. This is because the solutions to eq. 2.11 will result in the same vibrational frequencies no matter what integer n the wave-vector q is multiplied by. As seen in Fig. 2.2, the end of the Brillouin zone at $q = \pi/a$ has been marked by a dashed line. The center of the Brillouin zone at $q = 0$ has another significance, since it corresponds to the point of repetition of the reciprocal lattice vector, $\mathbf{G}$. For more information on this, please see Section 3.1. It is also called the Gamma point, Γ.

Let us now turn our attention to the values of M_1, M_2, K_1, and K_2, that gave us the fit of the experimental data shown in Fig. 2.2. These parameters determine the characteristics of this plot. For the relationship between the masses, we will assume that, rather than using the model in Fig. 2.1 to represent strictly one atom of the host structure and one atom of the guest structure, M_1 and M_2 will represent the ratio of host and guest atoms within a 54-atom unit cell. There is more than one style of cage within the unit cell of type-I clathrates, namely dodecahedrons and tetrakaidecahedrons (see Section 1.3.3), and many of the host atoms are actually shared between cages. It is more prudent, therefore, to try to represent masses M_1 and M_2 as weighted contributions of the host and guest atoms, respectively, within the 54 atoms of the unit cell, as was suggested by Christensen *et al.* [25]. For the type-I clathrate $Ba_{7.81}Ge_{40.67}Au_{5.33}$, therefore, we will assume that $M_2 = 8m_{Ba}$ and $M_1 = 40m_{Ge} + 6m_{Au}$ in order to represent the ordered structure $Ba_8Ge_{40}Au_6$.

Next, we fit the relationship between K_1 and K_2 such that they best represent what we know to occur experimentally. From Fig. 3(a) of Turner *et al.* [57], we see that the lowest lying optical branch, E_{Ba}, has an energy of 4.85 meV at the Gamma point Γ_{116} at 300 K (see also the black cross in Fig. 2.2). Similarly, the second lowest optical branch, E_{AuBa}, has an energy of 6.39 meV at Gamma point Γ_{007} (see also the black triangle in Fig. 2.2). Therefore, tuning K_1 and K_2 to this region of interaction between the acoustic branch and these low-lying optical branches, we find that $K_2 = 0.99$ N/m and $K_1 = 3.25K_2 = 3.22$ N/m. The resulting gray shaded region with a width of 0.54 meV in Fig. 2.2 represents the region of expected interaction between the low-lying optical branches and the approaching acoustic mode. This interaction region can also be viewed through the changes in displacement amplitudes of the acoustic and optical branches in Fig. 2.4, which will be addressed in the next section.

We find, therefore, that our linear chain model is able to replicate a simplified version of the interaction between the acoustic mode and the low-lying optical branches in clathrates fairly well. The main conclusion to draw from Fig. 2.2 is that the intense curving of the acoustic mode and decrease in $v_g(\omega)$ occurs at approximately $q = \pi/2a$, meaning that the acoustic mode is only allowed to disperse, unhindered, a fraction of what it should have dispersed to. This deviation from linearity of the dispersion mode corresponds to its loss of pure acoustic character, meaning that the atoms are no longer moving coherently all together. This is related to the notion of phonon participation ratio, which is detailed in Refs. [26, 85] for type-I clathrates.

We now know that the true interaction between the acoustic and optical branches in type-I clathrates is quite complex, even showing an experimentally-measured polarization dependence [57]. More globally speaking, the aim with clathrates and other similar cage-style systems is to be able to tune this gray shaded region in the figure, since, as shown in eq. 1.6, the onset of this interaction largely defines the lattice thermal conductivity of the material. Therefore, we can consider what would allow us to decrease the energy at which the acoustic mode disperses to. In other words, how to further suppress the acoustic, dispersive phonons.

For instance, we could consider tuning the K_2 parameter. The elastic spring constant K_2 controls the energy at the Γ point at which the optical modes begin (see blue arrows in Fig. 2.2). Decreasing K_2 decreases this energy, meaning that we can further limit the acoustic phonons in

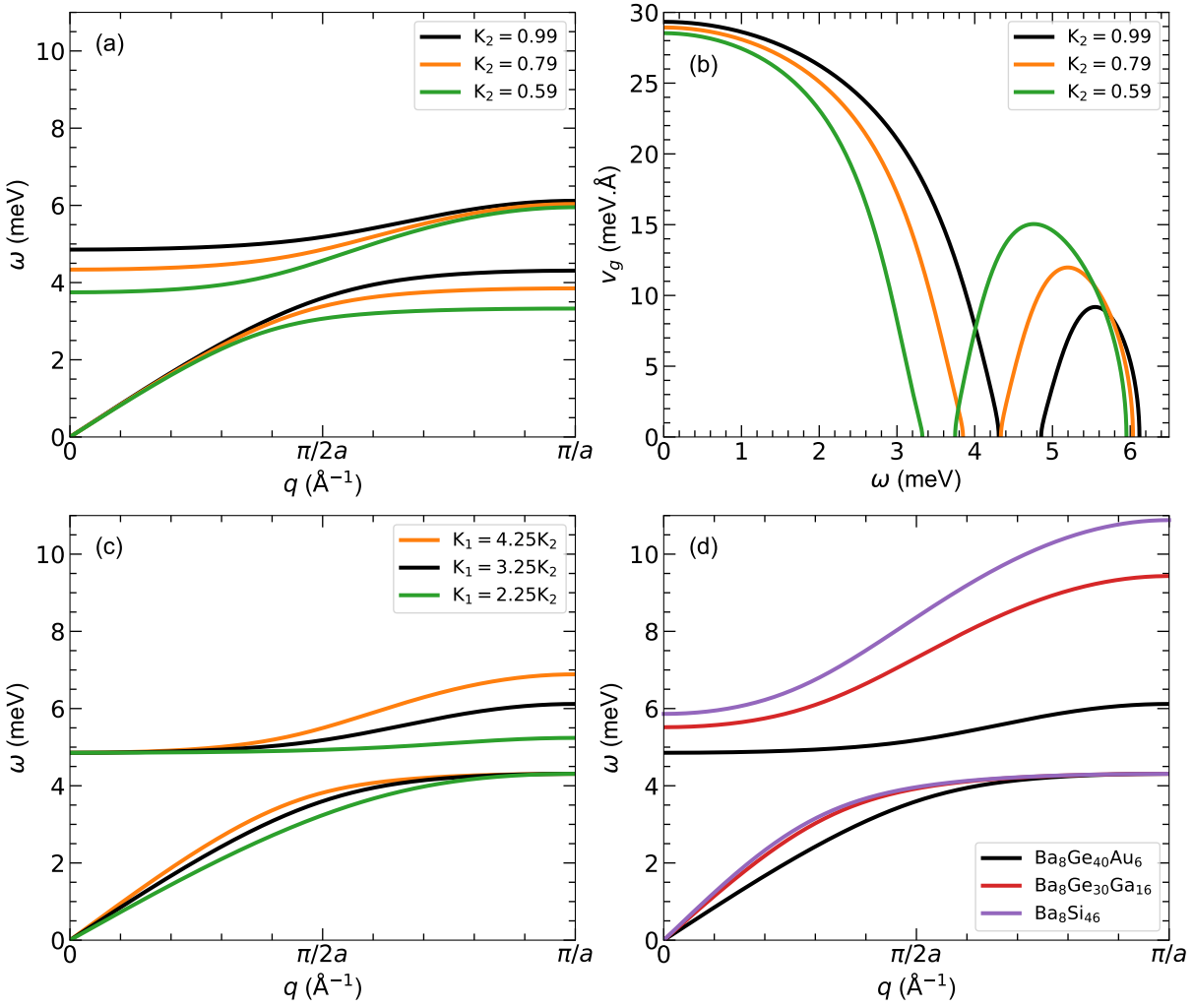

Figure 2.3: Investigation of mass and spring constant relationships. *In all four subplots, the black lines represent the same linear chain of atoms calculation for the type-I clathrate* $Ba_{7.81}Ge_{40.67}Au_{5.33}$ *as the one plotted in Fig 2.2. In (a), elastic spring constant* K_2 *has been varied. The resulting group velocities of the variation are shown in (b). In (c),* K_1 *has been varied. Finally, in (d), the masses have been adapted to replicate the mass ratios in type-I clathrates* $Ba_8Ge_{30}Ga_{16}$ *and* Ba_8Si_{46}*.*

this material by decreasing the elastic spring constant between the host and guest atoms, leading to a decrease in the overall lattice thermal conductivity. This is what is shown in Fig. 2.3(a), in which two smaller values of K_2 have been plotted along with the original. Experimentally this has actually been investigated as well by increasing the size of the cages [82].

The elastic spring constant K_2 also determines the width of the interaction region, because the values of both the acoustic mode at $q = \pi/a$ and the optical mode at $q = 0$, which define the shaded region shown in Fig. 2.2, depend only upon K_2, not K_1. Decreasing K_2 also decreases the sound velocity of the material, meaning that the phonons that are dispersing through the material travel with a lower velocity [24]. This is emphasized in (b), in which the numerical derivative, or group velocity v_g, of (a) is plotted so that the reader can more visually see this change. It also helps emphasize that a decreased K_2 appears to result in a more dispersive optical mode.

It is perhaps interesting to also develop the relationships between M_1 & M_2 and K_1 & K_2 a bit further in order to understand their impacts on eq. 2.11, and consider other ways we could

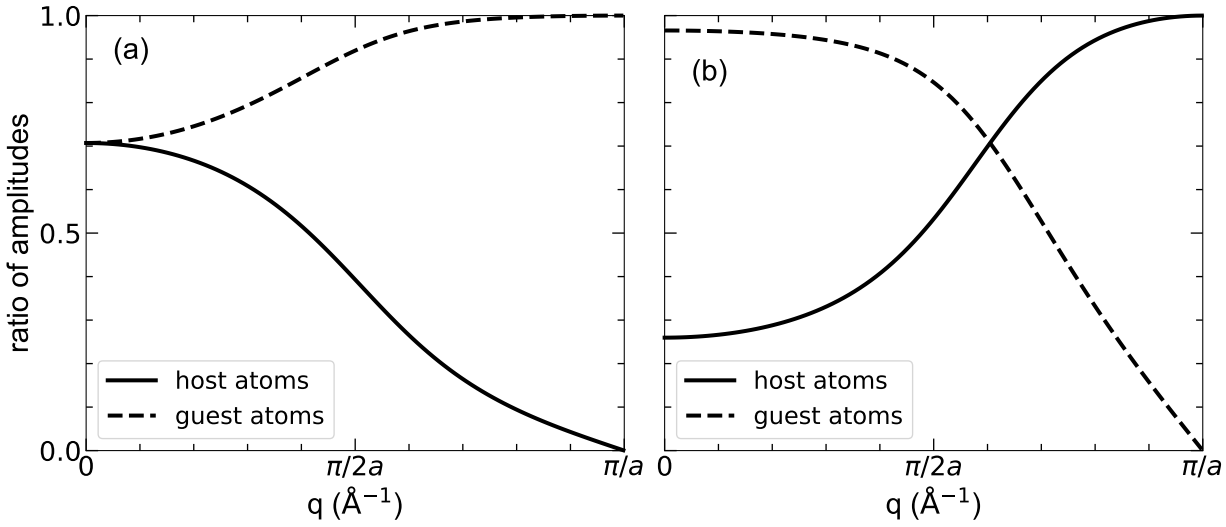

Figure 2.4: Amplitudes of Displacement for Guest and Host Atoms. *Amplitudes A_1 and A_2 are described across half of the first Brillouin zone for the acoustic phonon mode in (a), and for the optical phonon mode in (b) for the dispersion relation of the linear chain of atoms example for a clathrate plotted in Fig. 2.2. A_1 and A_2 represent host and guest atom contributions, respectively.*

tune thermal conductivity in clathrates. Turning our attention to Fig. 2.3(c), in order to isolate the influence of the ratio of K_1 to K_2, I have kept the M_1, M_2, and K_2 values the same as the original values, but have chosen a K_1 both larger and smaller than the original value. We can see that this relationship has no influence on the width of the interaction region, but rather impacts the energy of the optical mode at $q = \pi/a$, suggesting that the ratio of force constants controls the dispersive nature (or lack thereof) of the optical mode.

In Fig. 2.3(d), I have kept the original values of K_1, K_2, and M_1 values, but re-plotted eq. 2.11 assuming that $M_2 = 30m_{\mathrm{Ge}} + 16m_{\mathrm{Ga}}$ and $M_2 = 46m_{\mathrm{Si}}$ in order to represent the mass ratios found in the type-I clathrates $Ba_8Ge_{30}Ga_{16}$ and Ba_8Si_{46}, respectively. We can clearly see that in both cases, the energies of the optical mode at $q = 0$ and $q = \pi/a$ have both increased with respect to $Ba_8Ge_{40}Au_6$, widening the interaction region, and suggesting that the ratio of the masses also helps control the width of said interaction region. I emphasize, however, that these are not realistic simulations of the experimental dispersions found in these two additional clathrates, but rather just a way to discuss the impact of the weighted mass ratios between host and guest atoms. The K_1 & K_2 would need to be refit to experimental data in order to provide a true comparison. Nevertheless, this also tells us that the K_1 & K_2 spring constant strengths vary between type-I clathrates.

2.1.1.2 Amplitudes of the Dispersion Relation from the Linear Chain of Atoms Model for Clathrates

We can also further investigate the amplitudes of atomic displacements, A_1 and A_2, first seen in eq. 2.5, both for the acoustic and optical phonon solutions to eq. 2.11. We recall that A_1 and A_2 represent amplitudes of motion for host and guest atoms, respectively. As we will see, the relative contributions of the guest and host atoms to the resulting dispersion changes with q. In other words, for each quantized energy state of the acoustic and optical dispersions, a certain amount of guest atom and host atom displacements contribute, which also changes over the course of the first Brillouin zone.

We can rewrite the equations found in eq. 2.11 to solve for two ratios of amplitudes, which

will be called α_1 and α_2. The term α_1 therefore depends on M_1, and α_2 depends on M_2:

$$\alpha_1 = \frac{-K_2(e^{-iqa}+1)}{M_1\omega^2 + 2K_1(cos(qa)-1) - 2K_2}$$
$$\alpha_2 = \frac{-M_2\omega^2 + 2K_2}{K_2(e^{iqa}+1)} \tag{2.13}$$

Next, if we define a normalized vector $\mathbf{A}$ based on the ratio we have defined ($A_1 = \alpha A_2$), we can redefine amplitudes A_1 and A_2 as:

$$\mathbf{A} = \begin{pmatrix} A_1 \\ A_2 \end{pmatrix} = \begin{pmatrix} \frac{\alpha}{\sqrt{1+\alpha^2}} \\ \frac{1}{\sqrt{1+\alpha^2}} \end{pmatrix} \tag{2.14}$$

Recalling that the dispersion relation has two solutions, the acoustic and optical solutions, we can plot A_1 and A_2 for each of the two solutions. Fig. 2.4(a) represents the contributions of A_1 and A_2 within the acoustic branch. In order to preserve the translational symmetry of the material, the guest and host atoms contribute in equal amounts at $q = 0$. Closer to $q = \pi/a$, however, the guest atoms increase their amplitude of displacement and dominate in contribution to the acoustic phonon dispersion.

Fig. 2.4(b), on the other hand, represents the contributions of A_1 and A_2 within the optical branch. The guest atoms contribute a much larger amplitude of displacement at $q = 0$ than the host atoms do. However, at the region of interaction that begins at approximately $q = \pi/2a$ (see Figure 2.2), there is a spectral weight transfer between the acoustic and optical modes. As the contribution of the host atoms to the acoustic branch decreases, their contribution to the optical branch increases, and the spectral weight transfer is made.

2.1.2 Generalization into 3D

In reality, we are not working with a linear chain of atoms but a complete 3D lattice structure. There are therefore three degrees of freedom, or directions, in which the plane waves can propagate through the lattice. In order to illustrate these motions, let us first look at the two motions possible in a 2D lattice. These are shown in Fig. 2.5, in which we have zoomed in on three neighboring atoms along one of the two given directions within a larger plane of atoms.

In both examples shown in the figure, we assume that a wave is propagating in the direction of the blue arrow that is defined by $\mathbf{q}$. In the top example, this wave causes the atoms in the chain to displace parallel to the direction of propagation, or the blue arrow. This is called longitudinal displacement. In the bottom example, on the other hand, we assume a similar wave is propagating, but this causes atomic displacements that are perpendicular to the linear chain. This is called transverse displacement. Since there are two remaining directions in 3D in which a perpendicular displacement can occur, there are two possible transverse displacement directions. Given their definition, it follows that transverse displacements are possible only in 2D and 3D space, where coupling between chains of atoms occur perpendicular to the direction of propagation. We are therefore considering the interactions of planes of atoms instead of a 1D linear chain such as in a 1D lattice. Together with the longitudinal displacement definition, these two types of displacement account for the three directions of 3D space.

The blue arrows shown in the examples represent the direction of propagation, $\mathbf{q}$, which is also called the wave-vector. The red arrows drawn to the right of the examples, on the other hand, are called polarization vectors. The $\boldsymbol{\xi}^L$ and $\boldsymbol{\xi}^T$, represent longitudinal or transverse displacements, respectively. These two types of displacements are the basis for longitudinal

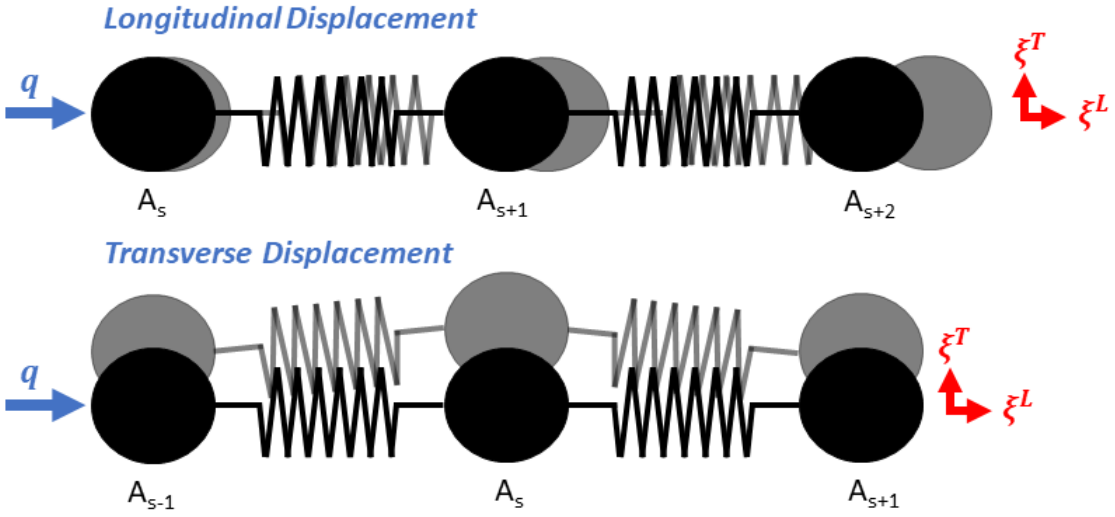

Figure 2.5: Longitudinal and Transverse Displacements. *This is a sketch of longitudinal and transverse displacements for a 2D lattice. Black circles represent the atoms at their equilibrium positions and gray circles represent the atoms after displacement. Longitudinal displacement occurs parallel to the direction of propagation,* $\mathbf{q}$*, and has a polarization vector* $\boldsymbol{\xi}^L$*. Transverse displacements occur perpendicular to the direction of propagation and has a polarization vector* $\boldsymbol{\xi}^T$*.*

and transverse phonon modes. There will be more discussion of polarization vector selection in Fig. 3.4.

We will now imagine that we have now taken a 1D chain of atoms to a 3D scale, still within the harmonic approximation. Following P. Bruesch's derivation [136], we assume that the force of each atom κ with mass m in unit cell ℓ is displaced u in direction α (= x, y, z) due to the sum of the negative potential energies of displacement in direction β of atoms κ' in unit cells ℓ'. The $\Phi_{\alpha\beta}(^{\ell\ell'}_{\kappa\kappa'})$ terms are called the interatomic force constants (IFCs).

$$m_\kappa \ddot{u}_\alpha(^{\ell}_{\kappa}) = -\sum_{\ell'\kappa'\beta} \Phi_{\alpha\beta}(^{\ell\ell'}_{\kappa\kappa'}) u_\beta(^{\ell'}_{\kappa'}) \tag{2.15}$$

Now that we have expanded this concept to a 3D material, let us imagine what longitudinal and transverse wave displacements on a simple cubic lattice might look like [31, 140]. In order to apply this model in 3D, we will assume that the dispersion is isotropic in all directions. Let us first assume that there is a longitudinal wave $\mathbf{u}$ in the x-direction, acting on cross-sectional area A of a material with a volume V, a mass m, and a subsequent density of $\rho = m/V$. (This is also referred to as the [100] direction.) This wave will cause a force of $F(x + dx)$ on the area which is proportional to displacement dx from its original position x. By the definition of longitudinal displacement in Fig. 2.5, we then assume that a longitudinal wave $\mathbf{u}$ in direction x displaces the lattice by dx in the same direction as $\mathbf{u}$:

$$m\ddot{u}_x = -\sum \Phi_x u_x. \tag{2.16}$$

Then we define σ_{xx} as the compression stress and ϵ_{xx} the deformation tensor caused by $\mathbf{u}$ such that

$$\rho\ddot{u}_x = \frac{\partial \sigma_{xx}}{\partial x}, \text{ where } \sigma_{xx} = C_{11}\epsilon_{xx}. \tag{2.17}$$

From here the longitudinal wave equation can be solved as before, where the resulting sound

velocity, v_{LA}, depends on ρ and elastic constant C_{11}:

$$v_{\mathrm{LA}} = \sqrt{\frac{C_{11}}{\rho}}. \tag{2.18}$$

On the other hand, there are two possible transversal displacements in a 3D lattice, as mentioned previously, and we recall that these are displacements perpendicular to the plane of motion. Therefore, following the sketch in Fig. 2.5, let us assume that there is a similar x-direction wave $\mathbf{u}$ that causes displacement dy.

$$\rho \ddot{u}_x = \frac{\partial \sigma_{yy}}{\partial x}, \text{ where } \sigma_{yy} = C_{44}\epsilon_{yy} \tag{2.19}$$

This results in a sound velocity dependent upon the elastic constant C_{44}:

$$v_{\mathrm{TA}} = \sqrt{\frac{C_{44}}{\rho}}. \tag{2.20}$$

As the same solution would result assuming displacements dz, the two transverse modes will have the same sound velocity, and therefore they are known as degenerate modes.

The terms C_{11} and C_{44} are two out of three unique elastic constants that are found in the elastic stiffness matrix C_{ij} for a cubic lattice [145–147]:

$$C_{\mathrm{cubic}} = \begin{pmatrix} C_{11} & C_{12} & C_{12} & \cdot & \cdot & \cdot \\ C_{12} & C_{11} & C_{12} & \cdot & \cdot & \cdot \\ C_{12} & C_{12} & C_{11} & \cdot & \cdot & \cdot \\ \cdot & \cdot & \cdot & C_{44} & \cdot & \cdot \\ \cdot & \cdot & \cdot & \cdot & C_{44} & \cdot \\ \cdot & \cdot & \cdot & \cdot & \cdot & C_{44} \end{pmatrix} \tag{2.21}$$

The sound velocities for the longitudinal and transverse plane waves derived above represent the solutions in the [100] direction of propagation. The third elastic constant, C_{12}, can similarly be derived by considering waves traveling in the [110] direction. Table 2.1 summarizes the sound velocities, $v = \sqrt{\frac{C_{\mathrm{eff}}}{\rho}}$, for the three phonon modes in the three high symmetry directions that are derived by using elastic constants C_{eff}.

Table 2.1: *The elastic constant values, or C_{eff}, for longitudinal and transverse phonons in each of the three high symmetry directions in a cubic lattice, are derived using the three unique elastic constants found in the elastic stiffness matrix for a cubic lattice, C_{11}, C_{12}, and C_{44}. The sound velocities, v, in each direction can then be calculated using the formula $v = \sqrt{\frac{C_{\mathrm{eff}}}{\rho}}$, where ρ is the density of the material.*

Mode	$\mathbf{q} \parallel [\mathbf{100}]$	$\mathbf{q} \parallel [\mathbf{110}]$	$\mathbf{q} \parallel [\mathbf{111}]$
LA	C_{11}	$(C_{11} + C_{12} + 2C_{44})/2$	$(C_{11} + 2C_{12} + 4C_{44})/3$
$\mathbf{TA_1}$	C_{44}	C_{44}	$(C_{11} - C_{12} + C_{44})/3$
$\mathbf{TA_2}$	C_{44}	$(C_{11} - C_{12})/2$	$(C_{11} - C_{12} + C_{44})/3$

Examples of the use of the relation between the elastic stiffness matrix and phonon sound velocities can be found in Turner *et al.* [57] and Turner *et al.* [106].

There are also certain verifications that ensure the stability of the lattice which are called the Born elastic stability conditions. For a cubic lattice, they are defined as [140]

$$C_{11} - C_{12} > 0, \; C_{11} + 2C_{12} > 0, \; C_{44} > 0. \tag{2.22}$$

The stiffness matrix is the bridge between microscopic phonon behavior and macroscopic material constants such as compressibility, χ, and resistance to compressibility, also called the Bulk modulus $B = 1/\chi$, and these micro/macroscopic relations allow us to discuss the impact of complexity at both lengthscales.

$$B = \frac{1}{\chi} = \sqrt{\frac{C_{11} + 2C_{12}}{3}} \tag{2.23}$$

An example of the use of this relationship can additionally be found in Turner *et al.* [57].

2.2 Properties of the Phonon Gas

It is also necessary to understand how phonons quantum-mechanically fill the acoustic and optical branches in the phonon dispersion relation. Phonons are bosons, which means that there is no limitation to the number of them that occupy a given quantum or energy state, unlike electrons, for example, which are fermions and are therefore limited by the Pauli exclusion principle [140]. The lowest energy state is equal to $E_0 = \frac{1}{2}\hbar\omega$, $\hbar$ being Planck's constant, and subsequent energy states are filled accordingly such that the harmonic phonon energy is

$$E = \sum_{\mathbf{q},i} \hbar\omega(\mathbf{q}, i)\Big(\frac{1}{2} + n(\omega, T)\Big), \tag{2.24}$$

where i is an integer branch number and $n(\omega, T)$ is the Bose-Einstein distribution,

$$n(\omega, T) = \frac{1}{\exp(\hbar\omega(\mathbf{q}, i)/k_B T) - 1}, \tag{2.25}$$

which depends on Boltzmann's constant. It describes the average number of phonons occupying the energy level with energy $\hbar\omega$.

Next, we must hypothesize about how, at a given temperature, the phonons are going to fill the available energy states. This is called the vibrational density of states, $g(\omega)$, in which we integrate over energy surface S_ω, for volume, V, of the Brillouin zone in reciprocal space, which is $V/8\pi^3$.

$$g(\omega) = \frac{V}{8\pi^3} \int \frac{dS_\omega}{v_g(\omega)} d\omega \tag{2.26}$$

We also make note now of the fact that the group velocity is in the denominator, since it will become important later in this section.

We can then rewrite eq. 2.24 to include $g(\omega)$:

$$E = \int \Big(\frac{1}{2} + n(\omega, T)\Big)(\hbar\omega) g(\omega) d\omega. \tag{2.27}$$

Heat capacity, on the other hand, is defined as the amount of energy required to change the temperature of a material by one degree at constant volume, or $C_V = \left(\frac{\partial U}{\partial T}\right)_V$. Following eq. 2.27, it is therefore written as

$$C_V = \frac{\partial}{\partial T} \int n(\omega, T)(\hbar\omega) g(\omega) d\omega. \tag{2.28}$$

From this point there are two main pathways for calculating heat capacity: the Debye and Einstein methods. Similar to the way that we have treated the linear chain of atoms model, Einstein hypothesized that each atom could be treated as a simple harmonic oscillator, and he

assumed that all atoms vibrate at the same mean frequency, ω_E. He then derived a simple density of states equation based on the fact that each oscillator would have three possible directions of oscillation. Assuming n oscillators in the unit cell, each with a frequency $\hbar\omega_{\mathrm{E}}$ with a small fluctuations around that central frequency described by the delta function, the density of states function for the Einstein model is

$$g_{\mathrm{E}}(\omega) = 3nN_{\mathrm{A}}\delta(\hbar\omega - \hbar\omega_{\mathrm{E}}). \tag{2.29}$$

Then, with the help of eq. 2.28, the heat capacity for the Einstein model is

$$C_V = 3nN_{\mathrm{A}}k_{\mathrm{B}}\left(\frac{\hbar\omega_{\mathrm{E}}}{k_BT}\right)^2 \frac{\exp\left(\hbar\omega_{\mathrm{E}}/k_BT\right)}{\left[\exp(\hbar\omega_{\mathrm{E}}/k_BT) - 1\right]^2}. \tag{2.30}$$

Heat capacity can be defined by several ranges of temperature. At high temperatures, it reaches an upper limit which is known as the Dulong-Petit limit:

$$C_V = 3nN_{\mathrm{A}}k_{\mathrm{B}}. \tag{2.31}$$

This tells us that for cubic Yttria-Stabilized Zirconia, with four atoms per unit cell in its FCC lattice, the maximum heat capacity should be 99 J.mol^{-1}.K^{-1}. For clathrates, on the other hand, with 54 atoms per unit cell, the value is 1346 J.mol^{-1}.K^{-1}. Indeed, these values hold well with experimental data [148, 149].

At very low temperatures, however, eq. 2.30 decreases with an $\exp\left(\hbar\omega_{\mathrm{E}}/k_BT\right)$ relationship. This does not correspond to what we see experimentally, and this is due to the fact that, close to zero, the only filled energy states will be those of the acoustic modes, which are far from the small fluctuations from ω_{E} described by $\delta(\hbar\omega - \hbar\omega_{\mathrm{E}})$. They are therefore not very well reproduced with this particular model.

While Einstein's approach cannot completely describe all temperature ranges, it is, however, well suited for describing the optical phonon modes of a complex system: While Einstein does not account for the fact that the acoustic phonons disperse in energy, nor for the fact that they do not actually remain centered around a given frequency, he did find an accurate way to describe the optical phonon modes, which do stay centered around a given frequency. It is important to note that since acoustic and optical phonons contribute in different ways to the heat capacity of a material, we should not necessarily expect them to be treated with the same formula.

This leads us to the next model for calculating the density of states and heat capacity: the Debye model. Debye understood that atoms were more than simple harmonic oscillators, and he looked for a way to describe the dispersive nature of acoustic phonons. He concluded that each material has an intrinsic sound velocity, v_s, and that phonons disperse at this rate until a maximum frequency called the Debye frequency, ω_{D}.

$$\omega = v_s q \tag{2.32}$$

The density of states for the Debye model then becomes

$$g_{\mathrm{D}}(\omega) = \frac{3V\omega^2}{2\pi^2 v_s^3}d\omega. \tag{2.33}$$

However, we recall from eq. 2.26 that there is a van Hove singularity [40] when $v_g(\omega)$ goes to zero. This point is never reached in the Debye approximation since the sound velocity remains constant and does not reflect the curvature of the dispersion relation which can usually be

approximated by a sine() function. Also recalling from eq. 2.26 that we are concerned with the entire Brillouin zone, we can solve for ω_{D} in a given material:

$$\omega_{\mathrm{D}} = v_s \sqrt[3]{\frac{6n\pi^2}{V}}. \tag{2.34}$$

Again, as a point of reference, the Debye frequency for clathrates should therefore be $\omega_D = 36$ meV, using the sound velocity of the linear chain of atoms example above. However, as we have already demonstrated in Fig. 2.2, the acoustic regime is stopped approximately 8 times sooner than this value. We therefore already see the limitations of this model as well for describing complex and disordered systems.

Finally, heat capacity for the Debye model is given as

$$C_V = 9nN_A k_B \left(\frac{k_B T}{\hbar\omega_D}\right)^2 \int_0^{\omega_D} \left(\frac{\hbar\omega}{k_B T}\right)^4 \frac{\exp\left(\hbar\omega/k_B T\right)}{\left[\exp(\hbar\omega/k_B T) - 1\right]^2}. \tag{2.35}$$

The Debye model also respects the Dulong-Petit limit at high temperatures, in addition to exhibiting a T^3 behavior at very low temperatures. The term Debye temperature, θ_{D}, is often coined to represent this low-temperature dependence in the Debye model. On the surface, therefore, and to the eye, a Debye model fit appears to work rather well. However, the description does not match the true microscopic meaning in complex and disordered systems, as per the limitations given above.

The Debye model can, however, be used to approximate acoustic phonon modes of a complex system because, at least at low q, acoustic phonons disperse linearly. If we combine this with the Einstein model's ability to replicate the behavior of optical modes, we have a heat capacity formula that is more adapted to the microscopic understanding in clathrates, in which there are very few Debye-style acoustic modes with a renormalized ω_{D} to match the acoustic mode filtering, and a continuum of many Einstein-style optical modes across a large frequency range. This phenomenological model is detailed in Lory *et al.* [27].

Now that we have a basic understanding of phonons and their properties, and since thermal conductivity and its formulas have already been discussed extensively in the previous chapter in Section 1.1, we will move on to detailing the theoretical models that are currently available to simulate the properties discussed throughout this chapter.

2.3 Theoretical simulations through the advancement of computer science

The following sections of this chapter will be dedicated to the advanced calculations that we use to more accurately model complexity and disorder in crystalline systems. The harmonic approximation, which was the focus in Section 2.1, can be reasonably expected to reproduce phonon spectra quite accurately, even for instances in complex and disordered systems in which anharmonicity can be treated as only a perturbation of the harmonic approximation, as shown in Turner *et al.* [57]. However, it is not enough for calculating physical properties, since phonons within the harmonic approximation have infinite lifetimes, and because lattice thermal expansion is not taken into account. This creates a domino effect, causing thermal properties such as thermal conductivity to be infinite.

Thankfully, new doors have now been opened due to developments in computer science and computing power. Theoreticians have had improved results in heat propagation calculations through the incorporation of disorder and/or anharmonicity for rock-salt and Bi_2Te_3-based

thermoelectric compounds [150–158], Ag-based materials [159–162], quasicrystals [122, 163–166], clathrates [85, 93, 167–169], oxides [94, 98, 170], and semiconductors in general [171–181], just to name a few examples.

There are two main divisions of theoretical models that will be discussed in these sections, namely Density Functional Theory (DFT) and Molecular Dynamics (MD). In order to discuss DFT, I will first mention developments that enhance the harmonic approximation, then I will introduce the quasiharmonic approximation which includes the effect of lattice expansion with temperature. Finally, I will highlight anharmonic perturbation theory, which is used for anharmonic crystals, or crystals with strong and/or locally concentrated anharmonicity. The MD section will cover several case study examples of how the inclusion of this method to computer simulations has brought about closer matching to experimental results.

One of the main differences between DFT and MD to keep in mind throughout the following sections is that DFT is limited in its ability to account for disorder in the structural model. Molecular Dynamics, on the other hand, tracks the interaction between atoms and has the advantage of being able to implement disorder into the structural model, even if it does not include quantum effects. We will come back to this concept momentarily.

2.3.1 Density Functional Theory Calculations

To date, several well-known coding structures such as Quantum ESPRESSO and VASP exist as packages that can be used for DFT calculations. At the time of writing, The Materials Project website has also gathered *ab-initio* calculations of an incredibly wide range of materials, creating a database of open-source information for the scientific community. Several incredibly thorough review articles have already summarized the state-of-the-art for such techniques [182–184], and therefore I will attempt to describe just a few relevant case studies for different types of DFT calculations.

2.3.1.1 The harmonic approximation

The harmonic approximation, first given in eq. 2.2, has been the focus of this chapter up until this point, and we have already seen the power in using even a simple linear chain of atoms model within the harmonic approximation to describe features of type-I clathrates. Indeed, full harmonic approximation simulations for the type-I clathrate Ba_8Si_{46} fit well with experimental results [85]. Several research teams have made the community aware, however, of the fact that *ab initio* harmonic approximation calculations made on multiple different ordered models of Ge-based clathrates seemed to require a scaling factor multiplied to the phonon dispersions in order to meet the energies of the experimentally measured ones [27, 167, 185], while this was not the case for Si-based clathrate simulations [85].

One recent advancement in harmonic approximation calculations, therefore, is atom-specific developments, such as what has been done for Ge-based clathrates: In 2019, H. Euchner and A. Groß applied the strongly constrained and appropriately normed (SCAN) meta-generalized-gradient (meta-GGA) functional [186] to a series of Ge-based clathrates [169] and found a much closer matching to experimental results without the need for any scaling factor. The difference appears to lie in the details of the exchange-correlation energy for the transition metal substitutions for semiconducting clathrates, which plays a more significant role in the energy phase space for these Ge-based clathrates. The findings were further confirmed in Turner *et al.* [57] for the clathrate $Ba_{7.81}Ge_{40.67}Au_{5.33}$. Preliminary results on disordered models of $Ba_{7.81}Ge_{40.67}Au_{5.33}$ using the SCAN meta-GGA functional also suggest that this method could help interpret the polarization dependence of the low-lying optical branches as well.

2.3.1.2 Treating anharmonicity

The following subsections will focus on the inclusion of anharmonicity, or the higher-order terms from the Taylor expansion series in eq. 2.1. While the harmonic approximation can provide us with a baseline or starting point for describing the quantized vibrations in a lattice, it works within a temperature-, pressure-, and volume-independent setting. To be more precise, this means that the IFCs from eq. 2.15 have no temperature dependence, and that thermal expansion cannot be considered. This acts as a domino effect on phonon behavior, since there are no phonon scattering mechanisms (see eq. 1.4) in the equation that would limit phonon lifetime or mean free path (MFP), and no temperature dependence that might change the influence of said scattering mechanisms. Therefore, the harmonic approximation is not quite enough to simulate phonon lifetimes or thermal conductivity in any system.

In order to study phonon lifetime, we must bring the infinite phonon lifetimes of the harmonic approximation towards finite lifetimes that are determined by the relevant phonon scattering mechanisms for a given crystalline structure. This is done by considering the higher-order anharmonic terms.

The quasiharmonic approximation still works within a constant temperature regime, in which the equation of state is $P = -\left(\frac{\partial F}{\partial V}\right)_T$ [136], but we quantify the anharmonic effect of the lattice moving from its equilibrium lattice parameter and the consequential phonon frequency renormalizations. In other words, the oscillators are volume-dependent, allowing us to track the thermal expansion of the lattice [187]. This method is often used in conjunction with perturbation theory (see the next paragraphs) in order to simulate the temperature dependence of thermal properties.

To now speak more generally, anharmonicity is defined as the deviation from harmonic oscillation. In other words, we are considering oscillators that do not oscillate strictly according to their simple harmonic potential. Anharmonic perturbation theory tells us that if these anharmonic effects are small in comparison to the harmonic components of the system, we can consider them as a perturbation of the original harmonic approximation calculation [95, 136, 140]. We are therefore returning to the inclusion of the $n = 3, 4, ...$ terms of eq. 2.1, given at the beginning of this chapter. Some examples of systems that require anharmonic perturbation theory are TiO_2 [124] and ScF_3 [188].

The $n = 3$ and $n = 4$ terms are interatomic force perturbations of the harmonic approximation that represent the ionic displacements from equilibrium within the crystal pertaining specifically to three- and four-phonon scattering processes, respectively, or the cubic and quartic anharmonicity terms. Fig. 2.6 summarizes these processes. Sketches (a) and (b) describe three-phonon scattering processes in which a phonon is either annihilated or created, respectively. Sketches (c)-(e) represent four-phonon scattering processes in which similar creation/annihilation processes are found through a combination of four phonons.

In terms of the representation of anharmonic processes in DFT, however, these are typically described by the Feynman diagrams of anharmonic self-energy [189–192]. Some of the relevant diagrams are shown in Fig. 2.7. The phonon propagator (solid lines) has a third or fourth-order interaction described by the vertices of each diagram (open circles) [193]. The tadpole in (a) and bubble (c) diagrams are associated with the cubic term, where the tadpole diagram contributes to phonon frequency renormalizations and the bubble diagram mainly brings about changes in phonon linewidth. Furthermore, (a) actually represents the optical component of the tadpole diagram. The tadpole diagram is also composed of an acoustic component, seen in (b), which is how thermal expansion (TE) is calculated [193]. An important limitation to current anharmonic perturbation theory is that thermal expansion cannot be calculated directly, because the acoustic dispersions, represented by the spring in diagram (b), diverge at low q. The quartic anharmonic term, on the other hand, contains the loop diagram in (e), which also contributes to phonon

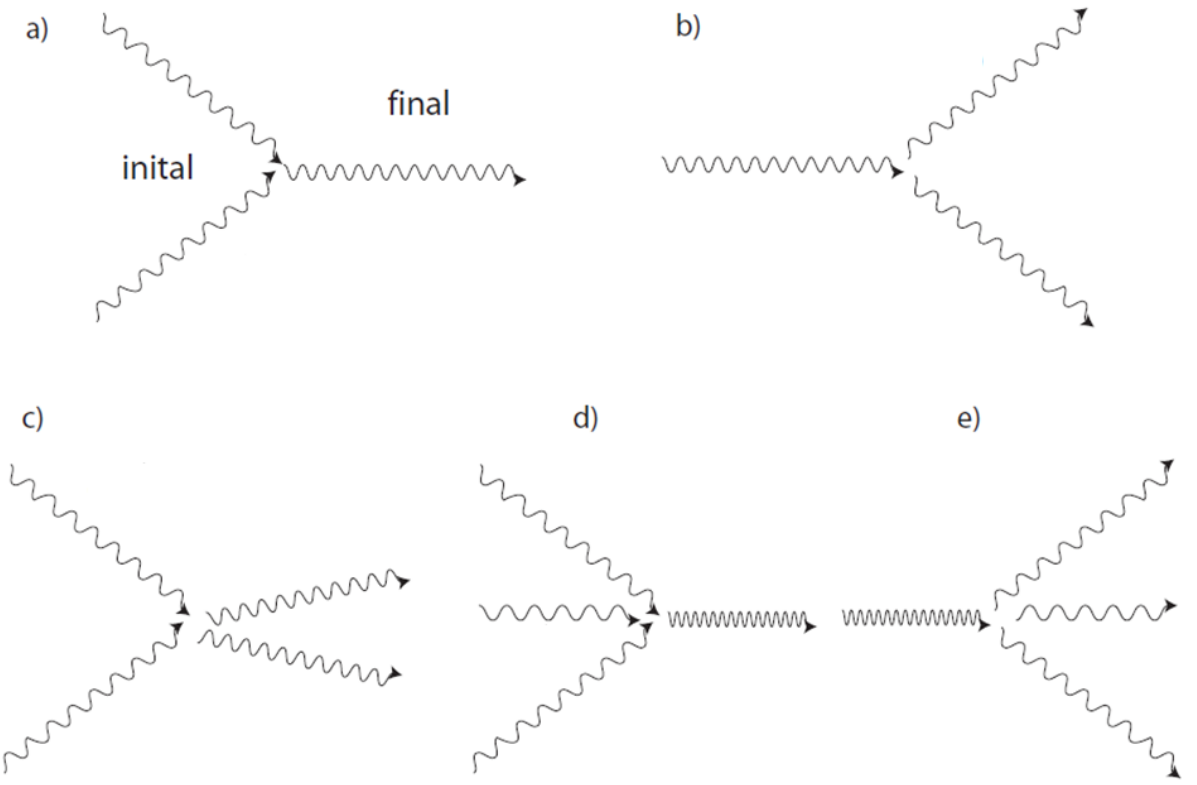

Figure 2.6: Sketches of three and four phonon scattering processes. *(a) and (b) describe three-phonon scattering processes, and (c)-(e) the four-phonon scattering processes. In (a), two lower frequency phonons scatter on each other, resulting one higher frequency phonon. Similar processes are sketched in (b)-(d). Figure has been adapted from Ref. [142].*

frequency renormalizations [189], and two other second order diagrams (not shown). We will come back to Fig. 2.7(d) momentarily.

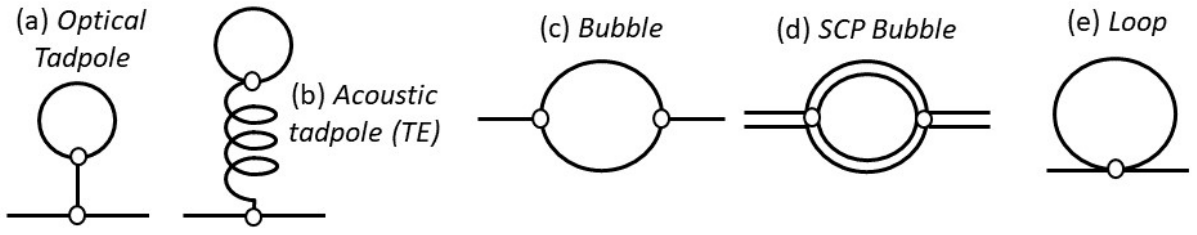

Figure 2.7: Feynman diagrams of anharmonic self-energy. *Feynman self-energy diagrams referring to three- and four-phonon scattering process diagrams, (a-d) and (e), respectively. (d) refers to the bubble diagram specific to the self-consistent phonon (SCP) method. Solid lines represent the phonon propagator and open circles represent the three and four phonon interaction vertices.*

Many intriguing advancements in *ab initio* theory have been made in recent years which center largely around the inclusion of third-order anharmonic phonon processes to calculations for semiconductors. For instance, the importance of electron-phonon [194] and phonon-phonon [171] scattering mechanisms in GaAs have been detailed in order to provide much-needed insight into the lifetimes of such processes in a widely-used semiconductor. The calculations were even able to differentiate between different phonon-phonon scattering processes, or Herring and non-Herring processes as termed in the article, in order to discuss the dominate scattering process within

different regimes of the energy-momentum phase space. This is an important theme which will be revisited in Turner *et al.* [106] and in Fig. 3.16 in the following chapter.

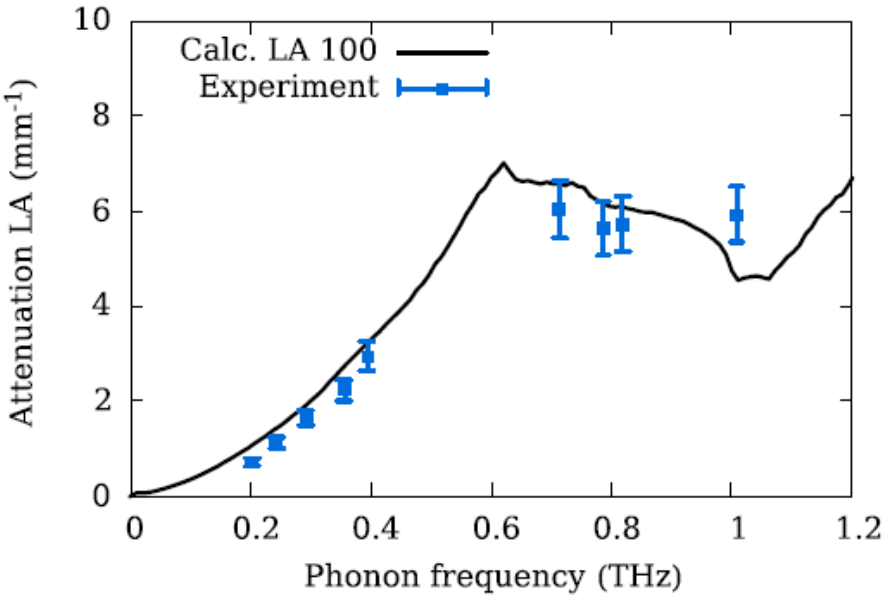

Figure 2.8: Frequency dependence of phonon attenuation in GaAs. *Figure comes directly from Ref [171]. The attenuation of longitudinal acoustic phonons propagating along the [100] direction has been calculated by ab-initio methods and compared to experimental data at 50 K.*

In addition to these studies, there is a variation to perturbation theory called the self-consistent approach [195] that has proved useful in calculating properties for complex and disordered systems. In this case we solve in steps: the harmonic approximation is calculated, along with the anharmonic perturbations, and then the calculation is self-consistently renormalized until it converges on a solution.

One example of this approach that is relevant to this thesis are the self-consistent calculations made for the type-I clathrate $Ba_8Ge_{30}Ga_{16}$ by T. Tadano *et al.* [93, 95], which self-consistently renormalize phonon frequencies through what is called the self-consistent phonon (SCP) method. These calculations are distinct from the self-consistent harmonic approximation (SCHA) because both self-consistent and perturbation theories have been applied in order to fully grasp the anharmonicity of clathrates. As seen in Fig. 2.9(a), using the SCP method (solid red lines) causes phonon frequency renormalizations which match the frequencies of the Raman-active low-lying optical branches as opposed to the harmonic approximation calculations (dashed gray lines). This brought about a much closer matching to lattice thermal conductivity, as seen in Fig. 2.9(b).

An extensive comparison of the phonon frequencies calculated by the SCP method to experimental results can be found in Turner *et al.* [57]. In addition, T. Tadano and co-authors have proven that the SCP method can be applied to other systems that exhibit strong anharmonicity [94, 96–98] as well.

I would also like to highlight a few interesting key features of these $Ba_8Ge_{30}Ga_{16}$-specific SCP calculations: (1) Since calculations were done self-consistently, the self-consistently-calculated Bubble term resembles the diagram in Fig. 2.7(d), rather than the Bubble term in the harmonic approximation. (2) The thermal expansion component that comes from acoustic tadpole Feynman diagram was not included, since it cannot be calculated directly. Instead, MD simulations of the fully ordered $Ba_8Ge_{30}Ga_{16}$ structure were used to calculate the lattice parameter at given

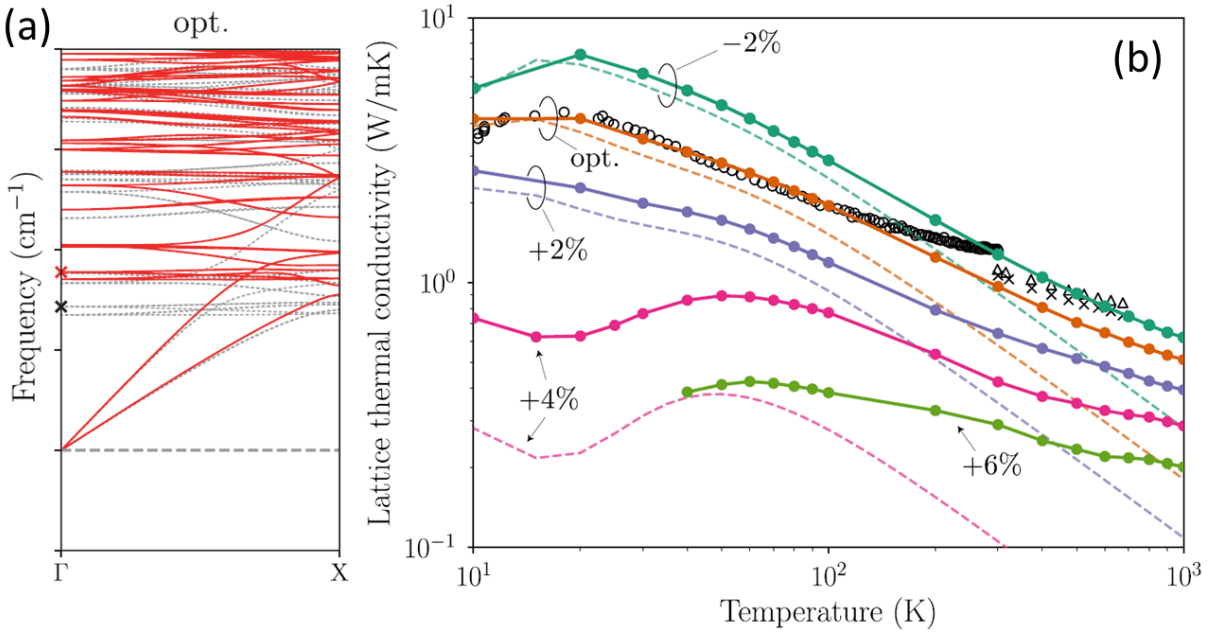

Figure 2.9: ***Self-consistent phonon method calculations for the type-I clathrate*** $Ba_8Ge_{30}Ga_{16}$. *Figures come directly from Ref [196]. (a) The phonon spectra along a given high symmetry direction, calculated using the ab-initio self-consistent phonon method (red solid lines). The red and black crosses at the center of the Brillouin zone mark the energies of the Raman active* T_{2g} *mode. (b) These phonon spectra are used to calculate the lattice thermal conductivity (*κ_L*), which has a much closer matching to the experimentally measured* κ_L *(open black circles, triangles, and squares- references for which can be found in Ref [196]). The particular lattice constant used to calculate the phonon spectra in (a) corresponds to the orange 'opt.' curve in (b).*

pressures, and then the temperature-dependent Grüneisen parameter was calculated from the cubic free energy constants in order to indirectly account for thermal expansion.

2.3.2 Molecular dynamics for complex and disordered crystals

In recent years, MD simulations have provided much needed insight into the anharmonic effects found many of the materials I have mentioned in the preceding sections. MD tracks the evolution of a group of interacting particles over time through their position and velocity trajectories in phase space. MD has been largely used to calculate the temperature dependence of κ, although re-interpretation of specific phonon behaviors with MD simulations alone has proven difficult [197]. The main advantage to MD simulations is that all anharmonic terms are included, allowing us to finitely model the strong and/or localized anharmonic effects known to exist in the types of materials that have been our focus. With the following two examples, I hope to demonstrate the usefulness of this technique in simulating complexity and disorder.

The first example is that which was done for the quasicrystal approximant o-$Al_{13}Co_4$ [122]. The authors found that by randomly removing several Al atoms from the generated supercell in order to simulate vacancies, the model with vacancies had a lower minimum-energy atomic configuration than the ordered model. This disordered model then provided a better match to the experimental phonon dispersions. As seen in Fig. 2.10(a), the disordered model simulation was able to much more closely match the experimental phonon signal, even reproducing the Lorentzian-like tail. For the κ shown in Fig. 2.10(b) as well, the disordered model was able to replicate a similar plateau region at higher temperature, confirming the significance of using a model that includes a representation of the disorder in the system.

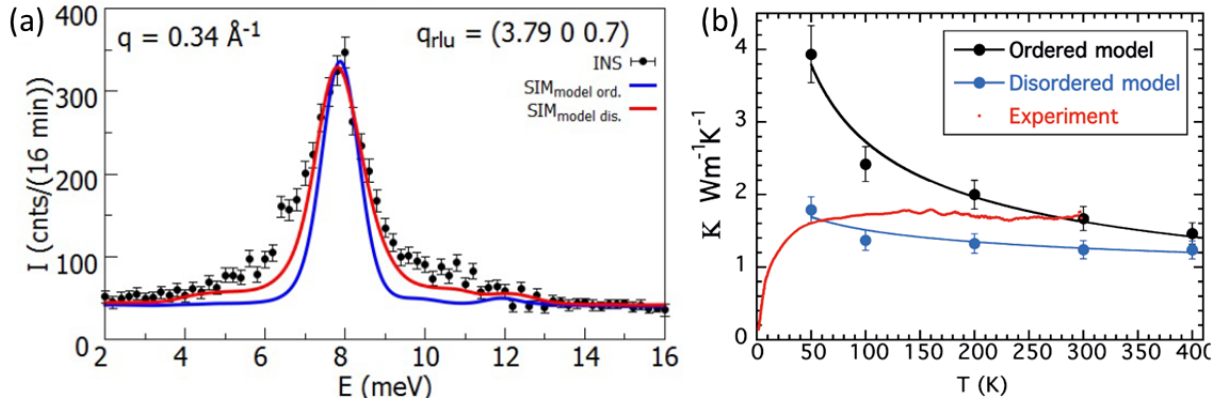

Figure 2.10: Ordered and disordered model simulation results for the quasicrystal approximant o-$Al_{13}Co_4$. *Figures come directly from Ref [122]. (a) An example energy scan of a transverse acoustic phonon mode measured experimentally by inelastic neutron scattering (solid black circles) and theoretically using both ordered (solid blue line) and disordered (solid red line) models. (b) The lattice thermal conductivity measured experimentally (solid red line) and theoretically using both ordered (solid black circles) and disordered (solid blue circles) models. (Note that the colors of the models have switched between the two figures. Please refer to the legends within the figures for clarification.)*

The second example comes from a recently published article on the perovskite $SrTiO_3$ [170]. Experimental evidence, in the form of inelastic neutron scattering measurements, was given for the disappearance of transverse acoustic phonon branches at low temperature, below the phase transition/distortion that begins at 105 K in the material. AIMD, or *ab initio* MD, simulations were used extract to renormalized force constants at 3 relevant temperatures for this system, allowing for the tracking of this intriguing occurrence with temperature, as seen in Fig. 2.11.

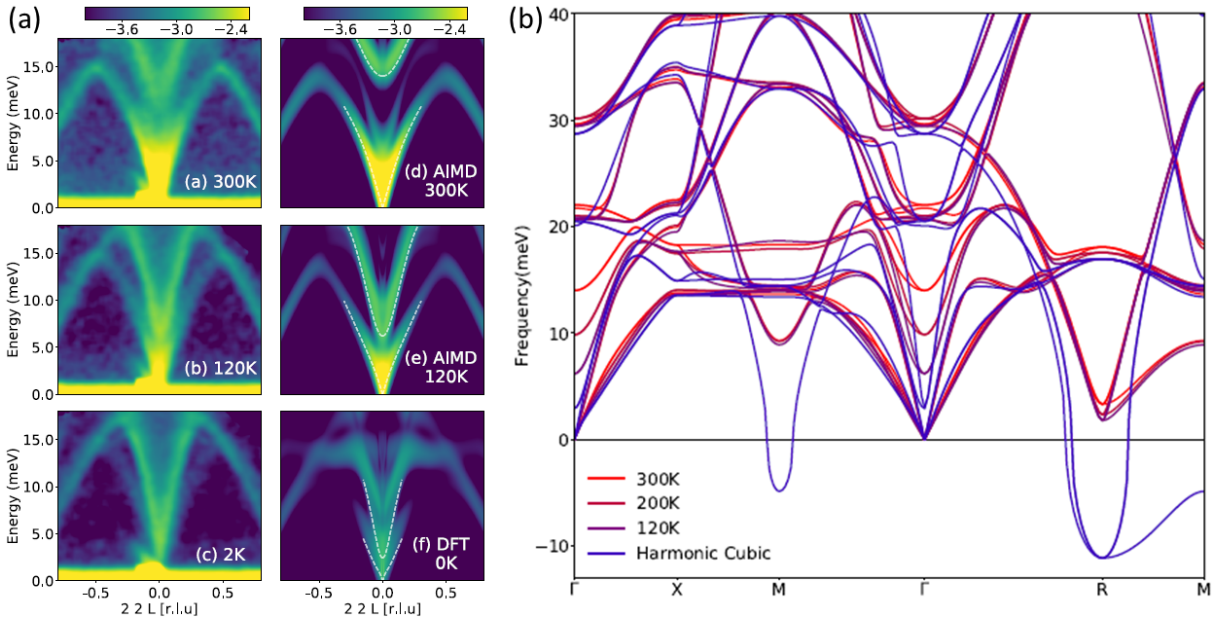

Figure 2.11: AIMD simulations for the perovskite $SrTiO_3$. *Figures come directly from Ref [170] and its corresponding Supplementary Material. (a) AIMD and TDEP method simulations at three temperatures for the point $\mathbf{Q} = [22L]$ in reciprocal space. (b) By computing AIMD trajectories initialized with experimental lattice constants, the phonon dispersions along high symmetry directions were calculated at three temperatures. For comparison, the harmonic approximation calculation is also shown, which contains unstable frequencies.*

There are many other equally pertinent examples of the use of MD simulations that could be included here, and I refer the reader to a few of these now: Refs [152, 155, 164, 187, 198–200]. The main limitations to MD, however, remain that it is extremely computationally intensive. This limits both the size of the simulated system and the length of time for which we want to observe its interactions. However, as computing power increases in the coming years, we will surely see correspondingly impressive developments in the field of MD simulations.

With these tools an concepts in mind, we will now move on to experimental methods for measuring phonon properties, with a focus on inelastic neutron and X-ray scattering techniques.

CHAPTER 3

Inelastic Scattering Techniques for Phonon Measurements

The dispersions, group velocities, response function intensities, mean free paths, lifetimes, and density of states are just a few properties of phonons that can be measured experimentally. When discussing phonon behavior, we are usually referring to an meV-scale, meaning that the types of instruments that can measure phonon properties must have extremely high resolution and precision. The focus of this chapter will be on inelastic scattering methods, namely inelastic neutron and X-ray scattering (INS, IXS) techniques, which are highlighted in Fig. 3.1. However, other complementary techniques include Brillouin scattering, Raman scattering, optical pump probe techniques, and X-ray transient grating spectroscopy.

The following sections on INS, Section 3.1, and IXS, Section 3.2, provide detailed explanations as to why neutrons and X-rays can be made into probes for measuring phonons, and the variety of instruments available for making these measurements.

3.1 Inelastic Neutron Scattering

Experimentally measuring the properties of phonons requires instruments with extremely high resolution. To elaborate, propagative acoustic phonon energies occur in the meV range and have lifetimes that are in the tens of µeV range, with the full phonon spectrum usually covering an energy range of a few tens of meV. Neutrons are ideal for measuring phonons in these ranges since one, their wavelengths are on the same order of magnitude as interatomic distances in a crystal lattice, and two, they have energies in the range of a few tens of meV, therefore making them sensitive to coherent lattice vibrations. If we can track this small change in energy of the neutron before and after scattering it onto a sample, we can measure a phonon excitation or annihilation.

This is easier said than done, however, since this means that we need to be able to capture energy shifts on the order of $\sim$1 meV. There are several different types of neutron spectrometers that make this kind of experiment possible, and I will discuss each in detail in this chapter. I will first, however, cover a typical neutron scattering experiment, and explain the different types of information we can gain from it. The following derivations come from those in literature detailed by G. L. Squires [201], Shirane *et al.* [202], H. Schober [203], and S. Pailhès *et al.* [204].

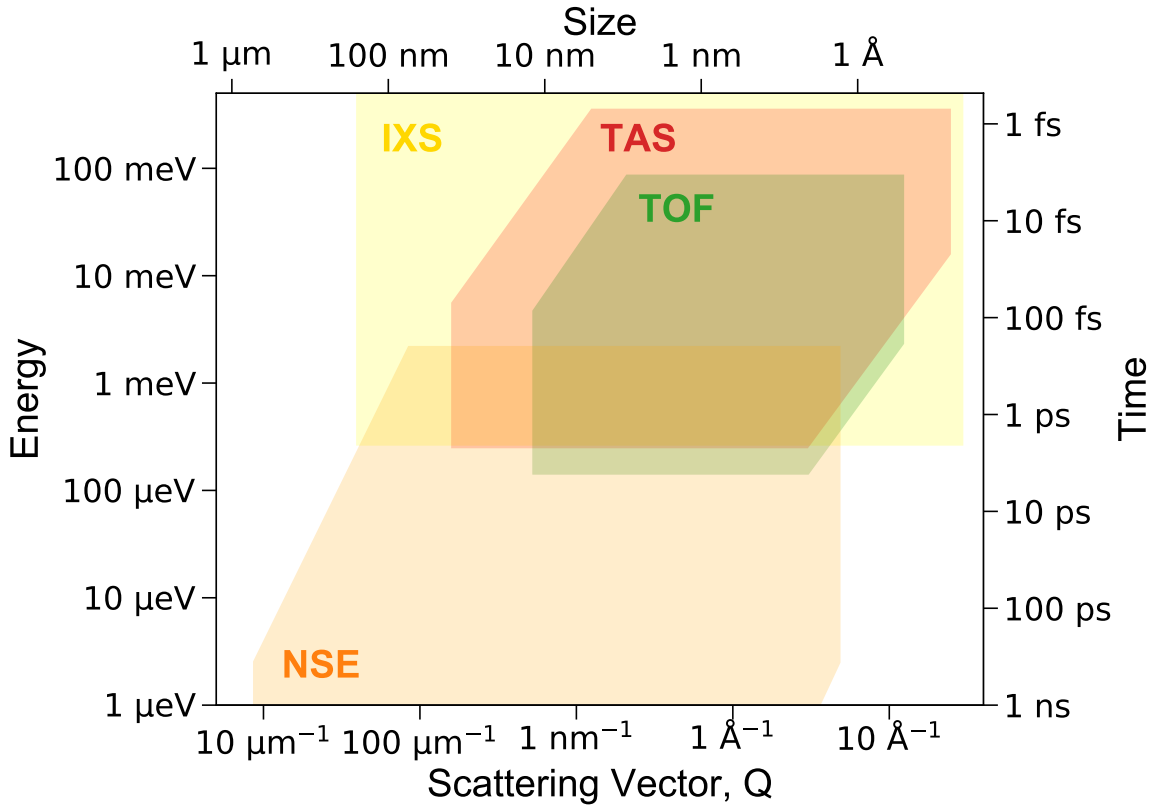

Figure 3.1: A comparison of inelastic neutron and X-ray scattering techniques. *The time, length, and energy transfer scales of different types of neutron and X-ray probe techniques that are suitable for measuring phonons are shown in the figure. These include inelastic X-ray scattering (IXS), triple-axis spectroscopy (TAS), time-of-flight (TOF) spectroscopy, and Neutron Spin-Echo (NSE). The TAS and TOF shaded regions focus on thermal neutron ranges. The neutron resonance spin-echo (NRSE) technique, not shown, will also be discussed in this chapter, and while it overlaps with TAS, it gives us access to a much higher energy resolution.*

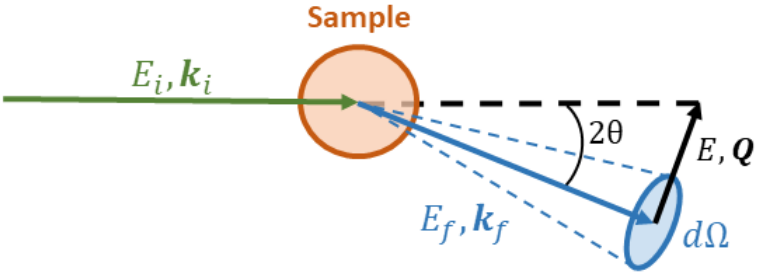

Figure 3.2: Generalized example of a scattering event. *An incoming beam of probe particles with incident energy E_i and wave-vector k_i strikes a sample, and said interaction causes the scattered beam to have an energy E_f and wave-vector k_f with an angle 2θ relative to the incident beam. A portion of all scattered probe particles are then collected in solid angle $d\Omega$.*

A scattering event, like the general case presented in Fig. 3.2, is controlled by momentum and energy conservation laws, seen in eqs. 3.1-3.3. In the case of INS, an incident neutron beam with incoming energy E_i and wave-vector $k_i = 2\pi/\lambda_i$ is scattered onto a sample such that the outgoing beam has energy E_f and wave-vector k_f with an angle 2θ relative to the incident beam.

$$\mathbf{Q} = \mathbf{k}_i - \mathbf{k}_f \tag{3.1}$$

$$Q^2 = k_i^2 + k_f^2 - 2\mathbf{k}_i\mathbf{k}_f \cos(2\theta) \tag{3.2}$$

$$\hbar\omega = E_i - E_f = \frac{\hbar^2}{2m_n}(k_i^2 - k_f^2) \tag{3.3}$$

In addition, there are two possible cases in which energy is conserved. The first is the case in which there is no energy exchange between the sample and incoming neutrons, $E_i = E_f$, and, by extension, $|\mathbf{k}_i| = |\mathbf{k}_f|$, resulting in an elastic neutron scattering event in which the interaction with the sample is purely momentum-based. Furthermore, when eq. 3.1 becomes $\mathbf{Q} = \mathbf{k}_f - \mathbf{k}_i = \mathbf{G}$, we call this the Bragg condition, in which $\mathbf{G}$ is the reciprocal lattice vector defined by d_{HKL}, the lattice spacing: $|\mathbf{G}| = 2\pi/d_{\text{HKL}}$. Then, using eq. 3.1 and again the relation $k = 2\pi/\lambda$ written above,

$$|\mathbf{G}| = 2|\mathbf{k}_i| \sin(\theta) = 2\pi/d_{\text{HKL}}, \tag{3.4}$$

leading to the formula for Bragg's law, where n is an integer that represents the Bragg reflection order:

$$n\lambda = 2d_{\text{HKL}} \sin(\theta). \tag{3.5}$$

The second case in which energy is conserved occurs when some of the energy of the neutron is transferred to (or taken from) the sample, creating (or annihilating) an excitation such as a phonon, causing $E_i \neq E_f$, and, again by extension, $\mathbf{k}_i \neq \mathbf{k}_f$ of the neutron. This is an inelastic neutron scattering event. We denote this small momentum transfer as $\mathbf{q}$, which, in our case of a phonon, is also called the phonon wave-vector, such that eq. 3.1 becomes

$$\mathbf{Q} = \mathbf{G} + \mathbf{q}. \tag{3.6}$$

Using eq. 3.3 in the case where $\hbar\omega = \frac{\hbar^2}{2m_n}(k_i^2 - k_f^2) > 0$, the neutron gives energy to the sample, creating an excitation. This is called Stokes scattering. Conversely, when $\hbar\omega = \frac{\hbar^2}{2m_n}(k_i^2 - k_f^2) < 0$, the neutron gains energy from the system, annihilating an excitation. This is called Anti-Stokes scattering.

By choosing a specific point $\mathbf{Q}$ in reciprocal space and energy transfer $\hbar\omega$, and ensuring that the condition in eq. 3.3 is still met when making our $\mathbf{Q} = \mathbf{G} + \mathbf{q}$ definition, we can probe the entire phase space of a material, tracking the quantized phonon excitations/annihilations dictated by the material's lattice and atomic configuration.

3.1.1 The Measurable Quantity of a Neutron Scattering Event

Referring once again to the general scattering event described in Fig. 3.2, after directing a spectrometer towards a certain point in phase space by using the known $\mathbf{k}_f$ and $\mathbf{k}_i$ to complete a scattering triangle defined by eq. 3.3, we measure the amount of flux of the initial neutron beam, Φ, that has been scattered into the solid angle element of interest, $d\Omega$. We define the cross-section, σ, as the number of neutrons scattered per second out of the number of incident neutrons per cm^2 per second. Then, only the neutrons that scatter with an angle of 2θ relative to the incident beam and that have a final energy between E_f and $E_f + dE_f$ are captured in solid angle $d\Omega$, creating the double differential cross-section for neutron scattering, $\frac{d^2\sigma}{d\Omega dE_f}$.

In order to derive $\frac{d^2\sigma}{d\Omega dE_f}$, we must consider the sum of the changes in quantum state of the sample from λ_i to λ_f caused by the interaction between the neutron and the sample defined by $\mathbf{k}_i \to \mathbf{k}_f$. From the conservation of energy, it then follows that

$$E_i + E_{\lambda_i} = E_f + E_{\lambda_f} \tag{3.7}$$

We then use $w_{(\mathbf{k}_i,\lambda_i)\to(\mathbf{k}_f,\lambda_f)}$ to represent the probability density of a transition from $(\mathbf{k}_i,\lambda_i)$ to $(\mathbf{k}_f,\lambda_f)$. This is otherwise known as Fermi's golden rule, we can relate this to the density of final states, $\rho_{\mathbf{k}_f}(E_f) = \frac{mk_f}{\hbar^2}$, and the interaction potential of the neutron with the sample, V.

$$w_{(\mathbf{k}_i,\lambda_i)\to(\mathbf{k}_f,\lambda_f)} = \frac{2\pi}{\hbar}\rho(E_f)\left|\langle\mathbf{k}_f,\lambda_f|V|\mathbf{k}_i,\lambda_i\rangle\right|^2 \tag{3.8}$$

Then in terms of the double differential cross-section, we have the following, in which $\delta((E_f - E_i) - (E_{\lambda_i} - E_{\lambda_f}))$ is a Dirac delta function that selects the more probable scattering events, coming from Fermi's golden rule.

$$\left(\frac{d^2\sigma}{d\Omega dE_f}\right)_{(\mathbf{k}_i,\lambda_i)\to(\mathbf{k}_f,\lambda_f)} = \frac{k_f}{k_i}\frac{(2\pi)^4 m^2}{\hbar^4}\left|\langle\mathbf{k}_f,\lambda_f|V|\mathbf{k}_i,\lambda_i\rangle\right|^2\delta((E_f - E_i) - (E_{\lambda_i} - E_{\lambda_f})) \tag{3.9}$$

However, this gives us $(\frac{d^2\sigma}{d\Omega dE_f})_{(\mathbf{k}_i,\lambda_i)\to(\mathbf{k}_f,\lambda_f)}$, the double differential cross-section over a given transition $\lambda_i \to \lambda_f$. There are two more steps before arriving at the final form of $(\frac{d^2\sigma}{d\Omega dE_f})$. The first is that we define p_{λ_i} as the statistical weight for each state λ_i such that $\sum_{\lambda_i} p_{\lambda_i} = 1$ through the partition function, Z, and the Boltzmann distribution.

$$p_{\lambda_i} = \frac{1}{Z}e^{\left(\frac{-E_{\lambda_i}}{k_B T}\right)},\ Z = \sum_{\lambda_i} e^{\left(\frac{-E_{\lambda_i}}{k_B T}\right)} \tag{3.10}$$

The second step involves the summation of the interactions of the incident neutron with each nucleus for N total nuclei in the sample. Let us assume that vector $\mathbf{r}$ and vector $\mathbf{R}_j$ give the positions of the neutron and the jth nucleus with respect to an arbitrary origin in the sample's lattice, respectively. We then define the interaction potential as

$$V(\mathbf{r}) = \sum_{j=1}^{N} V_j(\mathbf{r} - \mathbf{R}_j). \tag{3.11}$$

Then, by making the Fourier transform of the interaction potential, we define the form factor $V_j(\mathbf{Q})$ of the jth scatterer's potential $V_j(\mathbf{r})$ as

$$V_j(\mathbf{Q}) = \int e^{i\mathbf{Q}\cdot\mathbf{r}}V_j(\mathbf{r})d^3r = \frac{2\pi\hbar^2}{m}b_j, \tag{3.12}$$

where b_j is the neutron scattering length. This parameter will become important in Section 3.1.2. With these extra considerations, and the use of the closure relation $\sum_{\lambda_f}|\lambda_f\rangle\langle\lambda_f| = \mathbf{I}_\lambda$ [203], we arrive at

$$\begin{aligned}\left(\frac{d^2\sigma}{d\Omega dE_f}\right) &= \frac{k_f}{k_i}\frac{1}{2\pi\hbar}\sum_{\lambda_i}p(\lambda_i)\sum_{j,j'=1}^{N}b_j b_{j'}^*\int_{-\infty}^{\infty}\langle\lambda_i|e^{-i\mathbf{Q}\cdot\mathbf{R}_{j'}(0)}e^{i\mathbf{Q}\cdot\mathbf{R}_j(t)}|\lambda_i\rangle e^{-i\omega t}dt \\ &= \frac{k_f}{k_i}S(\mathbf{Q},\omega)\end{aligned} \tag{3.13}$$

This is known as the *master equation of scattering* [203]. Of equal importance is the scattering function, $S(\mathbf{Q},\omega)$, since it is the term by which we set all instrumental parameters for a neutron scattering experiment. In particular for an inelastic experiment designed to measure phonons, the scattering function tells us the probability that one of the particles in the incoming beam loses/gains the exact energy needed to produce a given phonon excitation/annihilation, allowing us to detect this exchange. The usefulness of $S(\mathbf{Q},\omega)$ will be discussed in Subsection 3.1.3.

3.1.2 Coherent and Incoherent Scattering

The double differential cross-section for neutron scattering given in eq. 3.13 is made up of coherent and incoherent scattering components, and they explain correlated atomic movements, or when $j \neq j'$, and individual atomic movements, or when $j = j'$, respectively.

$$\left(\frac{d^2\sigma}{d\Omega dE_f}\right)_{\text{tot}} = \left(\frac{d^2\sigma}{d\Omega dE_f}\right)_{\text{coh}} + \left(\frac{d^2\sigma}{d\Omega dE_f}\right)_{\text{inc}} \tag{3.14}$$

Assuming that we have a very large number of nuclei in the sample, we average these interactions such that the $b_j b^*_{j'}$ term in eq. 3.13 becomes $\overline{b_j b^*_{j'}}$. This leads to the definition of the coherent and incoherent scattering components:

$$\left(\frac{d^2\sigma}{d\Omega dE_f}\right)_{\text{coh}} = \frac{k_f}{k_i}\frac{1}{2\pi\hbar}\sum_{\lambda_i} p(\lambda_i) \sum_{j,j'=1}^{N} \overline{b_j b^*_{j'}} \int_{-\infty}^{\infty} \langle \lambda_i | e^{-i\mathbf{Q}\cdot\mathbf{R}_{j'}(0)} e^{i\mathbf{Q}\cdot\mathbf{R}_j(t)} | \lambda_i \rangle e^{-i\omega t} dt \tag{3.15}$$

$$\left(\frac{d^2\sigma}{d\Omega dE_f}\right)_{\text{inc}} = \frac{k_f}{k_i}\frac{1}{2\pi\hbar}\sum_{\lambda_i} p(\lambda_i) \sum_{j}^{N} (\overline{b_j^2} - (\overline{b_j})^2) \int_{-\infty}^{\infty} \langle \lambda_i | e^{-i\mathbf{Q}\cdot\mathbf{R}_{j'}(0)} e^{i\mathbf{Q}\cdot\mathbf{R}_j(t)} | \lambda_i \rangle e^{-i\omega t} dt \tag{3.16}$$

The coherent, σ_{coh}, and incoherent, σ_{inc}, scattering cross-sections in the monatomic lattice limit are defined as follows. The scattering length of an element is isotopic and spin dependent, meaning that different isotopes will have different coherent scattering lengths. In the case which a natural element contains different isotopes (or spins, such as for H), their random distribution in the studied sample will also lead to a Laue scattering.

$$\sigma_{\text{coh}} = 4\pi\left(\langle \bar{b} \rangle^2\right) \tag{3.17}$$

$$\sigma_{\text{inc}} = 4\pi\left(\langle \overline{b^2} \rangle - \langle \bar{b} \rangle^2\right) \tag{3.18}$$

When conducting a neutron scattering experiment it is important to have an idea of the amount of coherent and incoherent scattering you can expect from a given sample. Scattering cross-sections are usually given in barns (1 barn = 10^{-24} cm^2) and neutron scattering lengths are given in femtometers (1 fm = 10^{-13} cm), and the values can be found in literature [201, 205]. An example of the importance of the weighted coherent and incoherent scattering components can be found in the Appendix of Turner *et al.* [106], in which it can be shown that approximately 70% of the total neutron scattering cross-section can be expected to be incoherent scattering.

3.1.3 The Scattering Function

Coming back to the importance of the scattering function, we will consider both the coherent elastic and inelastic components, respectively. Coherent elastic scattering can be separated into the Bragg component, which gives us information on the nuclear (and magnetic, when applicable) structure, and the diffuse scattering component, which is related to the disorder. The latter is important in characterizing the nature of atomic disorder in a given system. The inelastic scattering signal is generally separated into the quasielastic signal, which is centered around $E = 0$ and is related to relaxation processes (atomic diffusion, cluster reorientation, etc.), and the coherent inelastic scattering, which is related to information about correlated motions of atoms, i.e. excitations such as phonons or magnons.

In order to derive the coherent elastic case, we recall that an elastic scattering event implies that $\mathbf{Q} = \mathbf{G}$ and also that there is no energy exchange in the scattering event. Therefore, the

double differential cross-section simplifies to

$$\left(\frac{d^2\sigma}{d\Omega dE_f}\right)_{\text{coh,el}} = N_{\text{c}}\frac{(2\pi)^3}{V_{\text{c}}}|F_{\text{el}}(\mathbf{Q})|^2\sum_{\mathbf{G}}\delta(\mathbf{Q}-\mathbf{G})\cdot\delta(\hbar\omega), \tag{3.19}$$

which tells us that the condition for coherent elastic scattering is only met when Bragg's law holds. This depends on the volume of a unit cell, V_{c} (not to be confused by V, the interaction potential seen previously); N_{c}, the number of unit cells in the sample; and the elastic nuclear form (also called structure) factors, $F_{\text{el}}(\mathbf{Q})$:

$$F_{\text{el}}(\mathbf{Q}) = \sum_j \overline{b}_j e^{-W_j(\mathbf{Q})}e^{i\mathbf{Q}\cdot\mathbf{d}_j}. \tag{3.20}$$

The Debye-Waller factor, W, encompasses the displacements from equilibrium of atoms at atomic positions $\mathbf{d}_j$ within the unit cell. Generally speaking, atomic parameters can be deduced from such an experiment through neutron diffraction in which we would obtain intensity corresponding to reciprocal lattice vectors $\mathbf{G}$, scaled by their corresponding nuclear structure factors.

In the coherent inelastic case, however, we consider an energy exchange between the neutron and the sample that results in a phonon creation/annihilation. Given that we have N atoms in a unit cell, the system will be characterized by 3N phonon modes, each with a distinct wave-vector $\mathbf{q}$, energy E, and polarization ξ_j^i following the quantized number. The scattering function then becomes

$$S_{\text{coh}}^{\text{1-ph}}(\mathbf{Q},\omega) = \frac{1}{2}\sum_i \frac{|F_{\text{inel}}^i(\mathbf{Q})|^2}{\omega_i(\mathbf{q})}\Big(\Big[\Big(1+n(\omega_{i,\mathbf{q}})\Big)\delta\Big(\omega-\omega_i(\mathbf{q})\Big)\Big] + \Big[n(\omega_{i,\mathbf{q}})\delta\Big(\omega+\omega_i(\mathbf{q})\Big)\Big]\Big), \tag{3.21}$$

for which we introduce $n(\omega_{i,\mathbf{q}}) = 1/(e^{\hbar\omega_i(\mathbf{q})/k_BT}-1)$, the Bose-Einstein occupation factor for phonon mode with ω_i, and $F_{\text{inel}}^i(\mathbf{Q})$, the inelastic structure factors. We denote M for the masses of the atoms, and all other parameters carry from previous definitions above. The dot product $\Big(\mathbf{Q}\cdot\xi_j^i(\mathbf{Q})\Big)$ is called the polarization term, which we will circle back to momentarily.

$$F_{\text{inel}}^i(\mathbf{Q}) = \sum_j \frac{b_j}{\sqrt{M_j}}e^{-W_j(\mathbf{Q})}e^{-i\mathbf{Q}\cdot\mathbf{R}_j(0)}\Big(\mathbf{Q}\cdot\xi_j^i(\mathbf{Q})\Big) \tag{3.22}$$

The two bracketed terms in eq. 3.21, $1+n(\omega_i)$ and $n(\omega_i)$, are proportional to excitation creation and annihilation, respectively. We can therefore write the following relation

$$S(-\mathbf{Q},-\omega) = e^{\frac{-\hbar\omega}{k_BT}}S(\mathbf{Q},\omega), \tag{3.23}$$

which is called the detailed balance condition of the scattering function. Given the temperature dependence of the equation, it therefore follows that there will not be an equal chance of having an excitation annihilation/creation at all temperatures. As temperature increases, the statistical probability of excitation annihilation remains lower than excitation creation. This appears in the intensity of Anti-Stokes and Stokes measurements, discussed at the beginning of this chapter. An example of this effect, along with a summary of the different types of elastic and inelastic scattering discussed so far, are shown in Fig. 3.3.

The $\Big(\mathbf{Q}\cdot\xi_j^i(\mathbf{Q})\Big)$ dot product in eq. 3.21 acts as a selection rule for the polarization of phonon that is measured. The transverse polarization vector, ξ^T, is always perpendicular to $\mathbf{q}$, while the longitudinal polarization vector, ξ^L, is parallel. The selection rule, or dot product, dictates that

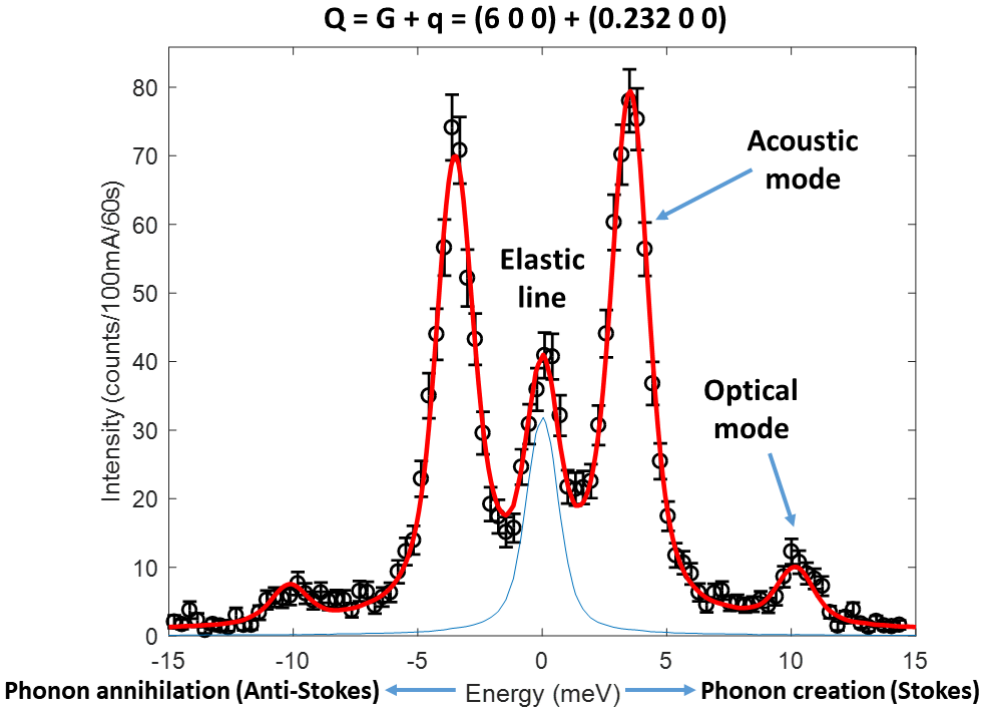

Figure 3.3: Example of elastic and inelastic X-ray scattering as seen by S(Q,ω). *An example is shown of a longitudinally-polarized constant-***Q** *energy scan (open black circles) at* $\mathbf{Q} = \mathbf{G} + \mathbf{q} = (6\ 0\ 0) + (0.232\ 0\ 0) = (6.232\ 0\ 0)$ *for the type-I clathrate* $Ba_8Cu_{4.8}Ge_{39.8}\square_{0.2}Ga$*, measured at 300 K on the inelastic X-ray scattering beamline ID28@ESRF. The longitudinal acoustic (LA) phonon mode is indicated, along with an optical branch centered at 10 meV. (See Section 2.1.1.1 for an explanation of acoustic and optical phonons.) The LA mode and optical branch are fit as damped harmonic oscillators and convoluted with the instrumental resolution of ID28@ESRF, the total resulting fit being the solid red line. At energy* $\omega = 0$ *the elastic line is depicted, its contribution to the total fit being the thin blue line. Finally, the phonon annihilation (neutron energy gain) side is referred to as the Anti-Stokes region, while the phonon creation (neutron energy loss) side is called the Stokes region.*

the polarization vector parallel to **Q** will always be selected. Since we generally work at large **Q**, we can assume that $\mathbf{Q} \sim \mathbf{G}$. In terms of phonon measurements, the phonon dispersion relation can be measured when the selection rule applies. Furthermore, the identification of a mode's polarization is embedded in the intensity distribution of the measured signal, and therefore it is not possible to directly extract the polarization of the mode. Rather, comparing the intensity allows one to discriminate between different modes.

Fig. 3.4 provides an example of this concept for a both a longitudinal and transverse mode that can be found in the scattering plane ([HH0];[00L]). In (a), the reciprocal lattice vector **G** brings us to the (222) Bragg peak and the small phonon vector **q** is parallel to **G**. Since ξ^L is always parallel to **q**, longitudinal phonons will be measured. In (b), however, **G** is on the (006) Bragg peak and **q** is perpendicular to the direction of **G**. Transverse phonons will be measured because ξ^T is parallel to **G** in this case. When discussing different phonon branches, we typically write them in terms of their propagation and polarization directions. For example, phonons in Fig. 3.4(b) would be from a transverse acoustic (TA) phonon branch, from the (006) Bragg peak, propagating along [110], polarized along [001]. This is written in shorthand as $\mathrm{TA}^{\text{polarization}}_{\text{propagation}} = \mathrm{TA}^{001}_{110}$.

Finally, while coherent one-phonon scattering allows us to track the energy dependence of phonons in reciprocal space, incoherent one-phonon scattering provides us with the generalized

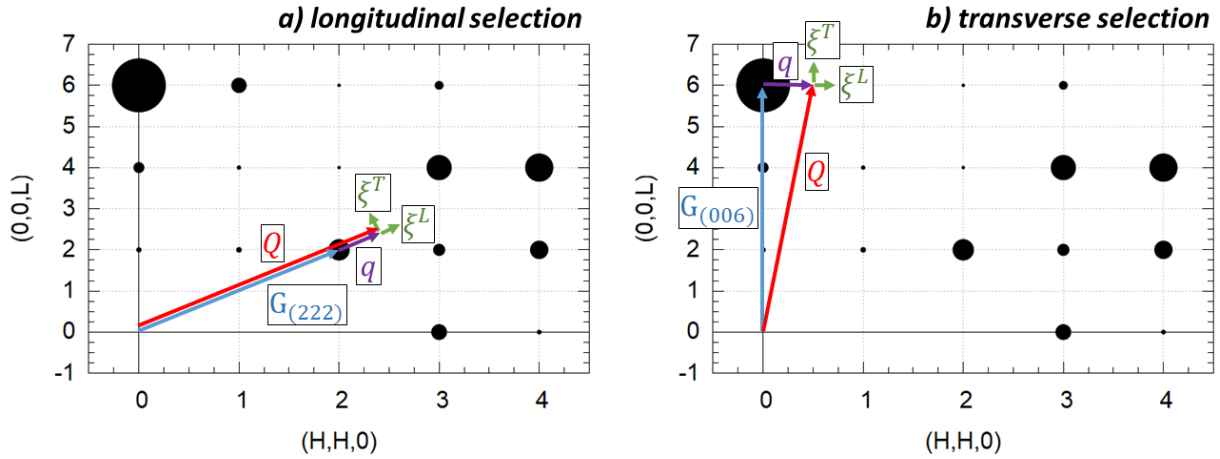

Figure 3.4: Illustration of the phonon polarization selection rule. *The scattering plane ([HH0];[00L]) is portrayed with black circles that are proportional to the elastic nuclear structure factors for the type-I clathrate* $Ba_{7.81}Ge_{40.67}Au_{5.33}$*. According to the selection rule controlled by the* $(\mathbf{Q}\cdot\xi_j^i(\mathbf{Q}))$ *polarization term in eq. 3.21, longitudinal phonons will be measured in (a), while transverse phonons will be measured in (b).*

vibrational density of states (GVDOS), where the GVDOS depends on the sum of the contributions from each mode, $g_j(\omega)$:

$$\left(\frac{d^2\sigma}{d\Omega dE_f}\right)_{\text{inc}}^{\text{1-ph}} = \frac{k_f}{k_i}Q^2\frac{N}{8\pi}e^{-2W(\mathbf{Q})}\frac{\text{GVDOS}(\omega)}{\omega}(1+n(\omega)),$$
$$\text{where GVDOS}(\omega) = \sum_j \frac{1}{M_j}(\overline{b_j^2}-(\overline{b_j})^2)e^{-2W_j(\mathbf{Q})}g_j(\omega). \tag{3.24}$$

If we assume that there is more than one type of atom in the primitive lattice, then the GVDOS is in fact a sum of individual atomic contributions and is therefore dependent upon the neutron scattering lengths of the different types of atoms, making eq. 3.24 inherently "neutron-weighted," as it is dependent upon this type of probe. There is also often a necessary multi-phonon scattering correction that must be made to such GVDOS calculations. Multi-phonon scattering describes the scattering events in which a neutron simultaneously creates/destroys two (or more) phonons, and is further discussed in Section 3.1.7.2.

Examples of the experimentally-measured, neutron-weighted GVDOS calculations made during my thesis work can be found in Turner *et al.* [57] and Turner *et al.* [106], and is discussed from a data analysis point-of-view in Section 3.1.7.2.

3.1.4 Introduction to Instrumental Resolution

In the following sections, I will show how the scattering function is applied to the common types of neutron spectrometers that are used to measure the various properties of phonons. In Sections 3.1.6 and 3.1.7, I will describe the instruments used to measure the energy position of phonons, GVDOS, and, resolution permitting, phonon linewidth. Then, in section 3.1.9, I will describe the instrument that can go beyond common resolution limits of other neutron spectrometers in order to measure even smaller phonon linewidths (longer phonon lifetimes).

Throughout the following discussions of techniques, details of the particular instrumental resolution of each spectrometer will be given. We must keep in mind that the intensity collected through a scattering experiment is in fact the convolution of the scattering function and the

instrumental resolution of the given technique, $R(\mathbf{Q},\omega)$, in which the instrumental resolution is a set volume within 4D space [206]:

$$I(\mathbf{Q},\omega) = S(\mathbf{Q},\omega) \otimes R(\mathbf{Q}-\mathbf{Q_0},\omega-\omega_0) \tag{3.25}$$

Once $S(\mathbf{Q},\omega)$ has been properly extracted, we can analyze the intrinsic phonon properties of the sample. We can also use the normalized intensity of $S(\mathbf{Q},\omega)$ to determine the acoustic character of a given phonon mode. It can be shown that for an acoustic phonon, the normalized dynamic structure factor, $\mathrm{DSF}_{i,\mathbf{q}}(\mathbf{Q},\omega,T)$, is constant, where the integral is taken over the measured phonon peak [122, 201, 206–208].

$$\mathrm{DSF}_{i,\mathbf{q}}(\mathbf{Q},\omega,T) = \frac{\omega_i(\mathbf{q})}{Q^2 \cdot n(\omega_{i,\mathbf{q}})} \int S_{i,\mathbf{q}}(\mathbf{Q},\omega,T)d\omega \tag{3.26}$$

This works in the long-wavelength limit, $|\mathbf{q}| \ll |\mathbf{Q}|$ and given that $\hbar\omega \ll k_B T$. Examples of the use of $\mathrm{DSF}_{i,\mathbf{q}}(\mathbf{Q},\omega,T)$ in my thesis work can be found in Turner *et al.* [81] and in the Supplementary Material of Turner *et al.* [106].

3.1.5 Neutron Thermalization and Neutron Guides

In order to prepare the following sections on different neutron techniques, I will briefly describe the process of neutron collection and transport from the source to the experimental measurement zones. Neutron spectrometers are categorized by the energy range of neutrons that they are set up to receive from the neutron source. It is a primary and defining instrumental parameter for a given spectrometer.

A fission reaction at a reactor will produce neutrons that have energies in the MeV range. These initial "source" neutrons are brought down to the thermal neutron range, or ∼25 meV (2,200 m/s), through moderators in a process called thermalization. Cold neutrons are further moderated to ∼5 meV. Some reactor sites, such as the National Institute of Standards and Technology, the Forschungs-Neutronenquelle Heinz Maier-Leibnitz, and the Institut Laue-Langevin, have designated cold neutron sources [209, 210].

These neutrons are then sent to the instruments through neutron guides that supply a range of wavelengths that each instrument can filter as needed for each experiment. In more detail, all of these particular instruments are placed in proximity to the nuclear reactor such that neutrons that are ejected from the fission reaction can be sent via neutron guides to the designated instrument space. Neutron guides limit the loss of neutrons while they are traveling from the reaction site to the instrument, sometimes a distance of 100 m or more, through the use of supermirrors. For a given wavelength range, supermirrors use total reflection to limit these losses and provide a maximum amount of flux at the sample possible.

Other instrument-specific features can be placed in the neutron guide to further customize the neutron wavelength, pulse, or monochromatization that can be done in advance of the neutrons arriving at the instrument site, and these will be discussed in the following sections. Neutron guides are also important since they determine the initial vertical and horizontal divergence at the monochromator, in the case of Triple-Axis Spectrometers described in Section 3.1.6, or at the sample, in the case of Time-of-Flight instruments described in Section 3.1.7.

3.1.6 Triple-Axis Spectrometers (TAS)

Triple-axis spectrometers are considered to be the workhorse technique for phonon measurements. As such, there are many variations of TAS instruments at different neutron sources, such as Thales, IN8, IN12, and IN22 at the Institut Laue-Langevin (ILL); PANDA and PUMA at the

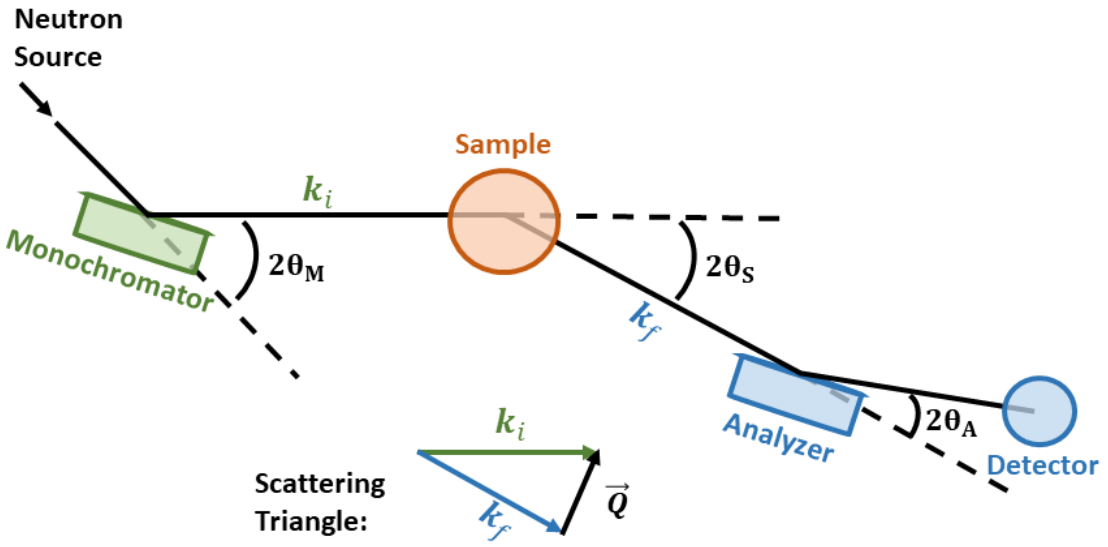

Figure 3.5: Example of a Triple-Axis Spectrometer (TAS). *Neutrons travel down a neutron guide before being monochromatized at the monochromator (in green) and scattered onto the sample (in orange). Scattered neutrons according to the scattering triangle shown are then registered at the analyzer (in blue) before reaching the detector (in blue). The three main angles of importance are also labeled for reference as $2\theta_M$, $2\theta_S$, and $2\theta_A$, for monochromator, sample, and analyzer, respectively.*

Forschungs-Neutronenquelle Heinz Maier-Leibnitz (FRM-II); and, formally, 4F, 1T, and 2T at the Laboratoire Léon Brillouin (LLB). (The LLB has since shutdown, however these instruments were vital to my Ph.D. work and therefore I mention them here.) As the name suggests, they function on three main axes: the monochromator, the sample, and the analyzer, as depicted in Fig. 3.5. By manipulating the configuration of the instrument, different regions of $S(\mathbf{Q}, \omega)$ in a given scattering plane are accessible. This type of instrument is therefore primed for following the full energy range of a phonon dispersion along a given polarization with high precision.

Briefly speaking, and following Fig. 3.5, the desired incoming neutron energy (E_i) is chosen at the monochromator. Then, after interacting with the sample, the neutrons come to the analyzer, where the final energy (E_f) is selected, and then they are counted at the detector. The principle of a TAS spectrometer relies on the scattering triangle, also shown in Fig. 3.5. The instrument can measure at a given point and energy in reciprocal space when the scattering triangle is closed. Recalling the momentum and energy conservation laws from eqs. 3.1-3.3, we navigate to the point of interest using eq. 3.3. This is done by fixing either $\mathbf{k}_i$ at the monochromator or $\mathbf{k}_f$ at the analyzer, and adjusting the other in order to match to the correct transfer of energy, or $\hbar\omega = E_i - E_f$. I will now focus on each of the components from Fig. 3.5 in more detail using an example of a fixed-$\mathbf{k}_f$ TAS configuration.

The neutron beam that reaches the instrument still contains a distribution of neutron wavelengths, and this "untreated" beam is usually referred to as a white beam. The selection of one wavelength is made possible through Bragg reflection at the monochromator. The monochromator is a single crystal with lattice plane spacing d_M, and, through Bragg's law, the neutrons with wavelength λ_i will be reflected off of the monochromator at a glancing angle θ_M:

$$k_i = \frac{2\pi}{\lambda_i} = \frac{\pi}{d_\mathrm{M} \sin(\theta_\mathrm{M})} \tag{3.27}$$

The alignment of the three angles of the TAS spectrometer are then set up such that when

a similar Bragg reflection is made at the analyzer,

$$k_f = \frac{2\pi}{\lambda_f} = \frac{\pi}{d_{\mathrm{A}} \sin(\theta_{\mathrm{A}})}, \tag{3.28}$$

we are able to measure $\hbar\omega = E_i - E_f$ at $\mathbf{Q} = \mathbf{k}_i - \mathbf{k}_f$ in reciprocal space.

The monochromator and analyzer are usually each a series of co-aligned crystals made of pyrolytic graphite (PG), Si, Ge, or Cu that are cut along a certain plane (h, k, l). These elements are chosen for their reflectivities, as maintaining high flux at the sample is of priority; for their specific mosaic spreads, which play a role in the instrumental resolution of the spectrometer and therefore in eq. 3.25; and for their small incoherent scattering cross-sections. To elaborate on the mosaic spread, the crystals chosen for monochromator crystals are what are called "mosaic crystals" or imperfect crystals. When a crystal is too perfect, i.e. a mosaic spread smaller than 1' [202], their resulting reflectivity is usually too low, causing one to forfeit intensity of the incident beam onto the sample. This is also called primary extinction [211]. This is compensated for by either co-aligning many small crystals in such a way that there is "controlled misalignment" or by heating and purposefully deforming the crystal several times [202].

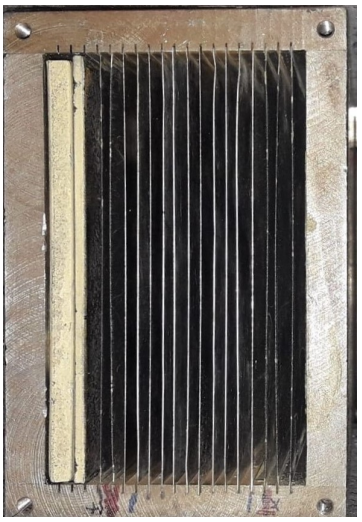

Figure 3.6: Example of Söller slit collimation. *Picture taken on 1T@LLB. Thin blades of a neutron absorbing material placed, in this case, directly after the monochromator and before the sample. The blades are spaced equidistant from one another in such a way as to provide 20' collimation according to eq. 3.29.*

A correction that is also often put into place when using single crystal monochromators and analyzers is to eliminate (as much as possible) the higher-order harmonics that are also reflected using Bragg reflection. When the wavelength λ is reflected using crystal plane (h, k, l), wavelengths $\lambda/2$, $\lambda/3$, etc. are also reflected from crystal planes $(2h, 2k, 2l)$, $(3h, 3k, 3l)$, etc. This is the reason that an Si111 monochromator is sometimes chosen, as the 222 reflection is extinct and therefore poses no potential $\lambda/2$ contamination [212]. Neutron beam filters, such as a Be polycrystalline filter maintained at low temperature of 77 K, can also act at low-pass filters, cutting off neutrons below a certain wavelength [213], which is 4 Å in the case of the Be filter [202]. This option was made possible at the 4F2@LLB beamline, for instance. Another common adaptation, designed for higher energy measurements, is the use of a PG filter before the analyzer. This filter specifically cuts $\lambda/2$ and $\lambda/3$ harmonics, but also restricts the E_f values to particular values such as $k_f = 2.662$ Å^{-1}. Finally, a specific type of ferromagnetic crystal is used for polarized neutron experiments and it will be discussed in Section 3.1.9.4.

Detectors on TAS instruments are usually proportional gas counters that contain ^{3}He or $^{10}BF_3$ gas under pressure. This acts as a cathode, with the anode being a wire attached to a high voltage. The ^{3}He gas reacts with the neutron that is scattered onto the detector tube such that the reaction products result in ionization which is measured in a wire. With significantly high voltage, the anode attracts a number of ionized electrons that is proportional to the reaction rate expected in the gas to the point of reaching an avalanche effect. The limitation to these gas counters is their response time, which is roughly 10,000 counts per second, meaning that a plexiglass attenuator is usually placed before the analyzer/detector for moments when extremely high count rates are expected, such as during a sample alignment when a scan across a Bragg peak is taking place [213].

Collimation can also be added to TAS in order to further enhance the resolution of the instrument. Söller-slit collimators, for example, are a series of thin vertical blades with coatings

made of a neutron-absorbing material, such as Gadolinium. Söller-slit collimators limit the horizontal divergence of the beam, and they can be placed before and after the monochromator, and before and after the analyzer. In other words, onto k_i and k_f, respectively.

An example of Söller-slit collimation is shown in Fig. 3.6. Each absorber blade is a rectangle with a length of $L = 40$ cm. The resulting angular divergence, α, can then be calculated by knowing the length of the gap between each blade, $d = 0.12$ cm [214]:

$$\alpha = \frac{2d}{L} = \frac{2 \times 0.12 \text{ cm}}{40 \text{ cm}} = 0.006 \text{ rad} = 20 \text{ min of arc} \tag{3.29}$$

This is often referred to as 60'/20'/20'/60' collimation, since 20 min collimation is placed just before and just after the sample, as described above. The use of collimation, however, is a trade-off between resolution and intensity, since we forfeit neutrons to the absorber blades in exchange for a lower allowed divergence.

The choice of fixed-k_f value for an experiment is tied to many parameters, such as the available monochromators and analyzers, the inelastic energy range of interest, flux at the instrument, and the neutron energy range that the instrument has been set-up to receive, i.e. cold or thermal neutrons. In addition to collimation, decreasing the size of the scattering triangle is typically one way to improve resolution. However, simple calculations should be made beforehand to ensure that Bragg peaks and directions that you hope to measure at during a TAS experiment can be reached. An example of different fixed-k_f phonon measurements is discussed in my unpublished manuscript, Turner *et al.* [81], where it is shown that with the improved resolution of using a smaller fixed-k_f, a new interpretation of the phonon dispersions in 9.5 mol.% Yttria-Stabilized Zirconia can be made.

3.1.6.1 Resolution of Triple-Axis Spectrometers

For triple-axis spectrometers, the resolution has an inclined and elongated ellipsoid shape due to the fact that Q and E resolutions are coupled, and it has a slope of approximately 3000 m/s, depending on the settings of the spectrometer [204]. Due to the inclination of the ellipsoid, we will have more narrow and intense measured intensity when the slope of the instrumental resolution most closely matches the local group velocity of the phonon dispersion. As seen in Fig. 3.7, when the elongated axis of the resolution ellipsoid is parallel to the dispersion velocity (focused), the resulting intensity is higher and narrower than if the ellipsoid is close to perpendicular to the dispersion (defocused). This is also called the focusing condition [202, 215, 216].

The derivation of TAS resolution has been detailed by M.J. Cooper and R. Nathans [217], B. Dorner [218], and M. Popovici [219], and additional information can be found in literature [202, 204, 216, 220]. Programs such as Takin [221] and ResCal (from Hargreave and Hullah, 1979) allow the user to input the necessary parameters in order to analytically calculate the resolution ellipsoid for a given set of experimental conditions. Such an example using Takin is shown in Fig. 3.8 for the type-I clathrate $Ba_{7.81}Ge_{40.67}Au_{5.33}$ in the scattering plane [110][001]. In order to simulate the resolution ellipsoid as seen for a 1 cm^3 cylindrical sample of $Ba_{7.81}Ge_{40.67}Au_{5.33}$, I have input all relevant spectrometer parameters (distances between monochromator, sample, and analyzer, mosaics of the monochromator and analyzer, etc.) for the 2T@LLB spectrometer with a fixed-$k_f = 2.662$ Å^{-1} according to those given by P.F. Lory [206] (see pg 86, Table 4-1). Assuming 60' (standard) collimation, Figs. 3.8(a-c) describe the shape and size of the resolution ellipsoid as seen by a transverse phonon at position (0.2 0.2 6) with an energy of 5 meV in terms of $\Delta Q_{\parallel}$ (longitudinal) and $\Delta Q_{\perp}$ (transverse) projections.

Fig. 3.8(d) emphasizes the role that the local slope of the phonon dispersion has on the effective energy resolution for the standard and high resolution setups, or 60' (standard) and 20'

(high) collimation. As seen in the figure, a resolution of only 0.2 meV can be reached using a local slope of 11 meV.Å at the phonon position (0.2 0.2 6).

During my thesis work, I used the program 'afitv,' an analysis tool developed by B. Hennion and P. Bourges at the LLB [222] specifically for the data analysis of TAS experiments, in order to analyze my TAS measurements. Afitv calculates the resolution ellipsoid of the given TAS instrument, accounts for the phonon position, group velocity, and sample mosaicity, and finally deconvolutes the phonon peak from the instrumental resolution in order to allow us to extract the intrinsic phonon position, intensity, linewidth, and group velocity. I emphasize the importance of using rigorous programs like afitv that are refined, well-tested, and founded upon the derivations of the resolution ellipsoid listed above. With programs like afitv, we can have confidence in the interpretation of our measurements.

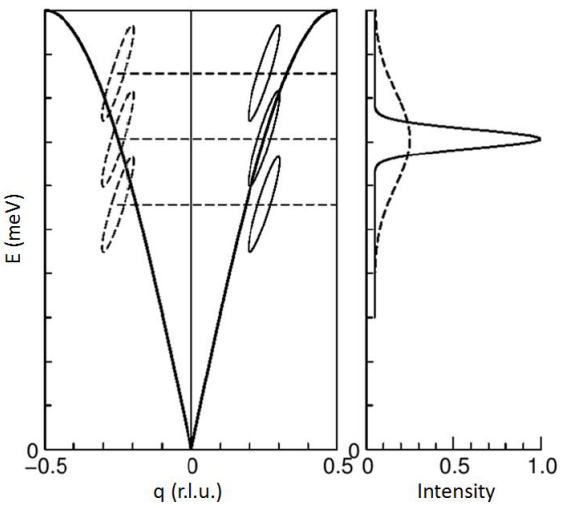

Figure 3.7: Focusing condition of a triple-axis spectrometer. *On the left, the TAS resolution ellipsoid is overlaid onto an example phonon dispersion, showing that, in this case, the resolution ellipsoid is more closely aligned with the sound velocity of the dispersion when moving along $q = 0 \rightarrow 0.5$, also called the "focusing" side, than from moving along $q = 0 \rightarrow -0.5$, or the "defocusing" side. Dashed horizontal lines highlight the position of the center of the ellipsoid. The right-hand side shows the intensity that would result from a constant* $\mathbf{Q}$ *scan that crosses the phonon dispersion using the focused side (solid line) and the defocused side (dashed line). Figure taken directly from [215].*

While afitv takes care of the convolution of the measured intensity, it still takes an experienced user to ensure that the program is converging onto a solution that makes sense and could be applicable to the experimental conditions at hand. There are many parameters at play that are still left up to the user to input, including but not limited to the background (and background slope) in the scan, the type of phonon peak fit (Gaussian, damped harmonic oscillator, etc.), and whether or not we make the fit assuming a localized linear dispersion fit ($\omega = v_g q$) or by calculating the cone of dispersion. All of these parameters impact the resulting phonon position, intensity, linewidth, and group velocity. Furthermore, we use the resulting normalized intensity values of the fits (see eq. 3.26) as a guide for determining when we are fitting an acoustic mode, or possibly a band of modes.

3.1.7 Time-of-Flight (TOF) Spectrometers

Examples of TOF INS spectrometers include IN5 and IN6-SHARP at the Institut Laue-Langevin; MAPS at the ISIS Neutron and Muon Source; and SEQUOIA at the Spallation Neutron Source (located at Oak Ridge National Laboratory).

TOF instruments are usually divided into direct and indirect geometry spectrometers. In direct geometry spectrometers, the incident wave-vector, and therefore energy, of interest from the white beam is fixed by a set of choppers and the final energy after interaction with the sample is then measured by the time-of-flight of the scattered neutrons. Indirect geometry spectrometers work in the reverse: the incoming white beam with various energies is measured by time-of-flight and the final energy is fixed using an analyzer bank in front of the detector bank [209]. Note also that, by convention for TOF instrument users, the scattering triangle is defined as $\mathbf{Q} = \mathbf{k}_f - \mathbf{k}_i$ rather than as $\mathbf{Q} = \mathbf{k}_i - \mathbf{k}_f$, which was written previously in eq. 3.1 and

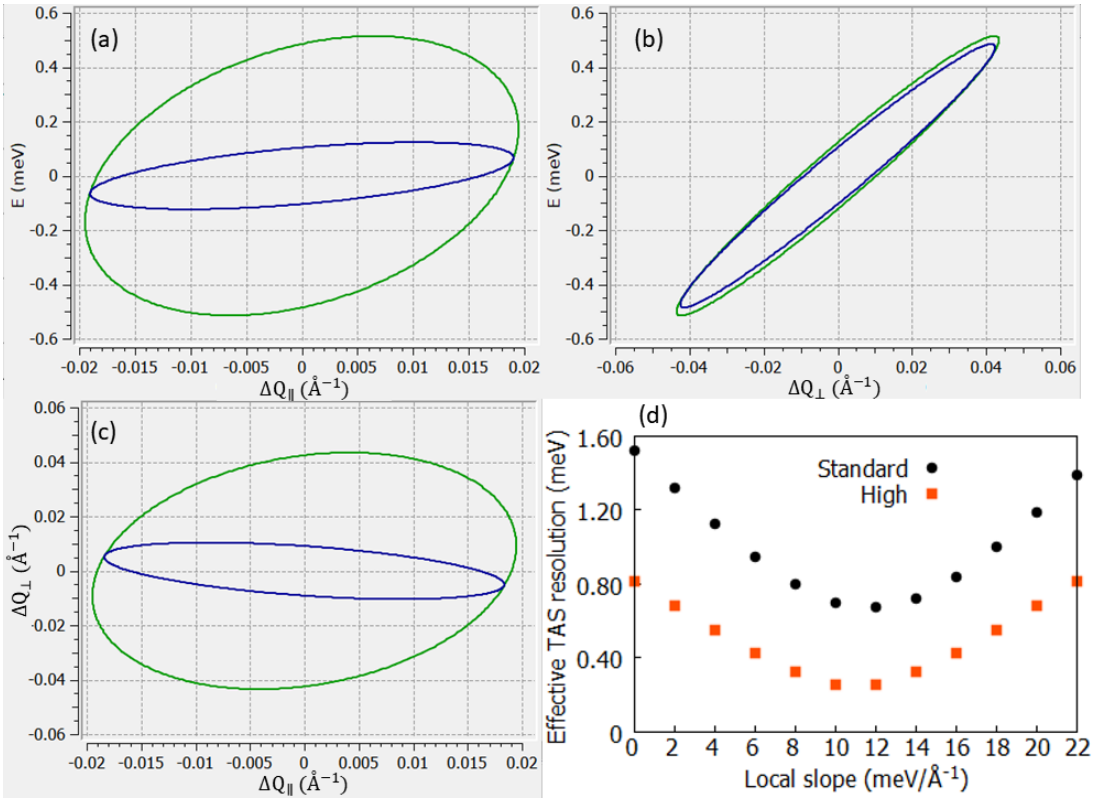

Figure 3.8: Description of the TAS resolution ellipsoid. *(a-c) describe the shape and size of the resolution ellipsoid as seen by a transverse phonon at position (0.2 0.2 6) with an energy of 5 meV in terms of $\Delta Q_{\parallel}$ (longitudinal) and $\Delta Q_{\perp}$ (transverse) projections. The cross-section of the ellipsoid in the plane are represented by blue lines, while the projection onto the plane are in green. The ellipsoid was calculated using Takin [221]. In (d), the effective energy resolution using 60' (standard resolution) and 20' (high) collimation are compared across different local dispersion slopes. A minimum occurs for a local slope of 11 meV.Å. (d) was taken directly from the Supplementary Material of Ref. [27].*

follows the TAS user convention.

Fig. 3.9 depicts an example of a direct geometry TOF instrument, modeled in particular after the cold-neutron TOF instrument IN5@ILL. Three sets of choppers are placed in the neutron guide which are responsible for creating the monochromatized pulse of neutrons and eliminating longer-wavelength harmonics from the pulse. The neutrons then impinge on the sample, and the results are collected in a 2D set of detector banks 4 m from the sample. We will return to each of these components in detail. However we will first discuss the principle of TOF spectrometers.

The success of a TOF instrument lies in the ability to measure the flight path of neutrons between the sample and detectors in the case of the direct geometry instruments. As stated in Section 3.1.5, cold neutrons have an energy of approximately 5 meV, corresponding to a velocity of ∼1,000 m/s. The time-of-flight of the neutrons can therefore be measured, assuming significant enough distance between the sample and detector banks is maintained in order to register individual neutrons coming in at this velocity. This condition is known as frame overlap. Frame overlap is a main design concern of TOF instruments, as it refers to the minimum time allowed between pulses. Neutrons from a first pulse must reach the detectors and be counted before a second pulse arrives in order to correctly measure the total time-of-flight of the neutrons of the first, and then subsequent, pulses.

Continuing with the direct geometry example, we can deduce the energy and location in reciprocal space that a given neutron at a given detector came from by time-of-flight and the

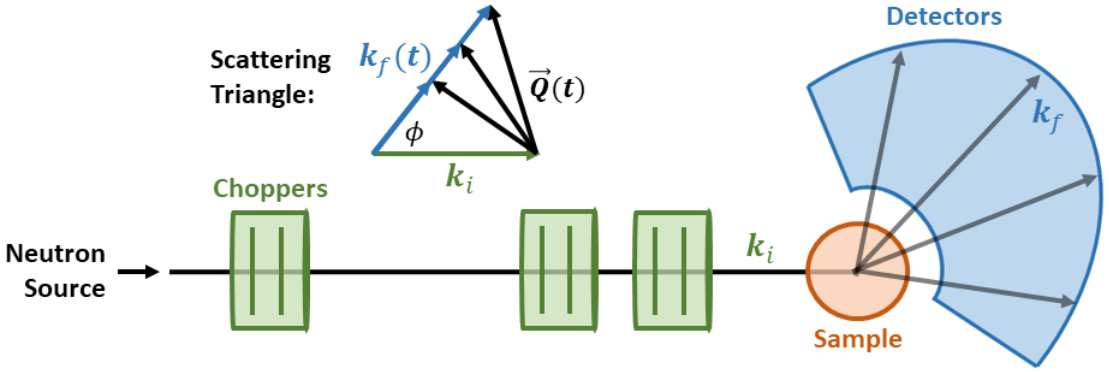

Figure 3.9: Example of a Direct Geometry Time-of-Flight (TOF) Spectrometer. *The main features include choppers (in green) placed along the neutron guide (black line) that define the neutron pulse that reaches the sample (in orange), before scattering into a 3D detector array (in blue). This particular schematic has been modeled after the instrument IN5@ILL.*

use of the cosine rule for the scattering triangle:

$$\mathbf{Q}^2 = \mathbf{k}_i^2 + \mathbf{k}_f^2 - 2\mathbf{k}_i\mathbf{k}_f \cos\phi \tag{3.30}$$

Since $\mathbf{k}_i$ and the distance from the last set of choppers to the sample, L, of the incoming beam are fixed, the time from chopper to sample $\tau_i = L/v_i$ for neutrons with velocity v_i, and the energy of the incoming neutrons, E_i, are therefore known. We also know the total time-of-flight of the neutrons from chopper to detector, τ_{tot}, meaning that the time-of-flight of a neutron with a final wave-vector $\mathbf{k}_f$ is $\tau_f = \tau_{\text{tot}} - \tau_i$ [209, 212]. Finally, using the inelastic scattering definition $\hbar\omega = E_i - E_f$,

$$\frac{\hbar^2\mathbf{Q}^2}{2m} = E_i + E_f - 2\big(E_iE_f\big)^{1/2}\cos\phi \tag{3.31}$$

$$\frac{\hbar^2\mathbf{Q}^2}{2m} = 2E_i - \hbar\omega - 2\Big[E_i\big(E_i - \hbar\omega\big)\Big]^{1/2}\cos\phi \tag{3.32}$$

Eq. 3.32 is made possible through the design of the choppers and detector banks. The choppers serve several key functions for TOF instruments, and we will take the example specifically of the IN5@ILL choppers. From left to right in Fig. 3.9, the first set of choppers defines the pulse of neutrons. Since IN5@ILL is placed at a steady-state neutron source, it is first necessary to create the pulse of neutrons. The second set of choppers eliminates longer-wavelength harmonics from the beam, such as what was described in Section 3.1.6, and ensures that there is no frame overlap. Their rotation speeds are set according to the minimum and maximum flight times of the fastest and slowest neutrons, respectively, in a given pulse such that the difference between the two is still less than the period of the pulse selected by the first set of choppers. Then, the final set of IN5@ILL choppers monochromatizes the beam to the incoming neutron wave-vector $\mathbf{k}_i$ of interest for the experiment [209].

The choppers in the Fig. 3.9 schematic are meant to represent disk choppers. As the name implies, these are disks made of a neutron absorbing material with only a small slit cut into them that let neutrons pass through. They are most efficient in pairs, rotating in opposite directions. This way, the first disk cuts a section of the beam, and then the phase angle and distance between the first and second disks define the velocity band that is selected [213]. IN5@ILL has a chopper velocity range of 2,000-17,000 rpm (or an angular speed range of 209-1780 rad/s), with chopper angle apertures of either 3.25° or 9°. The pulse is then defined based on the distances between the sets of choppers and the sample, and the ratio between the angular apertures over the angular speed.

After the incoming neutron beam interacts with the sample, a radial collimator is often placed between the sample and the large area detectors in order to prevent parasitic scattering from reaching the detectors. Due to the wide angular coverage of TOF detectors, there is more concern than for TAS spectrometers, for instance, that scattering coming from the sample environment interferes with the intrinsic scattering due to the sample. The radial collimator, designed after Venetian blinds, absorbs this type of scattering, reducing the background [209].

The detector bank has an effective detection height of 3 m and is made up of position sensitive ^{3}He counters similar to those on TAS instruments, with a key difference: the IN5@ILL detectors are vertical tubes with a diameter of 2.54 cm, and this vertical form of the gas counter allows for further precision of the neutron flight path for TOF instruments. The position sensitivity of the name comes from the fact that the detector is modified to contain a resistive wire with charge sensitive amplifiers at either end of the vertical tube, q_1 and q_2. The position, x, of the neutron along the vertical tube can therefore be calculated using the ratio of the charges measured at each amplifier: $x = q_1/(q_1 + q_2)$.

3.1.7.1 TOF Data Analysis

The initial data analysis of a TOF experiment is a bit more involved than that of a TAS experiment. In order to view and work with data from a TOF experiment, several programs including LAMP [223], Mantid [224], and the Horace functions for Matlab [225] exist for TOF instrument users. A combination of LAMP or Mantid, plus Horace can be used in order to process the information collected at each detector for each scan into a single $S(\mathbf{Q}, \omega)$ 4D dataset. The four parameters that can then be manipulated to view the neutron scattering intensity are the two scattering plane axes, the out-of-plane vertical axis, and energy.

Horace allows the user to view selections of the data along energy or a given $\mathbf{Q}$ axis. To be more precise, a slice, or integration in energy, at a given energy transfer can then depict the 2D inelastic neutron scattering intensity within the scattering plane. Examples of such kinds of 2D iso-energy plots can be seen in Fig. 5 of Turner *et al.* [57]. On the other hand, when a slice, in this case an integration in $\mathbf{Q}$, on one of the two scattering plane axes is made, the energy range along the second scattering plane axis can be viewed. Such kinds of 2D iso-$\mathbf{Q}$ plots can be seen in Fig. 12 of Turner *et al.* [57]. Finally, 1D constant-energy and constant-$\mathbf{Q}$ plots that integrate small selections in all but one of the four parameters allows the user to trace the $\mathbf{Q}$ range at a given energy transfer or the energy range at a given $\mathbf{Q}$ in reciprocal space, respectively. These scans most resemble what is typically measured on a TAS instrument. Examples can be found in Figs. 13-18 of Turner *et al.* [57].

An in-depth explanation of the instrumental resolution of IN5@ILL as it applied to an experiment made on the type-I clathrate $Ba_{7.81}Ge_{40.67}Au_{5.33}$ can be found in Appendix A.1 of Turner *et al.* [57] as well. Details include the calculation of q and E resolution due to step size and beam divergence specifically for measurements made on the Bragg peaks (006) and (222) in the scattering plane [110][001]. The IN5@ILL neutron guide has undergone upgrades since this particular 2016 experiment, so the reader should be advised that the particular values given in Appendix A.1 have since changed. Further information on the instrumental resolution of TOF instruments can be found in Ehlers *et al.* [226] and Violini *et al.* [227]

3.1.7.2 TOF Generalized Vibrational Density of States (GVDOS) Measurements

TOF instruments also offer great flexibility for measuring different phonon properties. Going beyond what can be measured in a given scattering plane for a single crystal measurement, when a powder sample is measured on a TOF instrument, the neutron-weighted generalized vibrational density of states (GVDOS) can be calculated from the experimental data as well.

(For an introduction to the GVDOS please see eq. 3.24.) For single crystal measurements, this can similarly be done, but it should be done with caution as we are making the non-trivial assumption that the given range in reciprocal space that we have measured in a single scattering plane reflects the behavior that could be measured not only in all other scattering planes but also in all reciprocal space not reached within the given measurement. It is generally agreed upon by experimentalists that when a sufficiently large range of reciprocal space, for instance one quadrant of the scattering plane, of a single crystal is measured, we can reasonably approximate the GVDOS for a single crystal as well for a symmetry-independent portion of the Brillouin zone. Furthermore, the fixed $\mathbf{k}_i$ of such GVDOS measurements should generally be long enough to reach at least one Bragg peak, as this allows acoustic behavior to be integrated into the GVDOS calculation, offering further reassurance. TOF instruments are also known for having potential spurious effects and/or detector accuracy issues in low-$\mathbf{Q}$ regions, and reaching the first Bragg peak can act as a general rule of thumb for ensuring that undue weight is not placed on this less precise region of $\mathbf{Q}$.

Either Mantid [224] or the MUPHOCOR (MUlti-PHOnon CORrection) routine [228] for LAMP [223] can each be used to calculate the GVDOS from a TOF measurement. MUPHOCOR takes several inputs such as the expected neutron scattering cross-section, the atomic mass of the sample, and other key instrumental parameters and makes a first approximation calculation of the GVDOS. It then self-consistently corrects for the multi-phonon processes contribution (See Section 3.1.3), leaving just the desired one-phonon DOS. It is further customizable when parameters such as the background, absorption correction, and the removal of known bad detectors are included. A further remark in favor of MUPHOCOR is the fact that the resulting energy scale reflects the natural time-of-flight step of the instrument, which is non-linear, allowing for a GVDOS calculation that is more "true" to the actual dataset collected on the given TOF instrument. Examples of my MUPHOCOR GVDOS calculations can be found in Turner *et al.* [57] and Turner *et al.* [106].

While Mantid does provide a user-friendly, Python-based environment for live plotting during an experiment, it lacks the important features such as the multi-phonon correction and natural time-of-flight step that make MUPHOCOR the more rigorous method of experimentally calculating the GVDOS, as least at the time of writing this manuscript.

3.1.8 TAS vs TOF, a comparison for lattice dynamics studies

My Ph.D. work focused largely on the use of TAS and TOF instruments for phonon measurements. Speaking strictly to their advantages/disadvantages in terms of use for phonon behavior and lattice dynamics studies, it is perhaps relevant to give a brief commentary or comparison of the two.

If I were to conduct an exploratory measurement of several phonon dispersions at room temperature, for instance, which is the typical way to begin a new experimental lattice dynamics study on a given crystalline system, I would expect the experiment to take 2-3 days on a TOF instrument vs 4-7 days on a TAS instrument. (This is completely generalized of course, as the length of time depends on flux at the sample and many other parameters.) The 2-3 day TOF experiment would have the added benefits of (1) a map of reciprocal space at any given energy within the experimental range, including the elastic scattering map, such as what a diffractometer could provide, and (2) further analysis results such as the GVDOS, which would help complete the exploratory lattice dynamics study. Creating similar reciprocal space maps with TAS are also possible, yet tedious.

In addition, TOF experiments typically explore a large portion of $S(\mathbf{Q},\omega)$ 4D space, possibly allowing one to pinpoint a specific region of interest that can then be further refined using a TAS instrument. These types of refined measurements, i.e. localized measurements that need to

be done at a given energy and/or precise direction with excellent statistics, such as the following of a phonon dispersion, are more optimized for the three-axis design of TAS instruments. TOF instruments, on the other hand, will collect a slice of reciprocal space that reflects the arc of the detectors, which will most likely not correspond to the specific direction of interest.

Where TAS instruments truly shine is in extracting intrinsic phonon linewidths with extreme precision. The TAS instrumental resolution ellipsoid and the programs to model it have been thoroughly studied by some of the "greats" in neutron scattering, including G. Shirane, S. M. Shapiro, B. Hennion, and others, and such programs have been tested and verified on a wide range of materials. Further customization such as the option to add Söller slit collimation, once the local region of interest is defined, allows users to refine certain characteristics, such as phonon linewidth broadening, with a more reactive and flexible experimental environment that can be changed multiple times during the actual experiment. The use of TAS instruments for measuring phonon linewidths has even led to the development of the Neutron Resonance Spin Echo technique for TAS, which will be discussed in detail in Sections 3.1.9-3.1.10.

To this I add a comparison of data treatment. The TAS instrument is perhaps more intuitive, especially for a new neutron facility user, since the user drives the instrument to the area of interest in phase space and directly scans a series of points with constant-energy or constant-$\mathbf{Q}$. The data can then be plotted live and preliminary analyses made directly. This can be important especially in an exploratory experiment since count time and step size can be adjusted based on preliminary results, making for a much more "dynamic" or on-the-moment experimental approach. TOF instruments, however, require lengthy data treatments that convert the time-of-flight data into one 4D $S(\mathbf{Q},\omega)$ data set that is on the order of several terabytes, often limiting the live plotting and interpretation of certain detailed features that can be done during the actual experiment beamtime.

Finally, a brief mention of the different strategies for sample alignment of single crystals: Extreme care is taken, in both TAS and TOF cases, to ensure that the crystal has been aligned into the desired scattering plane at the beginning of the experiment. While TAS instruments often offer a two-axis goniometer underneath the sample environment with a ∼5-10° tilt that can help bring slightly misaligned samples back into the scattering plane, this is not often the case for TOF instruments. For a TOF instrument, however, data treatment software like Horace [225] uses the available Bragg peaks measured within the data set to realign the observed spectrum in reciprocal space using the orientation matrix and adjust the lattice parameters post-experiment, at the data treatment stage.

While each type of spectrometer offers its own advantages and limitations, I have found during my Ph.D. experience that, when possible, a combination of both techniques results in a more comprehensive lattice dynamics study. In addition, when intrinsic phonon linewidths are outside the instrumental resolution range of available TAS and TOF techniques, NRSE for TAS offers improved resolution for exactly such types of measurements. This technique will be the topic of the following sections.

3.1.9 Neutron Resonance Spin Echo (NRSE) for TAS

Instead of following the change in energy of the neutron through an inelastic scattering process, like TAS and TOF, Neutron Spin Echo (NSE) uses the properties associated to the polarization of the neutron to follow the spin rotation of said neutron. This has an incredible advantage: resolution is not dependent on monochromatization of the beam, since NSE does not follow the energy change of the neutron, and because spin rotation is also a form of conservation of energy. This means that the trade-off between higher resolution and lower flux at the sample, lost through either collimation in the case of TAS or choppers in the case of TOF, does not apply to NSE.

Neutron Resonance Spin Echo (NRSE) developed out of the NSE technique in the late 1980's and was pioneered by R. Golub and R. Gähler [229, 230]. The NRSE technique applies this concept of following the spin rotation of neutrons to a TAS instrument, allowing us to take advantage of the TAS instrument's range in reciprocal space and energy for inelastic measurements while enhancing the resolution for linewidth measurements through the use of NSE.

In the following subsections, a brief introduction to NSE will be given, followed by a description of the modifications made to a triple-axis spectrometer that allow us to conduct an NRSE measurement. Then I will show how I applied these concepts towards the NRSE linewidth measurements made for the type-I clathrate $Ba_{7.81}Ge_{40.67}Au_{5.33}$ during my Ph.D work. Finally, I will present a variation on the NRSE for TAS setup called Neutron Larmor Diffraction.

3.1.9.1 Principles of NSE

The basic principle of NSE depends upon both the Larmor precession and the non-adiabatic condition. Firstly, Larmor precession is the rotational axis motion of a neutron in the presence of a magnetic field. Secondly, NSE relies on non-adiabatic transitions in order to pass seamlessly between designated magnetic field and zero field (or drift) regions. A non-adiabatic transition refers to when the field abruptly changes, such as in the case that we wish to create in the drift regions that will be introduced below. Rather than giving the polarization time to adapt progressively, a non-adiabatic transition forces the immediate precession about the direction perpendicular to the magnetic field of the coil [136, 220]. Its advantage is that, as a first approximation, we can neglect any influence of the field on the neutron's polarization [231].

In NSE, we let a neutron precess through designated magnetic fields that are engineered with static DC coils, and track its change in precession angle. All the necessary properties of both the neutron and the magnitude and direction of the magnetic fields are known. Therefore, any change in precession angle other than that which is due to the magnetic fields must, by consequence, be due to the change in velocity that occurs during a scattering event between the neutron and sample. The Larmor precession angle, ϕ, depends on the velocity of the neutron, v, the static magnetic field B put into place, and the length L of the region for which the neutron is under the influence of B.

The Larmor precession occurs when neutrons have a polarization component perpendicular to B. Let us therefore assume that a neutron polarized along the z-direction with velocity along the y-direction precesses through a magnetic field for time $t = L/v$, causing a Larmor frequency precession of ω_L in the y-direction due to field B, such that

$$\phi = \gamma B \frac{L}{v} = \omega_L t, \tag{3.33}$$

where the Larmor frequency is defined as $\omega_L = \gamma B$ and the Larmor constant is $\gamma = 2.916$ kHz/Oe [232].

We can start by applying this to a basic NSE configuration in which a polarized neutron beam precesses through a region with magnetic field of strength B for length L before scattering on the sample and precessing through a second field of equal and opposite strength for the same length, such as what is shown in Fig. 3.10. The second field reverses the rotation direction of the neutrons, and, in the case of an inelastic scattering event, the velocity of the incoming neutrons v_i will be different from the scattered neutrons with velocity v_f [233, 234].

This means that the final precession angle, ϕ_{NSE}, is the sum of the precession experienced in the first and second coils, or ϕ_1 and ϕ_2, respectively.

$$\phi_{NSE} = \phi_1 + \phi_2 = \frac{\gamma B_1 L_1}{v_i} - \frac{\gamma B_2 L_2}{v_f} \tag{3.34}$$

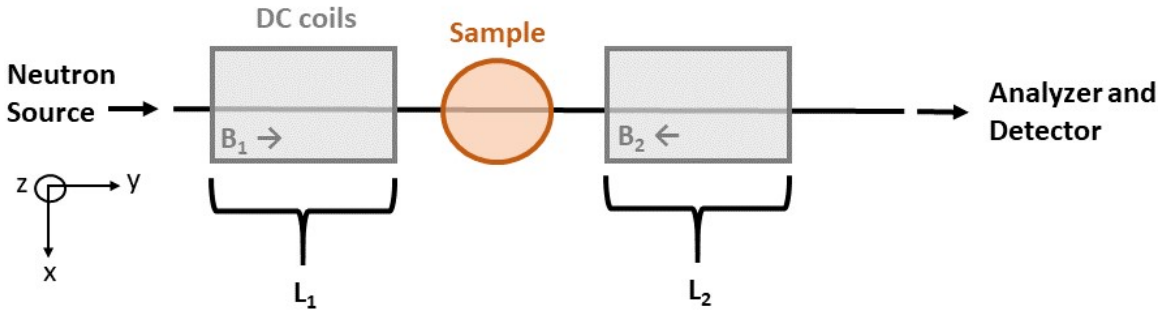

Figure 3.10: Simplified schematic of an NSE spectrometer. *The typical Neutron Spin Echo (NSE) spectrometer (as if viewed from the top) includes two static DC coils (in gray) of length $L_{1,2}$, which are placed before and after the sample (in orange), respectively. They have a field strength of equal but opposite strength with respect to one another. The DC coils create precession regions in which the neutron precesses according to its velocity and the strength and length of the field.*

At this point we reflect that B_1L_1 must equal B_2L_2 in order for the precession caused by the first coil to be reversed, creating the spin-*echo* effect, so we will continue the derivation with $B_1 = B_2 = B$ and $L_1 = L_2 = L$ [231]. Then we apply the definition $v_f = v_i + \delta v$, with $\delta v \ll v_f$ representing the small change in velocity due to interaction with the sample. Since the change is so small, we will assume that $v_f = v_i + \delta v \sim v$:

$$\phi = \omega_L L\left(\frac{(v_i + \delta v) - v_i}{v_i v_f}\right) = \omega_L L \frac{\delta v}{v_i v_f}\bigg|_{v_f = v_i} = \omega_L L \frac{\delta v}{v^2}. \tag{3.35}$$

Then, recalling that the scattering event will cause the neutron to go from having velocity v_i to velocity v_f, we define the energy transfer of the neutron scattering event as $\hbar\omega = \frac{m}{2}(v_i^2 - v_f^2) = mv\delta v$. We therefore obtain

$$\phi = \left(\frac{\hbar\omega_L L}{mv^3}\right)\omega = \omega\tau_{\mathrm{NSE}}, \tag{3.36}$$

in which τ_{NSE} is the spin-echo time, dependent upon energy transfer, which defines the energy resolution in the particular scattering event [235].

Continuing with the basic NSE configuration, the final intensity of the scattered beam, I, with polarization P_x is related to the initial intensity of the incident beam, I_0, by the following [236]:

$$I = \frac{I_0}{2}(1 + \langle P_x \rangle). \tag{3.37}$$

The final polarization, $\langle P_x \rangle$, is the average of the neutron spin component in the direction of polarization such that

$$\langle P_x \rangle = \langle \cos(\phi_{\mathrm{NSE}}) \rangle = \int S(\mathbf{Q}, \omega) \cos(\phi_{\mathrm{NSE}}) d\omega = \int S(\mathbf{Q}, \omega) \cos(\omega\tau_{\mathrm{NSE}}) d\omega \tag{3.38}$$

and the dependence of P_x on ϕ_{NSE} in turn is related to the Fourier transform of the scattering function, $S(\mathbf{Q}, \omega)$.

As we are preparing to focus on the NRSE application for inelastic scattering, we can first describe the NSE tuning condition for dispersionless inelastic scattering as a way of pinpointing its limitation for the measurement of phonon linewidths. Expanding on the NSE example above, we want to ensure that ϕ_{NSE} is a function of only the energy transfer $\hbar\omega$, and not of the spread of incident and scattered velocities dv_i and dv_f that enter into and exit out of the spectrometer, respectively. (Note that we define the spread dv differently from the change in velocity due to the

scattering event with the sample, which is defined above as δv, to avoid confusion of variables.) We will assume that the spread in velocity is centered around values $\overline{v_i}$ and $\overline{v_f}$, which correspond to an energy exchange $\hbar\omega_0 = \frac{m}{2}(\overline{v_i}^2 - \overline{v_f}^2)$ and precession angle ϕ_0 [232]. The velocity spreads are therefore defined as

$$v_i = \overline{v_i} + dv_i, \quad v_f = \overline{v_f} + dv_f. \tag{3.39}$$

In order for ϕ_{NSE} to be independent of the velocity spreads, the following condition must be met:

$$\frac{\gamma B_1 L_1}{\overline{v_i}^3} = \frac{\gamma B_2 L_2}{\overline{v_f}^3}, \tag{3.40}$$

and this is accomplished by tuning $B_1 L_1$ and $B_2 L_2$ for the given values of $\overline{v_i}$ and $\overline{v_f}$, respectively [231]. The number of precessions in the DC magnetic field must be matched to create the proper spin-echo effect.

3.1.9.2 The Development of the RF coil

The problem with this NSE tuning condition for inelastic scattering, however, is that it only allows for field tilt angles of up to 10°, which severely restricts the range of dispersive excitation group velocities that are measurable with NSE [234], effectively eliminating the possibility to measure linewidths of dispersive excitations such as phonons. In order to overcome this, the NSE DC coils were consequently replaced with RF spin flippers, which allow for a maximum tilt angle of ∼50-70° and therefore encompass a much more practical range of dispersive excitation group velocities that the coils can be tuned to. Through this innovation, the NRSE technique began.

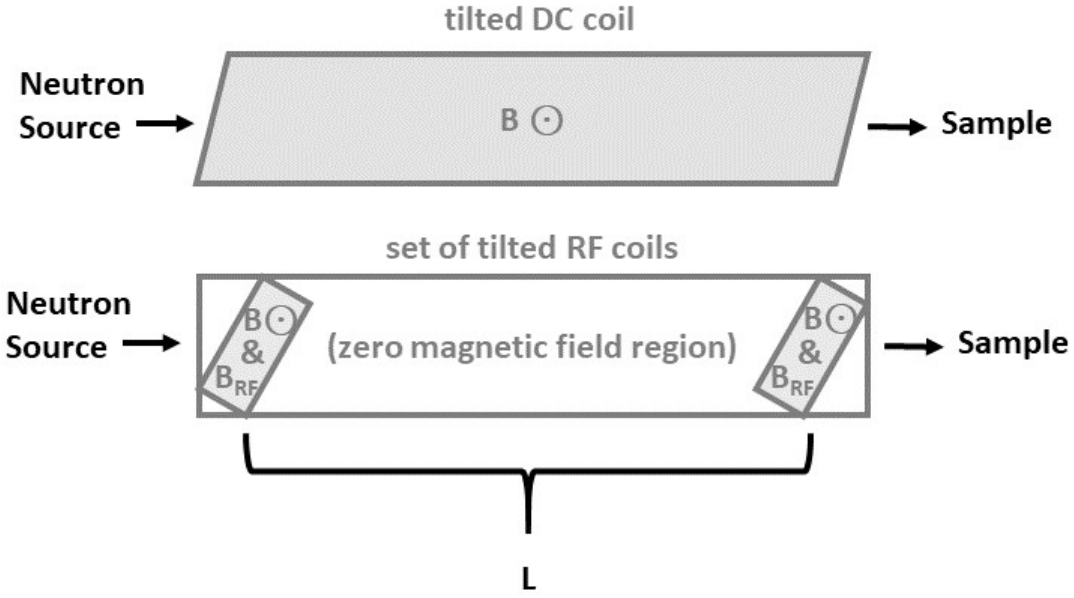

Figure 3.11: Explanation of the RF coil used in NRSE. *The top panel is a zoom onto one of the two DC coils in an NSE spectrometer (see Fig. 3.10). In the bottom panel, the DC coil is replaced by two RF coils for the NRSE technique that still contain static field B but also have a time-varying field B_{RF}. In between the two RF coils, where there would still normally be static field B in the NSE spectrometer, there is instead no magnetic field.*

For NRSE, the boundaries of the precession fields are defined by RF spin flippers, also called $\pi-$flippers, instead of DC coils. They each produce a static field B and resonant, time-varying field B_{RF} perpendicular to B. As seen in Fig. 3.11, for the same length L, we replace the long

solenoid of the NSE technique with two RF coils that rotate along their vertical axes in order to match the tilt angle to the dispersion slope (we will come back to this concept using Fig. 3.12 shortly). The emphasis, therefore, is on controlling the frequency of rotation rather than on maintaining a homogeneous static field, and, as the following paragraphs will demonstrate, the use of a set of RF coils produces a precession angle which is twice that of the NSE DC coil setup [231].

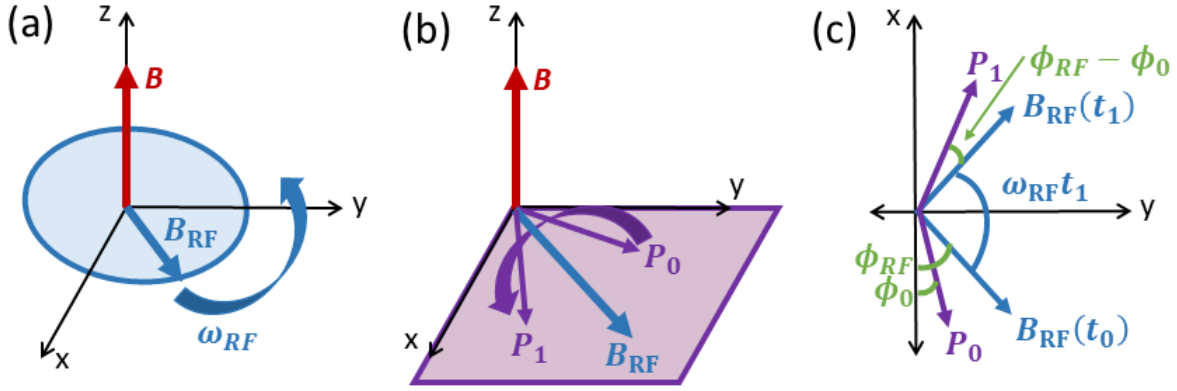

Figure 3.12: Operation of the RF coil. *(a) Each RF spin flipper has a time-varying field B_{RF} in the xy plane that varies according to ω_{RF} and a static field B in the z direction. (b) Each time a neutron passes through an RF spin flipper with initial polarization P_0 at arbitrary time t_0, it rotates for π about the time-varying field, coming out and back into the xy plane as shown in (b), and then it exits after time t_1 with final polarization P_1. A sketch of these vectors within the xy plane is shown in (c).*

Let us assume that an incoming neutron beam is first polarized into the xy-plane. We will consider each of the two π-flippers in Fig. 3.11 to be of length d and to produce both a static field B in the z-direction and a time-varying field B_{RF} perpendicular to B in the xy-plane, such as what is shown in Fig. 3.12(a).

There are two resonance conditions that the RF spin flipper must meet [231]:

$$\omega_{RF} = \gamma B \text{ and } \gamma B_{RF} d/v = \pi, \text{ where } B_{RF} = \frac{\pi v}{\gamma d}. \tag{3.41}$$

The neutron enters the π-flipper at arbitrary time t_0 with initial polarization P_0 and precession angle ϕ_0 with respect to the xy-plane, and with arbitrary precession angle ϕ_{RF} with respect to the time-varying field B_{RF}. In order for a rotation of π about B_{RF} to occur, a precession for time $t_\pi = t_1 - t_0 = d/v$ will pass before the neutron exits at time t_1. This causes the neutron to have a final precession angle of $\phi'_{RF} = \omega_{RF} t_\pi = \omega_{RF}(d/v)$ with respect to the time-varying field upon exiting the first coil. The polarization of the neutron at this point, P_1, will therefore correspond to a new precession angle, ϕ_1, following Fig. 3.12(c):

$$\phi_1 = \phi_{RF} + \phi'_{RF} + (\phi_{RF} - \phi_0) = 2\phi_{RF} + \omega_{RF}\left(\frac{d}{v}\right) - \phi_0. \tag{3.42}$$

This marks the end of the passage through the first coil. If we continue to follow the diagram in the bottom panel of Fig. 3.11, however, the neutron next passes through the zero magnetic field drift region without change to the polarization vector, meaning that, at the entrance to the second RF coil, the precession angle is still equal to ϕ_1. However, some time has passed in the zero drift region that is equal to L/v, meaning that the new precession angle upon entering the second coil, ϕ''_{RF}, is equal to $\phi_{RF} + \omega_{RF}\left(\frac{L}{v}\right)$. Using these guidelines, we follow the same formula

as in eq. 3.42 in order to pass through the second coil, noting that the second RF coil is tuned to the same Larmor frequency as the first (with synchronized B_{RF} fields) [231]:

$$\begin{aligned}\phi_2 &= 2\phi''_{RF} + \omega_{RF}\left(\frac{d}{v}\right) - \phi_1 \\ &= 2\left[\phi_{RF} + \omega_{RF}\left(\frac{L}{v}\right)\right] + \omega_{RF}\left(\frac{d}{v}\right) - 2\phi_{RF} - \omega_{RF}\left(\frac{d}{v}\right) + \phi_0 \\ &= 2\omega_{RF}\left(\frac{L}{v}\right) + \phi_0\end{aligned} \tag{3.43}$$

We can see from eq. 3.43 that, by using the set of RF coils instead of the one long DC coil, the precession angle doubles in comparison, and therefore also increases the resolution of the technique.

With the use of the RF coils came the ability to apply the field tilt angles to a much wider range of dispersive excitation group velocities. The RF coils can be tilted up to ∼50° on TRISP@FRM-II [237] and ∼70° for the ZETA option on IN22@ILL (NRSE instruments that will be formally introduced in Section 3.1.9.4), allowing them to be focused to the incline of the local slope on a linear dispersion. More specifically, the spin-echo phonon focusing condition is designed so that the boundaries of the precession fields with precession angle ϕ_{NRSE} are parallel to the dispersion curve [234], such as in Fig. 3.13(c).

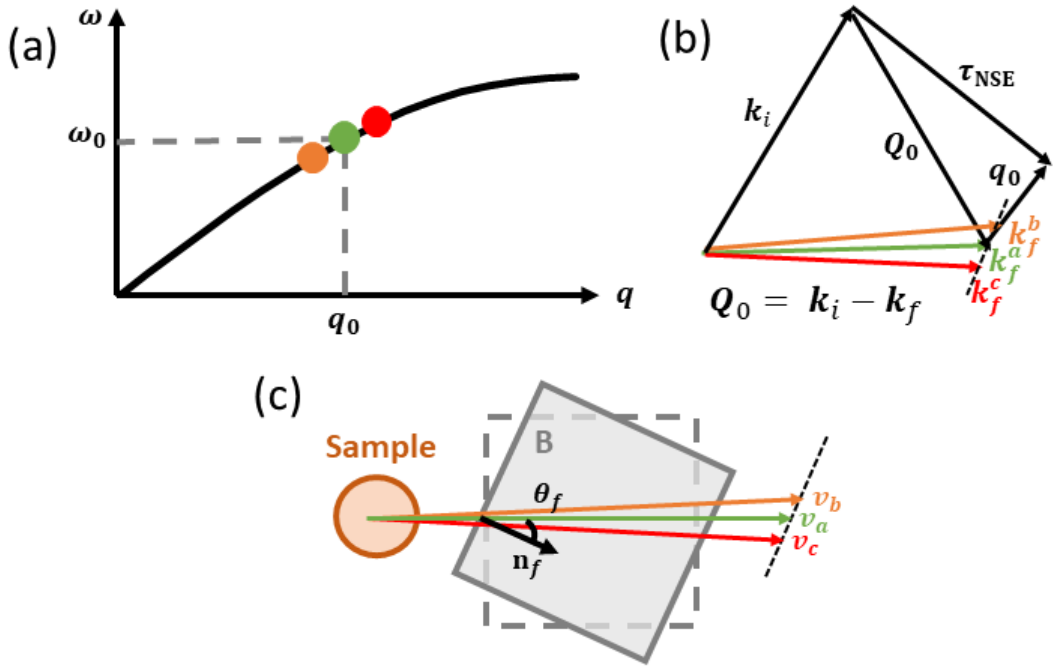

Figure 3.13: The tilt of the boundaries of the RF coil. *(a) Several closely located points along a given dispersion (orange, green, and red points) are centered around a phonon at* $(\mathbf{q}_0, \omega_0)$*. (b) The scattering triangle that results from this configuration for a phonon at* $(\mathbf{q}_0, \omega_0)$ *on the dispersion curve. (c) A partial schematic of the sample and second precession region, showing that the boundaries of the RF coil (with normal vector* n_f*) are tilted with angle* θ_f *to match the slope of the dispersion surface of the phonon dispersion, depicted with a black dashed line.*

To illustrate phonon focusing for NRSE, we will take an arbitrary point on a linear phonon dispersion curve at $(\mathbf{q}_0, \omega_0)$ that has a local group velocity of $\nabla_q \omega(\mathbf{q}_0)$. (We denote group velocity this way to avoid confusion between the phonon velocity and the neutron velocities that are defined in Fig. 3.13.) The RF coils before and after the sample are tilted with angles $\theta_{i,f}$,

respectively, forming normal vectors $\mathbf{n}_{i,f}$ with the coil surfaces. The non-zero linewidth of the phonon peak at $(\mathbf{q}_0, \omega_0)$ causes a spread in ϕ_{NSE} to the first order, such that

$$\phi - \phi_0 = \tau_{\mathrm{NSE}}\Big(\omega - \omega_0(\mathbf{q})\Big) = \tau_{\mathrm{NSE}}\Big(\omega - \Big[\omega_0(\mathbf{q}_0) + (\mathbf{q} - \mathbf{q}_0)\cdot\boldsymbol{\nabla}_q\omega(\mathbf{q}_0)\Big]\Big). \tag{3.44}$$

This means that the coil surfaces must be tuned according to the spread (centered around the green point with velocity v_a in Fig. 3.13) as seen by the mean neutron velocities [233],

$$\mathbf{n}_{i,f} || \Big(\overline{\mathbf{v}_{i,f}} - \boldsymbol{\nabla}_q\omega_0(\mathbf{q}_0)\Big), \tag{3.45}$$

such that

$$\cos(\theta_{i,f}) = \frac{\mathbf{v}_{i,f}\Big(\overline{\mathbf{v}_{i,f}} - \boldsymbol{\nabla}_q\omega_0(\mathbf{q}_0)\Big)}{|\mathbf{v}_{i,f}||\overline{\mathbf{v}_{i,f}} - \boldsymbol{\nabla}_q\omega_0(\mathbf{q}_0)|}. \tag{3.46}$$

This ensures that the scattered neutrons have the same travel time in the field: Looking again at Fig. 3.13(c), we see that the neutron with velocity v_b travels slightly longer in the field than either v_a or v_c. If we assume that $v_b > v_a > v_c$, then we can tune the tilt such that all neutrons still pass through the field while taking time t_1 [231].

It then follows that

$$\frac{(\omega_L L)_{i,f}}{(\overline{\mathbf{v}_{i,f}}\mathbf{n}_{i,f})^2}\mathbf{n}_{i,f} = \tau_{\mathrm{NSE}}\frac{m}{\hbar}\Big(\overline{\mathbf{v}_{i,f}} - \boldsymbol{\nabla}_q\omega_0(\mathbf{q}_0)\Big), \tag{3.47}$$

in order to arrive at the final expression for the spin-echo focusing condition:

$$\tau_{\mathrm{NSE}} = \frac{\hbar(\omega_L L)_i}{mv_i^2\cos(\theta_i)|\overline{\mathbf{v}_i} - \boldsymbol{\nabla}_q\omega_0(\mathbf{q}_0)|} = \frac{\hbar(\omega_L L)_f}{mv_f^2\cos(\theta_f)|\overline{\mathbf{v}_f} - \boldsymbol{\nabla}_q\omega_0(\mathbf{q}_0)|}. \tag{3.48}$$

The significance of this focusing condition is that the polarization measured during the experiment is no longer coupled to the already existing, or intrinsic, TAS resolution ellipsoid nor to the energy spread in the dispersion surface for the given dispersive excitation, giving us confidence that the measured inverse-exponential decay of the beam with increasing τ_{NSE} is due only to the interaction with the sample [206].

3.1.9.3 The bootstrap method upgrade

There are currently two TAS spectrometers in use that perform NRSE measurements, namely the ZETA option for IN22@ILL and TRISP@FRM-II, and their characteristics will be detailed in Section 3.1.9.4. However, before turning to the instrumentation of these spectrometers and, keeping in line with this explanation of the RF coil, there has been a second revolutionary upgrade to the NRSE technique that first deserves attention.

Both the ZETA option for IN22@ILL and TRISP@FRM-II can take advantage of what is called the bootstrap method, which was first proposed by R. Gähler and R. Golub [230] as a way of enhancing the instrumental resolution of the NRSE technique even further. This is done by turning each RF coil into a set of bootstrap RF coils that each consist of two π-flippers with DC fields that are opposite relative to each other ($\uparrow\downarrow$) [231, 234, 238]. We directly impact resolution since we increase the precession angle by sending the neutron through eight coils instead of four, and the final precession angle is doubled again in comparison to eq. 3.43. (The derivation can be found in Ref. [231]):

$$\phi_{\mathrm{bootstrap}} = 4\omega_{RF}\Big(\frac{L}{v}\Big) + \phi_0. \tag{3.49}$$

This method also helps create a more closed magnetic field environment, eliminating the field corrections usually needed in order to cancel out stray fields [239]. The two halves of a bootstrap coil are joined together in the case of TRISP@FRM-II, as seen in Fig. 3.14(a), while there is a small distance between the two halves of the coil that can be adjusted in the case of the ZETA option for IN22@ILL. Additional information on the bootstrap coils for the ZETA option for IN22@ILL and for TRISP@FRM-II can be found in Ref. [231] and Ref. [236], respectively.

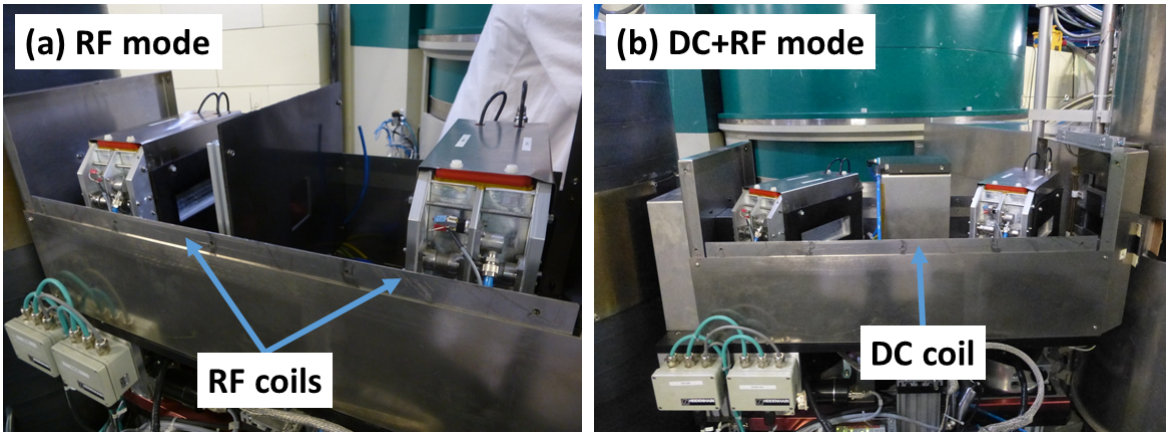

Figure 3.14: RF and DC coils on TRISP@FRM-II. *(a) Examples of the RF bootstrap coils placed after the sample on the neutron resonance spin echo triple-axis spectrometer TRISP@FRM-II. This particular RF mode allows for measurements in a range of 50-300 kHz. (b) The addition of a DC coil both before and after the sample and in between the two sets of RF coils in each case allows for measurements below 50 kHz.*

Fig. 3.14(a) shows examples of the RF coils on TRISP@FRM-II in the "arm" after the sample, and Fig. 3.14(b) shows an additional mode on TRISP@FRM-II in which a DC coil is inserted in between the two sets of RF bootstrap coils, allowing for a different range of measurement (see figure caption). These will be referred to as RF and DC+RF modes in future sections. The RF coils are designed such that operation with and without the bootstrap method can be conducted by simply adding the second RF coil in parallel or routing a relay that avoids this second coil, respectively [231].

3.1.9.4 NRSE for TAS Instrumentation

As mentioned in the previous section, there are currently two instruments capable of performing NRSE measurements: the ZEro field spin echo and Three Axis (ZETA) option on IN22@ILL, and TRISP@FRM-II. Both instruments are thermal-neutron triple-axis spectrometers that have been modified for NRSE measurements. These options make use of polarization neutron TAS set-ups with the addition of RF coils to create the NRSE environment. An NRSE spectrometer consists of four sets of RF spin flippers, C_{1-4}, each of length l, and two drift regions of lengths $L_{1,2}$, such as the ones shown in Fig. 3.15.

The coils $C_{3,4}$ have a static field of equal but opposite strength with respect to coils $C_{1,2}$ ($\uparrow\downarrow$), meaning that precessions for a given neutron velocity cancel across the spectrometer, again creating what is otherwise known as the spin-*echo* effect. More information including detailed walk-throughs of each step and resulting precession angle for an NRSE spectrometer can be found in Refs. [229, 231, 236].

For polarized neutron experiments, a specific type of ferromagnetic crystal, usually a Heusler alloy, is used for both the monochromator and analyzer. NRSE requires a crystal that not only monochromatizes the incoming neutron beam, but also spin-polarizes it. A beam is said to be

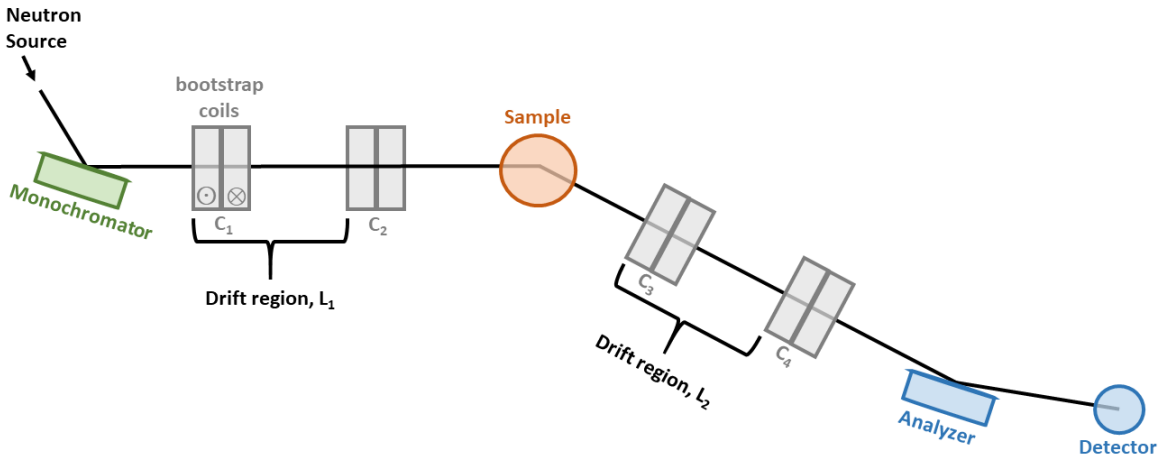

Figure 3.15: Example of a triple-axis spectrometer set up for the neutron resonance spin echo technique. *The main features include the spin-polarizing monochromator (in green) and analyzer (in blue) and the series of bootstrap RF coils (in gray) on either side of the sample (in orange) that are aligned anti-parallel with respect to each other. This combination allows the change in the neutron's spin trajectory due to interaction with the sample to be measured.*

completely polarized when the nuclear and magnetic structure factors are equal [209]. The (1,1,1) scattering reflection of the Heusler alloy Cu_2MnAl provides high neutron reflectivity for both magnetic and nuclear scattering, usually making it the top choice for such experiments [212]. The third important component to working with polarized neutrons during an NRSE experiment is a spin-flipper, which causes a 180° change in the polarization direction and was introduced previously [209, 212].

Due to IN22's multiple setups that need to be maintained at the spectrometer, the ZETA components need to be removable in order to re-obtain the other variations of IN22. Therefore, the IN22 ZETA option polarizes the incoming white beam with a Heusler monochromator, defining a fixed k_f of 1.64, 1.97, 2.662, 3.87, or 4.15 $Å^{-1}$, and it supports a Heusler analyzer as well. TRISP, however, is an instrument permanently set up for NRSE measurements, and therefore has not only a velocity selector, allowing the instrument to have a k_i range of 1.3 - 7.0 $Å^{-1}$, but also a polarizing supermirror bender placed in the guide, which can be manually turned on or off at the spectrometer. Since the bender polarizes the beam, TRISP can then work with a Pyrolytic Graphite monochromator. It also supports a Heusler analyzer to analyze the polarization.

Turning our attention to the setup of the coils once again, it can be helpful to take advantage of both the RF and DC+RF modes on the spectrometer TRISP@FRM-II that were introduced previously, since together they help provide us with a larger accessible range of τ_{NRSE} values. On TRISP@FRM-II, the minimum range in RF mode is ~50 kHz, since at lower frequency the instrumental performance (also known as the flipping ratio) decreases. This limits the accessible τ_{NRSE} range. The DC coils alone, on the other hand, form the "classical" NSE configuration with relatively small fields that bridge the gap between $\tau_{\mathrm{NRSE}} = 0$ and the minimum τ_{NRSE} of the RF coils, but with the limitation of having an inclination angle of zero. To achieve the phonon focusing condition with finite inclination, we apply the DC+RF mode: we switch the (inclined) RF coils on and pole the DC coils negative to subtract the field integral. This means that we start with the minimum τ_{NRSE} of the RF coils, and go towards $\tau_{\mathrm{NRSE}} = 0$ with increasing DC current. The inclination angle of the RF coils varies with the DC current, but the effective angle remains constant.

There is another vital difference between the NRSE configuration and the regular TAS mea-

surement configuration, which is that we put the TAS spectrometer into the defocused condition (see Fig. 3.7). We are limited by the maximum tilt angles of the NRSE spectrometer, and therefore in order to minimize the tilt angle parameter, this often means altering the scattering triangle and also forfeiting some intensity in the process [231]. This does, however, result the intersection between the dispersion surface and resolution ellipsoid being much smaller, allowing us to locally assume that the dispersion is linear, once again fulfilling the phonon focusing condition.

Finishing out our step through of the spectrometer schematic in Fig. 3.15, the intensity is registered at the detector, and in order to extract the polarization P_x from intensity I, we recall eq. 3.37. From the spectrometer point of view, this is done by translating RF coil C_4 through distance ΔL, starting from a given offset L_0. This causes the intensity to oscillate with period $L_{\text{per}} = 2\pi v_f/\omega_L$ [237, 238].

$$I(\Delta L) = I_0\left(1 + P_x \cos\left(2\pi \frac{\Delta L + L_0}{L_{\text{per}}}\right)\right) \tag{3.50}$$

Usually one period of L_{per} is enough to extract P_x for a given τ_{NRSE}, and an example of such a scan is shown in Fig. 3.17(a), the experimental context of which will be discussed in the next section. When several scans such as the one in Fig. 3.17(a) are taken for different τ_{NRSE} values at a given point on the phonon dispersion, the exponential decay of polarization vs τ_{NRSE} can be used to extract linewidth, such as what is shown in Fig. 3.17(b).

Finally, in terms of data interpretation, there are three corrections that are made to the raw polarization data: instrumental, curvature, and mosaic spread corrections. These must be carefully accounted for during the data treatment process, as they can cause additional depolarization of the beam that are unaffiliated to the interaction with the sample that we want to measure [206]. The instrumental correction involves mapping the depolarization of the direct beam with frequency for a given fixed $\mathbf{k}_f$. We must also account for the Bloch-Siegart effect, which introduces additional depolarization at low frequency due to the experimental constraint of not being able to create a true rotating field, but rather only a sinusoidal oscillating field. (For more information, see Ref. [240].)

The curvature function, on the other hand, is calculated using the value of $\boldsymbol{\nabla}_q\omega(\mathbf{q}_0)$ at the point of interest on the dispersion and the program SEResCal(). It is meant to account for lattice imperfections that cause curvature of the dispersion surface near the point of interest and lead to depolarization of the beam [241]. SEResCal() uses the Hessian matrix, $\hat{H}$, to calculate the second-order term of the spin-echo phase due to this curvature of the dispersion surface, and the program also calculates the phase shift at the specific reciprocal lattice vector $\mathbf{G}$ of interest due to the mosaic spread of the sample. The mosaic spread of the sample can also be measured using the NRSE for TAS technique, and will be discussed in Section 3.1.10. The mosaic spread, along with the instrumental parameters for the TAS instrument are used as input parameters to SEResCal() in order to calculate the intrinsic TAS resolution and effect of mosaic spread as well. More information on the SEResCal() program, developed by K. Habicht, can be found in Refs. [237, 241].

3.1.9.5 Application to the Type-I Clathrate $Ba_{7.81}Ge_{40.67}Au_{5.33}$

I will now give a brief example of how NRSE measurements can be applied to phonon linewidths that remain resolution-limited using standard TAS and TOF measurements. In the context of my thesis, the overall goal of this study was to experimentally measure transverse and longitudinal acoustic (TA, LA) phonon linewidths in different polarizations and in a range of temperature for the type-I clathrate $Ba_{7.81}Ge_{40.67}Au_{5.33}$ in order to understand how the different

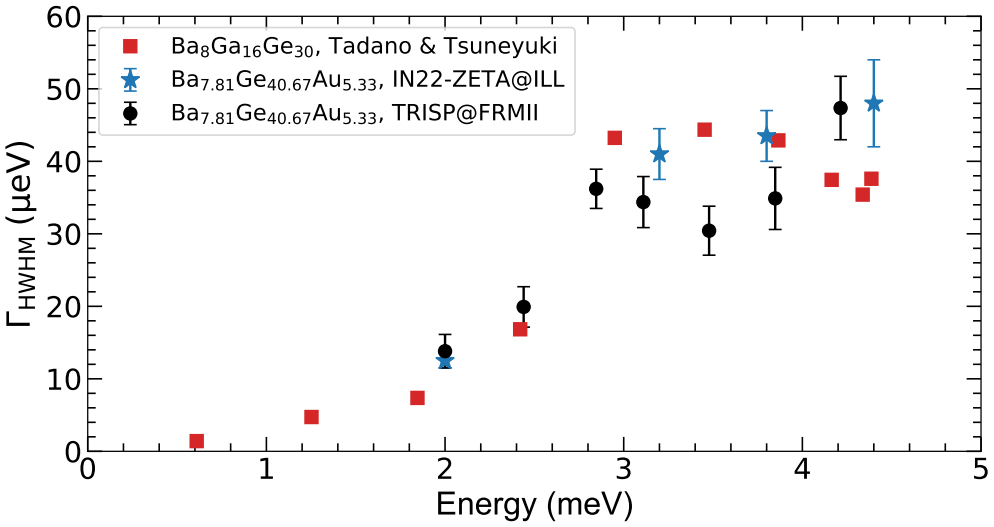

Figure 3.16: Example of intrinsic phonon linewidths measurements by Neutron Resonance Spin Echo (NRSE). *The intrinsic phonon linewidths of a transverse acoustic (TA) phonon branch from the intense (006) Bragg peak propagating along [110], polarized along [001] are shown for the type-I clathrate $Ba_{7.81}Ge_{40.67}Au_{5.33}$. Measurements have been made on the two European instruments for NRSE, IN22-ZETA@ILL (blue stars) and TRISP@FRM-II (black circles). The IN22-ZETA@ILL linewidths were taken from Lory et al. [27]. They are compared to the TA linewidth calculations for the type-I clathrate $Ba_8Ge_{30}Ga_{16}$, made with the ab initio self-consistent phonon method [93].*

phonon scattering mechanisms at play change with momentum and temperature. Furthermore, the use of the *ab initio* self-consistent phonon (SCP) method to calculate phonon frequency renormalizations in type-I clathrates by Tadano and Tsuneyuki [93] was experimentally confirmed in Turner *et al.* [57]. This, however, is only one half of the story needed to explain the low and temperature independent region of lattice thermal conductivity, κ_L, in clathrates. The phonon linewidths, not only the phonon frequencies, calculated by the SCP method also need to be experimentally confirmed in order to fully validate this method for explaining κ_L.

Fig. 3.16 summarizes the intrinsic phonon linewidths of the TA^{001}_{110} phonon branch from the intense (006) Bragg peak propagating along [110], polarized along [001] for $Ba_{7.81}Ge_{40.67}Au_{5.33}$. The new datapoints coming from TRISP@FRM-II are part of a continuation of the linewidths measured using IN22-ZETA@ILL and published in Lory *et al.* [27], which are also shown in Fig. 3.16. In this system, acoustic linewidths within this energy range are resolution-limited for measurements on a TAS instrument (see Fig. 5 from Ref. [27]), making $Ba_{7.81}Ge_{40.67}Au_{5.33}$ an excellent candidate for NRSE measurements.

As seen in Fig. 3.16, the TA^{001}_{110} linewidths calculated by the SCP method match beautifully with those experimentally measured at IN22-ZETA@ILL and TRISP-FRM-II. There appears to be a strong energy dependence before a break into a weaker dependence at higher energy, even into a plateau. Evidence of multiple regimes such as this have been shown to occur in other complex and disordered systems, and, for more information, please see the discussion section of my recently submitted work, Turner *et al.* [106]. Fig. 3.16 is also a wonderful example of the repeatability between IN22-ZETA@ILL and TRISP-FRM-II, which I emphasize is no small feat considering the extreme complexity of the NRSE configuration.

Diving into more details of the experiment, Fig. 3.17(a) is an example of the translation of RF coil C_4 through distance ΔL for a period of L_{per}, measured with $\tau_{\text{NRSE}} = 1.79$ ps, for the point $\mathbf{q}$ = (0 -0.143 -0.143) on the TA^{001}_{110} dispersion (see Appendix B, Fig. B.1 for a plot of the experimentally-measured dispersion). The polarization is then extracted using eq. 3.50 and

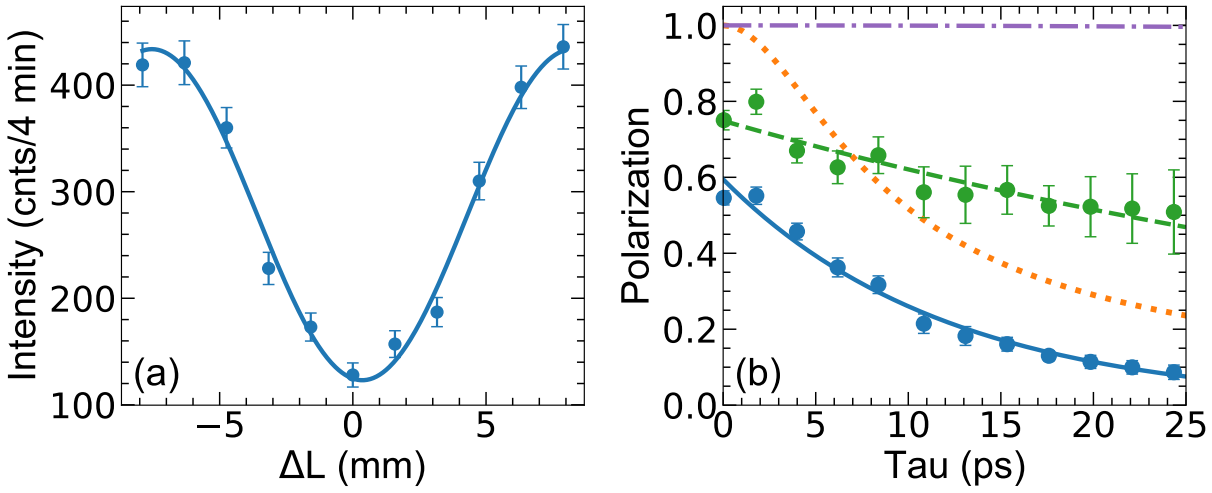

Figure 3.17: Example of an NRSE measurement for the type-I clathrate $Ba_{7.81}Ge_{40.67}Au_{5.33}$. *(a) shows the translation of RF coil C_4 through distance ΔL for a period of L_{per} for $\tau_{NRSE} = 1.79$ ps for the point $\mathbf{q}$ = (0 -0.143 -0.143) on the TA^{001}_{110} phonon branch from the intense (006) Bragg peak propagating along [110], polarized along [001]. The data has been fit with a cosine() function and an arbitrary background set to zero, as described in the text. (b) The τ_{NRSE} in (a) and others all measured at the same $\mathbf{q}$ point are plotted (blue circles and solid line) and then corrected for the instrumental resolution (purple dashed-dot line) and for curvature of the dispersion surface (orange dotted line), resulting in the corrected data (green circles and dashed line). The intrinsic phonon linewidth is then extracted, which is 13.81 μeV in this case.*

plotted in Fig. 3.17(b) along with the other τ_{NRSE} values measured at that particular dispersion point $\mathbf{q}$ = (0 -0.143 -0.143). The position at $\tau_{\mathrm{NRSE}} = 0$ was measured in DC+RF mode, while all other points were measured in RF mode. Those points are then corrected according to the instrumental and curvature corrections explained in Section 3.1.9.4, and the phonon linewidth is extracted from the exponential fit of the corrected data. This process was repeated for seven total $\mathbf{q}$ positions along the TA^{001}_{110} dispersion, and raw data and fits are provided in Appendix B.

In order to provide the reader with a visual meaning to the difficulty that we as experimentalists face in measuring intrinsic phonon linewidths in systems such as clathrates, I have re-plotted the experimentally-measured linewidths of Fig. 3.16 alongside the energy resolution of the cold-neutron time-of-flight spectrometer IN5@ILL in Fig. 3.18. With this one figure, one can instantly grasp both the experimental limitation of TAS and TOF techniques, and also fully appreciate the improved resolution that comes with the application of NRSE. The intrinsic linewidths, which can be captured by NRSE, are a full 1-2 orders of magnitude below the energy resolution of IN5@ILL for the given experimental conditions used in the TOF experiment described in Turner *et al.* [57].

I would also like to point out several difficulties faced during the data analysis and treatment stage of this particular NRSE experiment in order to highlight the different methods one can take in interpreting such data. These mainly pertain to (1) the interpretation of the background, (2) the balance between count time and the number of points on the exponential curve, and (3) the use of both RF and DC+RF mode points on the exponential curve.

Firstly, concerning the background, caution must be made when comparing polarization at $\tau_{\mathrm{NRSE}} = 0$ ps, as the background was not fit during these particular measurements and was arbitrarily set to zero. This means that polarization at $\tau_{\mathrm{NRSE}} = 0$ ps is not consistent from q to q point. This is not a concern, however, since a phonon linewidth is extracted from an

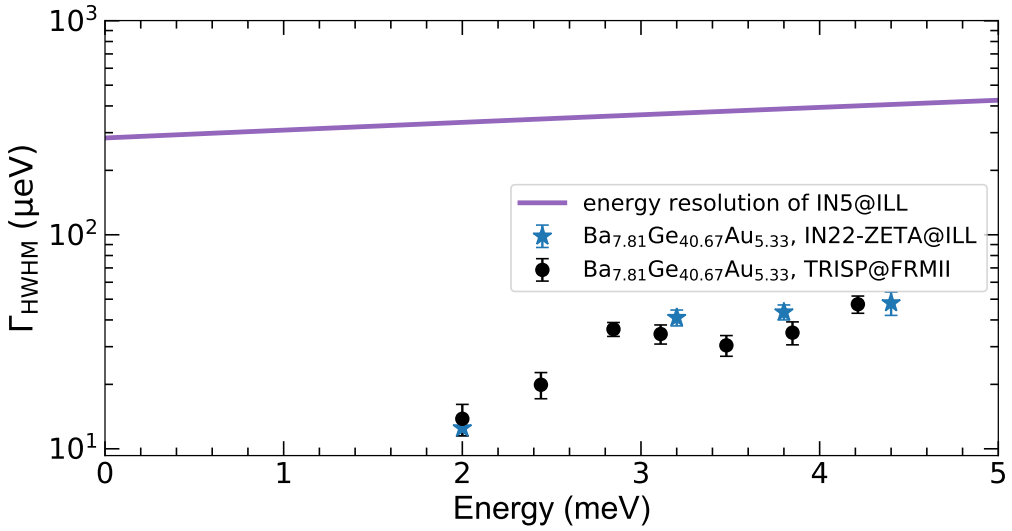

Figure 3.18: Visual representation of the improved energy resolution with the NRSE technique. *The experimentally-measured intrinsic linewidths of the type-I clathrate $Ba_{7.81}Ge_{40.67}Au_{5.33}$ shown in Fig. 3.16 are plotted against the energy resolution of the cold-neutron time-of-flight instrument IN5@ILL (purple solid line). This energy resolution was originally plotted in Fig. 8 of Turner et al. [57], and the experimental conditions used to calculate this resolution can be found in Appendix A.1 of the article.*

exponential decay of points all taken at the same q point. Alternatively, the background could have been estimated by measuring the background near the phonon peak in TAS configuration, and then the polarization of NRSE data subtracted from this background can be assumed to be constant and fixed in the fitting procedure, allowing polarization at $\tau_{\mathrm{NRSE}} = 0$ ps to be compared across q points and even fixed within the fits. This is what has been done for the linewidths measured on IN22-ZETA@ILL in Lory *et al.* [27].

Secondly, it should be noted that a minimum count time must be reached if a reasonable phonon lifetime is to be extracted. While this might seem obvious, it is important to remember that there are multiple analysis steps between the raw data and resulting linewidths like those shown in Fig. 3.16. If sufficient count times are not given to each τ_{NRSE}, then due to the propagation of error through these steps, the resulting phonon linewidth will be left with a large uncertainty. Specifically for this experiment, 11 points were measured within the period of ΔL_P at each τ_{NRSE} value in order to make a sufficient cosine() fit and extract polarization, like for the cosine() fit shown in Fig. 3.17(a). There was also less intensity at higher τ_{NRSE} values, and therefore the scans made between ~20-25 ps were repeated for better statistics (see Figs. B.2-B.8). A compromise must also be made between the time spent measuring each τ_{NRSE} value and the total number of τ_{NRSE} values measured. Looking again at Fig. 3.17(b), we found during the experiment that the fit of the exponential decay also became much more stable with the inclusion of 12 total points instead of the original 6 points measured during the first few days of the experiment.

Lastly, I remind the reader that TRISP@FRM-II has three modes of operation: RF, DC+RF, and DC modes. DC mode, which was not used in the results shown above, is a setup in which the RF coils are ramped down completely such that the neutron passes through the RF coils without influence from any field other than that caused by the DC coils. In terms of the data analysis, it is obvious that one can group and fit several τ_{NRSE} values measured using RF mode for the same **q** point with the same exponential curve, but one must be cautious with how to include τ_{NRSE} values measured using DC+RF and/or DC mode. DC+RF mode values can be added and fit

using the same exponential curve once the separate DC+RF mode instrumental correction has been made. The polarization extracted in DC mode, however, is not directly correlated to the polarization extracted in RF (or DC+RF) mode. Furthermore, there is a strong Gaussian-type decay in the low DC mode range that is not due to the phonon itself, meaning that there is not one single exponential decay function for all ranges of τ_{NRSE}. This should therefore be a point of consideration when planning an NRSE experiment.

3.1.10 Neutron Larmor Diffraction (NLD)

This NRSE for TAS setup is actually quite diverse in application, as it was proven by M. T. Rekveldt *et al.* [242] in 2001 that Larmor precession could also be used to measure changes in lattice spacing and the mosaic spread of crystalline samples through Neutron Larmor Diffraction (NLD).

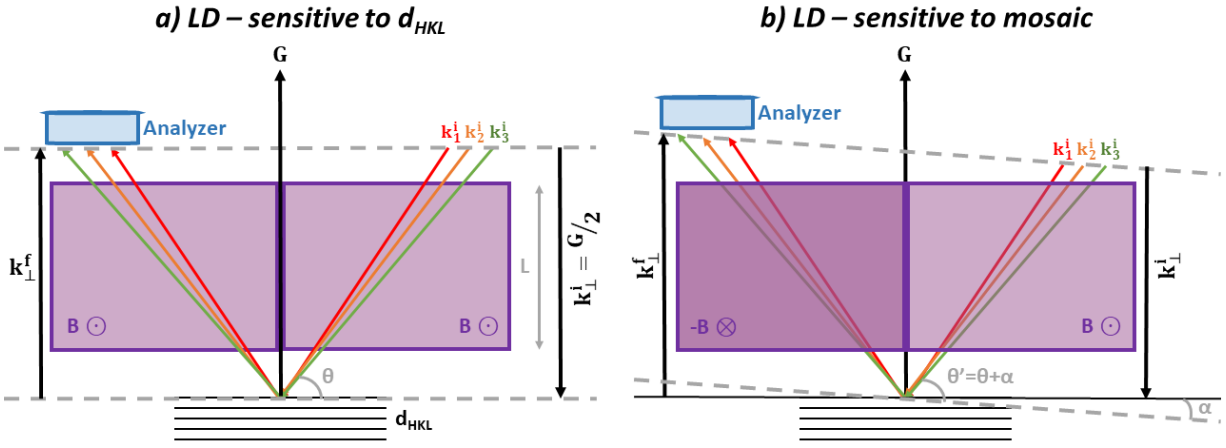

Figure 3.19: Example of Neutron Resonance Spin Echo (NRSE) spectrometer in Larmor Diffraction (LD) mode. *The instrumental configuration follows that of a NRSE for TAS spectrometer, shown in Fig. 3.15. However, in (a) the spectrometer is sensitive to lattice spacing d_{HKL} and can track changes to d_{HKL} with temperature, for instance, while in (b), the mosaic spread of the sample can be measured through the tilting of angle α.*

NLD works off of the principle that the two arms of the spectrometer are within precession field **B** in a parallel configuration (↑↑), meaning that the precessions for a given neutron velocity add rather than cancel across the spectrometer [234], such as in Fig. 3.19. We still have four sets of RF bootstrap coils, but they have been removed from these subplots in order to simplify the description. The bootstrap coils set the boundaries of the precession regions, and, following Fig. 3.19(a), when $\mathbf{G} = 2\pi/d_{\mathrm{HKL}}$ meets the condition for Bragg's law with angle θ and the boundaries of field **B** are parallel to the diffracting crystal planes, the instrument is sensitive to the spread of lattice spacing d_{HKL}.

If, instead, the two spectrometer arms are in an anti-parallel configuration (↑↓) while the boundaries of B_0 are still parallel to the diffracting crystal planes and when angle $\alpha = 0$, then the instrument is sensitive to the mosaic spread of the crystal, like in Fig. 3.19(b). The measurement is taken with the diffracting crystal planes tilted with angle α such that Bragg angle θ varies with phase [243]. Finally, an additional instrumental correction for Larmor diffraction mode is also made by measuring a perfect Ge single crystal at several fixed $\mathbf{k}_i$ values and interpolating the data for $\mathbf{k}_i$ values in between.

To expand on the lattice spacing condition in Fig. 3.19(a), the Larmor phase in the NLD

condition is defined as

$$\phi_{\mathrm{LD}} = \frac{4m\omega_L L}{\mathbf{G}} = \frac{2m\omega_L L}{\pi\hbar} d_{\mathrm{HKL}}. \tag{3.51}$$

Any temperature-dependent phase shift of d_{HKL} in Larmor phase ϕ_{LD} is tracked as

$$\Delta\phi_{\mathrm{LD}} = \phi_{\mathrm{LD}} \frac{\Delta d_{\mathrm{HKL}}}{d_{\mathrm{HKL}}} \tag{3.52}$$

through the final beam polarization, $P_{\mathrm{LD}}(\phi_{\mathrm{LD}})$, at the analyzer such that

$$P_{\mathrm{LD}}(\phi_{\mathrm{LD}}) = \langle \cos(\Delta\phi_{\mathrm{LD}}) \rangle = \int D\Big(\frac{\Delta d_{\mathrm{HKL}}}{d_{\mathrm{HKL}}}\Big) \cos\Big(\phi_{\mathrm{LD}} \frac{\Delta d_{\mathrm{HKL}}}{d_{\mathrm{HKL}}}\Big) d\Big(\frac{\Delta d_{\mathrm{HKL}}}{d_{\mathrm{HKL}}}\Big), \tag{3.53}$$

where $D\Big(\frac{\Delta d_{\mathrm{HKL}}}{d_{\mathrm{HKL}}}\Big)$ is a normalized distribution function [238, 243].

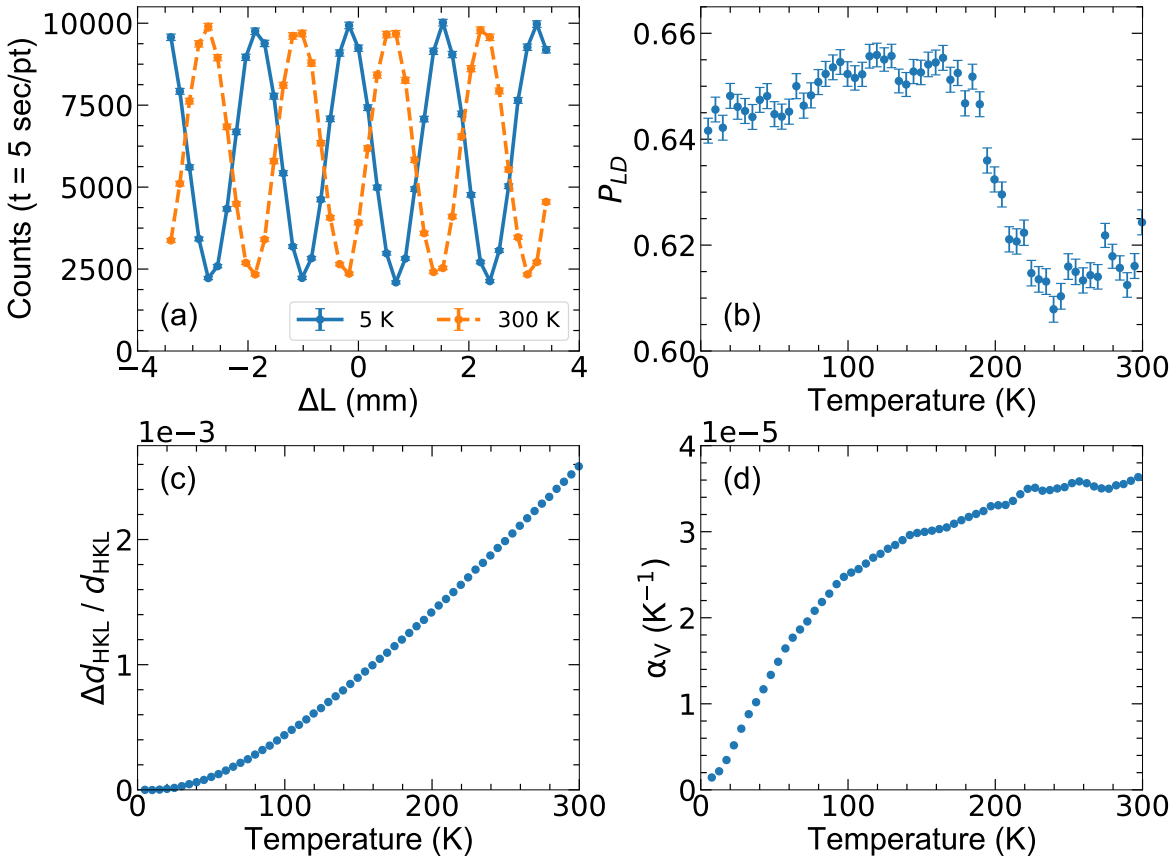

Figure 3.20: Neutron Larmor Diffraction (NLD) measurement for lattice spacing. *TRISP@FRM-II was placed into NLD mode, sensitive to d_{HKL}. The spectrometer was aligned onto the (006) Bragg peak, and (a) the phase shift was measured between 5 (blue solid line and markers) and 300 K (orange dotted line and markers) with increments of 5 K for the single crystal sample of the type-I clathrate $Ba_{7.81}Ge_{40.67}Au_{5.33}$. (b) The polarization, P_{LD}, was extracted from fits of the phase shift at each temperature, leading to the calculation of (c) the rate of thermal expansion, $\Delta a/a$, and (d) the volumetric thermal expansion coefficient, α_V. Subplots (c,d) were taken from Turner et al. [57], Fig. 2(a,b).*

The sensitivity to lattice spacing is particularly useful when measured with temperature, as it then allows for the rate of thermal expansion of the lattice to be characterized. An example of such a measurement can be found in Turner *et al.* [57], Fig. 2(a,b), for the type-I clathrate $Ba_{7.81}Ge_{40.67}Au_{5.33}$. Going step-by-step with how this figure was obtained, an example of the

phase shift between 5 and 300 K is shown in Fig 3.20(a). The measurable quantity, $P_{\mathrm{LD}}(\phi_{\mathrm{LD}})$, is extracted from the fit of the phase shift at each temperature, shown in Fig 3.20(b), and is then used to calculate $\frac{\Delta d_{\mathrm{HKL}}}{d_{\mathrm{HKL}}}$ using eq. 3.53. The resulting plot of $\frac{\Delta d_{\mathrm{HKL}}}{d_{\mathrm{HKL}}}$ vs temperature is shown in Fig.3.20(c). Finally, the linear thermal expansion coefficient, α_L, is the numerical derivative of $\frac{\Delta d_{\mathrm{HKL}}}{d_{\mathrm{HKL}}}$:

$$\begin{aligned} \frac{\Delta d_{\mathrm{HKL}}}{d_{\mathrm{HKL}}} &= \frac{d_{\mathrm{HKL}}(T_1) - d_{\mathrm{HKL}}(T_0)}{d_{\mathrm{HKL}}(T_0)} = \frac{d_{\mathrm{HKL}}(T_1)}{d_{\mathrm{HKL}}(T_0)} - 1 \\ \alpha_L &= \frac{\partial}{\partial T}\left(\frac{d_{\mathrm{HKL}}(T_1)}{d_{\mathrm{HKL}}(T_0)} - 1\right) = \frac{1}{d_{\mathrm{HKL}}(T_0)} \frac{\partial(d_{\mathrm{HKL}}(T_1))}{\partial T} \end{aligned} \tag{3.54}$$

This can also be written as the volumetric thermal expansion coefficient, $\alpha_V = 3\alpha_L$, such as in Fig. 3.20(d). In terms of the example of $Ba_{7.81}Ge_{40.67}Au_{5.33}$, α_V was used to give a quantitative value to the amount of anharmonicity seen in the system in terms of the material constant known as the Grüneisen parameter.

I would also like to briefly draw the reader's attention once again to Fig. 3.20(b). A sudden change in polarization, such as the one at 180 K, usually refers to a phase transition in a material. While a full interpretation of this finding is outside the scope of this thesis, I will propose several interpretations that can be explored in the future. Firstly, studies of phase transitions of type-I clathrates with temperature and/or under high pressure are widely covered topics in literature, with evidence of phase transitions in K_8Si_{46} [244], $Cs_8Sn_{44}\square_2$ [245], Si_{46}-I [147], Ba_8Si_{46} [246, 247], $Ba_8Ga_{16}Sn_{30}$ [248, 249], and $I_8Sb_8Ge_{38}$ [250], among others. Notably, however, no phase transition temperature appears to be found for $Ba_8Ge_{43}\square_3$ [251], nor for $Ba_8Ge_{40.7}Au_{5.3}$ [84], and therefore further investigation would need to be made in order to understand the potential evidence of a phase transition seen in Fig. 3.20(b).

A second avenue of interpretation could have to do with the off-centering of the guest atoms, as it has been shown that the Ba guest atoms in $Ba_{7.81}Ge_{40.67}Au_{5.33}$ are off-centered in three possible locations [27]. At low temperature, we can expect that each of the Ba atoms freeze in a given off-centering position, and perhaps in this Larmor diffraction measurement, we witness the increased thermal motions (the so-called "rattling") of the guest atoms as they unfreeze with increasing temperature.

Coming back now to the second use of Larmor diffraction in which we are sensitive to mosaic spread instead of lattice spacing, such as in Fig. 3.19(b), the following Larmor phase is tracked and used to extract polarization, similarly to eq. 3.53. Respecting the usual formulation, α here refers to the angle shown in Fig. 3.19(b), but note that it is not related to the thermal expansion coefficient described above [243].

$$\Delta\phi_{\mathrm{LD}}(\alpha) = \phi_{\mathrm{LD}}(\alpha) - \phi_{\mathrm{LD}}(\alpha = 0) \approx \phi_{\mathrm{LD}}\left(\frac{1}{2} + \cot^2(\theta)\right)\alpha^2 \tag{3.55}$$

The mosaic at the (006) Bragg peak of the same single-crystal sample of $Ba_{7.81}Ge_{40.67}Au_{5.33}$ was also measured during the experiment on TRISP@FRM-II, finding a mosaic of $7.14 \times 10^{-3} \pm 2.40 \times 10^{-3}$ degrees $= 0.428 \pm 0.144$ min. The decay of polarization with phase is shown in Fig. 3.21, and one can then extract the mosaic spread from the fit.

In summary of all of the neutron techniques that have been discussed in this chapter, it has been shown that there are a variety of neutron techniques that can aid the measurements of different properties of phonons. Technique and subsequent instrumental parameter selections require careful thought and consideration before starting a neutron-based experiment, as once the instrument has been chosen, the user is locked into the resolution that is available on a given instrument, which ultimately determines the quality of the data and rate of data collection that is possible during the allocated beamtime. The final section of this chapter will detail Inelastic X-ray Scattering.

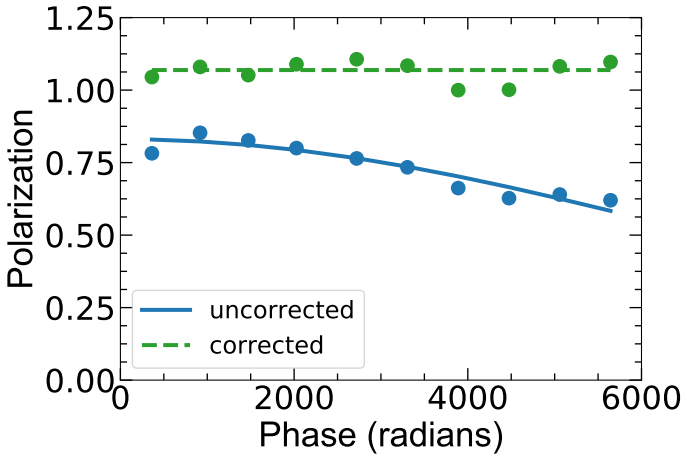

Figure 3.21: Neutron Larmor Diffraction (NLD) measurement for mosaic. *TRISP@FRM-II was placed into NLD mode, sensitive to mosaic spread. The spectrometer was aligned onto the (006) Bragg peak, and the polarization vs phase was used to extract the mosaic. The uncorrected data (blue solid line and markers) was fit with an exponential curve before using the correction described in the text, resulting (green dashed line and markers) in a mosaic of* $7.14\times10^{-3}\pm2.40\times10^{-3}$ *degrees* $=0.428\pm0.144$ *min for the single crystal sample of the type-I clathrate* $Ba_{7.81}Ge_{40.67}Au_{5.33}$*. Errorbars are within the size of the markers.*

3.2 Inelastic X-ray Scattering

Similar to INS, IXS can provide the extremely high resolution required to measure properties of phonons. Like neutrons, X-rays also have wavelengths on the same order of magnitude as interatomic distances, making them an ideal probe for measuring phonons. Unlike neutrons, however, which have the opportune energy resolution in the thermal range, i.e. ∼1 meV, beamlines for X-ray-based phonon measurements must have an energy resolution of 10^{-7} in order to match this necessary energy resolution.

This being said, IXS has several distinct advantages over neutron techniques, including the fact that multiple positions in reciprocal space can be measured at once, as opposed to TAS spectrometers, which can typically only measure one position at a time (an exception to this is the FlatCone Multianalyzer design of IN20@ILL). The average sample dimensions for an IXS experiment are ∼100×100×100 µm^3 as well, which can be helpful if a much larger ∼1×1×1 cm^3 sample needed for neutron experiments is difficult to synthesize, or to synthesize as a single grain with a low mosaic spread. IXS is a compliment to neutron techniques in many ways, and these comparisons will be developed throughout this next section.

Starting again from the same general scattering example given in Fig. 3.2 but using a photon as a probe particle, a photon with initial energy E_i, wave-vector $\mathbf{k}_i$, and polarization $\boldsymbol{\epsilon}_i$ is scattered into solid angle $d\Omega$ after an interaction with a sample causes it to have final energy E_f, wave-vector $\mathbf{k}_f$, and polarization $\boldsymbol{\epsilon}_f$. Using the adiabatic approximation, changes to the system between initial state λ_i with photon population p_{λ_i} and final state λ_f are assumed to come only from the nuclear component, or from the atomic density fluctuations, and not from the electronic component [212].

The double differential cross-section for an X-ray probe is written as the following, where $r_0 = e^2/m_ec^2$ is the radius of an electron in the system, and j refers to each electron and its position $\mathbf{r}_j$. (Note that we will use $\mathbf{r}$ and $\mathbf{R}$ to refer to the positions of electrons and atoms, respectively, in this case as opposed to the incident neutron and nucleus as was the case for

INS.)

$$\left(\frac{d^2\sigma}{d\Omega dE_f}\right) = r_0^2(\boldsymbol{\epsilon}_i \cdot \boldsymbol{\epsilon}_f)^2\left(\frac{k_f}{k_i}\right)\sum_{\lambda_i,\lambda_f} p_{\lambda_i}\left|\langle\lambda_f|\sum_j e^{i\mathbf{Q}\cdot\mathbf{r}_j}|\lambda_i\rangle\right|^2\delta(\hbar\omega + E_i - E_f) \tag{3.56}$$

This can be rewritten to contain the X-ray atomic form factor, f, which is related to the atomic charge density. As a first approximation, when $\mathbf{Q} = \mathbf{G}$, the atomic form factor for each element is defined as $f = Z^2$, where Z is the atomic number, directly from the Periodic Table of Elements. We then sum over k atoms in the system with their positions $\mathbf{R}_j$, to arrive at:

$$\begin{aligned}\left(\frac{d^2\sigma}{d\Omega dE_f}\right) &= r_0^2(\boldsymbol{\epsilon}_i \cdot \boldsymbol{\epsilon}_f)^2\left(\frac{k_f}{k_i}\right)\sum_{\lambda_i,\lambda_f} p_{\lambda_i}\left|\langle\lambda_f|\sum_k f_k(\mathbf{Q})e^{i\mathbf{Q}\cdot\mathbf{R}_k}|\lambda_i\rangle\right|^2\delta(\hbar\omega + E_i - E_f) \\ &= r_0^2(\boldsymbol{\epsilon}_i \cdot \boldsymbol{\epsilon}_f)^2\left(\frac{k_f}{k_i}\right)S(\mathbf{Q},\omega)\end{aligned} \tag{3.57}$$

This leads to another reason that IXS is a complementary technique to INS: the IXS form factor is dependent upon the atomic number, meaning that it is not limited in measuring a sample containing neutron-absorbing elements such as cadmium or boron, or to measuring an element such as vanadium, which has an almost purely incoherent neutron scattering cross-section. The caveats to this, of course, are that it can be very difficult to measure elements with a low atomic number, such as hydrogen, and that there is very little contrast between elements that are close together on the Periodic Table due to their similar atomic numbers [252].

Just as the neutron coherent and incoherent scattering cross-sections in eqs. 3.17-3.18 are dependent upon the neutron scattering length(s) b, the corresponding X-ray scattering cross-sections are dependent upon f. The coherent and incoherent X-ray scattering cross-sections, therefore, are written as follows [253]:

$$\sigma_{\text{coh}} = \langle\overline{f}\rangle^2 \tag{3.58}$$

$$\sigma_{\text{inc}} = \langle\overline{f^2}\rangle - \langle\overline{f}\rangle^2 \tag{3.59}$$

Incoherent X-ray scattering is usually negligible by comparison to coherent X-ray scattering. An in-depth example of coherent and incoherent neutron and X-ray scattering cross-section calculations for the high-entropy alloy FeCoCrMnNi can be found in the Supplementary Material of Turner *et al.* [106].

3.2.1 High-Resolution IXS Beamlines

There are currently three IXS beamlines in the world with the resolution necessary to measure phonon dispersions. This section will focus on beamline ID28 at the European Synchrotron Radiation Facility (ESRF), however BL35XU at the Super Photon ring-8 GeV (SPring-8) in Japan and Sector 30 at the Advanced Photon Source in the USA also have similar capabilities.

ID28 is one of approximately 40 beamlines at the ESRF, all of which connect to a single synchrotron storage ring that is periodically refilled, depending on the total electron current in the ring and the lifetime of those particles in the ring. The incoming beam from the storage ring has an energy of approximately 20 KeV, and therefore the challenge for measuring phonons at IXS beamlines is to detect a $\hbar\omega = E_i - E_f$ difference of approximately 1 meV from an incoming beam that is on the order of several KeV. Therefore, it is necessary to reach an extremely high resolution in order to take these measurements.

Fig. 3.22 is a schematic of ID28. The main components of the beamline will be discussed in terms of how they contribute to the overall resolution such that an energy bandwidth of $\Delta E/E \approx 10^{-7}$ is reached before the beam scatters on the sample.

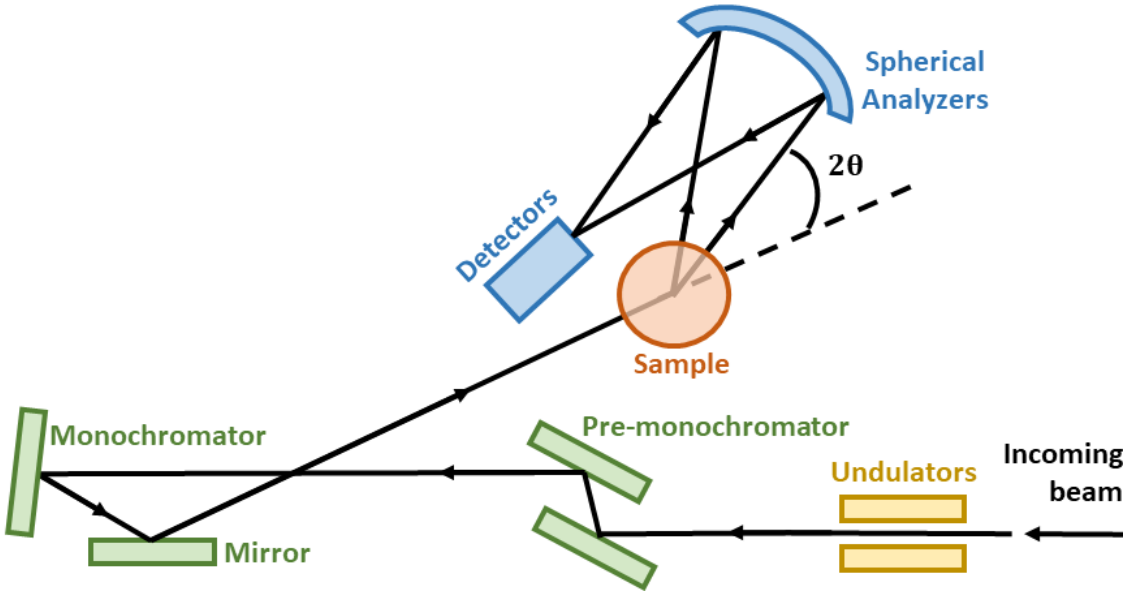

Figure 3.22: Example of a backscattering inelastic X-ray scattering spectrometer. *The main features include the undulators (in yellow), the pre-monochromator, monochromator, and mirror (in green), which all contribute to the necessary energy bandwidth of $\Delta E/E = 10^{-7}$. The beam then impinges on the sample (in orange) before reaching the spherical analyzers and detectors (in blue). This particular schematic has been modeled after beamline ID28 at the European Synchrotron Radiation Facility.*

From the main storage ring of the synchrotron, the incoming beam first passes through an insertion device, which is the reason for the 'ID' in the name ID28. The particular insertion device on ID28 is a periodic series of dipole magnets called undulators, and they are given this name because they alternate polarity and cause the beam to weakly undulate in the transverse direction. They cause the emission to form a narrow band with a peak photon energy of $E = h\nu_c$ such that the energy bandwidth is related to N_u, the number of periods the nth order harmonic of the beam is subjected to [254]:

$$\Delta E/E = \Delta h\nu/h\nu_c \approx 1/nN_u \tag{3.60}$$

The undulators can be tuned using the undulator parameter, K, which depends on the period of the undulator, L_u, the magnetic field with field strength B_0 of the magnets, the relativistic mass of an electron, m_0, and speed of light, c. The undulator parameter is then related to peak photon energy by the following, where the relativistic Lorentz factor is $\gamma = 1/\sqrt{1 - \frac{v^2}{c^2}}$, leading to a $\Delta E/E \approx 10^{-2}$ in the case of ID28:

$$h\nu_c \approx 2\gamma^2 \frac{hnc/L_u}{1 + K^2/2}, \text{ where } K = eB_0L_u/2\pi m_0 c \tag{3.61}$$

From the undulators, the beam moves to the pre-monochromator, which is a Si111 monochromator. The full monochromatization of the beam must be done in two steps using both the pre-monochromator and monochromator, since the undulators produce a high heat load. In order to avoid an intense local heating at the monochromator, which must be extremely temperature sensitive for reasons described below, and to reduce the large energy bandwidth that results from the use of insertion devices, the pre-monochromator is placed in the path of the beam before the monochromator. In the case of ID28 the pre-monochromator is actually a pair of parallel Si111 crystals. Similar to the monochromators described in Section 3.1.6, these crystals are also

controlled by Bragg's law with Bragg angle θ, and are separated by gap g such that the vertical offset between the two crystals is $2g\cos\theta$ [255]. At the end of this stage, $\Delta E/E \approx 10^{-4}$.

Next, the beam reaches the Si111 monochromator, and the key functionality of this monochromator is that it works in a backscattering geometry. The backscattering geometry is chosen since it provides a very high energy resolution. In this case, the 2θ angle must be as close as possible to 180°. Measuring meV-range phonon excitations using Bragg reflection requires a certain amount of angular acceptance, and working as closely to backscattering as possible allows for any large amount of divergence that comes from the beam source to be compensated for. Using backscattering also ensures that the resolution only depends on the quality of the monochromator. Physically speaking, although the beam is being reflected, in order for the reflected beam to just miss the incident beam, the monochromator is tilted at an angle of 0.02°. After this key stage, the resolution reaches the necessary $\Delta E/E \approx 10^{-7}$.

Since the silicon monochromator is cut on the (1,1,1) plane, all scattering on ID28 is based on this series of planes. This is the stage at which the incoming wave-vector $\mathbf{k}_i$ is defined. This particular beamline normally works with the (9,9,9), (11,11,11), and (12,12,12) planes, and energy resolution increases with reflection order [252]. Choosing the plane to work with is a compromise between flux and resolution. With the (9,9,9), for instance, the incoming beam has an energy of 17.793 keV and a resolution of 2.8 meV. When using the (11,11,11), the incoming energy is 21.747 keV with a resolution of 1.5 meV, and finally, when using the (12,12,12), the incoming energy is 23.724 keV with a resolution of 1.35 meV. The (13,13,13) also exists, with an energy of 25.701 keV, but this causes an extreme loss in flux. To give perspective to what this difference means for phonon measurements, IXS measurements for the type-I clathrate Ba_8Si_{46} have been made using the (12,12,12) reflection in Pailhès *et al.* [26], in which the co-authors used the high resolution to show the changes in the acoustic phonon dynamical structure factor with $\mathbf{q}$. On the other hand, only the (9,9,9) reflection was needed in order to extract intrinsic phonon linewidths in the high-entropy alloy FeCoCrMnNi in Turner *et al.* [106], proving that the choice of monochromator reflection remains not only a decision between flux and resolution, but also a sample-based decision, i.e. taking into account sample mosaicity, expected linewidths for a given system, etc.

We can use this sensitivity of the monochromator reflection to Bragg's law to our advantage in order to produce an energy scan at fixed-$\mathbf{Q}$. This is made possible because the silicon monochromator and the analyzers are all kept at a given initial temperature, T_0, which in the case of ID28 is 22.135 °C. The elastic line defines temperature T_0, where the temperature of both the Si monochromator and the analyzers are equal. These temperature-controlled environments can then be heated or cooled resistively or with water to adjust the environments of the monochromator and analyzers on the mK range. This temperature is related to the lattice spacing of the Si monochromator, which, in turn, can be related to energy in order to create an energy scan.

In more detail, by changing the temperature of the silicon monochromator, this crystal slightly expands or contracts. This thermal expansion changes the Bragg lattice spacing, d_{HKL}, in turn changing the λ that is reflected according to Bragg's law. The analyzers, however, stay at the constant temperature T_0 in order to compare the change with the monochromator and make the temperature, and therefore energy, scan through the range defined by thermal expansion. For more details on thermal expansion, please see Section 3.1.10.

After $\mathbf{k}_i$ is chosen at the monochromator, the beam is reflected off of a mirror intended to focus the beam onto the sample. Finally, just before and after the beam impinges on the sample, vertical and horizontal slits limit the amount of the original full beam that is allowed through in order to focus the beam to the size of the sample. We will circle back to the importance of the slits later in this section in order to discuss their influence on the horizontal and vertical ΔQ

resolution. After the slits, the sample is placed in the direct path of the beam, and is aligned so that the scattering will highlight phonons in the chosen scattering plane.

After impinging on the sample, and again following the schematic in Fig. 3.22, the analyzers are set at an angle of 2θ in relation to the incoming beam, and capture solid angle $d\Omega$ of scattering. Each analyzer is an Si111 crystal, similar to the ones designed to be monochromators, however each analyzer is usually made up of several thousand co-aligned crystals. The analyzers have a spherical geometry in order to collect a larger solid angle of scattered x-rays and focus them on the detector. Therefore, rather than stressing one single crystal into a spherical shape and possibly losing energy resolution in the process, it is much better to glue mm-sized single crystals into that spherical shape [256].

Specifically, ID28 supports nine analyzers which are mounted 7 m away from the sample. This 7 m distance refers to the Rowland circle geometry needed to match the angular acceptance of the spherical analyzers. The analyzer crystals must then all be placed on this arc to follow the path of the perimeter of the circle. This is the way to maximize the intensity and resolution that each analyzer is capable of receiving [212].

The analyzers are physically mounted into two rows: a front row with analyzers [6 7 8 9] and a back row with analyzers [1 2 3 4 5], making the full order of the analyzers [1 6 2 7 3 8 4 9 5]. They are separated from each other by a fixed 2θ angular distance of 1.54°. The same backscattering technique is used with the analyzers as well, in order to retain the resolution that was obtained before scattering.

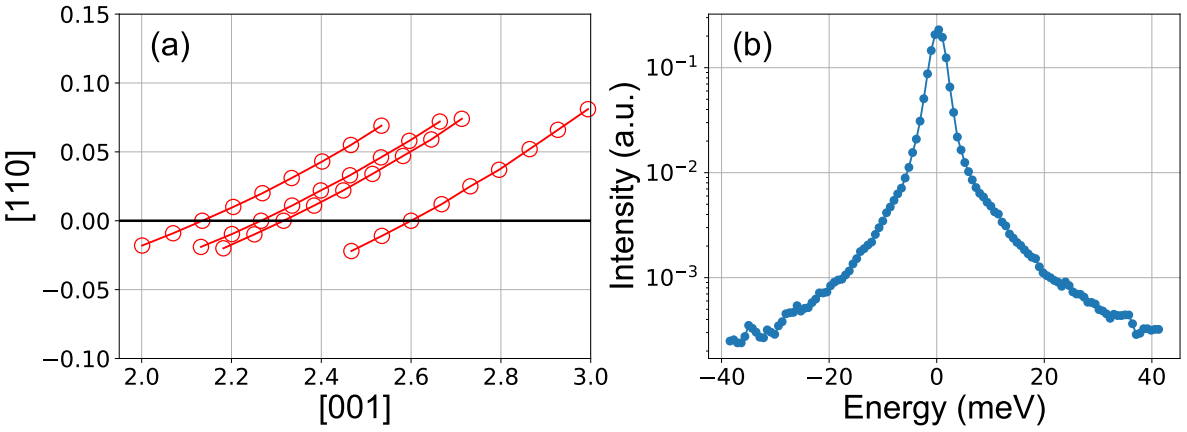

Figure 3.23: Visual Representation of Analyzers in the Scattering Plane and Analyzer Resolution. *(a) The nine ID28 analyzers as they are positioned in the scattering plane for the ID28 experiment for the high-entropy alloy FeCoCrMnNi from Turner et al. [106] are plotted to simulate the four positions that were measured for the longitudinal dispersion near the Bragg peak (002). Each line represents one setting with the spectrometer, and each analyzer (open red circles) measures an individual point in* **Q** *for that given setting. The visible arc shows the perimeter of the Rowland circle, since each analyzer sits on this circle, and from bottom to top the analyzer order is [1 6 2 7 3 8 4 9 5]. (b) An example of the resolution of analyzer 2 using the (9,9,9) Si111 monochromator configuration is shown in log scale. Resolution is measured using the same experimental conditions on a plexiglass sample that has been cooled down to 10 K.*

Again taking the example of the ID28 experiment for the high-entropy alloy FeCoCrMnNi from Turner *et al.* [106], Fig. 3.23(a) is a graph of the nine analyzers as viewed from within the given scattering plane [001][110]. The red circles represent the nine analyzers, and, from bottom to top along the y-axis, their order is [1 6 2 7 3 8 4 9 5]. In addition, the gradual arc that the analyzers follow marks the perimeter of the Rowland circle. Each line, from analyzer 1 to analyzer 5, provides the positions of the analyzers for a given setting of the spectrometer. In

this case, four positions were measured for this particular dispersion at 300 K in which analyzer 2 was placed "online," or at the pure longitudinal position.

It is important to note that the configuration of ID28 is more optimized for measuring longitudinal phonons than transverse phonons. This is because the analyzers are mounted in an arc such that **Q** is close to parallel with **G**, which denotes the selection of longitudinal phonons (see eq. 3.21). This can be seen visually in Fig. 3.23(a). It is also possible to measure transverse phonons using this ID28. However, only one analyzer at a time can be put into the right trajectory, meaning that all eight other analyzers would have a mix of longitudinal and transverse polarizations. Fig. 3.23(b) will be addressed in the next subsection.

Finally, continuing on to the last stage of the ID28 schematic in Fig. 3.22, the detection system for ID28 is in the form of Si diode detectors each containing a reverse-biased diode and Si sensor [256]. The Si sensors count a scattered photon when a certain threshold value is reached, and tuning the threshold value allows for the detector to act as a high-pass filter to keep out unwanted lower-energy background scattering [255].

3.2.2 Resolution of IXS Beamlines

Rather than using a neutron probe which has an incoming energy of roughly the same order of magnitude as the phonon excitation/annihilation, the photon probe retains an energy of roughly ∼4-5 orders of magnitude larger than the phonon interaction energy, regardless of **Q** [252]. This means that, for IXS spectrometers, the Q and E resolution when measuring a phonon has the shape of a thin vertical rod as opposed to the inclined ellipsoid shape of TAS spectrometers, because Q and E resolutions are decoupled [26].

The horizontal and vertical Q resolutions, ΔQ_H and ΔQ_V, are defined by the horizontal and vertical apertures of the detector slits, the beam divergence, and the wavelength spread. Due to the extremely high resolution, the latter can be neglected. The ΔQ_H and ΔQ_V are therefore dependent upon the incoming beam wavelength, λ, which can be calculated from the incoming energy defined at the monochromator, the radius of the Rowland circle, R, and the horizontal and vertical slit openings, H^{gap} and V^{gap}, respectively [206].

$$\Delta Q_H^{\text{Long,Tr}} = \frac{2\pi}{\lambda}\frac{H^{\text{gap}}}{R}\cos(\theta), \quad \Delta Q_V = \frac{2\pi}{\lambda}\frac{V^{\text{gap}}}{R} \tag{3.62}$$

The horizontal resolution ΔQ_H can be calculated for longitudinal and transverse polarizations for which $\theta = 0$ and $\theta =$ the angle described in Fig. 3.22 respectively, and these are usually denoted as ΔQ_H^{Long} and ΔQ_H^{Tr}. Continuing with the example of the ID28 experiment for the high-entropy alloy FeCoCrMnNi with an incoming wavelength of 0.697 Å, $H^{\text{gap}} = 20$ mm and $V^{\text{gap}} = 55$ mm, leading to $\Delta Q_H^{\text{Long}} = 0.0258$ Å^{-1} for a longitudinal phonon polarized along [001], and $\Delta Q_V = 0.0708$ Å^{-1}.

The energy resolution is defined by two components: the spectrometer energy resolution and the energy resolution that results from the slits. The spectrometer energy resolution component is defined by the energy resolution of each of the nine analyzers. This is quantified by measuring the elastic scattering of a plexiglass sample at 10 K for the given experimental conditions at **q** values close to the maximum of the elastic structure factor(s). An example of this is given in Fig. 3.23(b) for analyzer 2 and the (9,9,9) Si111 monochromator condition. This is then convoluted with the energy scans made for this particular analyzer, accounting for the instrumental resolution.

When measuring a dispersive excitation, a supplementary contribution must be added which is related to the finite Q resolution. In the case of a longitudinal excitation, the contribution is evaluated as the following.

$$\Delta E = v_g \Delta Q_H \tag{3.63}$$

This is particularly relevant at low q-points in the dispersion, as the intrinsic linewidth is usually small and the group velocity, v_g, is usually strong. As a first approximation, the total energy resolution can be estimated as the squared sum of each of these two contributions.

In summary, it has been shown that INS and IXS techniques are both extremely relevant and efficient methods for measuring phonons. Playing to the strengths of both IXS and INS allows for precise measurements of longitudinal and transverse acoustic phonons, respectively, and a combination of the two techniques, such as what was done in my submitted work Turner *et al.* [106] for the high-entropy alloy FeCoCrMnNi, leads to a more complete lattice dynamics understanding that can include the GVDOS, elastic scattering maps, and more. This particular article is also a nice example of the weight of coherent and incoherent scattering in each technique, and how the information from one technique can help explain the results of the other. With INS and IXS techniques, we test the limits of resolution for experimental phonon measurements, and help bring the scientific community closer to quantifying the transport of such quasiparticles in materials.

CHAPTER 4

Summary of Articles

I will now present the major contributions of my thesis work in the form of three articles. At the time of writing, the article on the type-I clathrate $Ba_{7.81}Ge_{40.67}Au_{5.33}$ has been published, Turner *et al.* [57], and the article on the high-entropy alloy FeCoCrMnNi has been submitted to an international peer-reviewed journal for review. The third article on Yttria-Stabilized Zirconia is presented as an unpublished manuscript. All three articles have been integrated into this chapter for the convenience of the reader.

The same general theme of understanding the effects of complexity and disorder on thermal conductivity through the study of phonons carries through in all of these articles: In each article, I address the types of complexity and disorder found in each system in order to both reference what is already understood by the community and give context to my new contributions. Each material is at a different stage of interpretation within the research community, but the overall goal remains the same, which is working towards a unified understanding of heat transport in complex and disordered crystalline systems through case studies of different types of complexity and disorder.

These articles represent only a selection of the work I completed during my Ph.D program. Several of my projects, specifically the type-I clathrate and high-entropy alloy projects, are part of on-going works to which I still have a major contribution. Also note that at the time of writing, my research and results on La-doped Barium Fluoride have not been drafted into an article, as we would like to further clarify and complement our results with theoretical models.

4.1 Impact of temperature and mode polarization on the acoustic phonon range in complex crystalline phases: A case study on intermetallic clathrates

Published in: Physical Review Research, January 8th, 2021 [57]
Authors: *Shelby R. Turner, Stéphane Pailhès, Frédéric Bourdarot, Jacques Ollivier, Stéphane Raymond, Thomas Keller, Yvan Sidis, John-Paul Castellan, Pierre-François Lory, Holger Euchner, Michael Baitinger, Yuri Grin, Helmut Schober, Marc de Boissieu, Valentina M. Giordano*

Type-I clathrates have been widely studied over recent decades not only for their potential use as thermoelectric materials, but also as a case study for interpreting different types of disorder and anharmonicity. The phonon behavior of such systems has been extensively detailed both experimentally and theoretically in an effort in particular to understand the interaction between the lowest-lying optical branches and the acoustic phonon regime [25, 26, 30, 93, 167, 196]. Within the research community, this phenomenon has been accepted as playing a major role in determining the thermal conductivity behavior in clathrates. With so much available data on Ge-based clathrates in particular, it was a natural next step to seek out the temperature and polarization of the low-lying optical branches, which was the topic of my work and the article I am presenting.

This article is proposed as a case study that validates the self-consistent phonon (SCP) method [93] for beyond simply the clathrate for which it was published, $Ba_8Ge_{30}Ga_{16}$. The anharmonicity calculated especially due to the quartic anharmonic term matches well with our experimental findings for a second Ge-based clathrate, $Ba_{7.81}Ge_{40.67}Au_{5.33}$, demonstrating the usefulness of the SCP method for complex and disordered systems that contain anharmonic features.

We also address the nature of the low-lying optical branches in $Ba_{7.81}Ge_{40.67}Au_{5.33}$, finding that the two lowest branches come from different sources of complexity. With the help of *ab initio* calculations using the meta-generalized-gradient approximation functional SCAN described in the paper, the lowest branch, E_{Ba}, is found to be associated with the motions of the guest atom at the center of the cage. The second lowest branch E_{AuBa}, however, is a result of the hybridized vibrations of the same guest atom with the Au atomic substitutions made on the Ge cages. Indeed, by attributing certain branches to their corresponding source of complexity, we come one step closer to engineering and manipulating the glasslike thermal conductivity in such systems.

This "conversation" between theoreticians and experimentalists that has been quite active in the last decade is important not only for driving novel theoretical methods based on experimental confirmations, but also for allowing us to use clathrates as case studies to target the effects of anharmonicity, atomic substitutions, and complex cage structures. The synthesis of such materials is at an advanced stage [84, 257], meaning that we should take full advantage of creating a series of such kinds of case studies, allowing us to draw broader conclusions.

Contributions of the Ph.D Candidate:

I played a central role in preparing and conducting the neutron experiments on IN5@ILL, IN12@ILL, 1T@LLB, and TRISP@FRM-II, and in the complete data analysis of said experiments. I then wrote the paper and developed the comparison to the self-consistent phonon method calculations for $Ba_8Ge_{30}Ga_{16}$ by T. Tadano and S. Tsuneyuki [93]. Finally, I participated in all of the discussions that led to the inclusion of the density functional theory *ab initio* harmonic calculations that use the meta-GGA SCAN functional, led by H. Euchner [169].

Perspectives/Further work that can be done:

Although it was not included in this article, my thesis work has also involved the measurement of intrinsic phonon linewidths of $Ba_{7.81}Ge_{40.67}Au_{5.33}$ at TRISP@FRM-II by the Neutron Resonance Spin Echo technique, which was a continuation of the linewidths measured on IN22-ZETA@ILL and published by Lory *et al.* [27]. This measurement is shown in Fig 3.16. These intrinsic phonon linewidth measurements continue to be of vital importance as they represent a necessary second checkpoint, beyond the first checkpoint of confirming the phonon energy spectrum, that we need in order to make a *full* experimental confirmation of the use of the SCP method for type-I clathrates. The linewidths calculated by T. Tadano and S. Tsuneyuki, shown in the Supplementary Material of Ref. [93], must be matched to experimental data, as we cannot rely on the correct temperature dependence of the phonon dispersions alone for confirming macroscale thermodynamic properties such as lattice thermal conductivity. Only a full investigation of the energy, temperature, and polarization dependencies of the phonon dispersions *and* phonon lifetimes will determine if the lattice thermal conductivity calculated by the SCP method can be correctly attributed to clathrates. This remains the next big challenge for experimentalists in the clathrate community.

Furthermore, the correspondingly grand challenge for theoreticians in the clathrate community is to push beyond the current computing limitations so that important features such as detailed disorder and polarization mixing, two aspects of state-of-the-art calculations that are often neglected at the moment, are incorporated into novel theoretical calculations such as the SCP method. The incorporation of disorder made a significant impact to the understanding of thermal conductivity in the quasicrystal approximant o-$Al_{13}Co_4$ [122], bringing in to question how much of the picture we are similarly missing in clathrates.

Impact of temperature and mode polarization on the acoustic phonon range in complex crystalline phases: A case study on intermetallic clathrates

S. R. Turner,[1,2,3] S. Pailhès,[3,*] F. Bourdarot,[4] J. Ollivier,[1] S. Raymond,[4] T. Keller,[5,6] Y. Sidis,[7] J.-P. Castellan,[7,8] P.-F. Lory,[1,2] H. Euchner,[9] M. Baitinger,[10] Yu. Grin,[10] H. Schober,[1] M. de Boissieu,[2] and V. M. Giordano[3]

[1]*Institut Laue-Langevin, Grenoble F-38042 Grenoble cedex, France*
[2]*Université Grenoble Alpes, CNRS, Grenoble-INP, SIMaP, F-38000 Grenoble, France*
[3]*Institute of Light and Matter, UMR5306 Université Lyon 1-CNRS, Université de Lyon F-69622 Villeurbanne cedex, France*
[4]*Université Grenoble Alpes, CEA, IRIG, MEM, MDN, F-38000 Grenoble cedex, France*
[5]*Max-Planck-Institut für Festkörperforschung, Heisenbergstr. 1, D-70569 Stuttgart, Germany*
[6]*Forschungsneutronenquelle Heinz Maier-Leibnitz, Technische Universität München, D-85748 Garching, Germany*
[7]*Université Paris-Saclay, CNRS, CEA, Laboratoire Léon Brillouin, F-91191, Gif-sur-Yvette, France*
[8]*Institut für Festkörperphysik, Karlsruher Institut für Technologie, D-76021 Karlsruhe, Germany*
[9]*Helmholtz Institute Ulm for Electrochemical Energy Storage, Helmholtzstr. 11, D-89081 Ulm, Germany*
[10]*Max-Planck-Institut für chemische Physik fester Stoffe, D-01187 Dresden, Germany*

(Received 13 July 2020; accepted 25 November 2020; published 8 January 2021)

The low and weakly temperature-varying lattice thermal conductivity, κ_L(T), in crystals with a complex unit cell such as type-I clathrates is assumed to originate from a reduced momentum and energy space available for propagative lattice vibrations, which is caused by the occurrence of low-energy optical phonon modes. In the context of *ab initio* self-consistent phonon (SCP) theory, it has been shown that the cubic and quartic anharmonic interactions result in a temperature-induced energy renormalization of these low-lying optical branches which contributes to the anomalous behavior of κ_L(T) in structurally ordered type-I clathrates [T. Tadano and S. Tsuneyuki, Phys. Rev. Lett. **120**, 105901 (2018)]. By means of inelastic neutron scattering, we provide evidence for this energy renormalization in temperature, which has been resolved for transversely and longitudinally polarized phonons in the single crystal type-I clathrate $Ba_{7.81}Ge_{40.67}Au_{5.33}$. By mapping the neutron intensity in the momentum space, we demonstrate the coherent character of the low-lying optical phonons. The overall phonon spectrum and dynamical structure factors are satisfactorily reproduced by *ab initio* harmonic calculations using density functional theory with the meta-GGA SCAN functional and a fully ordered structure. However, a polarization-dependent cutoff energy with opposing temperature shifts for longitudinal and transverse acoustic dispersions is experimentally observed which is not reproduced by the simulations. Anharmonicity affects the energies of the low-lying optical phonons in the transverse polarization, which compares quantitatively well with available results from SCP theory, whereas differences are observed for the longitudinal polarization.

DOI: 10.1103/PhysRevResearch.3.013021

I. INTRODUCTION

Tailoring the lattice thermal conductivity, κ_L, of energy-efficient semiconductors is a common materials issue in many applications such as for thermoelectric [1] and photovoltaic [2,3] conversion, phase change memories [4], and battery electrodes [5,6]. In the search for low κ_L, the main strategy is the use of "complexity" at multiple length scales, from structural complexity within the crystal unit cell, to disorder, short-range order, and nanostructuring [7–9]. Crystals with a high structural complexity and chemical bonding inhomogeneity [10], such as tetrahedrites [11] or type-I clathrates [12], often have a very low and almost temperature independent κ_L of ∼0.5–2 $Wm^{-1}K^{-1}$ in the 50–500 K range. The current understanding is that the heat conduction is mostly conveyed by well-defined acoustic phonons, which exist only in a limited range of the energy and momentum phase space, delimited by a continuum of nondispersive optical phonon bands [13–18]. The onset of this continuum at low energy, labeled E_1, defines the upper energy limit of the acoustic regime such that it has been associated with a phononic low-pass acoustic filter [15] or a modified Debye energy [16,19]. E_1 can be changed by varying the chemical composition [13] or the structural topology [20]. Using the Boltzmann transport equation for phonons, the acoustic contribution of κ_L^{ac} is given by a cumulative spectral integral [13,15,19]:

$$\kappa_L^{ac}(T) = \sum_{\nu} \int_0^{E_1^{\nu}(T)} \kappa_L^{ac,\nu}(\omega_{\mathbf{q}}) \rho^{\nu}(\omega_{\mathbf{q}})\, d\omega, \qquad (1)$$

*To whom correspondence should be addressed: stephane.pailhes@univ-lyon1.fr

where $\kappa_L^{ac,\nu}(\omega)$ is the mode thermal conductivity, $\rho^{\nu}(\omega)$ is the density of states per mode (DOS), ν is the longitudinal/transverse polarization index and $\omega_{\mathbf{q}}$ stands for the phonon relation dispersions. In addition, any variation in E_1 changes the whole phonon-phonon scattering phase space, thus impacting the acoustic phonon lifetimes entering into $\kappa_L^{\nu}(\omega)$ [17,21]. Explaining the combined relationship between the complex crystal structure and related defects, the acoustic phonon properties, and the nature of E_1, remains a fundamental challenge.

Type-I clathrates contain 46 framework atoms of mostly group 14 elements which arrange in a 3D covalent host network of face-sharing polyhedral cages that encapsulate alkali or alkali earth guest cations [12]. The structure is usually described using the cubic space group $Pm\bar{3}n$ (group 223) with a lattice parameter of about 1 nm. The cutoff energy E_1 is defined as the center of a distribution of optical phonon modes related to the dynamics of guest atoms located at the *6d*-Wyckoff sites in tetrakaidecahedral ($5^{12}6^2$) host cages. These modes lead to well-defined peaks in the phonon DOS [15,17,18,21] which results in a large deviation from the Debye-like T^3 temperature dependence of the lattice specific heat (C_p) at low temperature [25,26]. In literature, the temperature at the maximum of the T^3-normalized heat capacity is commonly referred to as an Einstein temperature and corresponds well to E_1 in the phonon spectrum which we recall as the upper limit of the integral in Eq. (1). Recently, a phenomenological universal relation has been revealed in type-I clathrates between κ_L and the product of the average sound velocity and E_1 [19]. The nature of the low-lying guest optical phonons with energies around E_1 is particularly intriguing. These modes are characterized by a very low phonon participation ratio ($\lesssim 0.1$), which is interpreted either as a signature of localization [27,28] or an effect of mode confinement [13,14,17]. In this latter case, the phonon is viewed as a Bloch state confined to a relatively small atomic pattern, the Ba(6*d*) atoms in this case, within the large complex unit cell whose periodic repetitions result in a special character. Moreover, the flatness of their dispersion and the concomitant high DOS provides a large momentum- and energy-conserving phase space for three-phonon scattering processes involving the acoustic modes [17,21].

The $Ba_{7.81}Ge_{40.67}Au_{5.33}$ structure [29–31], which will be dealt with in this paper, is shown in Fig. 1(a). Besides the structural complexity, the dative Au-Ba bonding of the Au-substitution in $Ba_{7.81}Ge_{40.67}Au_{5.33}$ results in an off-centering of Ba atoms in the tetrakaidecahedral cages [13,32,33]. No correlation among the off-centering sites has been observed experimentally, indicating that they can be viewed as point defects. In the type-I structure $Ba_8Ge_{40}Au_6$, molecular dynamics simulations performed at 300 K on a $2 \times 2 \times 2$ supercell with independent random substitutions of Au atoms found no evidence for a correlated Au/Ge defect structure, thus no ordering among the off-centered Ba positions (see the Supplementary Material in Ref. [13]).

All *ab initio* phonon and κ_L calculations reported for type-I clathrates have been carried out on the fully ordered model structure, with centered Ba atoms and full site occupation of all sites. The experimental phonon spectrum in type-I clathrates is qualitatively reproduced quite well by harmonic

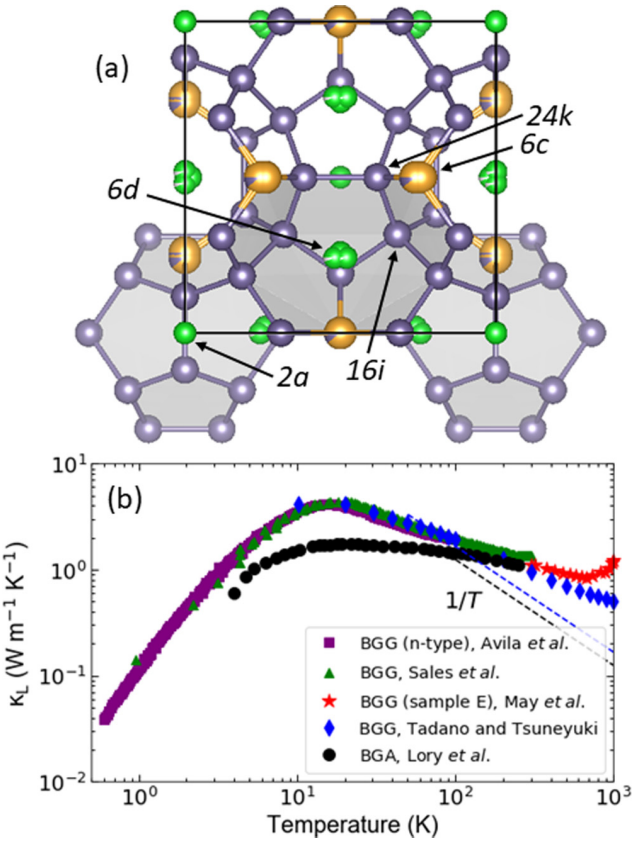

FIG. 1. (a) Crystallographic structure of the type-I clathrate $Ba_{7.81}Ge_{40.67}Au_{5.33}$ (BGA) The cubic unit cell (space group $Pm\bar{3}n$) contains two tetrakaidecahedral ($5^{12}6^2$) and five dodecahedral (5^{12}) host cages formed by Ge atoms (light gray) with guest Ba (green) atoms encapsulated inside. One to three Au atoms (gold) substitute Ge atoms at the Wyckoff site *6c*, which results in a slight distortion of the tetrakaidecahedron and an off-centering of the Ba atoms inside [13]. (b) The lattice thermal conductivity, κ_L, for BGA (black circles) [13] is compared to different experimental measurements of κ_L for $Ba_8Ge_{30}Ga_{16}$ (BGG), including those by Avila *et al.* [22], Sales *et al.* [23], May *et al.* [24], and the theoretical calculations of Tadano and Tsuneyuki [43]. Black and blue dashed lines show the deviation of κ_L from $1/T$ for both BGA and BGG, respectively, at higher temperatures.

ab initio calculations [13–15]. Quantitatively, *ab initio* lattice dynamics studies of Ge clathrates showed decreased acoustic and low-lying optical mode energies in comparison to the experimental data (up to 40%), a discrepancy which has been recently overcome by the use of the meta-generalized-gradient approximation (meta-GGA) functional SCAN (strongly constrained and appropriately normed) for the exchange and correlation energy [34]. *Ab initio* simulations in perturbation theory, when limited to three-phonon processes, predicts a $1/T$ temperature dependence for acoustic phonon lifetimes and $\kappa_L(T)$, which drastically fails to reproduce the experimental $\sim T^{-0.25}$ in $Ba_{7.81}Ge_{40.67}Au_{5.33}$ [13] [see Fig. 1(b)], and also in other complex crystals like the $\sim T^{-0.1}$ dependence in the quasicrystal approximant o-$Al_{13}Co_4$ [35]. For the latter case, molecular dynamics simulations on an ordered model structure yield a $T^{-0.5}$ dependence, whereas the inclusion

of random disorder results in much closer agreement with experiment. This points not only to the importance of disorder, but also to either higher order anharmonicity or the effect of phonon energy renormalization including the polarization mixing of phonon eigenvectors, which are included in the molecular dynamics simulations but not in most *ab initio* based calculations.

A significant improvement to the *ab initio* approach has been achieved by self-consistent phonon (SCP) theory, which nonperturbatively treats the effects of anharmonicity [36–42]. An SCP study on an ordered model of $Ba_8Ge_{30}Ga_{16}$ reveals that the quartic anharmonicity leads to a softening of $E_1(T)$ upon cooling, surpassing the usual hardening effect due to thermal expansion. Although this softening accounts for less than 10% of $E_1(T)$ in the 0–300 K range, i.e., about 1 meV $\sim$ 12 K, it leads to a closer $\kappa_L(T)$ matching [43]. This high sensitivity of $\kappa_L(T)$ to $E_1(T)$ results in the peculiar vibrational nature of the optical modes at $E_1(T)$. It should be mentioned here that the $Ba_8Ge_{30}Ga_{16}$ SCP calculations assume that phonon polarization vectors are not affected by anharmonicity [43], which is a common approximation in complex crystals in order to limit the computational cost [38,41].

In this paper, we provide substantial experimental evidence of the importance of the anharmonic processes (resulting from cubic and quartic terms) for the type-I clathrate $Ba_{7.81}Ge_{40.67}Au_{5.33}$ by investigating the propagation direction, and the polarization and temperature dependencies of the cutoff energy $E_1^{\nu}(T)$ by inelastic neutron scattering on a high-quality single crystal. By probing the mode symmetry in momentum space at different energies, we show that the distribution of the neutron intensity related to the low-lying optical vibrations is structured in the momentum space within a Brillouin zone, and from one Brillouin zone to another. This distribution of intensity in momentum as well as the overall phonon energies are satisfactorily reproduced by *ab initio* harmonic calculations using the (meta-GGA) functional SCAN done on a fully ordered structure. We confirm the agreement between the experimental results and simulations for phonon dispersions obtained along different high-symmetry directions and with both transverse and longitudinal polarizations.

However, some differences remain, especially in the region of the phase space where acoustic and optical phonons are hybridized. Experimentally, a polarization dependence of the acoustic-optical phonon coupling is observed such that the origin and the value of E_1 in the longitudinal and transverse acoustic (LA, TA) polarizations are different and exhibit opposite temperature dependencies, the effect of optical mode hardening with increasing temperature being found only for the lowest mode in the transverse polarization. This difference, which is not observed in our *ab initio* harmonic simulations using a fully ordered model, indicates either an effect of the particular defect cage structure caused by the Au substitutions or a more subtle anharmonic effect involving phonon polarization.

Furthermore, and in light of the recent SCP method calculations on $Ba_8Ge_{30}Ga_{16}$ [43], this experimental case allows us to quantitatively compare clathrate anharmonicity as found by both experimental and theoretical approaches. The rate of change in energy of $E_1(T)$ in $Ba_{7.81}Ge_{40.67}Au_{5.33}$ was properly measured in the temperature range 100–550 K. After the subtraction of the thermal expansion contribution from this rate of change, the anharmonic contribution in the thermal shift of $E_1(T)$ has been experimentally determined and directly compared to that of the quartic and cubic terms of the SCP method calculations for $Ba_8Ge_{30}Ga_{16}$, providing experimental validation of the SCP method calculations for determining anharmonic effects in clathrates.

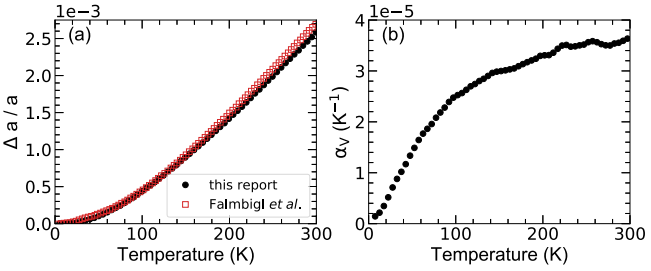

FIG. 2. (a) The rate of thermal expansion, $\Delta a/a$, for $Ba_{7.81}Ge_{40.67}Au_{5.33}$ has been measured with Larmor diffraction on TRISP@FRM-II (black circles) and compared to that of Falmbigl *et al.* (empty red squares) [50]. The numerical derivative of $\Delta a/a$ is the linear thermal expansion coefficient, α_L. The volumetric thermal expansion coefficient, $\alpha_V = 3\alpha_L$, is plotted in (b).

II. METHODS

Inelastic neutron scattering (INS) measurements were performed on the same high-quality single crystal of the type-I clathrate $Ba_{7.81}Ge_{40.67}Au_{5.33}$ as in our previous work [13], whose temperature dependence of the lattice thermal conductivity, $\kappa_L(T)$, is shown in Fig. 1(b). The structural study, the chemical disorder caused by Au substitutions, and the thermal characterizations were reported in Ref. [13]. In addition, we have precisely measured its lattice thermal expansion, as depicted in Fig. 2, by means of neutron Larmor diffraction on the triple-axis spectrometer TRISP at the Heinz Maier-Leibnitz Zentrum (FRM-II, Germany) (see Appendix A 3). The INS intensity was recorded over a wide range of the momentum and energy phase space at 150, 300, and 530 K on the cold-neutron time-of-flight (TOF) spectrometer IN5 at the Institut Laue-Langevin (ILL, France). Details on the experimental settings, on the TOF instrumental resolution in momentum and in energy, and on the integration parameters used to produce the experimental phonon dispersions from fits of 1D-energy cuts at constant momentum (raw data and fits are shown in Appendix F), the high resolution Generalized Vibrational Density of States (GVDOS) in Fig. 3, and the mappings shown in Fig. 5, are given in Appendix A 1. The temperature dependence of the low-lying optical bands was further investigated on the cold-neutron triple-axis spectrometer IN12 at the ILL (see Appendix A 2). Preliminary experiments were also conducted on the triple-axis spectrometer 1T at the Laboratoire Léon Brillouin (LLB, France). In all INS experiments, the single crystal was mounted in a cryofurnace and aligned in the ([110];[001]) scattering plane such that wave vectors of the form $\mathbf{Q} = \frac{2\pi}{a}(\zeta, \zeta, \xi)$, with $a = 10.7987(1)$ [13], were accessible.

Of particular importance in this work is the polarization term, which appears in the coherent one-phonon scattering

function, $S(\mathbf{Q}, \omega)$, which in turn is proportional to the double differential inelastic neutron cross section (see Appendix A). In the case of a coherent, one-phonon scattering process by a phonon of branch i, with energy $\omega_{q,i}$ and polarization vector $\xi^i_{\omega_{q,i}}$, the neutron scattering function is written as [44]

$$S_{ph}(\mathbf{Q}, \omega) = n(\omega)\frac{\left|F_D^i(\mathbf{Q})\right|^2}{\omega_{q,i}}\delta(\omega - \omega_{q,i})\delta(\mathbf{Q} - \mathbf{q} - \mathbf{G}), \quad (2)$$

where $n(\omega) = \frac{1}{1-\exp(-\hbar\omega/k_BT)}$ and comes from the detailed balance factor, and $\mathbf{Q} = \mathbf{q} + \mathbf{G}$ is the scattering vector given by the nearest reciprocal lattice vector $\mathbf{G}$ and the phonon wave vector $\mathbf{q}$. Usually, phonons are measured in a Brillouin zone far from the Γ-point (around Bragg peaks with high Miller indices) such that $|\mathbf{G}| \gg |\mathbf{q}|$ and $\mathbf{Q} \sim \mathbf{G}$. In this work, we mainly discuss measurements performed around the Bragg peaks (006) and (222) whose moduli are much higher than π/a. The function $F_D^i(\mathbf{Q})$ in Eq. (2) is called the dynamical structure factor (DSF) and is defined as [44]

$$F_D^i(\mathbf{Q}) = \sum_j e^{-W_j(\mathbf{Q})}\frac{b_j}{\sqrt{M_j}}e^{i\mathbf{Q}\cdot\mathbf{r}_j}\left\{\mathbf{Q}\cdot\xi_i^j(\mathbf{Q})\right\}, \quad (3)$$

where b_j, $\mathbf{r}_j$, M_j, and $W_j(\mathbf{Q})$ are the coherent scattering length, fractional coordinates, mass, and Debye-Waller factor of the jth element, respectively. This expression closely relates to the nuclear structure factor which determines the Bragg peak intensity. It includes an additional term, the scalar product $\{\mathbf{Q}\cdot\xi_i^j(\mathbf{Q})\} \sim \{\mathbf{G}\cdot\xi_i^j(\mathbf{Q})\}$, which contains the phonon polarization and can thus be used to distinguish longitudinal and transversal phonon modes by choosing the appropriate combination of phonon polarization wave vector and reciprocal lattice vector. The polarization vectors of longitudinal and transversal phonons are parallel and perpendicular to the phonon wave vector $\mathbf{q}$, respectively.

The lattice dynamics were simulated using a fully ordered model of a type-I clathrate with the $Ba_8Ge_{40}Au_6$ composition in which the gold atoms occupy all the *6c* host sites. The periodic density functional theory (DFT) code VASP [45–47] was used for structure optimization as well as for the determination of the harmonic force constants. While the projector augmented wave method was applied for describing the ionic cores, the meta-GGA functional SCAN was used to account for exchange and correlation [34,48]. The SCAN functional has been recently proven to reproduce the phonon spectrum in type-I clathrates with a much higher accuracy. The unit cell was relaxed to the ground state using a k-point mesh ($5 \times 5 \times 5$) centered at the zone center (Γ) and a convergence criterion of residual forces of less than 10^{-4} eV/Å using a plane wave energy cutoff of 500 eV. The lattice parameter of the optimized structures obtained by the SCAN functional is of 10.78 Å, very close to the experimental value of 10.7987(1) Å [13]. The Hellmann-Feynman forces were then calculated after introducing symmetrically non-equivalent displacements of ± 0.03 Å in the relaxed unit cell. These forces are given as an input to the Phonopy code [49] for the calculation of the dynamical matrix.

III. THE GRÜNEISEN PARAMETER

Before discussing anharmonicity at the phononic level, we first address the Grüneisen parameter, γ, which is a material constant that gives an idea about the amount of anharmonicity that exists in a material. This macroscopic property provides context to our experimental findings in this paper.

The mode specific Grüneisen parameter, γ_i, for a phonon mode E_i at molar volume V is defined as $\gamma_i = -\frac{V}{E_i}(\frac{\partial E_i}{\partial V})_T = -(\frac{\partial \ln E_i}{\partial \ln V})_T$. As a first approximation of the experimental Grüneisen parameter, however, we assume an averaged and temperature-dependent Grüneisen parameter for all modes, which, in the quasiharmonic approximation, depends on the volumetric thermal expansion coefficient α_V, the Bulk modulus B, the molar volume V, and the specific heat at constant volume C_V:

$$\gamma = \frac{\alpha_V BV}{C_V}. \quad (4)$$

The temperature dependence of $C_V(T)$ was deduced from the measurement of $C_p(T)$ as detailed in Appendix C. As discussed in the introduction, $C_p(T)$ in type-I clathrates is dominated by the contribution of the optical phonon branches and mostly by the lowest energy guest modes at E_1 such that the γ extracted from Eq. (4) is mainly specific to the contribution of the low-lying guest modes. The change in lattice spacing with temperature in our single crystal of $Ba_{7.81}Ge_{40.67}Au_{5.33}$ was experimentally measured by neutron Larmor diffraction on the most intense Bragg peak (006), and is plotted as black circles in Fig. 2(a). The result is compared to the miniature capacitance dilatometer measurement made by Falmbigl *et al.* [50] of a type-I clathrate with a similar chemical composition. Figure 2(a) shows the consistency between these two different experimental methods. The temperature dependence of the linear thermal expansion coefficient, α_L(T), is then the numerical derivative of $\Delta a/a$, and the volumetric expansion coefficient is $\alpha_V = 3\alpha_L$ [see Fig. 2(b)].

The temperature-dependent molar volume for $Ba_{7.81}Ge_{40.67}Au_{5.33}$ has been taken from the conversion of the coefficient of lattice expansion data in Fig. 2(a) to the experimental lattice parameter, and since we find no change in sound velocity within 300 ± 150 K (see Fig. 3), a temperature-independent B is assumed. For $Ba_{7.81}Ge_{40.67}Au_{5.33}$, we find B = 65.60 GPa from our measurement of the phononic sound velocities. (More details are given in Appendix B.)

The Grüneisen parameter can then be experimentally deduced from Eq. (4). It is found to be temperature independent in the range of interest for this study, with a value of γ = 1.38. A similar method was used by Ikeda *et al.* [19] for $Ba_8Ge_{30}Ga_{16}$ in which γ_{300K} = 1.67 was observed. In literature, the Grüneisen parameter of type-I clathrates, obtained by various methods and for different chemical compositions, is typically found to be in the range of 1.2–2.0 [16,33,50–58].

IV. EXPERIMENTAL RESULTS

A. Polarization dependence of optical branches

The LA and TA phonon dispersions obtained from the experimental mappings (see Appendix F) of the phonon energy at 150, 300, and 530 K covering several Brillouin zones are shown in Figs. 3(a) and 3(b). Measurements have been performed around the most intense Bragg peak (006) in

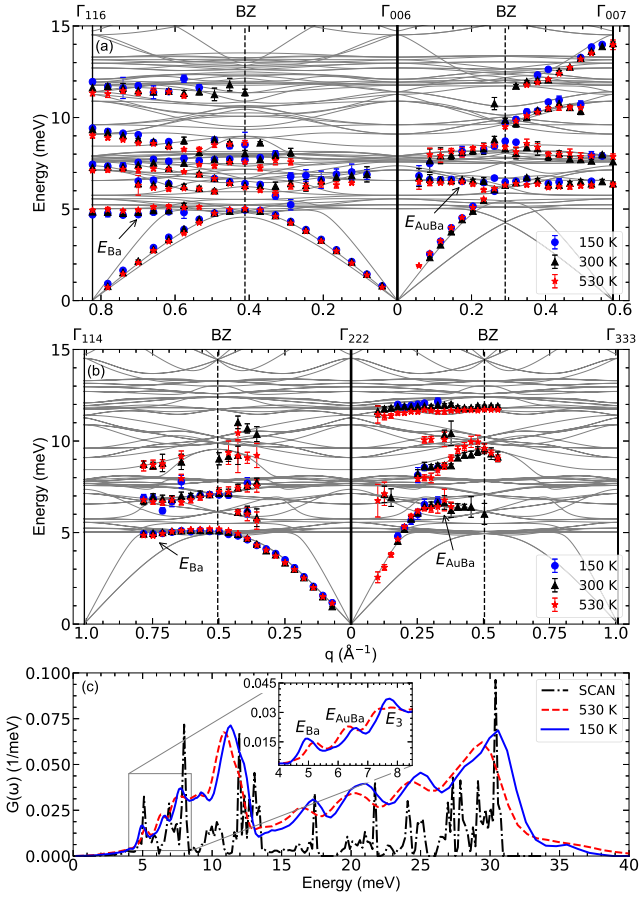

FIG. 3. (a) Transverse and longitudinal phonon dispersion curves extracted from IN5@ILL at 150 (blue circles), 300 (black triangles), and at 530 K (red stars) near the (006) Bragg peak. Gray solid lines depict the calculated dispersion curves. The wave vector q is referenced from the zone center (006) (Γ_{006}). Acoustic phonons with q increasing towards the zone center (116) (Γ_{116}) are mostly transversely polarized (left panel). Those with q increasing towards the zone center (007) (Γ_{007}) are mostly longitudinal (right panel). Also shown in gray is the simulated phonon spectrum. (b) Similar experimental phonon dispersions near the (222) Bragg peak, at the same three temperatures, and compared to simulations. Starting from the zone center (222) (Γ_{222}), the transverse (left panel) polarization can be traced until zone center (114) (Γ_{114}), while the longitudinal (right panel) polarization propagates towards the Γ_{333}. (c) Generalized vibrational density of states (GVDOS) obtained on IN5@ILL at 150 and 530 K, along with the calculated phonon DOS (intensity has been scaled down by a factor of 3.5). All simulations correspond to harmonic *ab initio* DFT calculations using the meta-GGA SCAN functional.

Fig. 3(a). For propagating wave vectors along the [001] direction, the longitudinal polarization is observed, while the transverse polarization for which the vibrational polarization is along the [001] direction is measured along the [110] direction. For Fig. 3(b), measurements were taken near the (222) Bragg peak, in which the longitudinal polarization is tracked along the [111] direction, and the transverse dispersion has a vibrational polarization along [111] and propagates along $[\bar{1}\bar{1}2]$.

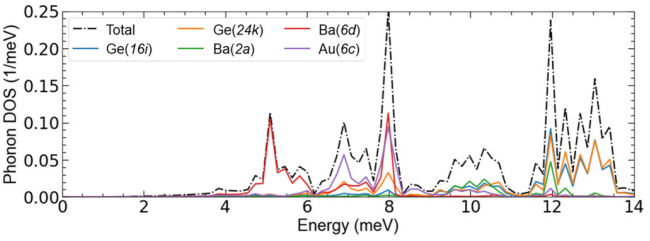

FIG. 4. Calculated partial phonon density of states (pDOS), using harmonic *ab initio* DFT calculations and the meta-GGA SCAN functional. The site-weighted partial pDOS lines of Wyckoff positions Ge(16*i*), Ge(24*k*), Ba(2*a*), Ba(6*d*), and Au(6*c*) show their respective contributions in energy as compared to the total pDOS.

The experimental phonon spectra are compared to the simulated phonon spectrum obtained by DFT calculations using the SCAN functional (see Methods section), as shown in Figs. 3(a) and 3(b) (gray lines are the simulated phonon dispersions). A good agreement is observed on the whole spectrum especially on the transverse and longitudinal acoustic branches which are well reproduced. That corresponds to a significant improvement in the theoretical approach in comparison to the simulations performed with the PBE functional for which acoustic phonon energies are strongly underestimated [13,15].

For all temperatures and both polarizations, the experimental phonon spectra exhibit an acoustic regime at low energy, which contains well-defined phonon peaks whose dispersions are delimited by low-lying optical bands. The energy

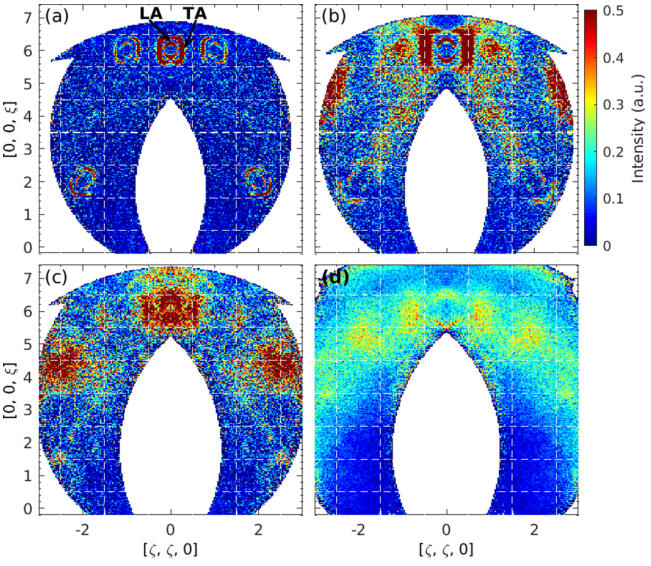

FIG. 5. Two-dimensional inelastic neutron scattering intensity distribution at fixed energy transfer in the momentum plane ([110]; [001]) for $Ba_{7.81}Ge_{40.67}Au_{5.33}$ at 300 K, recorded on IN5@ILL. The first three energy integrations (a)–(c) were taken at 3.5 ± 0.15, 4.8 ± 0.15, and 6.5 ± 0.15 meV, respectively. (d) represents a larger integration interval of 9.5 ± 2.5 meV. The color bar reflects a normalized intensity scale. Dashed white grids show the borders of the Brillouin zones.

at which the acoustic dispersions are interrupted is higher for the longitudinal polarization, 6.5 meV than for the transverse polarization, 4.8 meV. As emphasized by the use of the two sets of experimental data in Figs. 3(a) and 3(b), this is consistent across [001] and [111] longitudinal polarizations, and for [110] and [111] transverse polarizations. The cutoff effect of the acoustic branches by the low-lying optical branches is also seen in the simulated phonon spectrum. The simulation perfectly reproduces the TA dispersion, while for the longitudinal polarization, the computed acoustic branch is interrupted at 4.8 meV and not at 6.5 meV as observed experimentally.

Referring again to the $Ba_{7.81}Ge_{40.67}Au_{5.33}$ crystal structure in Fig. 1(a), the motions of Ba(6*d*) atoms in the soft plane of the large tetrakaidecahedral cages dominate the optical band centered at 4.8 meV (E_{Ba}) [59], and hybridized vibrations of Au(6*c*)-Ba(6*d*) atoms are thought to dominate the optical band centered at 6.5 meV (E_{AuBa}) [13,29]. This mode assignment is confirmed by the plot of the partial phonon density of states (pDOS) shown in Fig. 4. Indeed, only the Ba(6*d*) atoms contribute in the energy range around 4.8 meV while the optical band centered at 6.5 meV contains contributions of the Ba(6*d*) and the framework Au(6*c*) atoms. For energies higher than $E_{Ba,AuBa}$ up to a cutoff energy of around 35 meV, the phonon spectrum consists of several broad distributions of optical bands, such as those in the range E_{Ba}–15 meV in Fig. 3(a).

Figures 5(a)–5(c) report the two-dimensional mappings in the momentum plane ([110]; [001]) of the neutron intensity recorded at room temperature and at fixed energy of 3.5, 4.8, and 6.5 meV, respectively. These experimental mappings can be compared to DFT computed mappings of $S(\mathbf{Q}, \omega)$ in an equivalent range of momentum, shown in Figs. 6(a)–6(c). The section in momentum at 3.5 meV, in Fig. 5(a), is a cut through the acoustic branches. The Brillouin zones in which the zone center corresponds to an intense Bragg peak result in a strong dynamical structure factor of the acoustic modes and therefore contain two well-defined rings of high intensity. The intensity along the rings is not homogeneously distributed in momentum space as it is weighted by the polarization factor [described by Eq. (3)] such that when the phonon wave vector ($\mathbf{q}$) is aligned/perpendicular to the Bragg wave vector ($\mathbf{G}$), the longitudinal/transverse polarization is selected. Thus, looking at the two rings surrounding the zone center $\mathbf{G}_{006}$, the outer ring which is intense along the [110] direction (perpendicular to $\mathbf{G}_{006}$) corresponds to TA phonons, and, reciprocally, the inner ring with maximum intensity along [001] corresponds to LA phonons. The intensity maxima along the rings follow the polarization factor and are rotated by 45° between those surrounding the zone centers Γ_{006} and Γ_{222}. This intensity distribution is reproduced on the simulated map, shown in Fig. 6(a), and carries the signature of the coherent character of the acoustic modes.

The section in momentum at a fixed energy equal to E_{Ba}, shown in Fig. 5(b), reveals the intensity distribution of the lowest optical band which cuts the TA dispersion. It also contains the contributions of the LA modes which form the inner rings closest to the zone centers. The intensity of the optical band at E_{Ba} shows a distinct $\mathbf{Q}$-dependence in momentum space with intensity maxima at the zone boundaries that can be associated with the Bragg intensity at a zone center,

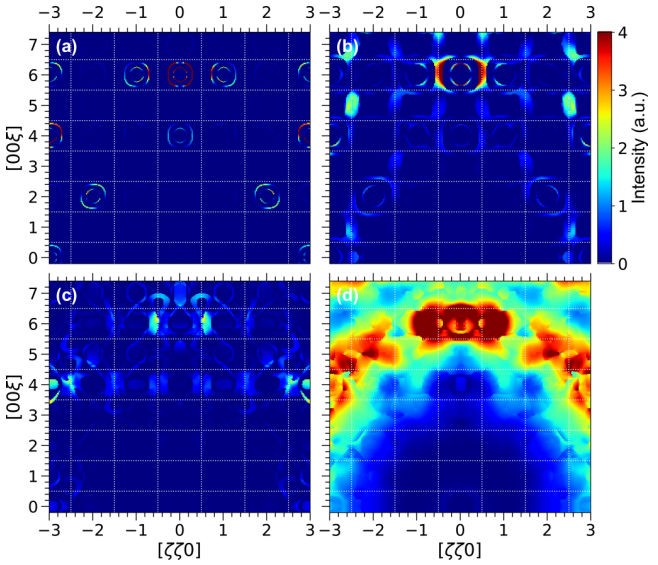

FIG. 6. Simulated two-dimensional neutron scattering function, S($\mathbf{Q}$,ω), at fixed energy transfer in the momentum plane ([110]; [001]) for an ideal ordered model of a type-I clathrate with the composition $Ba_8Ge_{40}Au_6$. The first three energy integrations (a)–(c) were taken at 3.5 ± 0.15, 4.8 ± 0.15, and 6.5 ± 0.15 meV, respectively. (d) represents a larger integration interval of 9.5 ± 2.5 meV. The intensity in each map has been normalized to the same intensity scale, which is reflected in the color bar. Dashed white grids show the borders of the Brillouin zones.

for instance, (1.5 1.5 6) and (1.5 1.5 3.5) with Bragg peaks (006) and (222), respectively. The intensities along these maxima follow the transverse polarization and are turned by 45° between the zone centers Γ_{006} and Γ_{222} as for the acoustic modes. This intensity distribution of the outer ring related to the optical mode at E_{Ba} is also reproduced in the simulated map shown in Fig. 6(b). It confirms the coherent nature of the optical modes contained in this band which thus cannot be associated with vibrations of localized and independent Einstein oscillators, in agreement with previous phonon studies on clathrates [14] and other cage compounds [60]. Indeed, an isolated Einstein oscillator-type behavior would result in a Q^2-dependent intensity distribution. Note that there are also intensity maxima at zone centers such as (116) and (114), which is not seen in the simulated map shown in Fig. 6(b) simply because the intensity is in the low range of the color scale.

Moving again in energy to E_{AuBa} in Fig. 5(c), one sees the maxima of intensity related to the distribution of the optical band which cuts off the LA dispersion, in addition to the ones related to E_{Ba} which are pinned at the zone boundary. The intensity distribution to E_{AuBa} around Γ_{006} is more spread in momentum space than that at E_{Ba} which is also observed in the simulated map shown in Fig. 6(c). Looking carefully at the experimental map, one can distinguish minima along the [110] direction following the longitudinal polarization factor which are less obvious to see in the simulated map. The optical vibrations at E_{AuBa} are much less coherent than at E_{Ba} and exhibit the trend of being polarized longitudinally.

TABLE I. Isobaric, isochoric, and thermal expansion (TE) rates of change in energy with increasing temperature of the lowest-lying optical bands in $Ba_{7.81}Ge_{40.67}Au_{5.33}$ (BGA) and $Ba_8Ge_{30}Ga_{16}$ (BGG), extracted from the inelastic neutron scattering (INS) data shown in Figs. 7(a)–7(d), the GVDOS shown in Fig. 3, and the INS measurements of Ref. [59]. $E_{\mathrm{Ba,AuBa}}$ and $E_{3,4}$ correspond to the peaks labeled in Fig. 7(e), and thermal expansion to the fit TE labeled in Fig. 7(f). Theoretical values from the Self-Consistent Phonon method, which includes the cubic and quartic contributions (SCPB), have been reported [43] and SCPB-based thermal expansion is also given, all in 1×10^{-4} meV/K.

	BGA		BGG	
	INS	GVDOS	INS	SCPB
$(\partial E_{\mathrm{Ba}}/\partial T)_P$	7.1	5.4	9.3	11.2
$(\partial E_{\mathrm{AuBa}}/\partial T)_P$	–	−6.3	–	–
$(\partial E_3/\partial T)_P$	−7.4	−7.9	–	–
$(\partial E_4/\partial T)_P$	−7.4	–	–	–
Thermal expansion	−2.6	−2.7	−3.8	−3.6
$(\partial E_{\mathrm{Ba}}/\partial T)_V$	9.7	8.1	13.1	14.8

Thus, the energy dispersions and momentum distributions shown in Figs. 3 and 5 demonstrate that the low-lying optical bands interact with the acoustic dispersion that is present in a given polarization. It appears that the TA dispersion couples largely with the 4.8 meV band (E_{Ba}), while the LA dispersion couples mainly with the 6.5 meV band (E_{AuBa}). Last, Fig. 5(d) is a experimental data integration in the interval 7–12 meV, which represents host optical band energies. A similar momentum map obtained by integrating the simulated data in the same interval is shown in Fig. 6(d). The intensity distribution of these modes on the experimental and simulated maps reveal the coherence of these host bands, which display mostly longitudinally polarized intensity.

B. Temperature dependence of optical branches

Focusing now on the temperature dependence, and in contrast to the acoustic phonon energies for which no change of their energies in temperature is observed, we clearly see sizable shifts with temperature of the optical band energies in Figs. 3(a) and 3(b). For the transverse polarization, the energy E_{Ba} increases upon heating, while the energies of the other optical bands, including E_{AuBa}, follow the opposite trend. As a consequence, the temperature-dependent changes of the energy range for acoustic phonons is opposite for TA and LA phonons as it is directly related to the temperature dependence of the optical cutoff bands $E_{\mathrm{Ba,AuBa}}$ [see Eq. (1)]. This is better seen by comparing the GVDOS between 150 K and 530 K, depicted in Fig. 3(c). In the low-energy range below 10 meV, the GVDOS exhibits mostly three peaks at energies E_{Ba}, E_{AuBa}, and E_3. Only E_{Ba} follows a hardening shift upon heating, which has been similarly reported in type-I clathrates of different chemical compositions [59,61–64]. The overall structure of the measured GVDOS is reproduced well by the phonon DOS obtained from *ab initio* simulations using the meta-GGA SCAN functional, as shown in Fig. 3(c).

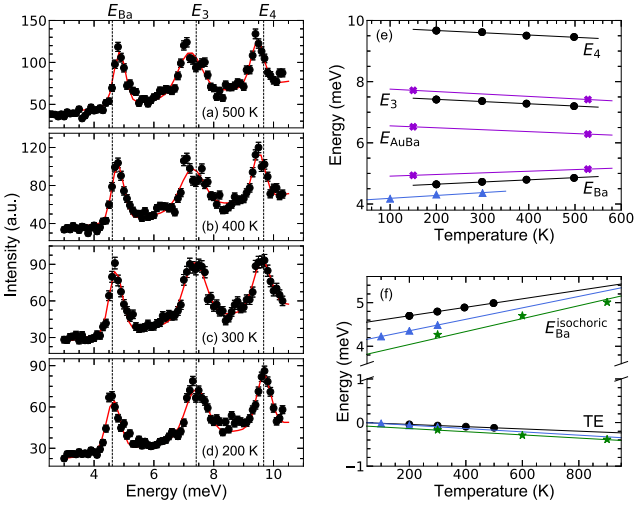

FIG. 7. (a)–(d) Inelastic neutron scattering (INS) intensity for constant $\mathbf{Q} = (113)$ scans as a function of energy (black circles) recorded on IN12@ILL between 200–500 K for $Ba_{7.81}Ge_{40.67}Au_{5.33}$. The solid red lines are Gaussian fits of the three optical bands whose energies are referred to as E_{Ba} and $E_{3,4}$. The vertical dotted black lines indicate their values at 200 K. (e) Temperature dependence of E_{Ba} and $E_{3,4}$ obtained from the fits shown in panels (a)–(d) (black circles) and from the $E_{\mathrm{Ba,Au}}$ and E_3 peaks in the generalized vibrational density of states shown in Fig. 3(c) (purple crosses). Blue triangles show the temperature dependence of E_{Ba} in $Ba_8Ge_{30}Ga_{16}$ [59]. In (f), the temperature dependence of E_{Ba} for $Ba_{7.81}Ge_{40.67}Au_{5.33}$ (black circles) and $Ba_8Ge_{30}Ga_{16}$ (blue triangles), corrected for the thermal expansion (TE), are shown and compared to that of the $Ba_8Ge_{30}Ga_{16}$ self-consistent phonon theory calculation that includes cubic and quartic terms (SCPB) [43] (green stars). The rates of TE of $Ba_{7.81}Ge_{40.67}Au_{5.33}$ and $Ba_8Ge_{30}Ga_{16}$ by INS and SCPB (same symbols/colors) are also plotted.

Some differences appear in the energy range between 5 and 7 meV, which might be linked to those observed for the LA dispersions in Figs. 3(a) and 3(b).

We then more systematically investigated these temperature dependencies by use of a triple-axis spectrometer between 200 and 500 K. Performing energy scans at constant wave-vector $\mathbf{Q} = (113)$, where the acoustic phonon intensity is expected to be very low, allows for a more selective study of the optical branches, as seen in Figs. 7(a)–7(d). E_{AuBa} is not visible in this polarization. However, following the GVDOS peaks in Fig. 3(c), we find a similar $E_3 = 7.5$ meV peak, and a higher energy peak at $E_4 = 9.8$ meV. The energy fits of E_{Ba} and $E_{3,4}$, along with $E_{\mathrm{Ba,AuBa}}$ and E_3 from the GVDOS, are then plotted in Fig. 7(e). All bands display linear trends in the overall temperature range, with only E_{Ba} hardening with a rate of 7.0×10^{-4} meV/K. For comparison, the 9.3×10^{-4} meV/K temperature dependence of E_{Ba} for $Ba_8Ge_{30}Ga_{16}$, measured by inelastic neutron scattering [59], has been included as well in Fig. 7(e). The rates of softening of the other optical bands in $Ba_{7.81}Ge_{40.67}Au_{5.33}$ are summarized in Table I.

V. DISCUSSION

From Eq. (1), it is evident that the reproduction of the experimentally observed κ_L(T) can be achieved only if the temperature dependence of the low-lying phonon modes is correctly accounted for. Therefore, we now seek direct comparison of the experimentally observed temperature dependence of the E_{Ba} band to results from SCP theory. The combined cubic and quartic anharmonicity terms give the isochoric contribution of the thermal change of phonon energy, $(\frac{\partial E}{\partial T})_V$, while experimental measurements, such as the ones presented above, are usually performed at constant pressure and give access to the isobaric thermal variation, $(\frac{\partial E}{\partial T})_P$. To the first order, the thermodynamic relation between those quantities is given by

$$\left(\frac{\partial E}{\partial T}\right)_V = \left(\frac{\partial E}{\partial T}\right)_P + E(T)\alpha_V(T)\gamma, \tag{5}$$

where the far right term corresponds to the mode-specific thermal expansion which we have experimentally quantified in $Ba_{7.81}Ge_{40.67}Au_{5.33}$ and $Ba_8Ge_{30}Ga_{16}$ through their volumetric thermal expansion coefficients, α_V(T), average Grüneisen parameters, γ, and energies of the mode under investigation (with the help of α_V and inelastic neutron scattering measurements in Refs. [19,59] for $Ba_8Ge_{30}Ga_{16}$). While experimentally we cannot further separate the cubic from the quartic anharmonic term, we discuss a conceptual first approximation in Appendix E. In Table I the isochoric dependencies of $Ba_{7.81}Ge_{40.67}Au_{5.33}$ and $Ba_8Ge_{30}Ga_{16}$, shown in Fig. 7(f), are deduced using Eq. (5) and thermal expansion contributions. For the lowest optical band at E_{Ba}, anharmonicity accounts for 9.7×10^{-4} meV/K for $Ba_{7.81}Ge_{40.67}Au_{5.33}$, and 13.1×10^{-4} meV/K for $Ba_6Ge_{30}Ga_{16}$. The difference between $Ba_{7.81}Ge_{40.67}Au_{5.33}$ and $Ba_8Ge_{30}Ga_{16}$ can be attributed to difference of the Ba local environment in the tetrakaidecahedral cages.

Conversely, for the SCP simulations, the SCP calculation which includes the quartic and cubic contributions (SCPB) with a rate of 14.8×10^{-4} meV/K can be used along with $\gamma^{\mathrm{SCPB}}(T)$ in order to find the equivalent isobaric rate of 11.2×10^{-4} meV/K. (More details are given for SCPB in Appendix D.) We therefore find close isochoric matching between SCPB and experimentally deduced anharmonicity in $Ba_8Ge_{30}Ga_{16}$, allowing us to experimentally validate the SCPB method in clathrates.

VI. CONCLUSIONS AND PERSPECTIVES

In summary, we confirm the good agreement between our measurements and the *ab initio* harmonic calculations using the meta-GGA SCAN functional of the overall phonon spectrum along different directions and for the transverse and longitudinal polarizations on the type-I clathrate $Ba_{7.81}Ge_{40.67}Au_{5.33}$. However, experimentally, the TA and LA branches are delimited by two optical phonon bands of different nature which is not reproduced by our simulations. While the former hybridizes with transverse optical vibrations centered at $E_{\mathrm{Ba}} = 4.8$ meV associated with the coherent guest motions of Ba(6*d*) in the soft plane of the tetrakaidecahedral cages, the latter is interrupted by the longitudinal optical band centered at $E_{\mathrm{AuBa}} = 6.5$ meV related to the coherent hybridized motions of the substituted Au(6*c*) host and the Ba(6*d*) guest atoms. The TA dispersion is perfectly reproduced by our *ab initio* simulation in the whole Brillouin zone. On the other hand, a difference appears on the longitudinal branch in the region of the phase space where optical and acoustic modes hybridize such that the LA branch is predicted to be cut off at the same energy as the transverse one.

Upon cooling, E_{AuBa} increases, following a rate of change guided by thermal expansion, while E_{Ba} decreases. The experimental isochoric rate of change of E_{Ba} extracted in $Ba_8Ge_{30}Ga_{16}$, which quantifies the amount of cubic and quartic anharmonicity, is in good agreement with the SCPB simulations in $Ba_8Ge_{30}Ga_{16}$. In $Ba_{7.81}Ge_{40.67}Au_{5.33}$, a much lower rate of change is found which is assumed to originate from the difference of the defect structure. On the other hand, the difference between the transverse and the longitudinal cutoff energies observed experimentally, which is not seen in the simulations, indicates a more subtle polarization dependent mechanism involving either the disorder and/or the anharmonic polarization mixing whose consideration in the SCP-like approach will surely reveal an improved $\kappa_L(T)$ dependence, especially in the intermediate temperature range as seen in Fig. 1(b).

Data from inelastic neutron scattering measurements at the ILL are available at [65], and LLB measurements correspond to proposal 657.

ACKNOWLEDGMENTS

S.R.T. acknowledges financial support from the ISP program of the IDEX Université Grenoble Alpes. S.P. acknowledges support from the Lyon IDEX Scientific Breakthrough program for funding of the project IPPON. This work has been carried out within the European C-MetAC network [66]. The authors would like to thank T. Tadano, N. Vast, and T. Nakayama for fruitful discussions.

APPENDIX A: INELASTIC NEUTRON SCATTERING MEASUREMENTS

A neutron scattering event involves incident neutrons with initial energy and wave vector ($|E_i, \mathbf{k}_i\rangle$) impinging on a sample and being scattered, resulting in scattered neutrons with ($|E_f, \mathbf{k}_f\rangle$). An inelastic neutron scattering (INS) experiment measures the amount of flux of the initial neutron beam that has been scattered into the solid angle element of interest, $d\Omega_f$, within energy range of interest dE_f. The cross section, σ, is defined as the number of neutrons scattered per second out of the number of incident neutrons per cm^2 per second. The double differential of σ for neutron scattering, $\frac{d^2\sigma}{d\Omega_f dE_f}$, can be related to the coherent inelastic scattering function, $S(\mathbf{Q}, \omega)$, by $\frac{d^2\sigma}{d\Omega_f dE_f} = N\frac{k_f}{k_i}S(\mathbf{Q}, \omega)$, where N is the number of nuclei [44,67].

1. Time-of-flight spectroscopy

Inelastic neutron scattering measurements depicted in Figs. 3 and 5 of the main text and Figs. 12–18 in Appendix F were made using cold-neutron time-of-flight spectroscopy. The time-of-flight measurements took place on IN5@ILL

TABLE II. For the given experimental conditions on IN5@ILL, the components of q resolution are summarized. Values were calculated for dispersions near the (006) Bragg peak in the momentum plane ([110]; [001]) and are categorized by horizontal resolutions for the primary, [110], and secondary, [001], axes of the scattering plane, followed by the vertical resolution for the out-of-plane direction, [$\bar{1}$10]. Pixel/step divergence refers to the divergence due to the size of the IN5 detector tubes as seen from the sample distance and to the step size of 0.5° chosen for this particular experiment for the [110] direction. Beam divergence refers to the divergence that occurs due to the IN5 neutron guide. Values are given in Å^{-1}.

	Pixel/step divergence	Beam divergence
Along [001]	5.66×10^{-3}	9.96×10^{-3}
Along [110]	3.06×10^{-2}	3.92×10^{-2}
Along [$\bar{1}$10]	1.25×10^{-2}	3.29×10^{-2}

using an incident neutron wavelength of $\lambda = 3.2$ Å and a cryofurnace. Scans covered an Ω range of 54°, with a sample rotation of 0.5° in between each scan. Time-of-flight data were reduced using Mantid [68] and then processed into a four-dimensional $S(\mathbf{Q}, E)$ file and further analyzed with the Horace package [69] under Matlab.

Considerable effort was made to understand q and E resolution (dq, dE) of the instrument in order to make realistic data integrations with Horace. The overall instrumental resolution is governed by the incoming neutron beam energy and monochromatization, the beam divergence in horizontal and vertical directions, the sample mosaic, the receiving slit sizes in front of the detector, and the final neutron energy [70]. This then must be compared to the minimum step size that can be achieved with the instrument, as explained hereafter.

By taking into account the divergence due to the size of the detector tubes of IN5@ILL and the beam divergence while in the $\lambda = 3.2$ Å condition, we have defined the resolution for the [001] and [110] directions while near the (006) Bragg peak. More specifically, detector tubes on IN5 have a diameter of 2.54 cm, meaning that with a distance of 4 m between the sample and detectors, there is a beginning divergence of 0.36° due to instrumental conditions. To this we add the corresponding horizontal and vertical beam divergences, 0.64° and 0.96°, respectively, due to the incident neutron wavelength and neutron guide horizontal and vertical super-mirror indices on IN5 [70]. Using these starting points, we then calculated the local resolution limits around our Bragg peak of interest, the (006). These are summarized in Table II.

Next, as a first approximation, we consider that q and E are decoupled for a time-of-flight spectrometer, unlike on a triple-axis spectrometer. This means that the effective phonon energy resolution depends on the effect of energy broadening due to the reciprocal space, $\Delta E_{\text{sound vel}}$, and on the instrumental resolution for a given energy transfer, ΔE_{instr}. The latter has been calculated using the incident neutron wavelength, speed of the IN5@ILL choppers (12 000 rpm), and additional spectrometer parameters [70]. For our given experimental conditions, Fig. 8 depicts the energy resolution as it changes with the energy of the scattering event. The former, on the other hand, refers to $\Delta E_{\text{sound vel}} = v_s \Delta q$, where v_s is the sound velocity of the particular dispersion

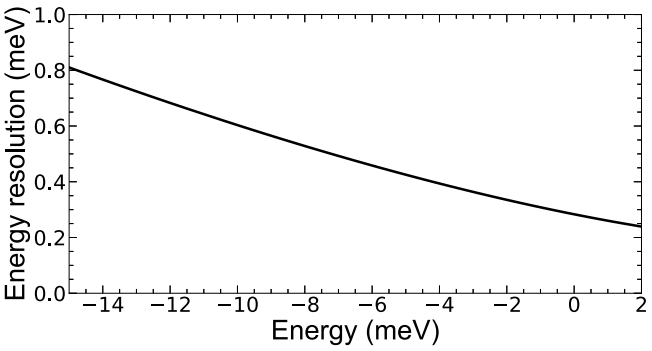

FIG. 8. The energy resolution, given our specific experimental conditions, of the cold-neutron time-of-flight spectrometer IN5@ILL is plotted in the energy range of interest for results discussed in this article. The calculation is made by considering the incident neutron wavelength, chopper speed, and other instrumental parameters specific to IN5. The equation for calculating energy resolution is derived in Ref. [70].

of interest. For LA_{001} near the (006) Bragg peak with $v_s = 25.84$ meV Å, the resulting $\Delta E_{\text{sound vel}} = 0.30$ meV, while for TA_{110}^{001} with $v_s = 16.99$ meV Å, $\Delta E_{\text{sound vel}} = 0.25$ meV. The total effective phonon energy resolution is therefore $\sqrt{(\Delta E_{\text{sound vel}})^2 + (\Delta E_{\text{instr}})^2}$.

The minimum step size that can be chosen when preparing the 4D data matrix in Horace is therefore given by the step sizes due to detector pixel sizes, step rotation, and step size in energy. These steps are generally smaller than the effective instrumental resolution. It should be noted that dq_T, or the transversal dq step size, is strongly Q dependent, since it is equal to $\Delta(\text{rotation}) \times Q$, where $\Delta(\text{rotation})$ is the rotation step size expressed in radians. As stated above, there is a 0.5° step size for these experimental data. The final Horace integration limits are derived from Table II, in which the overall dq resolution is: $\sqrt{(\Delta q_{\text{step div.}})^2 + (\Delta q_{\text{beam div.}})^2}$.

Figure 12 contains two-dimensional plots showing the energy spectrum in a given direction within the momentum plane were cut and then folded along symmetries using the appropriate Horace functions. For subplots (a), (c), and (e), $dq = 0.018$ r.l.u. for 0–5.75 meV, 0.036 r.l.u. for 5.75–6.3 meV, and 0.072 for 6.3–15 meV, while $dE = 0.075$ meV between 0 and 5.75 meV and 0.1 for 5.75–15 meV. For subplots (b), (d), and (f), $dq = 0.037$ r.l.u., and $dE = 0.075$ meV between 0 and 7 meV, and 0.1 meV between 7 and 15 meV. The energy is then squared in order to display $S(q, E) \times E^2$ in the final subplots of Fig. 12.

The Fig. 5 subplots reflect intensity seen across the measured part of the momentum plane ([110];[001]) at a given energy. Each pixel on the surface plot is a 0.03×0.03 r.l.u. square. Subplots (a)–(c) were made using an energy integration of E ± 0.15 meV, where E is 4.8, 6.5, 7.5 in the cases of subplots (a)–(c), and for subplot (d), 9.5 ± 2.5 meV. Similar cut and folded symmetry Horace functions were used.

In Fig. 3(a) 1D scans around the intense (006) Bragg peak along transverse and longitudinal polarizations (see Appendix F) were once again cut using Horace functions. A tight data integration along the propagation axis was chosen in order to selectively measure along a given polarization in a focusing condition. For Figs. 13(a), 14(a), and 15(a),

$dq = 0.018$ r.l.u. along the propagation axis $[\zeta\,\zeta\,0]$, 0.04 r.l.u. along $[00\xi]$, and 0.06 r.l.u. along the out-of-plane axis $[\bar{\zeta}\,\zeta\,0]$. For Figs. 13(b), 14(b), and 15(b), $dq = 0.037$ r.l.u. along the propagation axis $[00\xi]$, 0.02 r.l.u. along $[\zeta\,\zeta\,0]$, and 0.06 r.l.u. along $[\bar{\zeta}\,\zeta\,0]$.

For the one-dimensional scans around the (222) Bragg peak in Fig. 3(b), the same procedure as described above has been completed to reflect the resolution limits near this new position in reciprocal space. As there is less intensity in this region, however, integrations slightly larger than those of the strict minimums were taken: $dq = 0.08$ r.l.u. along the propagation axis $[\zeta\,\zeta\,0]$, 0.08 r.l.u. along $[00\xi]$, and 0.06 r.l.u. along the out-of-plane axis $[\bar{\zeta}\,\zeta\,0]$. The 1D scans used to create Fig. 3(b) are shown in Figs. 16(a) and 16(b), Figs. 17(a) and 17(b), and Fig. 18(a) and 18(b).

In addition, high-resolution time-of-flight measurements were taken with $\lambda = 4.8$ Å in order to obtain the neutron-weighted generalized vibrational density of states (GVDOS) plot in Fig. 3(c), calculated by the MUPHOCOR (MUlti-PHOnon CORrection) routine [71] in the LAMP program [72] for single crystal data. Scans covering an Ω range of 46° at 150 K and 34° at 530 K, both with sample-rotation step sizes of 2°, were used to make the calculation, and the atomic mass and expected neutron scattering cross section of $Ba_{7.81}Ge_{40.67}Au_{5.33}$ were used as initial starting parameters.

2. Triple-axis spectroscopy

Figures 7(a)–7(d) reflect the measurements taken on the cold-neutron triple-axis spectrometer (TAS) IN12@ILL. The experiment was conducted with a fixed $k_f = 1.55$ Å^{-1}, and with the k_i velocity selector, k_f Be filter, and cryofurnace options. The three optical bands shown in subplots (a)–(d) were fitted as Gaussian peaks because the signal is not a single phonon but a distribution of optical branches.

Preliminary experiments, performed on the triple-axis spectrometer 1T@LLB with a fixed $k_f = 2.662$ Å^{-1}, were extremely important in this work. Indeed, the polarization dependence of the low-lying optical phonon band at E_{Ba} was formerly observed in these experiments.

3. Neutron Larmor diffraction

Neutron Larmor diffraction takes advantage of the neutron resonance spin echo technique for triple-axis spectrometers in order to measure the change in lattice spacing with temperature with extreme sensitivity (1.5×10^{-6}) [73–76]. Such a measurement was made on the (006) Bragg peak position between 3 and 300 K, and is shown in Fig. 9(a) (also see Fig. 2). Measurements were taken in increments of 5 K with a fixed k_i of 2.13 Å^{-1} on the thermal-neutron triple-axis spectrometer TRISP@FRM-II.

APPENDIX B: CALCULATION OF BULK MODULUS FROM ELASTIC CONSTANTS

Given that we have measured acoustic phonons in several high-symmetry directions, we can use the sound velocities to estimate certain mechanical properties such as the bulk modulus, B. Sound velocities of transverse, v_{TA}, and longitudinal, v_{LA}, polarizations can be related to the single crystal elastic

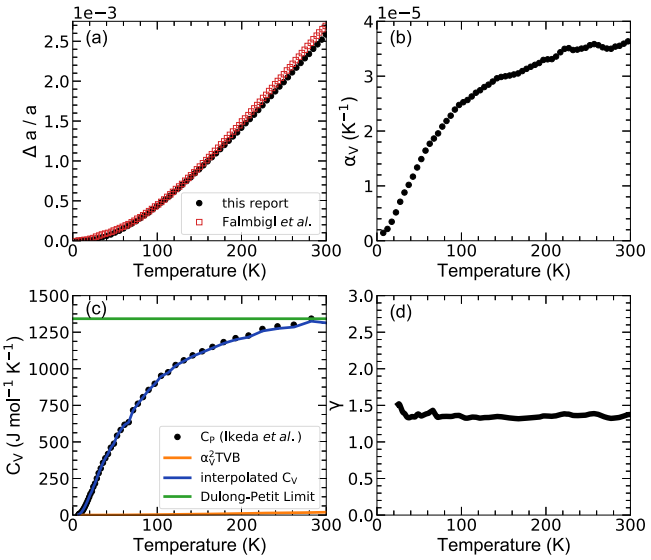

FIG. 9. The temperature-dependent Grüneisen parameter (γ) in (d) for $Ba_{7.81}Ge_{40.67}Au_{5.33}$ is calculated using the rate of thermal expansion ($\Delta a/a$) in (a), the volumetric coefficient of thermal expansion (α_V) in (b), the constant volume specific heat in (c), and the bulk modulus calculated in Appendix B. The rate of thermal expansion has been measured by Larmor diffraction on TRISP@FRM-II (black circles), and compared to that of Falmbigl *et al.* (empty red squares) [50]. Its numerical derivative is used to find $\alpha_L = \alpha_V/3$. The measurement of C_P (black circles) from Ikeda *et al.* [19] was used to calculate C_V (solid blue line).

constants at 0 K, c_{ij}, through the following [16,77–79]:

$$v_{\mathrm{LA}_{001}} = \sqrt{\frac{c_{11}}{\rho}}\,,\quad v_{\mathrm{TA}_{110}^{001}} = \sqrt{\frac{c_{44}}{\rho}},$$
$$v_{\mathrm{TA}_{1\bar{1}2}^{111}} = \sqrt{\frac{c_{11}-c_{12}+c_{44}}{3\rho}}. \tag{B1}$$

For $Ba_{7.81}Ge_{40.67}Au_{5.33}$, we find $v_{\mathrm{LA}_{001}} = 3{,}926$ m/s, $v_{\mathrm{TA}_{110}^{001}} = 2{,}582$ m/s, and $v_{\mathrm{TA}_{1\bar{1}2}^{111}} = 2{,}234$ m/s at 300 K. Therefore, $c_{11} = 103.15$ GPa, $c_{44} = 44.61$ GPa, and $c_{12} = 47.49$ GPa at 0 K. Okamoto *et al.* have experimentally measured c_{ij} for $Ba_8Ge_{30}Ga_{16}$ and found $c_{ij}^{300\mathrm{K}}$ within 10% of our values [80]. Similar values have been found for other type-I clathrates as well [81].

Using these elastic constants, we can calculate the material bulk modulus at 0 K, B, through Eq. (B2), which gives us $B = 65.60$ GPa. Again, the same value is found for $Ba_8Ge_{30}Ga_{16}$ with almost no temperature dependence [19,80]:

$$B = \frac{1}{\chi} = \sqrt{\frac{c_{11}+2c_{12}}{3}}. \tag{B2}$$

APPENDIX C: CALCULATION OF EXPERIMENTAL GRÜNEISEN PARAMETER (CONTINUED)

This section expands on the experimental Grüneisen parameter results discussed in the main text, in particular on Eq. (4). Figures 9(a) and 9(b) have already been presented in Fig. 2. From Ikeda *et al.* [19] we have experimental C_P for $Ba_{7.81}Ge_{40.67}Au_{5.33}$. To calculate C_V, we use the relation

$C_P = C_V + \alpha_V^2 TVB$ [82], and this is plotted in Fig. 9(c). Finally, using the given equation for calculating the average Grüneisen parameter, $\gamma(T)$ is calculated and plotted in Fig. 9(d). This method of experimental deduction gives $\gamma_{300\mathrm{K}} = 1.38$, which is temperature independent within the temperature range of study.

APPENDIX D: COMPARING TO SCP METHOD CALCULATIONS

There are two different calculations of the E_{Ba} optical band in $Ba_8Ge_{30}Ga_{16}$ that have been summarized by Tadano and Tsuneyuki in the Supplementary Material of Ref. [43]: (1) SCP: SCP method calculations in which the real part of the quartic anharmonic term, or the Loop free energy diagram, determines phonon frequency renormalizations in the system, and (2) SCP+Bubble: the same calculation, but made by also including the real part of the cubic anharmonic term, the Bubble free energy diagram. (The second calculation will be referred to as SCPB in this discussion.) We therefore reflect that the SCPB calculation directly provides us with $(\frac{\partial E}{\partial T})_V$ of E_{Ba} and that the self-energy terms in the SCPB calculation self-consistently include the renormalized phonon energies including the effect of the quartic anharmonicity. (This is an important distinction for Appendix E, as this means that we cannot extract the *harmonic* Bubble term but only the self-consistent Bubble term.)

In order to move between isobaric and isochoric representations of the SCPB calculation discussed in the main text, we have calculated the SCPB-based thermal expansion: $E^{\mathrm{SCPB}}(T)\alpha_V\gamma^{\mathrm{SCPB}}(T)$. In this way, the determination of the thermal expansion is much more exact than by using the quasiharmonic approximation for which only the harmonic phonon energies are considered. As will be shown in the following paragraphs, $\gamma^{\mathrm{SCPB}}(T)$ and $E^{\mathrm{SCPB}}(T)$ come from the information given in the Supplementary Material of Ref. [43], and as a first approximation we use the experimental α_V for $Ba_8Ge_{30}Ga_{16}$ from Ikeda *et al.* [19].

The isochoric rate of change in energy of E_{Ba} with temperature for the SCP calculation is 17.9×10^{-4} meV/K, and 14.8×10^{-4} meV/K for the SCPB calculation. Next, with the use of the mode-specific definition of the Grüneisen parameter, $\gamma_i = -\frac{V}{E_i}(\frac{\partial E_i}{\partial V}) = -(\frac{\partial \ln E_i}{\partial \ln V})_T$, the SCPB-based Grüneisen parameter for the E_{Ba} mode can be calculated using Fig. 10(b). The mode-specific Grüneisen parameter for the SCP calculation [Fig. 10(a)] is 4.71, 2.57, 2.06, and 1.76 for temperatures of 0, 300, 600, and 900 K, respectively, and in similar fashion for the SCPB calculation [Fig. 10(b)]: 4.81, 2.98, 2.34, and 1.94. Although these Grüneisen parameters appear to be slightly larger than the average clathrate experimental values discussed in the main text, we note that these parameters reflect the anharmonicity found specifically in the E_{Ba} optical band. With these mode-specific Grüneisen parameter results, the SCPB thermal expansion shown in Fig. 7(f) was calculated and, by extension, the isobaric form of the SCPB calculation was found to have a rate of change of 11.2×10^{-4} meV/K.

We also note that there are experimental rates of change for $Ba_8Ge_{30}Ga_{16}$ that match the isochoric SCP (no cubic component) calculation. The Raman measurements of Takasu *et al.* [61–63], with a rate of change of 17.1×10^{-4} meV/K, cause

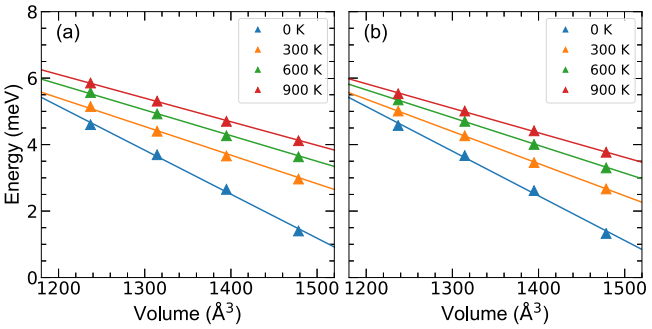

FIG. 10. Calculations from Table S2 of Ref. [43] are plotted in order to obtain $(\frac{\partial E_i}{\partial V})_T$ for the E_{Ba} optical band, namely, the rate of change in volume of $Ba_8Ge_{30}Ga_{16}$ with energy for "SCP" (a) and "SCP+Bubble" (b).

a discrepancy between Raman measurements of $Ba_8Ge_{30}Ga_{16}$ measured by this group and by those of Christensen *et al.* [59]. We emphasize, however, that the isobaric 17.1×10^{-4} meV/K should not be compared to the isochoric quartic-only calculation.

APPENDIX E: FIRST APPROXIMATION DECOUPLING OF CUBIC AND QUARTIC ANHARMONICITY

Even though we cannot definitively isolate the cubic and quartic anharmonicity terms from an inelastic neutron scattering $(\frac{\partial E}{\partial T})_P$ measurement, we will attempt to qualitatively interpret their weighted importance on E_{Ba}.

The generalized vibrational density of states (GVDOS), as seen in Fig. 3(c), represents the isobaric temperature dependence of $Ba_{7.81}Ge_{40.67}Au_{5.33}$. However, if the energy axis of the data at 530 K is scaled by 3% of the original values, as seen in Fig. 11, then globally, all peaks except for E_{Ba} now align. This is already a powerful conclusion about the uniqueness of E_{Ba}, pointing to the strong anharmonicity that governs its behavior as opposed to all other higher energy peaks, for which one scaling factor can explain the complete temperature dependencies.

This 3% scaling factor can be understood to be made up of the thermal expansion and cubic components, since

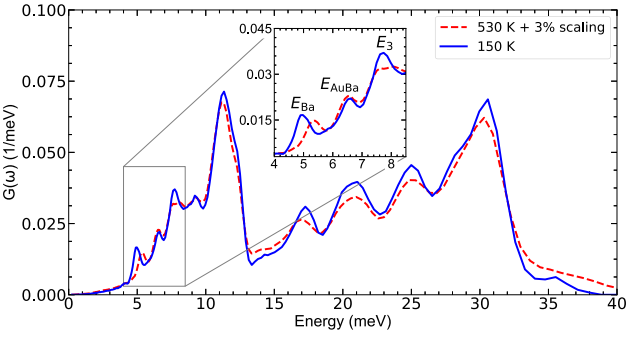

FIG. 11. Generalized vibrational density of states obtained from the data collection recorded on IN5@ILL at 150 and 530 K. The energy axis of the data at 530 K has been scaled by 3%, leading to an alignment of all but the lowest peaks.

we will assume that the quartic term is localized onto only E_{Ba} as a first approximation. This simplification is supported by Tadano and Tsuneyuki [43], who find that the quartic anharmonic phonon energy renormalizations of the SCP (*not* SCPB; see Appendix D for more details) calculation are focused onto modes below 9.92 meV (80 cm^{-1}) for $Ba_8Ge_{30}Ga_{16}$. We therefore extrapolate to say that modes higher than E_{Ba} are controlled by only thermal expansion and the cubic term, while E_{Ba} has contributions from thermal expansion, the cubic term, *and* the quartic term.

Let us first look at GVDOS peaks between 10 and 35 meV, for which we must consider only thermal expansion and cubic components. To reiterate, by studying the 3% scaling factor, we are studying the isobaric rate of change for peaks between 10 and 35 meV. We recall that, using Eq. (5), the peak-specific thermal expansion for each of the GVDOS peaks between 10 and 35 meV in Fig. 11 can be calculated, and the result is that thermal expansion consistently accounts for 45%–50% of the total isobaric rate of change. Given our assumption that these modes are controlled only by the thermal expansion and cubic terms, this leaves a remaining 50%–55% of the 3% scaling which must be understood as the rate of change of the cubic anharmonicity. In this manner, the 3% scaling factor of peaks between 10 and 35 meV is fully accounted for.

Expanding on this 3% scaling concept to E_{Ba}, we recall the values given in Table I: E_{Ba} has an isobaric rate of change of 5.4×10^{-4} meV/K and a thermal expansion rate of change of -2.7×10^{-4} meV/K, giving the isochoric rate of change of 8.1×10^{-4} meV/K. However, this time we expect for the isobaric rate of change to reflect thermal expansion, cubic, *and* quartic contributions. As stated above, the rate of thermal expansion for E_{Ba} is already known, leaving the cubic and quartic contributions, for which we also know the total isochoric (cubic and quartic) contribution. However, after the 3% scaling shown in Fig. 11, the rate of change for E_{Ba} becomes 9.4×10^{-4} meV/K. Therefore, the difference between the 3% scaling factor and isochoric rate of change, which is -1.3×10^{-4} meV/K, must be due to cubic anharmonicity, meaning that 9.4×10^{-4} meV/K is the quartic contribution to E_{Ba}.

While we cannot directly compare the Bubble contribution of the "SCP+Bubble" (SCPB) calculation (see Appendix D) to the cubic contribution using this GVDOS rescaling method, we note that -1.3×10^{-4} meV/K has the correct sign for the cubic component [43].

APPENDIX F: INELASTIC NEUTRON SCATTERING ENERGY SCANS

Figure 12 uses the experiment performed on the cold-neutron time-of-flight spectrometer IN5@ILL to map the phonon spectra in a wide range of energy and momentum at 530 [(a),(b)], 300 [(c),(d)], and 150 K [(e),(f)]. (Further experimental conditions and data integration parameters are detailed in Appendix A.) Figures 12(a), 12(c), and 12(e) follow the transverse polarization centered around the intense (006) Bragg peak in which phonons propagate along [110] and are polarized along [001]. Figures 12(b), 12(d), and 12(f) display the longitudinal polarization, again centered around the (006) Bragg peak, in which phonons propagate along [001].

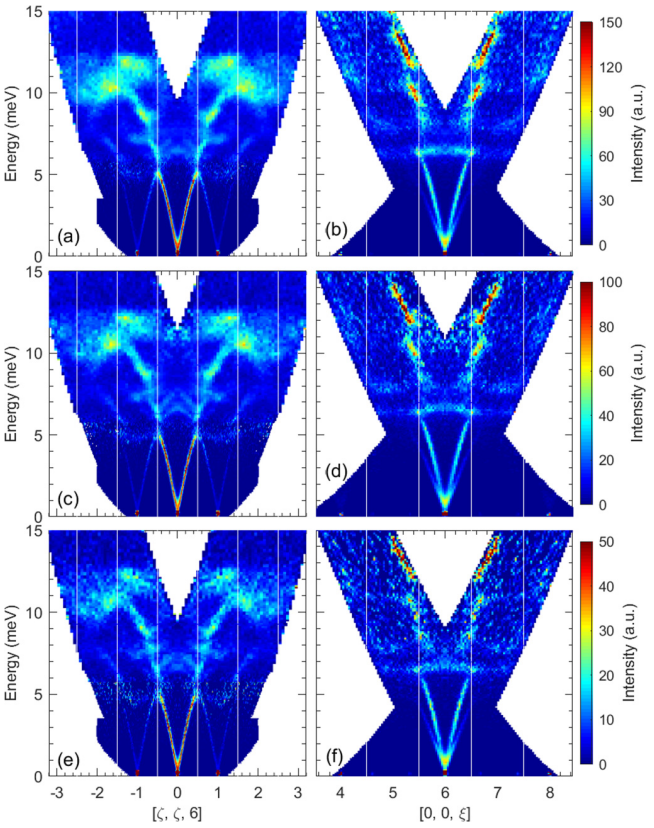

FIG. 12. Two-dimensional inelastic neutron scattering intensity reported as function of the energy transfer and along the [110] [(a), (c), (e)] and [001] [(b), (d), (f)] directions in $Ba_{7.81}Ge_{40.67}Au_{5.33}$, recorded on IN5@ILL. The data have been taken at three temperatures: 530 K [(a), (b)], 300 K [(c), (d)], and 150 K [(e), (f)]. Measurements were centered at the zone center Γ_{006} ($Q = 3.5$ Å^{-1}), from which the acoustic phonon polarization is longitudinal when the propagation direction is [001] [panels (b), (d), (f)], and transversely polarized [001] when the propagation direction is [110] [panels (a), (c), (e)]. The Brillouin zones are indicated with vertical solid white lines.

Figures 13–15 depict the energy scans taken on IN5@ILL ($\lambda = 3.2$ Å) around the Bragg peak (006) at 523 K, 300 K, and 150 K respectively. (Experimental conditions and analytical tools also discussed in Appendix A.) These energy scans are like the one-dimensional cuts of the mappings in Fig. 12, and they were used to construct Fig. 3(a). Figures 13(a), 14(a), and 15(a) follow the transverse acoustic phonon dispersion polarized along [001], propagating along [110]. Figures 13(b), 14(b), and 15(b) follow the longitudinal acoustic phonon dispersion polarized along [001], propagating along [001].

Similarly for Fig. 3(b), Figs. 16–18 depict the energy scans taken on IN5@ILL ($\lambda = 3.2$ Å) around the Bragg peak (222) at 523 K, 300 K, and 150 K, respectively. Figures 16(a), 17(a), and 18(a) follow the transverse acoustic phonon dispersion polarized along [111], propagating along $[\bar{1}\bar{1}2]$. Figures 16(b), 17(b), and 18(b) follow the longitudinal acoustic phonon dispersion polarized along [111], propagating along [111]. Phonons were fitted as Gaussian peaks with a flat background.

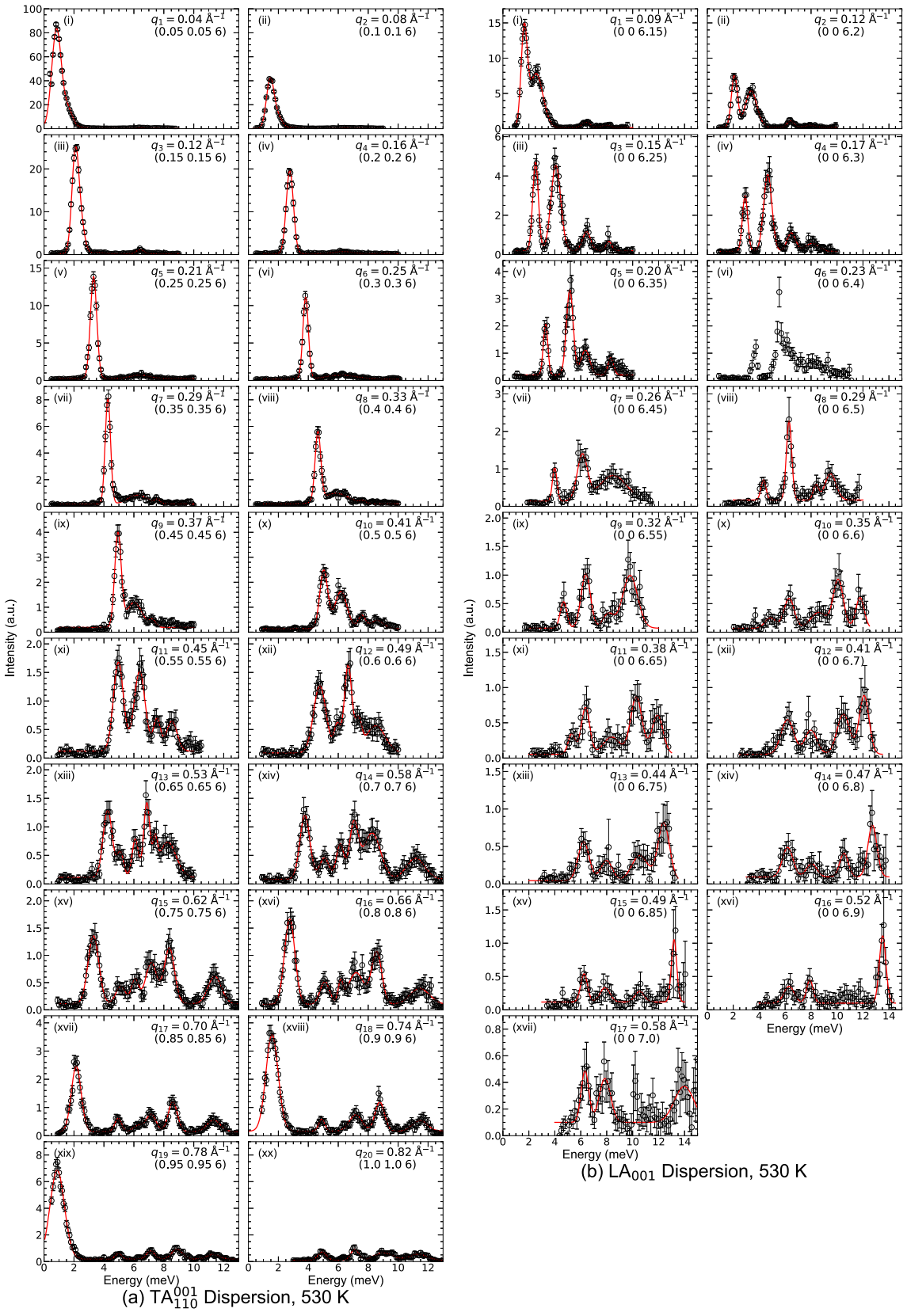

FIG. 13. Energy scans taken on IN5@ILL near the (006) Bragg peak with $\lambda = 3.2$ Å at 530 K. Plots reflect a normalized intensity scale, with data points as empty black circles, and their fit as a solid red line.

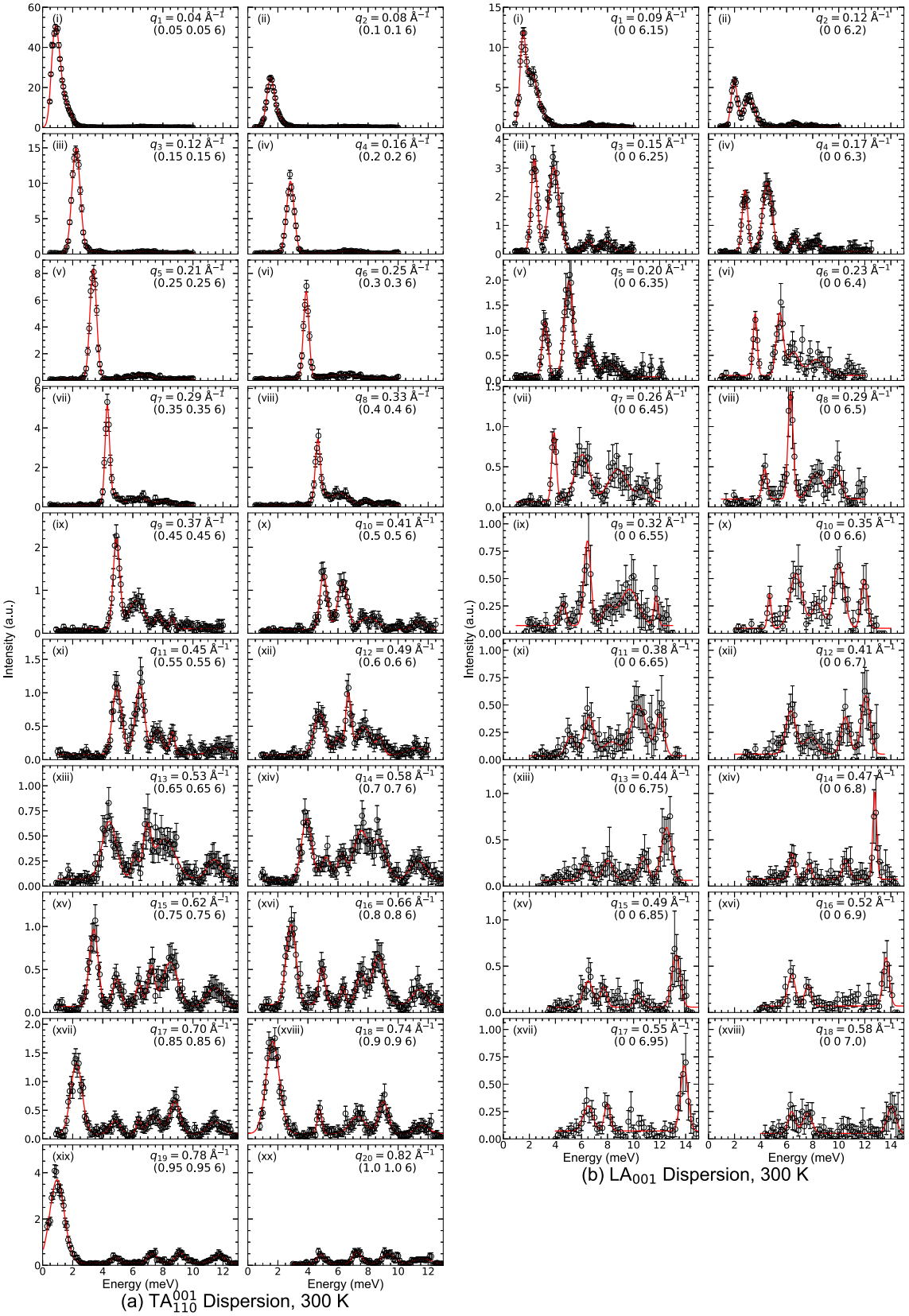

FIG. 14. Energy scans taken on IN5@ILL near the (006) Bragg peak with $\lambda = 3.2$ Å at 300 K. Plots reflect a normalized intensity scale, with data points as empty black circles, and their fit as a solid red line.

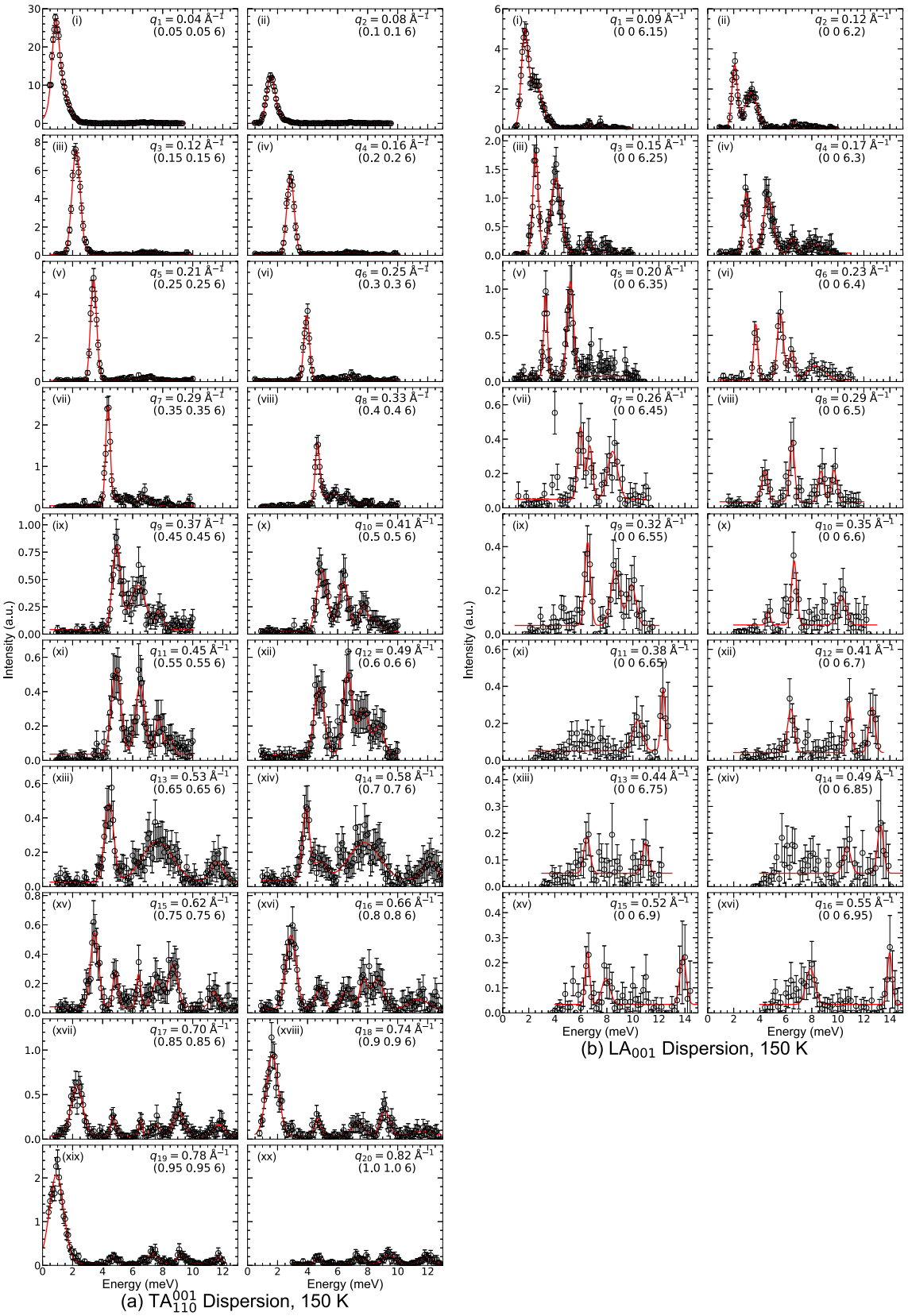

FIG. 15. Energy scans taken on IN5@ILL near the (006) Bragg peak with $\lambda = 3.2$ Å at 150 K. Plots reflect a normalized intensity scale, with data points as empty black circles, and the fit as a solid red line.

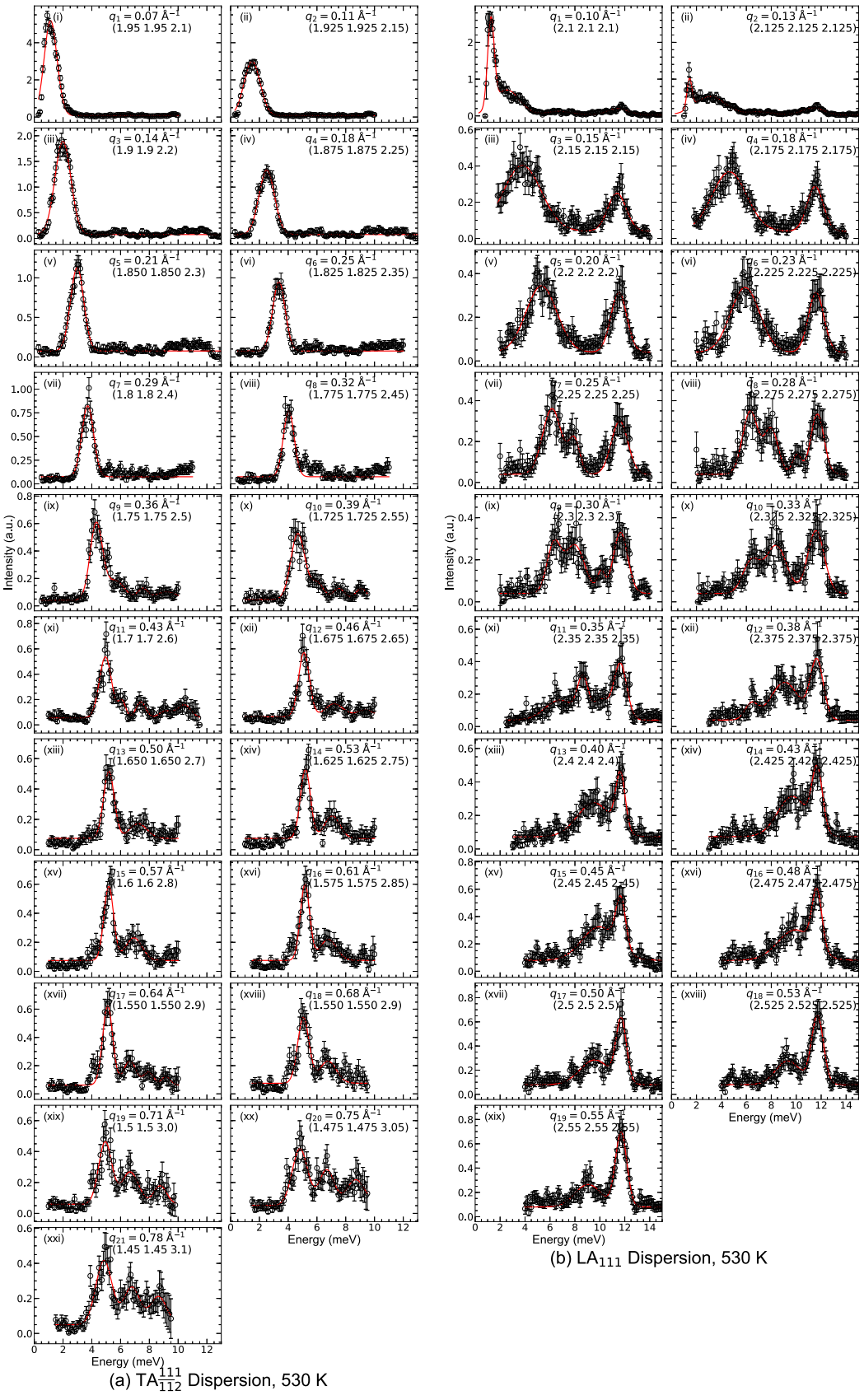

FIG. 16. Energy scans taken on IN5@ILL near the (222) Bragg peak with $\lambda = 3.2$ Å at 530 K. Plots reflect a normalized intensity scale, with data points as empty black circles, and their fit as a solid red line.

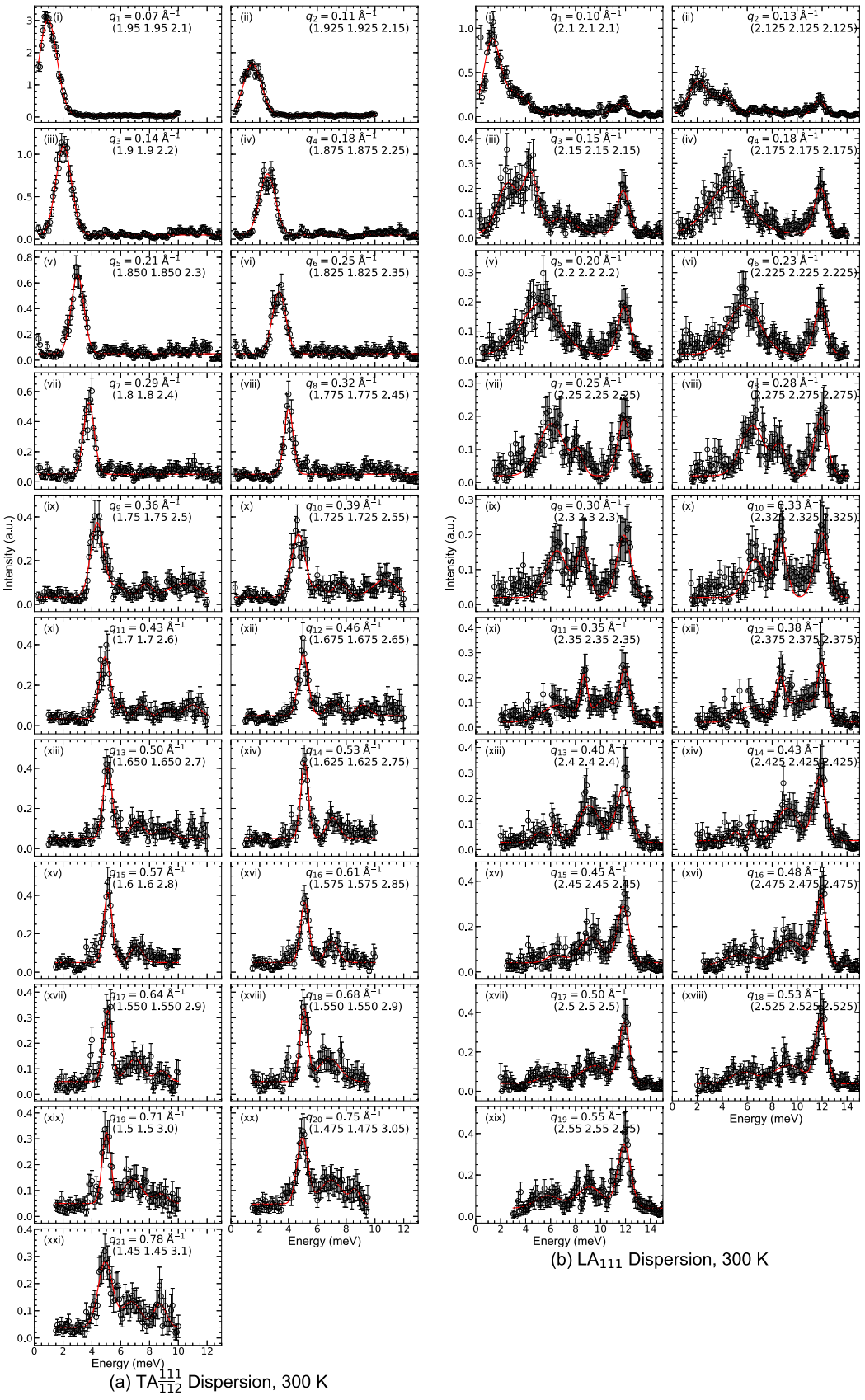

FIG. 17. Energy scans taken on IN5@ILL near the (222) Bragg peak with $\lambda = 3.2$ Å at 300 K. Plots reflect a normalized intensity scale, with data points as empty black circles, and their fit as a solid red line.

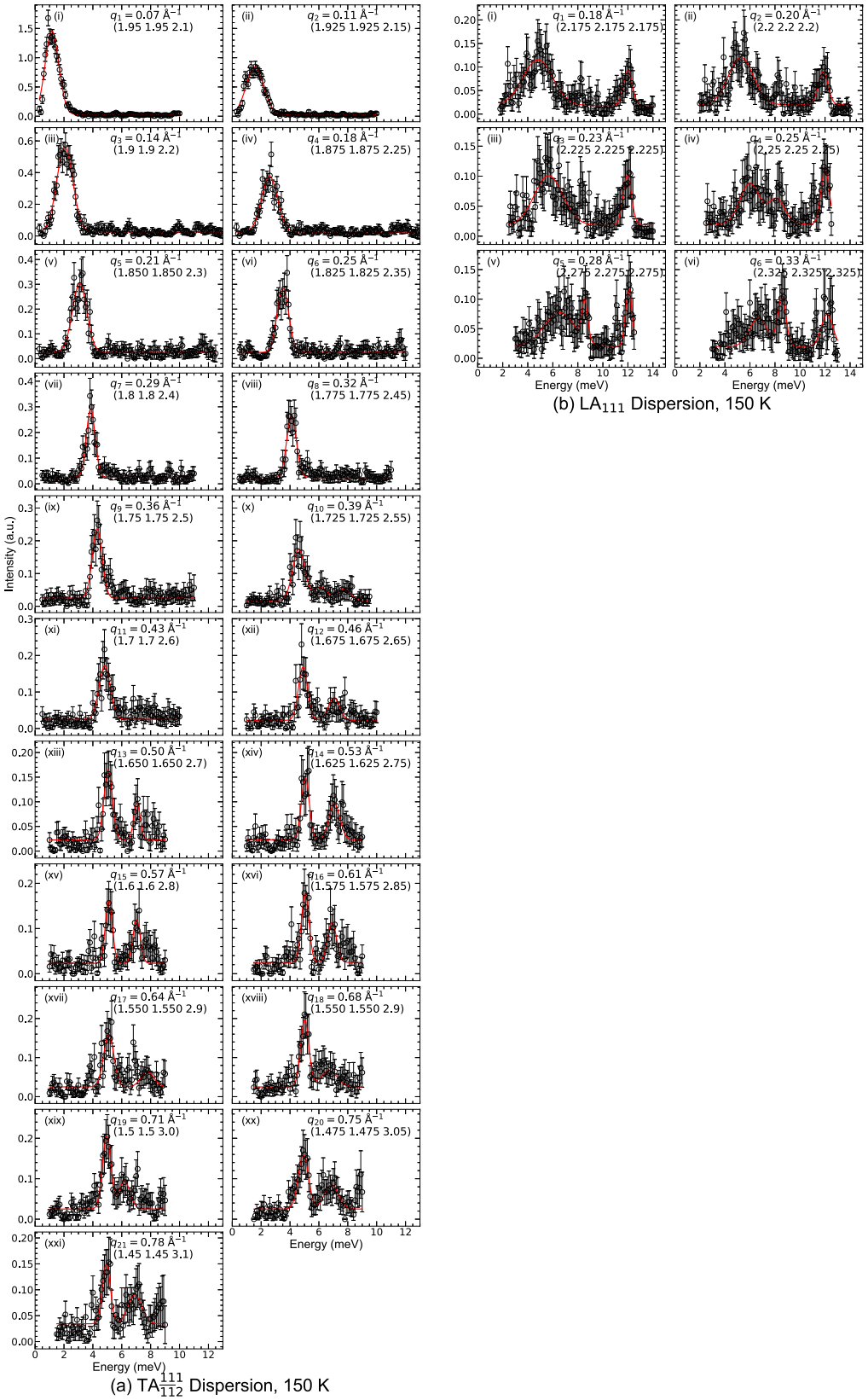

FIG. 18. Energy scans taken on IN5@ILL near the (222) Bragg peak with $\lambda = 3.2$ Å at 150 K. Plots reflect a normalized intensity scale, with data points as empty black circles, and the fit as a solid red line.

[1] G. J. Snyder and E. S. Toberer, Complex thermoelectric materials, Nat. Mater. **7**, 105 (2008).

[2] J. Klarbring, O. Hellman, I. A. Abrikosov, and S. I. Simak, Anharmonicity and Ultra-Low Thermal Conductivity in Lead-Free Halide Double Perovskites, Phys. Rev. Lett. **125**, 045701 (2020).

[3] J. Even, S. Paofai, P. Bourges, A. Letoublon, S. Cordier, O. Durand, and C. Katan, Carrier scattering processes and low energy phonon spectroscopy in hybrid perovskites crystals, in *Physics, Simulation, and Photonic Engineering of Photovoltaic Devices V*, edited by A. Freundlich, L. Lombez, and M. Sugiyama (SPIE, 2016), Vol. 9743, pp. 78–85.

[4] Y. Yu, M. Cagnoni, O. Cojocaru-Mirédin, and M. Wuttig, Chalcogenide thermoelectrics empowered by an unconventional bonding mechanism, Adv. Funct. Mater. **30**, 1904862 (2019).

[5] H. Yang, J.-y. Yang, C. N. Savory, J. M. Skelton, B. J. Morgan, D. O. Scanlon, and A. Walsh, Highly anisotropic thermal transport in $LiCoO_2$, J. Phys. Chem. Lett. **10**, 5552 (2019).

[6] K. Hoang and M. D. Johannes, Defect physics in complex energy materials, J. Phys.: Condens. Matter **30**, 293001 (2018).

[7] E. S. Toberer, L. L. Baranowski, and C. Dames, Advances in thermal conductivity, Ann. Rev. Mater. Res. **42**, 179 (2012).

[8] E. S. Toberer, A. Zevalkink, and G. J. Snyder, Phonon engineering through crystal chemistry, J. Mater. Chem. **21**, 15843 (2011).

[9] A. Verchère, S. Pailhès, S. L. Floch, S. Cottrino, R. Debord, G. Fantozzi, S. Misra, C. Candolfi, B. Lenoir, S. Daniele, and S. Mishra, Optimum in the thermoelectric efficiency of nanostructured Nb-doped TiO_2 ceramics: From polarons to Nb–Nb dimers, Phys. Chem. Chem. Phys. **22**, 13008 (2020).

[10] Y. Grin, Inhomogeneity and anisotropy of chemical bonding and thermoelectric properties of materials, J. Solid State Chem. **274**, 329 (2019).

[11] Y. Bouyrie, C. Candolfi, S. Pailhès, M. M. Koza, B. Malaman, A. Dauscher, J. Tobola, O. Boisron, L. Saviot, and B. Lenoir, From crystal to glass-like thermal conductivity in crystalline minerals, Phys. Chem. Chem. Phys. **17**, 19751 (2015).

[12] T. Takabatake, K. Suekuni, T. Nakayama, and E. Kaneshita, Phonon-glass electron-crystal thermoelectric clathrates: Experiments and theory, Rev. Mod. Phys. **86**, 669 (2014).

[13] P.-F. Lory, S. Pailhès, V. M. Giordano, H. Euchner, H. D. Nguyen, R. Ramlau, H. Borrmann, M. Schmidt, M. Baitinger, M. Ikeda *et al.*, Direct measurement of individual phonon lifetimes in the clathrate compound $Ba_{7.81}Ge_{40.67}Au_{5.33}$, Nat. Commun. **8**, 491 (2017).

[14] S. Pailhès, H. Euchner, V. M. Giordano, R. Debord, A. Assy, S. Gomès, A. Bosak, D. Machon, S. Paschen, and M. de Boissieu, Localization of Propagative Phonons in a Perfectly Crystalline Solid, Phys. Rev. Lett. **113**, 025506 (2014).

[15] H. Euchner, S. Pailhès, L. T. K. Nguyen, W. Assmus, F. Ritter, A. Haghighirad, Y. Grin, S. Paschen, and M. de Boissieu, Phononic filter effect of rattling phonons in the thermoelectric clathrate $Ba_8Ge_{40+x}Ni_{6-x}$, Phys. Rev. B **86**, 224303 (2012).

[16] P. Norouzzadeh and C. W. Myles, A first-principles lattice dynamical study of type-I, type-II, and type-VIII silicon clathrates, J. Mater. Sci. **51**, 4538 (2016).

[17] H. Euchner, S. Pailhès, V. M. Giordano, and M. de Boissieu, Understanding lattice thermal conductivity in thermoelectric clathrates: A density functional theory study on binary Si-based type-I clathrates, Phys. Rev. B **97**, 014304 (2018).

[18] J. Dong, O. F. Sankey, and C. W. Myles, Theoretical Study of The Lattice Thermal Conductivity in Ge Framework Semiconductors, Phys. Rev. Lett. **86**, 2361 (2001).

[19] M. S. Ikeda, H. Euchner, X. Yan, P. Tomeš, A. Prokofiev, L. Prochaska, G. Lientschnig, R. Svagera, S. Hartmann, E. Gati, M. Lang, and S. Paschen, Kondo-like phonon scattering in thermoelectric clathrates, Nat. Commun. **10**, 887 (2019).

[20] R. Viennois, M. M. Koza, R. Debord, P. Toulemonde, H. Mutka, and S. Pailhès, Anisotropic low-energy vibrational modes as an effect of cage geometry in the binary barium silicon clathrate $Ba_{24}Si_{100}$, Phys. Rev. B **101**, 224302 (2020).

[21] T. Tadano, Y. Gohda, and S. Tsuneyuki, Impact of Rattlers on Thermal Conductivity of a Thermoelectric Clathrate: A First-Principles Study, Phys. Rev. Lett. **114**, 095501 (2015).

[22] M. A. Avila, K. Suekuni, K. Umeo, H. Fukuoka, S. Yamanaka, and T. Takabatake, Glasslike versus crystalline thermal conductivity in carrier-tuned $Ba_8Ga_{16}X_{30}$ clathrates (X = Ge, Sn), Phys. Rev. B **74**, 125109 (2006).

[23] B. C. Sales, B. C. Chakoumakos, R. Jin, J. R. Thompson, and D. Mandrus, Structural, magnetic, thermal, and transport properties of $X_8Ga_{16}Ge_{30}$ (X = Eu, Sr, Ba) single crystals, Phys. Rev. B **63**, 245113 (2001).

[24] A. F. May, E. S. Toberer, A. Saramat, and G. J. Snyder, Characterization and analysis of thermoelectric transport in n-type $Ba_8Ga_{16-x}Ge_{30+x}$, Phys. Rev. B **80**, 125205 (2009).

[25] C. Candolfi, M. M. Koza, U. Aydemir, W. Carrillo-Cabrera, Y. Grin, F. Steglich, and M. Baitinger, Vibrational dynamics of the type-I clathrates$A_8Sn_{44}\square_2$ (A = Cs, Rb, K) from lattice-dynamics calculations, inelastic neutron scattering, and specific heat measurements, J. Appl. Phys. **127**, 145104 (2020).

[26] G. S. Nolas, J. L. Cohn, J. S. Dyck, C. Uher, and J. Yang, Transport properties of polycrystalline type-I Sn clathrates, Phys. Rev. B **65**, 165201 (2002).

[27] Y. Liu, Q. Xi, J. Zhou, T. Nakayama, and B. Li, Phonon-glass dynamics in thermoelectric clathrates, Phys. Rev. B **93**, 214305 (2016).

[28] Q. Xi, Z. Zhang, J. Chen, J. Zhou, T. Nakayama, and B. Li, Hopping processes explain linear rise in temperature of thermal conductivity in thermoelectric clathrates with off-center guest atoms, Phys. Rev. B **96**, 064306 (2017).

[29] S. Johnsen, M. Christensen, B. Thomsen, G. K. H. Madsen, and B. B. Iversen, Barium dynamics in noble-metal clathrates, Phys. Rev. B **82**, 184303 (2010).

[30] H. Zhang, H. Borrmann, N. Oeschler, C. Candolfi, W. Schnelle, M. Schmidt, U. Burkhardt, M. Baitinger, J.-T. Zhao, and Y. Grin, Atomic interactions in the p-type clathrate I $Ba_8Au_{5.3}Ge_{40.7}$, Inorg. Chem. **50**, 1250 (2011).

[31] Z. Ye, J. Y. Cho, M. M. Tessema, J. R. Salvador, R. A. Waldo, J. Yang, H. Wang, W. Cai, M. Kirkham, J. Yang, and W. Zhang, Thermoelectric properties of Au-containing type-I clathrates $Ba_8Au_xGa_{16-3x}Ge_{30+2x}$, J. Alloys Compd. **587**, 747 (2014).

[32] M. Christensen, N. Lock, J. Overgaard, and B. B. Iversen, Crystal structures of thermoelectric n- and p-type $Ba_8Ga_{16}Ge_{30}$ studied by single crystal, multitemperature, neutron diffraction, conventional X-ray diffraction and resonant synchrotron X-ray diffraction, J. Am. Chem. Soc. **128**, 15657 (2006).

[33] G. K. H. Madsen, A. Katre, and C. Bera, Calculating the thermal conductivity of the silicon clathrates using the quasi-harmonic approximation, Phys. Status Solidi A **213**, 802 (2015).

[34] H. Euchner and A. Groß, Predicting accurate phonon spectra: An improved description of lattice dynamics in thermoelectric clathrates based on the SCAN meta-GGA functional, Chem. Mater. **31**, 2571 (2019).

[35] P.-F. Lory, V. M. Giordano, P. Gille, H. Euchner, M. Mihalkovič, E. Pellegrini, M. Gonzalez, L.-P. Regnault, P. Bastie, H. Schober *et al.*, Impact of structural complexity and disorder on lattice dynamics and thermal conductivity in the o-$Al_{13}Co_4$ phase, Phys. Rev. B **102**, 024303 (2020).

[36] T. Tadano and S. Tsuneyuki, First-principles lattice dynamics method for strongly anharmonic crystals, J. Phys. Soc. Jpn. **87**, 041015 (2018).

[37] I. Errea, M. Calandra, and F. Mauri, Anharmonic free energies and phonon dispersions from the stochastic self-consistent harmonic approximation: Application to platinum and palladium hydrides, Phys. Rev. B **89**, 064302 (2014).

[38] T. Lan, C. W. Li, O. Hellman, D. S. Kim, J. A. Muñoz, H. Smith, D. L. Abernathy, and B. Fultz, Phonon quarticity induced by changes in phonon-tracked hybridization during lattice expansion and its stabilization of rutile TiO_2, Phys. Rev. B **92**, 054304 (2015).

[39] T. Tadano and S. Tsuneyuki, Self-consistent phonon calculations of lattice dynamical properties in cubic $SrTiO_3$ with first-principles anharmonic force constants, Phys. Rev. B **92**, 054301 (2015).

[40] W. Sano, T. Koretsune, T. Tadano, R. Akashi, and R. Arita, Effect of van Hove singularities on high-T_c superconductivity in H_3S, Phys. Rev. B **93**, 094525 (2016).

[41] Y. Oba, T. Tadano, R. Akashi, and S. Tsuneyuki, First-principles study of phonon anharmonicity and negative thermal expansion in ScF_3, Phys. Rev. Materials **3**, 033601 (2019).

[42] Y.-N. Wu, W. A. Saidi, J. K. Wuenschell, T. Tadano, P. Ohodnicki, B. Chorpening, and Y. Duan, Anharmonicity explains temperature renormalization effects of the band gap in $SrTiO_3$, J. Phys. Chem. Lett. **11**, 2518 (2020).

[43] T. Tadano and S. Tsuneyuki, Quartic Anharmonicity of Rattlers and its Effect on Lattice Thermal Conductivity of Clathrates from First Principles, Phys. Rev. Lett. **120**, 105901 (2018).

[44] S. Pailhès, V. M. Giordano, P.-F. Lory, M. D. Boissieu, and H. Euchner, X-rays and neutrons spectroscopy for the investigation of individual phonons properties in crystalline and amorphous solids, in *Nanostructured Semiconductors*, edited by K. Termentzidis (Jenny Stanford Publishing, New York, 2017), Chap. 19.

[45] G. Kresse and J. Hafner, *Ab initio* molecular dynamics for liquid metals, Phys. Rev. B **47**, 558 (1993).

[46] G. Kresse and J. Furthmüller, Efficient iterative schemes for *ab initio* total-energy calculations using a plane-wave basis set, Phys. Rev. B **54**, 11169 (1996).

[47] G. Kresse and D. Joubert, From ultrasoft pseudopotentials to the projector augmented-wave method, Phys. Rev. B **59**, 1758 (1999).

[48] J. Sun, A. Ruzsinszky, and J. P. Perdew, Strongly Constrained and Appropriately Normed Semilocal Density Functional, Phys. Rev. Lett. **115**, 036402 (2015).

[49] A. Togo and I. Tanaka, First principles phonon calculations in materials science, Scr. Mater. **108**, 1 (2015).

[50] M. Falmbigl, G. Rogl, P. Rogl, M. Kriegisch, H. Müller, E. Bauer, M. Reinecker, and W. Schranz, Thermal expansion of thermoelectric type-I-clathrates, J. Appl. Phys. **108**, 043529 (2010).

[51] G. D. Mukherjee, C. Bansal, and A. Chatterjee, Thermal Expansion Study of Ordered and Disordered Fe_3Al: An Effective Approach for the Determination of Vibrational Entropy, Phys. Rev. Lett. **76**, 1876 (1996).

[52] W. Han-Fu, C. Wei-Guo, G. Yan-Jun, and J. Hao, Thermal transport property of Ge_{34} and d-Ge investigated by molecular dynamics and the Slack's equation, Chinese Phys. B **19**, 076501 (2010).

[53] R. L. González-Romero, C. R. Miranda, M. A. Avila, and A. Antonelli, Hosting of La^{3+} guest ions in type-I Ge clathrates: A first-principles characterization for thermoelectric applications, Comput. Mater. Sci. **122**, 46 (2016).

[54] A. Bhattacharya, Deviation from guest dominated glass like lattice dynamics in prototypical ternary $Ba_8Ni_xGe_{46-x-y-\square}$ clathrates, J. Phys.: Condens. Matter **32**, 175502 (2020).

[55] A. Khabibullin, T. Huan, G. Nolas, and L. Woods, Cage disorder and gas encapsulation as routes to tailor properties of inorganic clathrates, Acta Mater. **131**, 475 (2017).

[56] X. Tang, J. Dong, P. Hutchins, O. Shebanova, J. Gryko, P. Barnes, J. K. Cockroft, M. Vickers, and P. F. McMillan, Thermal properties of Si_{136}: Theoretical and experimental study of the type-II clathrate polymorph of Si, Phys. Rev. B **74**, 014109 (2006).

[57] W. Zhang, Z. Zeng, N. Ge, and Z. Li, Lattice dynamics study of phonon instability and thermal properties of type–I clathrate K_8Si_{46} under high pressure, Materials **9**, 616 (2016).

[58] M. Zebarjadi, E. Keivan, and C. Gang, Thermal conductivity of cage-like structures, *ASME/JSME 2011 8th Thermal Engineering Joint Conference, Honolulu, Hawaii, USA* (ASME International, 2011).

[59] M. Christensen, A. B. Abrahamsen, N. B. Christensen, F. Juranyi, N. H. Andersen, K. Lefmann, J. Andreasson, C. R. H. Bahl, and B. B. Iversen, Avoided crossing of rattler modes in thermoelectric materials, Nat. Mater. **7**, 811 (2008).

[60] M. M. Koza, M. R. Johnson, R. Viennois, H. Mutka, L. Girard, and D. Ravot, Breakdown of phonon glass paradigm in La- and Ce-filled Fe_4Sb_{12} skutterudites, Nat. Mater. **7**, 805 (2008).

[61] Y. Takasu, T. Hasegawa, N. Ogita, M. Udagawa, M. A. Avila, K. Suekuni, I. Ishii, T. Suzuki, and T. Takabatake, Dynamical properties of guest ions in the type-I clathrate compounds $X_8Ga_{16}Ge_{30}$ (X = Eu, Sr, Ba) investigated by Raman scattering, Phys. Rev. B **74**, 174303 (2006).

[62] Y. Takasu, T. Hasegawa, N. Ogita, M. Udagawa, M. A. Avila, K. Suekuni, and T. Takabatake, Off-Center Rattling and Anisotropic Expansion of Type-I Clathrates Studied by Raman Scattering, Phys. Rev. Lett. **100**, 165503 (2008).

[63] Y. Takasu, T. Hasegawa, N. Ogita, M. Udagawa, M. A. Avila, K. Suekuni, and T. Takabatake, Off-center rattling and cage vibration of the carrier-tuned type-I clathrate $Ba_8Ga_{16}Ge_{30}$ studied by Raman scattering, Phys. Rev. B **82**, 134302 (2010).

[64] M. M. Koza, M. R. Johnson, H. Mutka, M. Rotter, N. Nasir, A. Grytsiv, and P. Rogl, Vibrational dynamics of the type-I clathrate $Ba_8Zn_xGe_{46-x-y}\square_y$ ($x = 0, 2, 4, 6, 8$), Phys. Rev. B **82**, 214301 (2010).

[65] Data for this paper are available at https://doi.ill.fr/10.5291/ILL-DATA.7-01-494 and https://doi.ill.fr/10.5291/ILL-DATA.7-01-449.

[66] www.ecmetac.eu.

[67] G. Shirane, S. M. Shapiro, and J. M. Tranquada, *Neutron Scattering with a Triple-Axis Spectrometer* (Cambridge University Press, Cambridge, 2015).

[68] O. Arnold, J. Bilheux, J. Borreguero, A. Buts, S. Campbell, L. Chapon, M. Doucet, N. Draper, R. F. Leal, M. Gigg *et al.*, Mantid—Data analysis and visualization package for neutron scattering and μ SR experiments, Nucl. Instrum. Meth. A **764**, 156 (2014).

[69] R. Ewings, A. Buts, M. Le, J. van Duijn, I. Bustinduy, and T. Perring, Horace: Software for the analysis of data from single crystal spectroscopy experiments at time-of-flight neutron instruments, Nucl. Instrum. Meth. A **834**, 132 (2016).

[70] G. Ehlers, A. A. Podlesnyak, J. L. Niedziela, E. B. Iverson, and P. E. Sokol, The new cold neutron chopper spectrometer at the Spallation Neutron Source: Design and performance, Rev. Sci. Instrum. **82**, 085108 (2011).

[71] W. Reichardt, MUPHOCOR, A Fortran program to determine the phonon density of states from neutron scattering experiments, Report No. 13.03.01P06L, Institut für Nukleare Festkorper Physik, Kernforschung Szentrum, Karlsruhe GMBH, Germany.

[72] D. Richard, M. Ferrand, and G. J. Kearley, Analysis and visualisation of neutron-scattering data, J. Neutron Res. **4**, 33 (1996).

[73] M. T. Rekveldt, T. Keller, and R. Golub, Larmor precession, a technique for high-sensitivity neutron diffraction, Europhys. Lett. **54**, 342 (2001).

[74] T. Keller, M. Rekveldt, and K. Habicht, Neutron Larmor diffraction measurement of the lattice-spacing spread of pyrolytic graphite, Appl. Phys. A: Mater. **74**, s127 (2002).

[75] M. Ono, Y. Waku, K. Habicht, and T. Keller, Neutron larmor diffraction measurement of strain in a ductile composite $Al_2O_3/Y_3Al_5O_{12}$ (YAG), Appl. Phys. A: Mater. **74**, s73 (2002).

[76] T. Keller, P. Fabrykiewicz, R. Przeniosło, I. Sosnowska, and B. Keimer, Neutron Larmor diffraction on powder samples, J. Appl. Crystallogr. **53**, 88 (2020).

[77] F. I. Fedorov, *Theory of Elastic Waves in Crystals* (Springer US, New York, 1968).

[78] A. Authier and A. Zarembowitch, in *International Tables for Crystallography*, edited by A. Authier, Vol. D (Springer, Dordrecht, 2006), Chap. 1.3, pp. 72–98.

[79] F. Mouhat and F.-X. Coudert, Necessary and sufficient elastic stability conditions in various crystal systems, Phys. Rev. B **90**, 224104 (2014).

[80] N. L. Okamoto, T. Nakano, K. Tanaka, and H. Inui, Mechanical and thermal properties of single crystals of the type–I clathrate compounds $Ba_8Ga_{16}Ge_{30}$ and $Sr_8Ga_{16}Ge_{30}$, J. Appl. Phys. **104**, 013529 (2008).

[81] I. Zerec, V. Keppens, M. A. McGuire, D. Mandrus, B. C. Sales, and P. Thalmeier, Four-Well Tunneling States and Elastic Response of Clathrates, Phys. Rev. Lett. **92**, 185502 (2004).

[82] F. H. Stillinger, *Energy Landscapes, Inherent Structures, and Condensed-Matter Phenomena* (Princeton University Press, Princeton, 2015).

4.2 Phonon behavior in a random solid solution: A lattice dynamics study on the high-entropy alloy FeCoCrMnNi

State of the article: submitted to an international peer-reviewed journal for review.
Authors: *Shelby R. Turner, Stéphane Pailhès, Frédéric Bourdarot, Jacques Ollivier, Yvan Sidis, John-Paul Castellan, Jean-Marc Zanotti, Quentin Berrod, Florence Porcher, Alexei Bosak, Michael Feuerbacher, Helmut Schober, Marc de Boissieu, Valentina M. Giordano*

This article has provided a first analysis of the full lattice dynamics study of a five-element random solid solution. As these are the first results of this kind, I have taken the time to methodically compare the evolution of chemical disorder from the single element Ni, to the random binary alloys NiFe and NiCo, and finally the fully disordered, random solid solution high-entropy alloy (HEA) FeCoCrMnNi itself through experimentally-measured phonon dispersions, intrinsic linewidths, and the generalized vibrational density of states (GVDOS).

Along with elemental and binary alloy comparisons, this article acts as a critical review of sorts, with comparisons made across other complex metallic alloys (CMAs) and glasses, and, in particular metallic glasses which are the forerunner to HEAs. Besides the technical relevance that this presents, which will be discussed in the following paragraph, it also serves as a call to these research communities, signaling a pattern that is detailed in this article and that links these different complex and disordered systems.

There is a visible change in regime in the energy dependence of the intrinsic phonon linewidths in FeCoCrMnNi that hints at a change in the way phonons interact with the disorder on local and long-range atomic scales. This change in regime has been evidenced in clathrates [27] (see also Fig. 3.17 in this thesis), quasicrystals [122, 207, 208, 258], and glasses [259–262]. For glasses, the change in regime has been widely accepted as linked to the Boson peak, and to the moment that the phonons go from propagative to diffusive. For clathrates and quasicrystals, it is more associated to the onset of low-lying optical branches that interact with or otherwise interrupt the pure acoustic regime. Moreover, in all of these systems, the energy of the crossover is correlated to the energy in the density of states at which we depart from the Debye regime. Even if the reasoning is different, the general conclusion between these studies and the one now of FeCoCrMnNi is that this regime crossover takes place at the wavelength in which the acoustic phonon becomes sensitive to the local disorder or complexity of each system.

By publishing this work, I acknowledge this pattern, pointing out that this feature should be checked for in other similarly disordered and complex systems. These kinds of global similarities between types of disordered and complex systems will help lead us towards a unified understanding of their heat transport mechanisms.

Contributions of the Ph.D Candidate:

I played a central role in preparing and conducting the X-ray and neutron experiments on 1T@LLB, 3T2@LLB, IN5@ILL, IN6-SHARP@ILL, and ID28@ESRF. I then made the full data analysis and wrote the paper.

Perspectives/Further work that can be done:

HEAs provide us with a wide range of elemental combinations that can each emphasize or reduce certain forms of complexity. Future work should include similar lattice dynamics studies on a series of HEAs to target different types of chemical short-range ordering, atomic size and mass differences, and force constant fluctuations. Like clathrates, HEAs should each be viewed as case studies with which we can build up a large database of in order to draw broader conclusions.

A further advantage in favor of HEA case studies is the fact that intrinsic phonon linewidths were measured by Inelastic X-ray Scattering, which is a much more accessible measurement than Neutron Resonance Spin Echo which was needed for the clathrate $Ba_{7.81}Ge_{40.67}Au_{5.33}$ linewidths.

Again in comparison with type-I clathrates, which all form simple cubic structures, HEAs can form three possible lattices: BCC, FCC, and HCP. Therefore, another possible avenue of interest would be to complete similar lattice dynamics studies for BCC and HCP HEAs: not only are these structures generally formed with atoms of stronger size and mass contrast, but they are also characterized by different interatomic distances, therefore changing the possible lattice distortions in comparison to those of the FCC structure. A first-principles study has already been published on phonon broadening found in four and five element BCC HEAs [263].

Phonon behavior in a random solid solution: a lattice dynamics study on the high-entropy alloy FeCoCrMnNi

Shelby R. Turner,[1,2,3] Stéphane Pailhès,[3] Frédéric Bourdarot,[4] Jacques Ollivier,[1] Yvan Sidis,[5] John-Paul Castellan,[5,6] Jean-Marc Zanotti,[5] Quentin Berrod,[7] Florence Porcher,[5] Alexei Bosak,[8] Michael Feuerbacher,[9] Helmut Schober,[1] Marc de Boissieu,[2] and Valentina M. Giordano[3,*]

[1] *Institut Laue-Langevin, F-38042 Grenoble cedex, France*
[2] *Université Grenoble Alpes, CNRS, Grenoble-INP, SIMaP, F-38000 Grenoble, France*
[3] *Institute of Light and Matter, UMR5306 Université Lyon 1-CNRS, Université de Lyon, F-69622 Villeurbanne cedex, France*
[4] *Université Grenoble Alpes, CEA, IRIG, MEM, MDN, F-38000 Grenoble cedex, France*
[5] *Université Paris-Saclay, CNRS, CEA, Laboratoire Léon Brillouin, F-91191 Gif-sur-Yvette, France*
[6] *Institut für Festkörperphysik, Karlsruher Institut für Technologie, D-76021 Karlsruhe, Germany*
[7] *Université Grenoble Alpes, CEA, CNRS, IRIG-SyMMES, F-38000 Grenoble cedex, France*
[8] *European Synchrotron Radiation Facility, BP 220, F-38043 Grenoble cedex, France*
[9] *Peter Grünberg Institut PGI-5 and ER-C, FZ Jülich GmbH, D-52425 Jülich, Germany*

(Dated: August 23, 2021)

High-Entropy Alloys (HEAs) are a new family of crystalline metallic alloys which are currently at the forefront of materials research for their exceptional mechanical properties. They are random solid solutions containing four or more elements in a simple cubic or hexagonal cell. Despite the simplicity of the structure, the inherently strong chemical disorder is believed to deeply affect the physical properties of the material, and, more specifically, to strongly scatter acoustic phonons, which are responsible for the thermal properties. Similar properties have also been reported in glasses and some complex metallic alloys, where phonon dynamics are dominated by the topological disorder and the structural complexity, respectively. As such, HEAs offer a unique opportunity to shed light on the effect of disorder and increasing complexity on vibrational properties, bridging the gap between glasses and complex crystalline materials.

Here we present the first experimental investigation of the lattice dynamics in the HEA $Fe_{20}Co_{20}Cr_{20}Mn_{20}Ni_{20}$ using inelastic neutron and X-ray scattering. Despite the strong chemical disorder, well-defined acoustic phonons are found to propagate across the whole Brillouin zone, with dispersions very similar to the ones of the simple elements composing this HEA. Still, force-constant fluctuations are found to play a major role in determining phonon linewidths by causing an increased broadening at the unit cell lengthscale, as predicted by recent theoretical models,. The global dynamics are found to be very different from both glasses and complex metallic alloys, in which acoustic phonons can propagate only in a limited $(q, \hbar\omega)$ space. Still, a similar strong phonon scattering regime is found in some directions and polarizations, which can be ascribed to the force-constant fluctuations, and which arises simultaneously with the deviation of the acoustic dynamics from the Debye prediction.

I. INTRODUCTION

In recent years, a new family of crystalline metallic materials has been discovered and has come to the forefront of materials research for their exceptional mechanical properties: High-Entropy Alloys (HEAs), credited to both Yeh *et al.* [1] and Cantor *et al.* [2], who simultaneously published in 2004. These materials, obtained with casting techniques from the melt, are characterized by improved mechanical strength, high resistance to corrosion, magnetic properties, high-temperature capabilities, and many other unique characteristics [3–6], which are believed to be the result of the high entropy mixing of many elements. Indeed, HEAs are single-phase, equiatomic alloys with four or more elements that are evenly dispersed in an ordered, close-packed, and simple crystalline structure, forming a random solid solution [7, 8]. Despite their long range ordered and simple structure, HEAs exhibit thermal conductivities much lower than in simple metals, going from some tens of W/mK [9] down to less than 2 W/mK, corresponding to a lattice contribution of less than 1 W/mK [10], which is comparable to non-crystalline materials. Moreover, a non-monotonic temperature dependence of this latter has often been reported [9–11], indicating the presence of different mechanisms at play that rule thermal transport in these materials. Interestingly, an almost temperature independent thermal conductivity close to room temperature has been recently reported in $Ni_2CuCrFeAl_x$ [12].

Similar mechanical and thermal properties have previously been found in two other similar, yet intrinsically different, families, namely, metallic glasses (MGs) and complex metallic alloys (CMAs), the former characterized by a disordered atomic structure with strong short range order [13–16] and the latter by a large unit cell (10 Å or larger) containing a large number of atoms organized in local (sub)nanostructures and frequently associated with intrinsic disorder [17–19]. Indeed, both glasses [20] and many CMAs [19, 21–26] exhibit a low and weakly temperature dependent lattice thermal conductivity, along with the emergence of a low temperature plateau. Still, such similar thermal properties have been

ascribed to very different mechanisms: a strong phonon scattering due to the presence of elastic heterogeneities at the nanoscale in glasses [27, 28], and the modification of the acoustic phonon spectrum due to the presence of a large number of optic modes in CMAs [29–34].

The question then arises on the position of HEAs in this context: characterized by a long range order on a very simple FCC, BCC, or HCP unit cell, they should in principle belong to the CMAs family, although their lattice parameter is only a few Å. Still, as random solid solutions, they present a strong local chemical disorder, which introduces disorder at a larger lengthscale, disrupting the translational invariance, and drawing them closer to glassy materials. The question is then whether they can be associated to one of these families or whether they represent a new family of materials whose complexity is at the frontier somewhere between them.

The aim of this paper is to answer this question by thoroughly investigating the phonon dynamics in a prototype HEA, and comparing its vibrational properties to the ones which have been dubbed as responsible for similar thermal behavior in glasses and CMAs. As such, unveiling the effect of the strong chemical disorder on phonons in HEAs carries the promise of bridging the gap between complex metallic alloys and fully disordered glasses, disentangling the effect of three different kinds of disorder present in random crystalline alloys and which are responsible for phonon scattering: i) atomic mass, ii) atomic size, whose differences induce strain in the lattice, and iii) force constants. Even if the effect of atomic mass difference has been largely investigated in binary alloys both experimentally and theoretically [35–37], the effect of force-constant fluctuations, although already evidenced experimentally in a few binary alloys [38, 39], has been more challenging to calculate [39] and has only recently been explored both theoretically and experimentally in ternary alloys [40, 41]. In this context, HEAs offer a unique playground for tuning the relative weight of these different features thanks to the possibility of customizing their composition [41, 42].

Here we provide the first experimental investigation of phonon dynamics in an HEA, made possible by the recent and successful synthesis of large single-grain crystals for the HEA of composition $Fe_{20}Co_{20}Cr_{20}Mn_{20}Ni_{20}$ (from now on FeCoCrMnNi) [43]. Built from 5 direct-neighbor elements in the periodic table, FeCoCrMnNi exhibits large differences in neither atomic mass nor atomic size [44]. As we will show, this HEA presents simple phonon dynamics which closely matches those of binary alloys and simple elements that make up its composition. However, while its dispersions are close to those of the single elements, HEA lifetimes are much shorter, and can be understood in terms of scattering from force-constant fluctuations, as predicted by recent theoretical developments [41]. Even if our HEA shares a main source of scattering with glasses at a lengthscale of a few tens of Angstroms, the phonons remain well defined and propagate over the entire Brillouin zone, loosing their propagative character only at a lengthscale comparable with the nearest neighbors distance. As opposed to both glasses and CMAs, the present HEA actually keeps a large propagative acoustic phase space up to energies of ∼20-30 meV and wavevectors larger than 1 $Å^{-1}$.

II. SAMPLE CHARACTERIZATION

FeCoCrMnNi is known as the Cantor-Wu HEA, as it was Cantor *et al.* [2] that detailed FeCoCrMnNi as a single-phase, multi-component alloy of FCC structure. The results in this paper come from the use of both polycrystalline and single crystal samples of FeCoCrMnNi, prepared following the procedure detailed in Appendix A of the Supplementary Material [45].

The samples were then investigated by Scanning Electron Microscopy (SEM) using a JEOL 840 microscope, equipped with an EDAX Energy-Dispersive X-ray (EDX) system, as seen in Appendix A of the Supplementary Material [45]. The homogenized polycrystalline samples had an overall composition of $Fe_{19.89}Co_{20.97}Cr_{17.82}Mn_{19.54}Ni_{21.78}$ at.% with a homogeneous matrix. Small Cr-rich precipitates of about 1 μm in diameter were found with a volume fraction far below 1%. The overall composition of the Bridgman single crystal was determined to be $Fe_{20.00}Co_{19.64}Cr_{20.33}Mn_{20.10}Ni_{19.94}$ at.%. Optical microscopy of etched surfaces shows the presence of a dendritic structure on a 100 μm scale, which may be due to slight composition fluctuations. The single crystalline state and the primary orientation of the Bridgman crystal was determined using a Philips Micro X-ray Laue apparatus in back-reflection geometry. The produced crystal consisted of one dominant single grain with a volume of about 6 to 7 cm^3, and a number of minor secondary grains, which were cut off by spark erosion before further preparation. Oriented single crystalline samples were cut from the dominant single grain by spark erosion.

The FCC structure and space group of the polycrystalline sample were also confirmed by neutron diffraction at the Laboratoire Léon Brillouin (LLB). The thermal-neutron two-axis powder diffractometer 3T-2@LLB with an incident wavelength $\lambda = 1.225$ Å was used to measure the polycrystalline sample at 300 K. The diffraction pattern is shown in Fig. 1. All available Bragg peaks can be indexed to an FCC structure within the $Fm\bar{3}m$ space group using a pattern matching fit, and the lattice parameter was found to be 3.595(1) Å, confirming that our FeCoCrMnNi is a single phase material with no phase separation.

Possible short range ordering and strain distribution were investigated by X-ray diffuse scattering at the ID28 beamline of the European Synchrotron Radiation Facility (ESRF). The observed intensity distribution around the Bragg peaks corresponds to the sum of the temperature-dependent thermal diffuse scattering and Huang scattering, the latter of which is not expected to show a strong

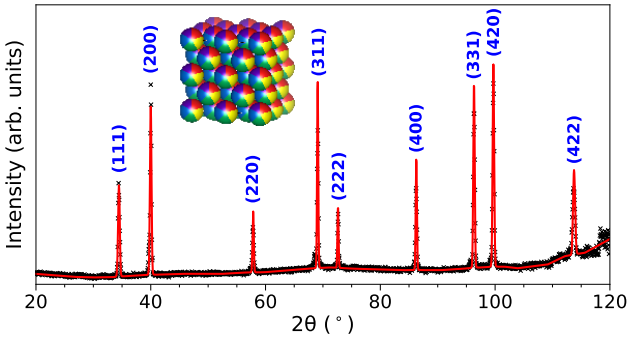

FIG. 1. "Color" Neutron diffraction pattern of the polycrystalline sample of FeCoCrMnNi used for neutron experiments, measured at 3T-2@LLB with an incident neutron wavelength of 1.225 Å at 300 K. All peaks have been indexed to an FCC structure, space group $Fm\bar{3}m$. The pattern matching fit is reported as a solid red line. The inset is a visual interpretation of the FeCoCrMnNi FCC structure (made with VESTA [46]) in which each of the 5 elements has equal chance of occupying each atomic position, creating a random solid solution.

temperature dependence. The Huang scattering contribution reflects the strain associated with the atomic size spread in the sample. More details are reported in Appendix A of the Supplementary Material [45]. In a preliminary neutron diffuse scattering experiment at the D7 beamline of ILL, we could observe weak signatures of a possible short range ordering on a 10 Å lengthscale. However, this result needs to be confirmed by further studies [47].

III. METHODS

We investigated the phonon dynamics by means of inelastic X-ray and neutron scattering (IXS,INS) on both polycrystalline and single crystalline samples. The Generalized Vibrational Density of States (GVDOS) was measured using the cold-neutron Time-of-Flight (TOF) technique at the Institut Laue-Langevin (ILL). The measurements on the polycrystalline sample were performed on the IN6-SHARP beamline at 100, 200 and 300 K. The neutron incident wavelength was $\lambda = 5.1$ Å, resulting in a $\mathbf{Q}$ range of 0-2.1 Å^{-1} at $S(\mathbf{Q}, E = 0)$.

The measurements on the single crystal, on the other hand, were performed on the IN5 beamline at 300 K. The crystal was aligned in the scattering plane ([100]; [010]), allowing wavevectors of $\mathbf{Q} = \frac{2\pi}{a}(\zeta, \xi, 0)$. The neutron incident wavelength was $\lambda = 3.2$ Å, resulting in a $\mathbf{Q}$ range of 0-3.6 Å^{-1} at $S(\mathbf{Q}, E = 0)$, and encompassing the first Bragg peak visible in the given scattering plane, (200). Details on the TOF data integration and treatment for the resulting GVDOS plots can be found in Appendix B of the Supplementary Material [45].

The individual phonon dispersions were measured on two different single crystals, one for INS and one for IXS. The INS sample, a cylinder rod 10 cm long and 2 cm wide, was aligned in the scattering plane ([100]; [010]), and measurements were taken on the thermal-neutron Triple-Axis Spectrometer (TAS) 1T-1 at LLB at 3, 100, and 300 K, with a fixed $k_f = 2.662$ Å^{-1} near the intense Bragg peaks (020) and (220). The standard cryostat environment was used for all temperature measurements. The IXS sample, a $\sim 100\mu$m length needle chemically etched from the INS one, was aligned in the ([001]; [110]) scattering plane for measurements taken on the ID28 beamline at ESRF at 15, 100, and 300 K with the help of a displex closed cycle cryocooler. The [999] reflection of the silicon monochromator was used, resulting in an incoming X-ray wavelength of 0.697 Å and an energy resolution of 2.8 meV. More information about the experiment specifics can be found in Appendix B of the Supplementary Material [45].

IV. GENERALIZED VIBRATIONAL DENSITY OF STATES

In order to first have a global view of the phonon behavior in FeCoCrMnNi, we have measured its GVDOS using both the polycrystalline and single crystalline samples. In Fig. 2(a), we report the GVDOS, which is normalized by the Bose-Einstein temperature dependence, of the polycrystalline sample as measured at 100, 200, and 300 K. The most striking feature here is the lack of a clear acoustic regime at low energy: rather than the usual Debye-like $(\hbar\omega)^2$ behavior, we observe a purely linear dependence up to about 12 meV. Moreover, the signal in this energy range does not follow the Bose-Einstein dependence on temperature, increasing in intensity with decreasing temperature, and we observe the appearance of a small additional peak at 14 meV at 100 K.

This behavior is in fact due to a dominant magnetic scattering signal also detected in the neutron TOF experiment when measuring at low $\mathbf{Q}$. Indeed, FeCoCrMnNi is known to be magnetic and to exhibit a magnetic transition at low temperature [49–55]. A full interpretation of magnetism in FeCoCrMnNi is outside the scope of this article. Still, it may be expected that magnetic fluctuations can also play a role in enhancing phonon scattering in this HEA, as recently pointed out within the community [42, 56].

In order to avoid the magnetic contamination, the measurements were performed with a smaller neutron wavelength on a single-grain crystal at room temperature. Here, as specified in Section III, the data collection encompasses a larger $\mathbf{Q}$ range (up to 3.6 Å^{-1} as opposed to 2.1 Å^{-1} for the polycrystalline sample), minimizing the relative weight of the low $\mathbf{Q}$ magnetic scattering in the average. As shown in Fig. 2(b), the result is that we now recapture a squared dependence of the acoustic region between 0-12 meV, confirming the Debye-like behavior of acoustic phonons in this HEA, and in agreement with previous calculations on random alloys [57]. This GV-

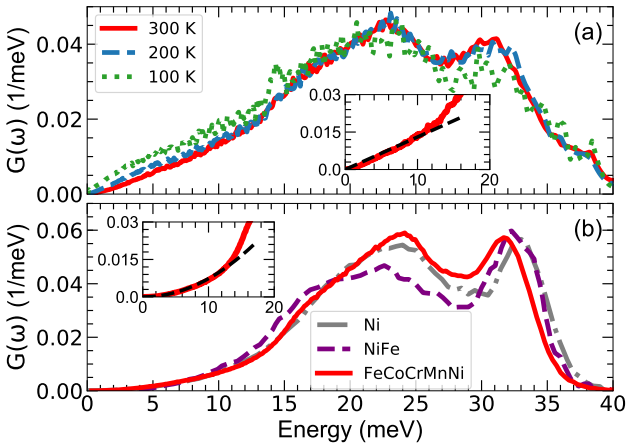

FIG. 2. "Color" Generalized Vibrational Density of States (GVDOS) of single-crystal and polycrystalline samples of the HEA FeCoCrMnNi. (a) GVDOS measured on the polycrystalline sample at IN6-SHARP@ILL with an incident neutron wavelength $\lambda = 5.1$ Å at three temperatures. (b) GVDOS measured on the single crystalline sample on IN5@ILL with a neutron wavelength $\lambda = 3.2$ Å, compared to that of the single element Ni [48] and the binary alloy NiFe [48]. Insets report the linear and squared dependencies (fits in black dashed lines) of FeCoCrMnNi in (a) and (b) at 300 K, respectively.

DOS compares very well to those of Ni and NiFe [48], also reported in the figure.

This progression from a single element, to a binary alloy, to an HEA has similarly been analyzed for other binary alloys of the same elements [48, 58–60] and the HEA FeCoCrNi [55, 61] in Appendix D of the Supplementary Material [45]: the GVDOS of these two HEAs appear to most closely match that of Ni. This can be explained by the fact that the neutron coherent scattering cross section of Ni and Fe are very similar to each other and almost 5 times the ones of Cr and Mn, and 10 times the one of Co.

V. INDIVIDUAL ACOUSTIC PHONON PROPERTIES

In an effort to further understand the acoustic regime of FeCoCrMnNi, the longitudinal and transverse acoustic (LA,TA) phonon dispersions in two high symmetry directions at 300 K have been measured. In Fig. 3, we report some selected spectra of four measured polarizations, specifically the TA mode propagating along $[\bar{1}00]$, polarized along [010] ($TA^{010}_{\bar{1}00}$), and the TA mode propagating along $[\bar{1}10]$, polarized along [110] ($TA^{110}_{\bar{1}10}$) (Fig. 3(a,b)), as measured by INS and the LA mode propagating along the [001] direction (LA_{001}) and the TA mode propagating along $[00\bar{1}]$, polarized along [110] ($TA^{110}_{00\bar{1}}$) (Fig. 3(c,d)), as measured by IXS. The measurements were performed around the intense (002) and (220) Bragg peaks. We remind the reader here that, given the cubic symmetry, $TA^{110}_{00\bar{1}}$ and $TA^{010}_{\bar{1}00}$ correspond to the same propagation direction but different polarizations. Additional scans of each of these four polarizations, and those of the LA mode propagating along the [110] direction (LA_{110}) and the TA mode propagating along [110], polarized along [001] (TA^{001}_{110}), can be found in Appendix E of the Supplementary Material [45].

Surprisingly for a system with such a strong chemical disorder, a well-defined phonon peak (*i.e.* $\Gamma \ll \hbar\omega$) is seen propagating in all polarizations until 25-30 meV, at the Brillouin zone boundary. In the INS scans, the phonon disperses on top of a broad, textured band in energy, which is roughly constant at all q within a given direction, as evidenced by overlaying all scans (see Fig. S8 in the Supplementary Material [45]), but appears to have slightly different texture and shape in each direction while still exhibiting two major features centered at 20 and 30 meV, as seen in Fig. 3(a.ii) and (b.iii), for example.

We have assigned this to incoherent neutron scattering, which, as a first approximation, leads to a signal proportional to the density of states multiplied by the square of the energy. Using a simple elemental neutron scattering cross-section calculation for FeCoCrMnNi, including the Laue contribution due to the random atomic distribution, the incoherent signal is expected to be ∼2.3 times the coherent one. Further evidence lies in the fact that the textured band has completely disappeared in the IXS measurements, where the X-ray incoherent contribution, which is related to the different atomic scattering factors of the elements, is negligible, thanks to the similar atomic numbers found in FeCoCrMnNi. A more detailed comparison between the expected incoherent signal for both probes and the experimental spectra is reported in Appendix B of the Supplementary Material [45].

The temperature dependencies of the observed inelastic excitations are reported in Fig. 4, after normalization by the expected Bose-Einstein temperature dependence. It can be seen that, in the INS experiment between 3 and 300 K, both acoustic phonons and the broad band respect the Bose-Einstein dependence and show no evolution in their energy position and shape with temperature, within our instrumental resolution. Concerning the IXS data measured between 15 and 300 K, the difficulties in the sample alignment at each temperature do not allow us to quantitatively compare the intensities at different temperatures. Still, we can confirm the independence of the phonons' energy positions and shape within our instrumental resolution.

Next, we have fit the data to extract phonon energies, normalized intensity, and linewidths. For this, we have modeled the coherent inelastic signal using a damped harmonic oscillator (DHO) convoluted with the instrumental resolution. More details on the calculation and deconvolution of the latter in the neutrons and X-ray experiments are reported in Appendices B.2 and B.3 of the Supplementary Material [45]. First, we can confirm the acoustic nature of the observed phonon mode, as it

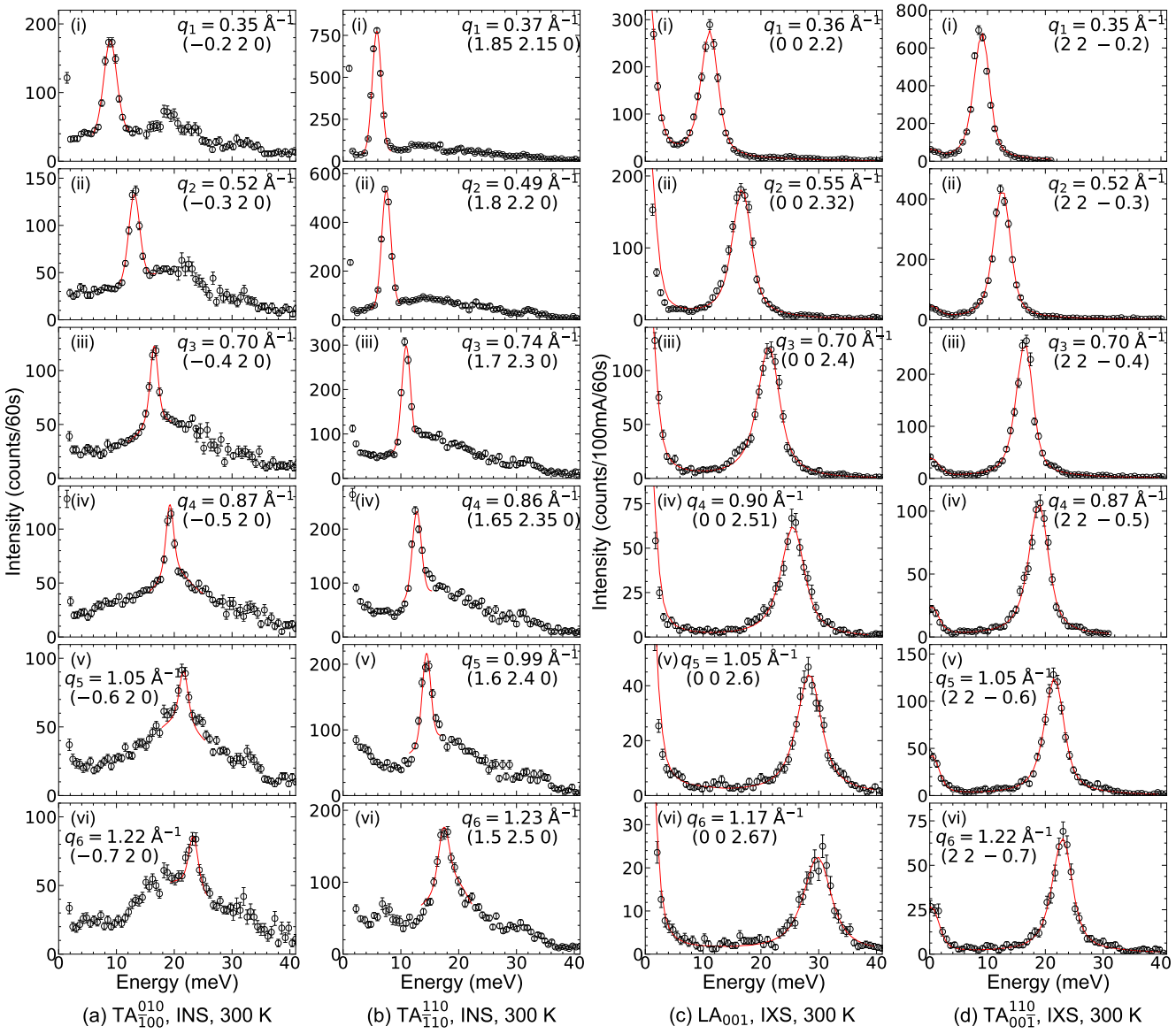

FIG. 3. "Color" Longitudinal and transverse acoustic (LA,TA) phonon energy scans measured at 300 K. (a) The TA dispersion propagating along $[\bar{1}00]$, polarized along [010], and (b) the TA dispersion propagating along $[\bar{1}10]$, polarized along [110]. (c) The LA dispersion propagating along [001], and (d) the TA dispersion propagating along $[00\bar{1}]$, polarized along [110]. Subplots in (a,b) have been measured by inelastic neutron scattering (INS), and those in (c,d) have been measured by inelastic X-ray scattering (IXS). All phonon modes were fit as damped harmonic oscillators (solid red lines). IXS scans represent different detectors on the instrument ID28@ESRF, and intensities have not been scaled for efficiencies between detectors. (This is also the reason some subplots have small $[\zeta\zeta 0]$ components.) The phonon wavevector has been matched across the different polarizations as best as possible.

keeps a constant normalized intensity over almost all of the Brillouin zone (more details in Appendix C of the Supplementary Material [45]). The LA and TA dispersions for the $[00\zeta]$ and $[\zeta\zeta 0]$ directions at different temperatures are reported in Fig. 5. We report the sound velocities extracted from our acoustic dispersions at low q in Table I, which are in good agreement with the ones calculated from the experimentally measured elastic constants reported in literature on the same material [64].

Also reported in Fig. 5 are the literature dispersions of pure Ni [62] and the random binary alloy NiFe [63]. The three materials appear to have similar acoustic dispersions in each direction. We have also verified the global agreement with the acoustic dispersions of Fe [65], Cr [66–68], Ni [62, 69], and binary alloys Fe-Ni [41, 63, 70, 71], Fe-Mn [72], Fe-Co [73], and Co-Ni [41, 74], not reported here. This can be understood in

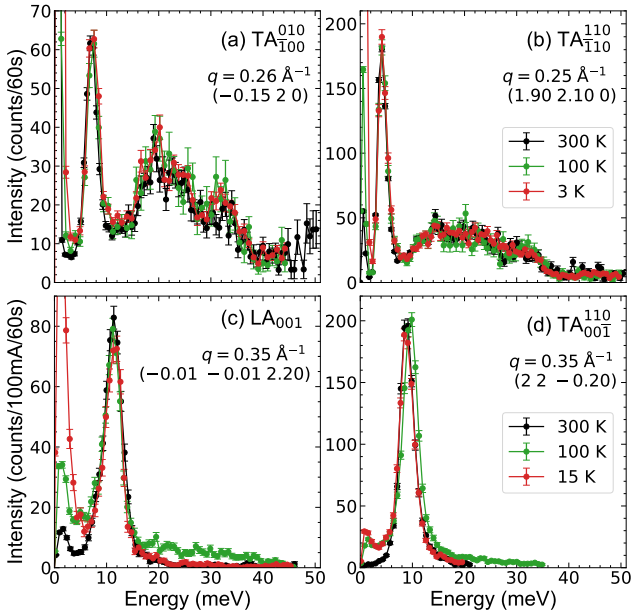

FIG. 4. "Color" Temperature dependence of representative energy scans across the acoustic phonon dispersions shown in Fig. 3. Subplots (a,b) have been measured by inelastic neutron scattering, and (c,d) by inelastic X-ray scattering. The mode polarization and wavevector are indicated in each subplot.

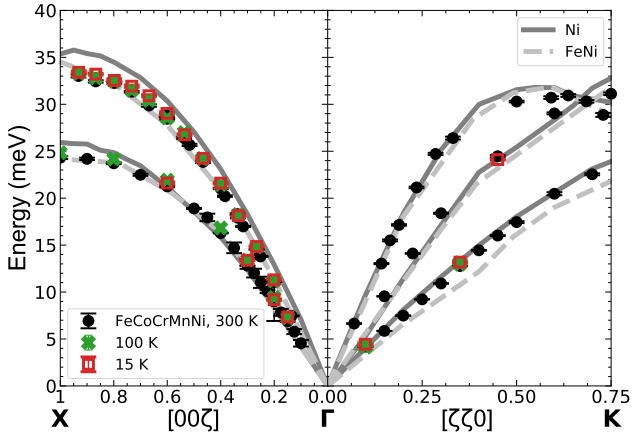

FIG. 5. "Color" The energies of the longitudinal and transverse acoustic phonons of FeCoCrMnNi measured in the high symmetry directions [00ζ] and [ζζ0] seen in Fig. 3 have been fit (details in Appendix B of the Supplementary Material [45]) and plotted at three temperatures against those of the single element Ni [62] and equimolar NiFe [63] measured at 300 K.

terms of the similarity of the force constants of the component elements, as pointed out by Körmann *et al.* [75].

We now turn our attention to the phonon linewidth, Γ_{FWHM}, which is directly related to phonon lifetime, $\tau = 2\hbar/\Gamma_{\mathrm{FWHM}}$, and thus to the phonon mean free path $l = v\tau$. Unfortunately, we could reliably extract it only from

TABLE I. "Color" The LA$_{001}$, degenerate branches TA$^{110}_{00\bar{1}}$ and TA$^{010}_{\bar{1}00}$, LA$_{110}$, TA$^{001}_{110}$, and TA$^{110}_{\bar{1}10}$ mode sound velocities of FeCoCrMnNi are given in the table below. In the [ζζ0] direction, TA$_1$ refers to the TA$^{001}_{110}$ branch, and TA$_2$ to the TA$^{110}_{\bar{1}10}$ mode. They are compared to the sound velocities calculated using the experimentally measured single-crystal elastic constants from Wu *et al.* [64], marked by *. Velocities are written in km/s.

	[00ζ]	[ζζ0]
LA	4.7(1)	5.7(1)
	5.034*	5.834*
TA$_1$	3.8(2)	3.8(2)
	3.681*	3.681*
TA$_2$	3.8(2)	2.3(2)
	3.681*	2.181*

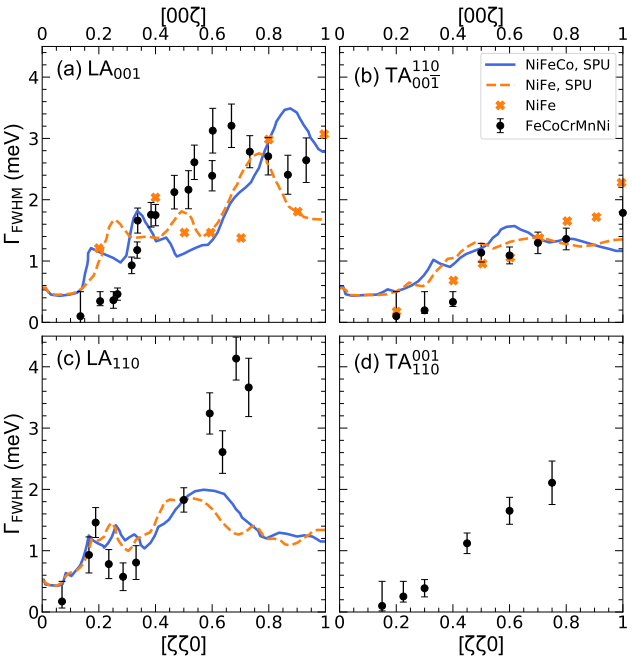

FIG. 6. "Color" Intrinsic phonon linewidths of FeCoCrMnNi, measured by inelastic X-ray scattering at 300 K for (a) LA$_{001}$, (b) TA$^{110}_{00\bar{1}}$, (c) LA$_{110}$, and (d) TA$^{001}_{100}$. Experimental data on binary NiFe together with SPU calculations predictions for NiFe and NiFeCo linewidths after Mu *et al.* [41] are also reported. (SPU calculations were not made for the FeCoCrMnNi polarization shown in (d).)

X-ray inelastic scattering data, due to the presence of the strong incoherent scattering in the neutron data and its entanglement with the acoustic phonon, which made the fitting procedure challenging in that case. Details on its extraction in IXS experiments are given in Appendix B.3 of the Supplementary Material [45].

In Fig. 6 we report the phonon linewidths at 300 K of the LA$_{001}$ and TA$^{110}_{00\bar{1}}$ polarizations in the [ζ00] direc-

tion (panels a and b), and of LA_{110} and TA^{001}_{110} polarizations in the [ζζ0] direction, (panels c and d). Interestingly, the q dependence of phonon broadening appears to be anisotropic and polarization-dependent: longitudinal modes exhibit several regimes, while transverse modes have a smoother dependence with a monotonic increase. In more detail, for LA_{001} we observe a steep increase at low q, followed by a weaker dependence going into a maximum for $q \sim 0.6$ r.l.u. For LA_{110}, a plateau at low q then leads into an increase in the second half of the Brillouin zone.

VI. DISCUSSION

A. Origin of phonon linewidth in FeCoCrMnNi

The first question to address is about the origin of the observed phonon broadening. We can immediately rule out a dominant role of anharmonicity, as well as scattering from magnetic fluctuations. Indeed, we could not observe any sizable temperature dependence in either phonon position and/or shape between our 300 and 15 K measurements, temperatures which are respectively well above and below the magnetic transition reported at 25 K for our HEA [49–51]. The observed broadening should therefore be related to the other disorder-induced scattering sources associated with the random alloy nature of our HEA. As such, the enhancement of phonon broadening with respect to the simple-element monatomic materials is expected to reflect the role of disorder.

Unfortunately, there is very little literature available on intrinsic phonon linewidths in the simple elements constituting our FeCoCrMnNi. In the case of Cr [76], measured by IXS with the same energy resolution as our study, the broadening remained resolution limited. It is therefore clear that the disorder intrinsic to HEAs does increase phonon broadening, which now lies within the experimental resolution.

It is interesting to note however that, despite the large number of elements in our HEA, the phonon linewidths are very similar to the ones reported in random binary alloys of the same elements, such as FeCo and FeNi, the latter of which is also reported in Fig. 6 [41].

The difficulty of modeling phonon linewidth in random alloys comes from the complexity of taking into account the quoted three ingredients, *i.e.* local strain due to the different atomic sizes, mass fluctuations, and force-constant fluctuations. A simple analytical model, which has been successfully used in mass disorder alloys [77], assumes phonon scattering from isolated defects and leads to the expression $\Gamma_{\mathrm{FWHM}} = \pi/2(\hbar\omega)^2 g(\hbar\omega)\langle\epsilon^2\rangle$, where $g(\hbar\omega)$ is the GVDOS and ϵ represents the sum of mass, force-constant, and atomic size fluctuations contributions [78]. Using this model, we find that the expected broadening from mass fluctuations in our HEA is negligibly small, accounting for a broadening of at most 0.2 meV. Ascribing the whole observed linewidth to force-constant fluctuations, we find that the global behavior is reproduced quite well along the [ζ00] direction using an average force-constant fluctuation $\epsilon = \langle \Delta F_{ij}/F_{ij} \rangle \sim 20\%$. Still, as can be appreciated in Fig. 7, this is not so along the [ζζ0] direction. The observed anisotropy then calls for more complex models.

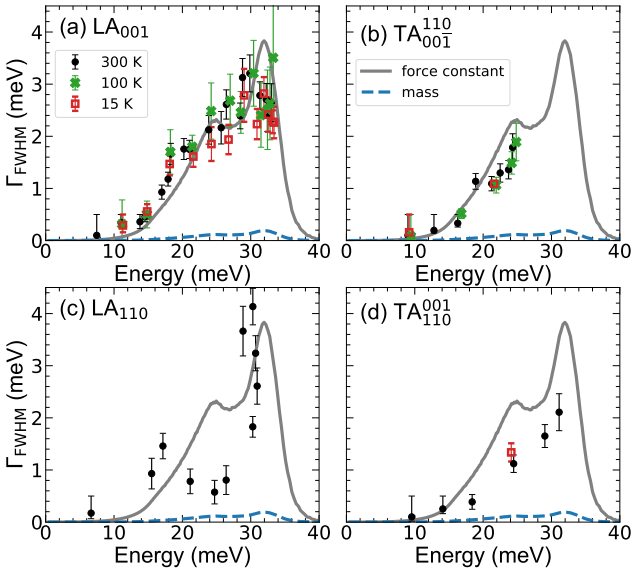

FIG. 7. "Color" Intrinsic phonon linewidths, measured by inelastic X-ray scattering at three temperatures for (a) LA_{001}, (b) $TA^{110}_{00\bar{1}}$, (c) LA_{110}, and (d) TA^{001}_{100}, reported as a function of energy and compared with a perturbation theory calculation of the broadening, based on calculated mass fluctuations and estimated force-constant fluctuations.

We therefore turn to the very recent advancement in the theoretical treatment of phonons in random alloys by Mu *et al.* [41]. Using the *ab initio* supercell phonon-unfolding (SPU) simulations method, the authors demonstrate that, in weak mass disorder alloys such as FeNi, FeCo, and FeNiCo, which are made out of the same constituents of our FeCoCrMnNi, the force-constant fluctuations play a determining role, being enhanced by the random environment of the atomic pairs. This leads to a significant phonon broadening on the order of 1-2 meV and mainly above $q = 0.7$ r.l.u, as observed both in IXS experiments and calculations, which are also reported in Fig. 6. Unfortunately they did not calculate the same polarization for the transverse mode along the [ζζ0] direction as we have measured, limiting a direct comparison. The behavior looks similar in these materials and our HEA, with different regimes in longitudinal broadening, including the presence of a maximum, and a smoother behavior in transverse broadening. One should note however that the long-wavelength low-q part of the spectrum could not be reliably reproduced by the simulation, due to the rather small supercell of only 64 atoms that was used for the DFT calculations. Interestingly, the force-constant fluctuations per atomic pair found from the simulation is between 20 and 50%,

in nice agreement with our simplistic estimation for FeCoCrMnNi.

As expected, the more advanced theoretical modeling of Mu *et al.* [41] presents an anisotropy as well, specifically between $TA^{110}_{00\bar{1}}$ and $TA^{\bar{1}10}_{110}$. This confirms that it is intrinsic to the random alloys, and cannot be fully ascribed to the presence of a local chemical short range order (SRO). Other contributions play a role, such as an anisotropic strain distribution. Finally, we note that, at high energy, theoretical models [41, 77] predict a significant phonon lineshape anisotropy with low-energy tails due to the presence of a continuum of optical excitations because of the different masses and force constants involved. Within our experimental resolution, we could not observe any anisotropy, and could reproduce the spectral shape with a single DHO excitation quite well, even at high energy. This indicates that phonons remain well-defined in our HEA and that the effect of mass and force-constant fluctuations can be treated using perturbative approaches.

B. Phonon linewidth and mean free path in FeCoCrMnNi vs glasses and CMAs

We now focus on the energy dependence of phonon linewidth along the [ζ00] propagation direction, where we have observed a crossover from a strong to a weak dependence in the longitudinal polarization. In order to analyze this latter in more detail, we report these data as a function of energy in logarithmic scale in Fig. 8. The first two broadening regimes in LA_{001} appear as clear power laws: at smaller energies the strong dependence is compatible with a power law such as $\Gamma_{FWHM} \sim (\hbar\omega)^{4.5\pm1}$, and is followed until ∼18 meV, at which point there is a sudden break to a weaker dependence, fit with $(\hbar\omega)^{1.7\pm0.2}$.

The crossover from a steep to a weaker energy dependence in the LA_{001} phonon broadening reminds us of the $(\hbar\omega)^4 - to - (\hbar\omega)^2$ crossover in glasses, typically observed at lengthscales of a few tens of Angstroms, and which has been associated to the breakdown of the propagative nature of the phonon [27, 79–82].

The origin of the $(\hbar\omega)^4$ regime in glasses has long been debated [83–86], and has lately been ascribed to the presence of a distribution of force-constants at a nanometric lengthscale, due to the disordered atomic arrangement (the elastic heterogeneities at the nanoscale mentioned in the introduction) [27, 79–82, 87–90]. Interestingly, the same phenomenology arises in random matrix approaches, which model the vibrational properties of a glass through a random network of force-constants over a regular lattice, quite similarly to the case of our HEA [85, 86]. This regime is usually found at energies corresponding to the deviation of the GVDOS from the Debye behavior and ending at the Boson Peak.

In Fig. 8(a) we display the GVDOS divided by energy squared, superposed to the attenuation's logarithmic dependence: we clearly see that the strong scattering regime corresponds to the deviation of the GVDOS from the Debye behavior, and the second regime settles in when the reduced GVDOS reaches its maximum, very similarly to glasses, although the corresponding lengthscale is slightly shorter (10 Å in our HEA, as opposed to ∼20-30 Å in glasses). However, a fundamental difference appears: this crossover usually corresponds to the reaching of the Ioffe-Regel limit (IR) in glasses, identified by the condition that the phonon mean free path becomes comparable to the phonon wavelength, $l \sim \lambda$, such that phonons with smaller wavelengths cannot be considered as propagative anymore [91]. This is not the case for FeCoCrMnNi, as can be seen in Fig. 8(c,d), where we report the longitudinal and transverse mean free paths

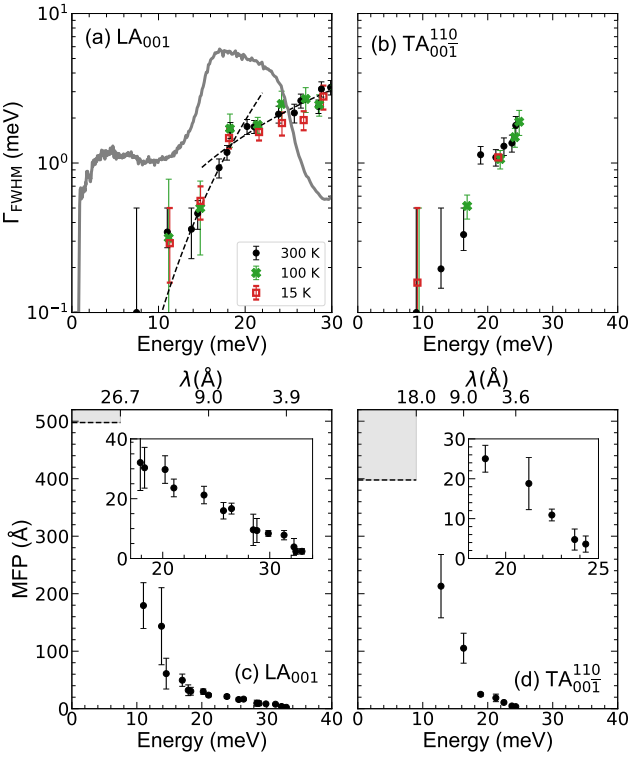

FIG. 8. "Color" Intrinsic phonon linewidths, measured by inelastic X-ray scattering. Subplots (a,b) show linewidths measured at three temperatures. For the sake of clarity, in (a) we report only the first two broadening regimes, up to 30 meV, for the longitudinal mode, together with $(\hbar\omega)^{4.5}$ and $(\hbar\omega)^{1.7}$ lines (black dashed lines) as a guide to the eye. The FeCoCrMnNi generalized vibrational density of states (GVDOS) originally shown in Fig. 2(b), divided by energy squared and scaled, is plotted in gray in (a) for reference. Subplots (c,d) are mean free paths (MFPs), calculated from the intrinsic linewidths at 300 K. Below ∼10 meV the phonon linewidth could not be resolved with our experimental resolution. This allows us only to estimate an upper limit for intrinsic linewidth, *i.e.* a lower limit for lifetime and MFP. The shaded areas in the figure indicate the region in which, on this basis, the real MFP lies.

as a function of phonon energy. Focusing on the longitudinal polarization, we see that only for energies above $\sim$ 30 meV, where the phonon group velocity is still non zero, is the mean free path comparable with the phonon wavelength. The IR crossover in our HEA is thus located at wavelengths on the order of magnitude of the unit cell size, *i.e.* one order of magnitude smaller than in glasses. It is interesting to note the IR crossover may be found at much smaller lengthscales in metallic glasses as well. Indeed, in MGs, acoustic modes are found to be persistent, dispersing over the whole Brillouin zone and well above the Boson peak [92–95]. Contradictory results have been reported on the presence of the typical strong scattering regime in this family of glasses [93, 96, 97]. Interestingly, and quite similarly to the case of our HEA, the possible sequence of regimes $(\hbar\omega)^4 - (\hbar\omega)^2 - (\hbar\omega)$ has been reported [94], with the two crossovers being located at the Boson Peak position [94] and at the Ioffe-Regel energy, respectively [93].

A similar strong scattering regime ($\Gamma_{FWHM} \propto (\hbar\omega)^4$) has been reported as well in some directions or polarizations in the case of some quasicrystals [98–103], and in the periodic quasicrystal approximant o-$Al_{13}Co_4$ [30]. Phenomenological models and atomic scale simulations have ascribed its presence to acoustic-optic hybridization, mode mixing and/or atomic site disorder [30, 101, 102, 104, 105]. Interestingly, in both these CMAs and our HEA, this regime arises at wavelengths of about 20-30 Å and extends down to wavelengths of about 12-10 Å. It is worth noticing that the quasicrystal cluster, the approximant's unit cell, as well as our possible indication for SRO in our HEA have the same order of magnitude, i.e. about 12-10 Å. Even if this suggests a strong similarity between HEAs and CMAs, a global view of their dynamics establishes major differences.

First, it is important to underline that the presence of a strong scattering regime is not characteristic of all CMAs. Specifically, it is absent in clathrates, where the lifetimes and mean free paths are also much longer than in quasicrystals and approximants [33]. Still, all CMAs, including clathrates, are characterized by the separation of the phonon spectrum in a reduced acoustic phase space, which is typically limited to wavevectors smaller than 0.3-0.5 Å^{-1} and energies smaller than 8-10 meV, and a large phase space dominated by dispersionless optic modes. The situation in our HEA is clearly different: first, the continuum of dispersionless excitations is not observed, and second, the acoustic regime extends to much higher energies and wavevectors, up to 22 and 30 meV for TA and LA respectively, which is very near the Brillouin zone boundary. Moreover, phonon attenuation, while larger than in clathrates, is not as strong as in quasicrystals and becomes comparable to these latter only at much larger wavevectors, in the second half of the Brillouin zone.

VII. CONCLUSIONS

In conclusion, we have reported the first ever investigation of the acoustic phonon dynamics in a High-Entropy Alloy, complemented by the GVDOS survey, at room and low temperature. FeCoCrMnNi is a 5-element random alloy, and, despite the inherent disorder, we have shown that its phonon dynamics closely resembles that of the pure elements composing it and the corresponding binary alloys, which is in agreement with the low mass, atomic size, and force constant contrast existing among the constituents of this HEA [75]. More specifically, acoustic phonons disperse throughout the whole Brillouin zone up to energies between 20 and 30 meV, exhibiting an attenuation which, while stronger than in simple elements, remains on the same order of magnitude as in binary alloys. We have shown that the whole attenuation behavior can then be understood in terms of scattering from force-constant fluctuations, which have been estimated to amount to $\sim$ 20% using a simple theoretical model, and which is in quite good agreement with calculations of Mu and co-authors on binary and ternary alloys made of the same elements.

The analysis of our results thus confirms that, while they share similar mechanical and, in some cases, thermal properties with glasses and CMAs, HEAs exhibit specific phonon dynamics, with marked differences from the ones of those systems: the acoustic regime is preserved across the whole Brillouin zone, while in glasses and CMAs it is reduced in a rather small $(q, \hbar\omega)$ range, except in metallic glasses. Moreover, despite the strong chemical disorder, phonon attenuation remains much smaller than in glasses and quasicrystals, and more similar to that of simple binary alloys. Still, we have been able to draw a parallelism with these materials on the basis of the presence in some polarizations and directions of a strong phonon scattering regime, $\Gamma_{FWHM} \propto (\hbar\omega)^4$, which arises simultaneously to the deviation of the acoustic dynamics from the Debye behavior.

In order to further understand the effect of increasing disorder in going from a perfect crystal to random alloys, to glasses, we may expect that increasing the force-constant disorder would bring us a step closer to glasses. This could be the case for BCC HEAs, which are made from more dissimilar elements and for which attenuation is therefore expected to be enhanced [75]. Understanding the way phonon dynamics change along this path is not only fundamentally interesting, but will also give us the microscopic understanding necessary for engineering defects and disorder into materials for thermal applications. This work is a step in this direction, allowing us to identify the subsequent challenges.

ACKNOWLEDGMENTS

S.R.T. acknowledges financial support from the ISP program of the IDEX Université Grenoble Alpes. S.P.

and V.M.G. acknowledge support from the Lyon IDEX Scientific Breakthrough program for funding of the project IPPON. V.M.G. acknowledges the ANR for funding the project MAPS-ANR-20-CE05-0046. M.F. thanks the German Research foundation (DFG) for financial support through grant No. FE 571/4 within the priority programme SPP2006. This work has been carried out within the European C-MetAC network [106]. Data from INS measurements at the ILL are available at [107] and [108], LLB measurements correspond to proposal 658, and ESRF measurements to proposal hc-4327.

* To whom correspondence should be addressed: valentina.giordano@univ-lyon1.fr

[1] J.-W. Yeh, S.-K. Chen, S.-J. Lin, J.-Y. Gan, T.-S. Chin, T.-T. Shun, C.-H. Tsau, and S.-Y. Chang, Nanostructured high-entropy alloys with multiple principal elements: Novel alloy design concepts and outcomes, Adv. Eng. Mater. **6**, 299 (2004).

[2] B. Cantor, I. Chang, P. Knight, and A. Vincent, Microstructural development in equiatomic multicomponent alloys, Mat. Sci. Eng. A **375-377**, 213 (2004).

[3] B. Gludovatz, A. Hohenwarter, D. Catoor, E. H. Chang, E. P. George, and R. O. Ritchie, A fracture-resistant high-entropy alloy for cryogenic applications, Science **345**, 1153 (2014).

[4] W.-L. Hsu, H. Murakami, J.-W. Yeh, A.-C. Yeh, and K. Shimoda, A heat-resistant $NiCo_{0.6}Fe_{0.2}Cr_{1.5}SiAlTi_{0.2}$ overlay coating for high-temperature applications, J. Electrochem. Soc. **163**, C752 (2016).

[5] D. Miracle and O. Senkov, A critical review of high entropy alloys and related concepts, Acta Mater. **122**, 448 (2017).

[6] M. Jadhav, S. Singh, M. Srivastava, and G. V. Kumar, An investigation on high entropy alloy for bond coat application in thermal barrier coating system, J. Alloy. Compd. **783**, 662 (2019).

[7] M. Gao, J.-W. Yeh, P. Liaw, and Y. Zhang, eds., *High–Entropy Alloys* (Springer-Verlag GmbH, 2016).

[8] E. P. George, D. Raabe, and R. O. Ritchie, High-entropy alloys, Nat. Rev. Mater. **4**, 515 (2019).

[9] M.-H. Tsai, Physical properties of high entropy alloys, Entropy **15**, 5338 (2013).

[10] Z. Fan, H. Wang, Y. Wu, X. Liu, and Z. Lu, Thermoelectric performance of PbSnTeSe high-entropy alloys, Materials Research Letters **5**, 187 (2016).

[11] A. Karati, M. Nagini, S. Ghosh, R. Shabadi, K. G. Pradeep, R. C. Mallik, B. S. Murty, and U. V. Varadaraju, Ti2nicosnsb - a new half-heusler type high-entropy alloy showing simultaneous increase in seebeck coefficient and electrical conductivity for thermoelectric applications, Scientific Reports **9**, 10.1038/s41598-019-41818-6 (2019).

[12] L. Kush, S. Srivastava, Y. Jaiswal, and Y. Srivastava, Thermoelectric behaviour with high lattice thermal conductivity of nickel base ni2cucrfealx (x = 0.5, 1.0, 1.5 and 2.5) high entropy alloys, Materials Research Express **7**, 035704 (2020).

[13] M. M. Trexler and N. N. Thadhani, Mechanical properties of bulk metallic glasses, Progress in Materials Science **55**, 759 (2010).

[14] W. Wang, C. Dong, and C. Shek, Bulk metallic glasses, Materials Science and Engineering: R: Reports **44**, 45 (2004).

[15] A. Inoue, Stabilization of metallic supercooled liquid and bulk amorphous alloys, Acta Materialia **48**, 279 (2000).

[16] C. A. Schuh, T. C. Hufnagel, and U. Ramamurty, Mechanical behavior of amorphous alloys, Acta Materialia **55**, 4067 (2007).

[17] K. Urban and M. Feuerbacher, Structurally complex alloy phases, Journal of Non-Crystalline Solids **334-335**, 143 (2004), 8th International Conference on Quasicrystals.

[18] J.-M. Dubois and E. Belin-Ferré, eds., *Complex Metallic Alloys* (Wiley-VCH Verlag GmbH & Co. KGaA, 2010).

[19] A. Ovchinnikov, V. Smetana, and A.-V. Mudring, Metallic alloys at the edge of complexity: structural aspects, chemical bonding and physical properties, Journal of Physics: Condensed Matter **32**, 243002 (2020).

[20] D. G. Cahill and R. O. Pohl, Lattice vibrations and heat transport in crystals and glasses, Annual Review of Physical Chemistry **39**, 93 (1988).

[21] D. G. Cahill, S. K. Watson, and R. O. Pohl, Lower limit to the thermal conductivity of disordered crystals, Phys. Rev. B **46**, 6131 (1992).

[22] E. S. Toberer, L. L. Baranowski, and C. Dames, Advances in Thermal Conductivity, Annual Review of Materials Research **42**, 179 (2012).

[23] M. A. Chernikov, A. Bianchi, and H. R. Ott, Low-temperature thermal conductivity of icosahedral $Al_{70}Mn_9Pd_{21}$, Phys. Rev. B **51**, 153 (1995).

[24] M. Bobnar, P. Jeglič, M. Klanjšek, Z. Jagličić, M. Wencka, P. Popčević, J. Ivkov, D. Stanić, A. Smontara, P. Gille, and J. Dolinšek, Intrinsic anisotropic magnetic, electrical, and thermal transport properties of *d*-al-co-ni decagonal quasicrystals, Phys. Rev. B **85**, 024205 (2012).

[25] T. Takeuchi, N. Nagasako, R. Asahi, and U. Mizutani, Extremely small thermal conductivity of the Al-based Mackay-type 1/1-cubic approximants, Phys. Rev. B **74**, 054206 (2006).

[26] J. Dolinšek, M. Komelj, P. Jeglič, S. Vrtnik, D. Stanić, P. Popčević, J. Ivkov, A. Smontara, Z. Jagličić, P. Gille, and Y. Grin, Anisotropic magnetic and transport properties of orthorhombic $al_{13}co_4$, Phys. Rev. B **79**, 184201 (2009).

[27] G. Monaco and V. M. Giordano, Breakdown of the debye approximation for the acoustic modes with nanometric wavelengths in glasses, Proceedings of the National Academy of Sciences **106**, 3659 (2009).

[28] H. Mizuno, S. Mossa, and J.-L. Barrat, Relation of vibrational excitations and thermal conductivity to elastic heterogeneities in disordered solids, Physical Review B **94**, 10.1103/physrevb.94.144303 (2016).

[29] H. Euchner, T. Yamada, S. Rols, T. Ishimasa, J. Ollivier, H. Schober, M. Mihalkovič, and M. de Boissieu,

Lattice dynamics of the icosahedral quasicrystals i-ZnMgSc and i-ZnAgSc and the cubic 1/1-approximant zn6sc, Journal of Physics: Condensed Matter **26**, 055402 (2014).

[30] P.-F. Lory, V. M. Giordano, P. Gille, H. Euchner, M. Mihalkovič, E. Pellegrini, M. Gonzalez, L.-P. Regnault, P. Bastie, H. Schober, S. Pailhes, M. R. Johnson, Y. Grin, and M. de Boissieu, Impact of structural complexity and disorder on lattice dynamics and thermal conductivity in the o-$Al_{13}Co_4$ phase, Phys. Rev. B **102**, 024303 (2020).

[31] S. Pailhès, H. Euchner, V. Giordano, R. Debord, A. Assy, S. Gomès, A. Bosak, D. Machon, S. Paschen, and M. de Boissieu, Localization of propagative phonons in a perfectly crystalline solid, Phys. Rev. Lett. **113**, 025506 (2014).

[32] H. Euchner, S. Pailhès, V. M. Giordano, and M. de Boissieu, Understanding lattice thermal conductivity in thermoelectric clathrates: A density functional theory study on binary Si-based type-I clathrates, Phys. Rev. B **97**, 014304 (2018).

[33] P.-F. Lory, S. Pailhès, V. M. Giordano, H. Euchner, H. D. Nguyen, R. Ramlau, H. Borrmann, M. Schmidt, M. Baitinger, M. Ikeda, P. Tomeš, M. Mihalkovič, C. Allio, M. R. Johnson, H. Schober, Y. Sidis, F. Bourdarot, L. P. Regnault, J. Ollivier, S. Paschen, Y. Grin, and M. de Boissieu, Direct measurement of individual phonon lifetimes in the clathrate compound $Ba_{7.81}Ge_{40.67}Au_{5.33}$, Nat. Commun. **8**, 491 (2017).

[34] S. R. Turner, S. Pailhès, F. Bourdarot, J. Ollivier, S. Raymond, T. Keller, Y. Sidis, J.-P. Castellan, P.-F. Lory, H. Euchner, M. Baitinger, Y. Grin, H. Schober, M. de Boissieu, and V. M. Giordano, Impact of temperature and mode polarization on the acoustic phonon range in complex crystalline phases: A case study on intermetallic clathrates, Phys. Rev. Research **3**, 013021 (2021).

[35] P. G. Klemens, The scattering of low-frequency lattice waves by static imperfections, Proceedings of the Physical Society. Section A **68**, 1113 (1955).

[36] D. W. Taylor, Vibrational Properties of Imperfect Crystals with Large Defect Concentrations, Phys. Rev. **156**, 1017 (1967).

[37] W. A. Kamitakahara and D. W. Taylor, Comparison of single-site approximations for the lattice dynamics of mass-disordered alloys, Phys. Rev. B **10**, 1190 (1974).

[38] Y. Tsunoda, N. Kunitomi, N. Wakabayashi, R. M. Nicklow, and H. G. Smith, Phonon dispersion relations in the disordered $ni_{1-x}pt_x$ system, Phys. Rev. B **19**, 2876 (1979).

[39] H. Katayama and J. Kanamori, An extension of taylor's theory of lattice vibration in disordered alloys, Journal of the Physical Society of Japan **45**, 1157 (1978).

[40] S. Ghosh, P. L. Leath, and M. H. Cohen, Phonons in random alloys: The itinerant coherent-potential approximation, Phys. Rev. B **66**, 214206 (2002).

[41] S. Mu, R. J. Olsen, B. Dutta, L. Lindsay, G. D. Samolyuk, T. Berlijn, E. D. Specht, K. Jin, H. Bei, T. Hickel, B. C. Larson, and G. M. Stocks, Unfolding the complexity of phonon quasi-particle physics in disordered materials, npj Computational Materials **6**, 4 (2020).

[42] S. Mu, Z. Pei, X. Liu, and G. M. Stocks, Electronic transport and phonon properties of maximally disordered alloys: From binaries to high-entropy alloys, J. Mater. Res. **33**, 2857 (2018).

[43] M. Feuerbacher, E. Würtz, A. Kovács, and C. Thomas, Single-crystal growth of a FeCoCrMnAl high-entropy alloy, Mater. Res. Lett. **5**, 128 (2016).

[44] C.-S. Wu, P.-H. Tsai, C.-M. Kuo, and C.-W. Tsai, Effect of atomic size difference on the microstructure and mechanical properties of high–entropy alloys, Entropy **20**, 967 (2018).

[45] See Supplemental Material (SM) at [url will be inserted by publisher] for details of the experimental conditions, data analysis, and sample characterization.

[46] K. Momma and F. Izumi, *VESTA3* for three-dimensional visualization of crystal, volumetric and morphology data, J. Appl. Crystallogr. **44**, 1272 (2011).

[47] S. R. Turner, S. Pailhès, F. Bourdarot, M. Feuerbacher, H. Schober, M. de Boissieu, and V. M. Giordano3, A neutron diffuse scattering investigation of hea fecrcomnni hig-entropy alloy, preliminary data have been collected on the D7 beamline at ILL. Weak signatures of short range ordering have been observed, to be confirmed in future experiments.

[48] M. S. Lucas, L. Mauger, J. A. Muñoz, I. Halevy, J. Horwath, S. L. Semiatin, S. O. Leontsev, M. B. Stone, D. L. Abernathy, Y. Xiao, P. Chow, and B. Fultz, Phonon densities of states of face-centered-cubic Ni-Fe alloys, J. Appl. Phys. **113**, 17A308 (2013).

[49] P. Koželj, S. Vrtnik, M. Krnel, A. Jelen, D. Gačnik, M. Wencka, Z. Jagličić, A. Meden, G. Dražić, F. Danoix, J. Ledieu, M. Feuerbacher, and J. Dolinšek, Spin-glass magnetism of the non-equiatomic CoCrFeMnNi high-entropy alloy, Journal of Magnetism and Magnetic Materials **523**, 167579 (2021).

[50] K. Jin, B. C. Sales, G. M. Stocks, G. D. Samolyuk, M. Daene, W. J. Weber, Y. Zhang, and H. Bei, Tailoring the physical properties of ni-based single-phase equiatomic alloys by modifying the chemical complexity, Sci. Rep. **6**, 20159 (2016).

[51] O. Schneeweiss, M. Friák, M. Dudová, D. Holec, M. Šob, D. Kriegner, V. Holý, P. c. v. Beran, E. P. George, J. Neugebauer, and A. Dlouhý, Magnetic properties of the CrMnFeCoNi high-entropy alloy, Phys. Rev. B **96**, 014437 (2017).

[52] F. Körmann, D. Ma, D. D. Belyea, M. S. Lucas, C. W. Miller, B. Grabowski, and M. H. F. Sluiter, "treasure maps" for magnetic high-entropy-alloys from theory and experiment, Appl. Phys. Lett. **107**, 142404 (2015).

[53] C. Niu, A. J. Zaddach, A. A. Oni, X. Sang, J. W. Hurt, J. M. LeBeau, C. C. Koch, and D. L. Irving, Spin-driven ordering of Cr in the equiatomic high entropy alloy NiFeCrCo, Appl. Phys. Lett. **106**, 161906 (2015).

[54] F. Tian, L. K. Varga, N. Chen, L. Delczeg, and L. Vitos, Ab initio investigation of high-entropy alloys of 3*d* elements, Phys. Rev. B **87**, 075144 (2013).

[55] M. S. Lucas, L. Mauger, J. A. Muñoz, Y. Xiao, A. O. Sheets, S. L. Semiatin, J. Horwath, and Z. Turgut, Magnetic and vibrational properties of high–entropy alloys, J. Appl. Phys. **109**, 07E307 (2011).

[56] Y. Ikeda, F. Körmann, B. Dutta, A. Carreras, A. Seko, J. Neugebauer, and I. Tanaka, Temperature-dependent phonon spectra of magnetic random solid solutions, npj Computational Materials **4**, 7 (2018).

[57] T. Brink, L. Koch, and K. Albe, Structural origins of the boson peak in metals: From high-entropy alloys to

metallic glasses, Phys. Rev. B **94**, 224203 (2016).
[58] M. S. Lucas, A. Papandrew, B. Fultz, and M. Y. Hu, Partial phonon densities of states of ^{57}Fe in fe-cr: Analysis by a local-order cluster expansion, Phys. Rev. B **75**, 054307 (2007).
[59] M. S. Lucas, M. Kresch, R. Stevens, and B. Fultz, Phonon partial densities of states and entropies of Fe and Cr in bcc Fe-Cr from inelastic neutron scattering, Phys. Rev. B **77**, 184303 (2008).
[60] M. S. Lucas, J. A. Muñoz, L. Mauger, C. W. Li, A. O. Sheets, Z. Turgut, J. Horwath, D. L. Abernathy, M. B. Stone, O. Delaire, Y. Xiao, and B. Fultz, Effects of chemical composition and B2 order on phonons in bcc Fe–Co alloys, J. Appl. Phys. **108**, 023519 (2010).
[61] M. S. Lucas, G. B. Wilks, L. Mauger, J. A. Muñoz, O. N. Senkov, E. Michel, J. Horwath, S. L. Semiatin, M. B. Stone, D. L. Abernathy, and E. Karapetrova, Absence of long-range chemical ordering in equimolar FeCoCrNi, Appl. Phys. Lett. **100**, 251907 (2012).
[62] R. J. Birgeneau, J. Cordes, G. Dolling, and A. D. B. Woods, Normal modes of vibration in nickel, Phys. Rev. **136**, A1359 (1964).
[63] E. D. Hallman and B. N. Brockhouse, Crystal dynamics of nickel–iron and copper–zinc alloys, Canadian Journal of Physics **47**, 1117 (1969).
[64] Y. Wu, W. H. Liu, X. L. Wang, D. Ma, A. D. Stoica, T. G. Nieh, Z. B. He, and Z. P. Lu, In-situ neutron diffraction study of deformation behavior of a multi-component high-entropy alloy, Appl. Phys. Lett. **104**, 051910 (2014).
[65] V. J. Minkiewicz, G. Shirane, and R. Nathans, Phonon dispersion relation for iron, Phys. Rev. **162**, 528 (1967).
[66] H. B. Møller and A. R. Mackintosh, Observation of resonant lattice modes by inelastic neutron scattering, Phys. Rev. Lett. **15**, 623 (1965).
[67] W. M. Shaw and L. D. Muhlestein, Investigation of the phonon dispersion relations of chromium by inelastic neutron scattering, Phys. Rev. B **4**, 969 (1971).
[68] J. Trampenau, W. Petry, and C. Herzig, Temperature dependence of the lattice dynamics of chromium, Phys. Rev. B **47**, 3132 (1993).
[69] G. A. deWit and B. N. Brockhouse, The lattice dynamics of ferromagnetic and paramagnetic nickel, Journal of Applied Physics **39**, 451 (1968).
[70] E. Maliszewski and S. Bednarski, The lattice dynamics of ni0.88fe0.12, ni0.76fe0.24 and ni single crystals, physica status solidi (b) **200**, 435 (1997).
[71] E. Maliszewski and S. Bednarski, Lattice dynamics of Fe0.65Ni0.35 classical invar, physica status solidi (b) **211**, 621 (1999).
[72] Y. Endoh, Y. Noda, and M. Iizumi, Lattice dynamics and invar properties in f.c.c. FeMn alloy, J. Phys. Soc. Jpn. **50**, 469 (1981).
[73] S. M. Shapiro and S. C. Moss, Lattice dynamics of face–centered–cubic $Co_{0.92}Fe_{0.08}$, Phys. Rev. B **15**, 2726 (1977).
[74] F. Menzinger, F. Sacchetti, and M. C. Spinelli, Concentration dependence of the phonon dispersion relations in substitutional fcc Co-Ni alloys, Phys. Rev. B **12**, 2253 (1975).
[75] F. Körmann, Y. Ikeda, B. Grabowski, and M. H. F. Sluiter, Phonon broadening in high entropy alloys, npj Computational Materials **3**, 36 (2017).
[76] D. Lamago, M. Hoesch, M. Krisch, R. Heid, K.-P. Bohnen, P. Böni, and D. Reznik, Measurement of strong phonon softening in Cr with and without Fermi-surface nesting by inelastic x-ray scattering, Phys. Rev. B **82**, 195121 (2010).
[77] W. A. Kamitakahara and B. N. Brockhouse, Vibrations of a mixed crystal: Neutron scattering from $ni_{55}pd_{45}$, Phys. Rev. B **10**, 1200 (1974).
[78] R. Gurunathan, R. Hanus, M. Dylla, A. Katre, and G. J. Snyder, Analytical models of phonon–point-defect scattering, Physical Review Applied **13**, 10.1103/physrevapplied.13.034011 (2020).
[79] G. Baldi, V. M. Giordano, G. Monaco, and B. Ruta, Sound attenuation at terahertz frequencies and the boson peak of vitreous silica, Phys. Rev. Lett. **104**, 195501 (2010).
[80] G. Baldi, V. M. Giordano, and G. Monaco, Elastic anomalies at terahertz frequencies and excess density of vibrational states in silica glass, Phys. Rev. B **83**, 174203 (2011).
[81] G. Baldi, V. Giordano, G. Monaco, and B. Ruta, High frequency acoustic attenuation of vitreous silica: New insight from inelastic x-ray scattering, Journal of Non-Crystalline Solids **357**, 538 (2011), 6th International Discussion Meeting on Relaxation in Complex Systems.
[82] G. Baldi, V. M. Giordano, B. Ruta, R. Dal Maschio, A. Fontana, and G. Monaco, Anharmonic damping of terahertz acoustic waves in a network glass and its effect on the density of vibrational states, Phys. Rev. Lett. **112**, 125502 (2014).
[83] D. A. Parshin, Soft potential model and universal properties of glasses, Physica Scripta **T49A**, 180 (1993).
[84] W. Schirmacher, G. Diezemann, and C. Ganter, Harmonic vibrational excitations in disordered solids and the "boson peak", Phys. Rev. Lett. **81**, 136 (1998).
[85] Y. M. Beltukov and D. A. Parshin, Theory of sparse random matrices and vibrational spectra of amorphous solids, Physics of the Solid State **53**, 151 (2011).
[86] Y. M. Beltukov and D. A. Parshin, Density of states in random lattices with translational invariance, JETP Letters **93**, 598 (2011).
[87] H. Mizuno, S. Mossa, and J.-L. Barrat, Measuring spatial distribution of the local elastic modulus in glasses, Phys. Rev. E **87**, 042306 (2013).
[88] H. Mizuno, S. Mossa, and J.-L. Barrat, Elastic heterogeneity, vibrational states, and thermal conductivity across an amorphisation transition, Europhysics Letters **104**, 56001 (2013).
[89] H. Mizuno, S. Mossa, and J.-L. Barrat, Beating the amorphous limit in thermal conductivity by superlattices design, Scientific Reports **5**, 14116 (2015).
[90] W. Schirmacher, B. Schmid, C. Tomaras, G. Viliani, G. Baldi, G. Ruocco, and T. Scopigno, Vibrational excitations in systems with correlated disorder, physica status solidi c **5**, 862 (2008).
[91] Y. M. Beltukov, D. A. Parshin, V. M. Giordano, and A. Tanguy, Propagative and diffusive regimes of acoustic damping in bulk amorphous material, Phys. Rev. E **98**, 023005 (2018).
[92] P. Bruna, G. Baldi, E. Pineda, J. Serrano, M. Duarte, D. Crespo, and G. Monaco, Acoustic properties of metallic glasses in the mesoscopic regime by inelastic X-ray scattering, Journal of Alloys and Compounds **509**, S95 (2011), xVII International Symposium on Metastable, Amorphous and Nanostructured Materials.

[93] P. Bruna, G. Baldi, E. Pineda, J. Serrano, J. B. Suck, D. Crespo, and G. Monaco, Communication: Are metallic glasses different from other glasses? a closer look at their high frequency dynamics, The Journal of Chemical Physics **135**, 101101 (2011).

[94] D. Crespo, P. Bruna, A. Valles, and E. Pineda, Phonon dispersion relation of metallic glasses, Phys. Rev. B **94**, 144205 (2016).

[95] X. Y. Li, H. P. Zhang, S. Lan, D. L. Abernathy, T. Otomo, F. W. Wang, Y. Ren, M. Z. Li, and X.-L. Wang, Observation of high-frequency transverse phonons in metallic glasses, Phys. Rev. Lett. **124**, 225902 (2020).

[96] A. Tlili, S. Pailhès, R. Debord, B. Ruta, S. Gravier, J.-J. Blandin, N. Blanchard, S. Gomès, A. Assy, A. Tanguy, and V. Giordano, Thermal transport properties in amorphous/nanocrystalline metallic composites: A microscopic insight, Acta Materialia **136**, 425 (2017).

[97] T. Ichitsubo, W. Itaka, E. Matsubara, H. Kato, S. Biwa, S. Hosokawa, K. Matsuda, J. Saida, O. Haruyama, Y. Yokoyama, H. Uchiyama, and A. Q. R. Baron, Elastic inhomogeneity and acoustic phonons in Pd-, Pt-, and Zr-based metallic glasses, Phys. Rev. B **81**, 172201 (2010).

[98] M. de Boissieu, M. Boudard, R. Bellissent, M. Quilichini, B. Hennion, R. Currat, A. I. Goldman, and C. Janot, Dynamics of the AlPdMn icosahedral phase, Journal of Physics: Condensed Matter **5**, 4945 (1993).

[99] M. Boudard, M. de Boissieu, S. Kycia, A. I. Goldman, B. Hennion, R. Bellissen, M. Quilichini, R. Currat, and C. Janot, Optic modes in the AlPdMn icosahedral phase, Journal of Physics: Condensed Matter **7**, 7299 (1995).

[100] K. Shibata, R. Currat, M. de Boissieu, T. J. Sato, H. Takakura, and A. P. Tsai, Dynamics of the ZnMgY icosahedral phase, Journal of Physics: Condensed Matter **14**, 1847 (2002).

[101] M. de Boissieu, R. Currat, S. Francoual, and E. Kats, Sound-mode broadening in quasicrystals: A simple phenomenological model, Phys. Rev. B **69**, 054205 (2004).

[102] M. de Boissieu, S. Francoual, M. Mihalkovič, K. Shibata, A. Q. R. Baron, Y. Sidis, T. Ishimasa, D. Wu, T. Lograsso, L.-P. Regnault, F. Gähler, S. Tsutsui, B. Hennion, P. Bastie, T. J. Sato, H. Takakura, R. Currat, and A.-P. Tsai, Lattice dynamics of the Zn-Mg-Sc icosahedral quasicrystal and its Zn-Sc periodic 1/1 approximant, Nat. Mater. **6**, 977 (2007).

[103] F. Dugain, M. de Boissieu, K. Shibata, R. Currat, T. J. Sato, A. R. Kortan, J.-B. Suck, K. Hradil, F. Frey, and A. P. Tsai, Inelastic neutron scattering study of the dynamics of the alnico decagonal phase, The European Physical Journal B - Condensed Matter and Complex Systems **7**, 513 (1999).

[104] T. Janssen, G. Chapuis, and M. de Boissieu, *Aperiodic Crystals. From modulated phases to quasicrystals (second edition)*, IUCr Monographs on Crystallography, Vol. 20 (Oxford University Press, Oxford, 2018).

[105] M. D. Boissieu, Phonons, phasons and atomic dynamics in quasicrystals, Chem. Soc. Rev. **41**, 6778 (2012).

[106] `www.ecmetac.eu`.

[107] S. R. Turner, F. Bourdarot, M. de Boissieu, V. M. Giordano, J. Ollivier, S. Pailhès, and H. Schober, Lattice dynamics of high entropy alloy (2019).

[108] S. R. Turner, F. Bourdarot, M. de Boissieu, G. de Laitre, V. M. Giordano, S. Pailhès, H. Schober, and J.-M. Zanotti, Phonon dynamics in high entropy alloys (2019).

Supplementary Material for "Phonon behavior in a random solid solution: A lattice dynamics study on the high-entropy alloy FeCoCrMnNi"

Shelby R. Turner,[1,2,3] Stéphane Pailhès,[3] Frédéric Bourdarot,[4] Jacques Ollivier,[1] Yvan Sidis,[5] John-Paul Castellan,[5,6] Jean-Marc Zanotti,[5] Quentin Berrod,[7] Florence Porcher,[5] Alexei Bosak,[8] Michael Feuerbacher,[9] Helmut Schober,[1] Marc de Boissieu,[2] and Valentina M. Giordano[3,*]

[1] *Institut Laue-Langevin, F-38042 Grenoble cedex, France*
[2] *Université Grenoble Alpes, CNRS, Grenoble-INP, SIMaP, F-38000 Grenoble, France*
[3] *Institute of Light and Matter, UMR5306 Université Lyon 1-CNRS, Université de Lyon, F-69622 Villeurbanne cedex, France*
[4] *Université Grenoble Alpes, CEA, IRIG, MEM, MDN, F-38000 Grenoble cedex, France*
[5] *Université Paris-Saclay, CNRS, CEA, Laboratoire Léon Brillouin, F-91191 Gif-sur-Yvette, France*
[6] *Institut für Festkörperphysik, Karlsruher Institut für Technologie, D-76021 Karlsruhe, Germany*
[7] *Université Grenoble Alpes, CEA, CNRS, IRIG-SyMMES, F-38000 Grenoble cedex, France*
[8] *European Synchrotron Radiation Facility, BP 220, F-38043 Grenoble cedex, France*
[9] *Peter Grünberg Institut PGI-5 and ER-C, FZ Jülich GmbH, D-52425 Jülich, Germany*

(Dated: August 23, 2021)

APPENDIX A: SAMPLE SYNTHESIS AND CHARACTERIZATION

The sample material was produced using an equiatomic composition of high-purity elements Fe, Co, Cr, Mn, and Ni. The elements were alloyed in an inductively coupled high-frequency levitation furnace. After several remelting cycles, included to achieve a high homogeneity, cylindrical ingots were slip cast into a water cooled copper mold. Pieces of $\sim$1 cm^3 were cut from the ingots and subjected to a heat treatment of 1200 °C for 48 hrs for homogenization. These were used as polycrystalline samples for further investigation.

Single crystals were grown using ingots of about 70 g by means of the Bridgman technique. The pre-alloyed material was fit in a cylindrical, alumina crucible of about 10 cm length and an internal diameter of 20 mm and a 30° tip-shaped bottom, and inserted in a vertical tube furnace. The tip of the crucible was placed on a movable rod equipped with a cold finger to create a defined and steep temperature gradient. The furnace temperature was set to 1340 °C, which is above the melting temperature of 1330 °C of the alloy, and kept constant during the growth process. The growth process is carried out under argon atmosphere of 200 mbar. Solidification is effected by lowering the crucible vertically out of the hot zone of the furnace at a velocity of 50 mm/h. Further information on similar synthesis procedures for single crystal HEAs can be found in Feuerbacher *et al.* [1].

As stated in Section II of the main text, the samples were investigated by Scanning Electron Microscopy (SEM) using a JEOL 840 microscope, equipped with an EDAX Energy-Dispersive X-ray (EDX) system, as seen in Fig. S1.

Diffraction data were collected at the ID28@ESRF diffractometer at a wavelength of $\lambda = 0.697$ Å with a typical beam size of about 40μm FWHM. Data were recorded by the single-photon-counting PILATUS3 1M detector in shutterless mode over a rotation of 360° with a step of 0.25°. The detector was positioned 244 mm away from the sample with a 19° elevation above the horizontal plane, thus covering a scattering angle up to $\sim$40°. The experimental geometry and the orientation matrix were refined using CrysAlis software (by Rigaku Oxford Diffraction) and locally developed software was used for high-resolution 2D reconstructions.

There is a clear anisotropic distribution of diffuse scattering located around the Bragg peaks. The usual thermal diffuse scattering (TDS) leads to an anisotropy characterized by a stronger diffuse scattering in the transverse than in the longitudinal direction. Looking at the diffuse scattering around the 200 Bragg peaks, shown in Fig. S2, it is clear that the opposite is true: there is a minimum of diffuse scattering in the transverse direction.

Such a signal was confirmed by measuring the purely elastic signal in transverse and longitudinal geometries during phonon measurements by IXS, shown in Fig. S3. Here we report the elastic signal from scans made (a) along 0 0 2+x and x x 2 lines and (b) along 2+x 2+x 0 and 2 2 x lines. The plots clearly show a significantly larger intensity in the LA directions that, in both cases, follows $1/q^2$ decay fit. This is a clear signature of the so-called Huang scattering. It is beyond the scope of this paper to provide a full quantitative analysis of it, but this illustrates the presence of strain induced by the distribution of atomic size differences of the five elements.

APPENDIX B: METHODS: INELASTIC SCATTERING MEASUREMENTS

Taking first the example of a neutron scattering experiment, the measured quantity is the double differential cross-section, $\frac{d^2\sigma^n}{d\Omega_f dE_f}$,which is the number of neutrons out of incident neutrons that are scattered from a sample and into solid angle element Ω_f in a given energy range E_f. This has coherent and incoherent scattering components [2] and for incoming wave-vector k_i and outgoing wave-vector k_f, it is dependent upon the response

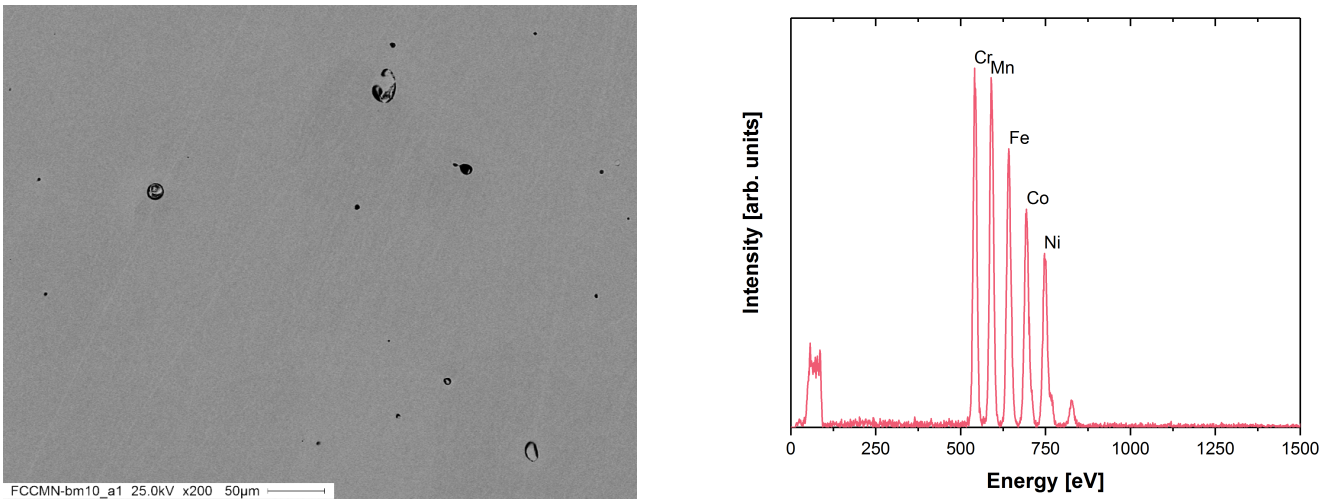

FIG. S1. The left image shows a backscattered-electron image of a polished surface of the FeCoCrMnNi crystal. Apart from several visible pores (black spots), the gray contrast is homogeneous. This means that the composition is homogeneous. The right image is an EDAX Energy-Dispersive X-ray (EDX) spectrum of an area corresponding to about the same size as the lefthand image.

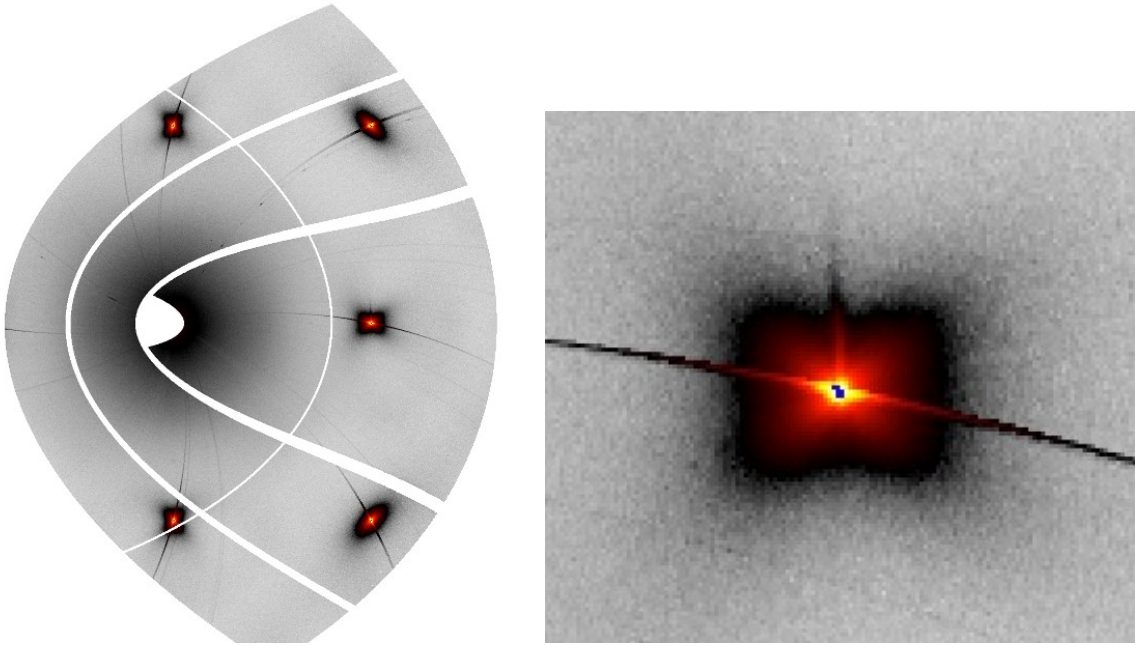

FIG. S2. Diffuse X-ray scattering of the FeCoCrMnNi single crystal sample measured in the HK0 Plane at 90 K (left) and around the 200 Bragg in the HK0 plane (right). There is a clear anisotropy with a minimum of diffuse scattering intensity along the 2 x 0 line as compared to the 2+x 0 0 line. This is opposite to the usual thermal diffuse scattering, and is typical for Huang scattering. Data are represented in a mixed lin-log scale as implemented in Albula by Dectris.

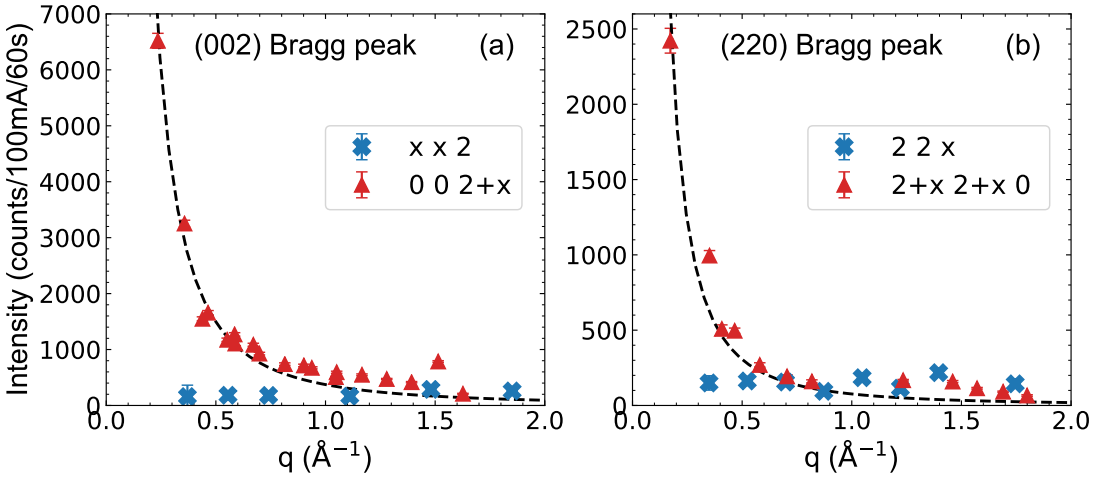

FIG. S3. Anisotropy of the elastic signal measured around the (002) and (220) Bragg peaks. In (a), elastic signal measured around the (002) Bragg peak for 0 0 2+x (longitudinal direction, red triangle) and x x 2 lines (transverse direction, blue crosses). The black dashed line is a $1/q^2$ decay fit. In (b), elastic diffuse scattering measured around the (220) Bragg for 2+x 2+x 0 (longitudinal direction, red triangle) and 2 2 x lines (transverse direction, blue crosses), with a similar $1/q^2$ decay fit. All intensities have been normalized based on efficiencies of the analyzers in order to compare scans across different ID28@ESRF analyzers.

function, $S(\mathbf{Q},\omega)$:

$$\begin{aligned}\frac{d^2\sigma^{\mathrm{n}}}{d\Omega_f dE_f} &= \left.\frac{d^2\sigma^{\mathrm{n}}}{d\Omega_f dE_f}\right|_{\mathrm{coh}} + \left.\frac{d^2\sigma^{\mathrm{n}}}{d\Omega_f dE_f}\right|_{\mathrm{inc}} \\ &= \frac{k_f}{k_i} S(\mathbf{Q},\omega)\end{aligned} \tag{S1}$$

$\mathbf{Q} = \mathbf{G} + \mathbf{q}$ being the position in reciprocal space we are measuring according to reciprocal lattice vector $\mathbf{G}$ and small displacement $\mathbf{q}$.

Coherent scattering and incoherent scattering, also called self-scattering, explain correlated atomic movements and individual atomic movements, respectively. When conducting a neutron or x-ray scattering experiment it is important to have an idea of the amount of incoherent and coherent scattering you can expect from a given sample. Continuing with the example of a neutron scattering experiment, we rely on the coherent neutron scattering length, b, of each element. The coherent, $\sigma^{\mathrm{n}}_{\mathrm{coh}}$, and incoherent, $\sigma^{\mathrm{n}}_{\mathrm{inc}}$, scattering cross-sections are defined as the following [3, 4]:

$$\begin{aligned}\sigma^{\mathrm{n}}_{\mathrm{coh}} &= 4\pi\langle b\rangle^2 \\ \sigma^{\mathrm{n}}_{\mathrm{inc}} &= 4\pi(\langle b^2\rangle - \langle b\rangle^2)\end{aligned} \tag{S2}$$

The neutron scattering lengths and scattering cross-sections for the elements of FeCoCrMnNi are given in Table S1. For FeCoCrMnNi, $\sigma^{\mathrm{n}}_{\mathrm{coh}} = 2.465$ barns/atom, and the total (spin, isotopic, and Laue scattering in the case of FeCoCrMnNi) $\sigma^{\mathrm{n}}_{\mathrm{inc}} = 2.526 + 3.280 = 5.806$ barns/atom, meaning that we expect 2.3× as much incoherent scattering as coherent scattering, and that incoherent scattering makes up 70% of the total neutron scattering cross-section of the material. In our experiment,

TABLE S1. The neutron scattering lengths, b, and neutron coherent and incoherent scattering cross-sections, $\sigma^{\mathrm{n}}_{\mathrm{coh}}$ and $\sigma^{\mathrm{n}}_{\mathrm{inc}}$, are provided for the elements present in FeCoCrMnNi. Scattering cross sections are given in barns (1 barn = 10^{-24} cm^2) and neutron scattering lengths are given in femtometers (1 fm = 10^{-13} cm) [3].

	b	$\boldsymbol{\sigma^{\mathrm{n}}_{\mathrm{coh}}}$	$\boldsymbol{\sigma^{\mathrm{n}}_{\mathrm{inc}}}$
Fe	9.45	11.22	0.4
Co	2.49	0.779	4.8
Cr	3.635	1.66	1.83
Mn	-3.73	1.75	0.4
Ni	10.3	13.3	5.2

assuming that the phonon modes represent the amount of coherent inelastic neutron scattering for a given $\mathbf{Q}$ scan and that the observed broad band accounts for the incoherent neutron scattering, we find this latter to be ∼2.8 times the coherent phonon signal for $\mathrm{TA}^{010}_{\bar{1}00}$ and ∼2.1 times for $\mathrm{TA}^{110}_{\bar{1}10}$, in very good agreement with the expected incoherent-to-coherent ratio.

In addition, the measured incoherent component of the response function, $S_{\mathrm{inc}}(\mathbf{Q},\omega)$, is written as

$$S_{\mathrm{inc}}(\mathbf{Q},\omega) = Q^2 g(\omega)(n(\omega)+1)/\omega, \tag{S3}$$

where $g(\omega)$ is the generalized vibrational density of states (GVDOS), and $n(\omega)$ is the Bose occupation factor.

Using the measured GVDOS from the main text and applying the $(n(\omega)+1)/\omega$ rescaling, the incoherent signal has been simulated. It is shown as a red line in Fig. S4 where it is compared to the data for two transverse excitations measured at high q positions. The incoherent

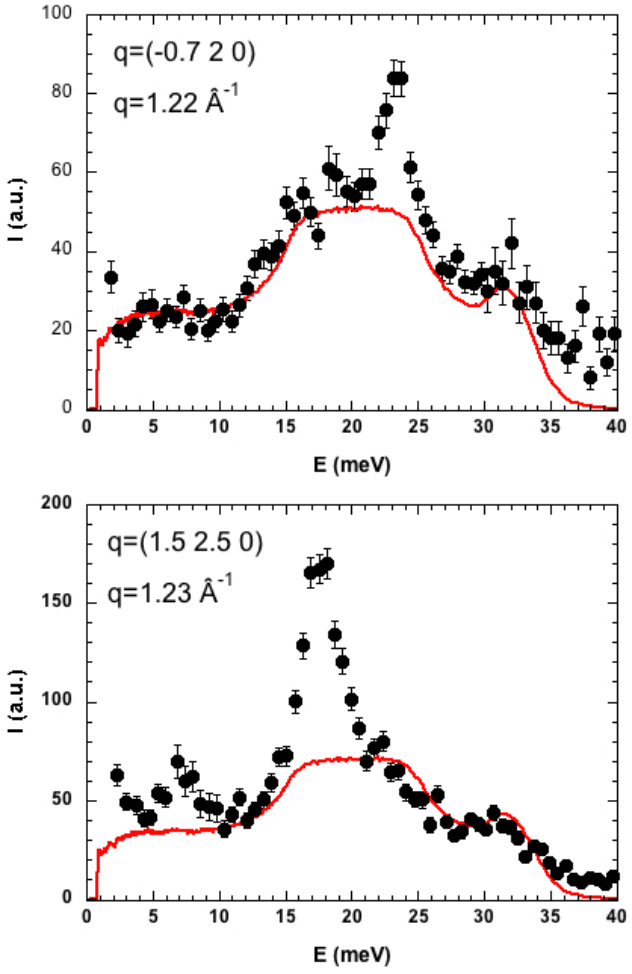

FIG. S4. Comparison between the measured inelastic neutron scattering intensity for two transverse acoustic (TA) excitation (solid black circles) and the simulated incoherent contribution (solid red line, see text). The top panel is for the TA phonon (-0.7 2 0) and the bottom panel is for the TA phonon (1.5 2.5 0).

signal is clearly dominating, noticing, in particular, the constant intensity observed and simulated at low q. To be rigorous, however, a multiphonon contribution should be added at high energy.

The coherent and incoherent X-ray scattering can as well be calculated by starting again from the double differential cross-section for a scattering event, such as the one given for neutrons in eq. S1. In this case we are dependent on the radius of the electron, r_e, and the polarization of the incoming (outgoing) photon, $\hat{\epsilon}_i$ ($\hat{\epsilon}_f$) [5].

$$\frac{d^2\sigma^{\mathrm{x}}}{d\Omega_f dE_f} = r_e^2(\hat{\epsilon}_f \cdot \hat{\epsilon}_i)^2 \frac{k_f}{k_i} S(\mathbf{Q},\omega) \tag{S4}$$

Then the coherent and incoherent X-ray scattering cross-sections, $\sigma^{\mathrm{x}}_{\mathrm{coh}}$ and $\sigma^{\mathrm{x}}_{\mathrm{inc}}$, respectively, depend upon the atomic form factors, f, and are written as follows [6]:

$$\begin{aligned} \sigma^{\mathrm{x}}_{\mathrm{coh}} &= \langle f \rangle^2 \\ \sigma^{\mathrm{x}}_{\mathrm{inc}} &= \langle f^2 \rangle - \langle f \rangle^2 \end{aligned} \tag{S5}$$

As a first approximation we will take the values at $\mathbf{q} = 0$, i.e. $\mathbf{Q} = \mathbf{G}$, meaning that the atomic form factor for each element is defined as $f = Z$, where Z is the atomic number, directly from the Periodic Table of Elements. Therefore, $\sigma^{\mathrm{x}}_{\mathrm{coh}} = 676$, and $\sigma^{\mathrm{x}}_{\mathrm{inc}} = 2$, confirming that incoherent X-ray scattering for FeCoCrMnNi is minimal in comparison to the coherent component.

1. Time-of-Flight Spectroscopy

Time-of-Flight (TOF) spectroscopy was used to measure the neutron-weighted generalized vibrational density of states (GVDOS) reported in Fig. 2 from the main text. A single crystal sample of FeCoCrMnNi (cylinder-shaped with a height of 1 cm and diameter of 0.8 cm) was measured on the cold-neutron TOF spectrometer IN5@ILL with an incident wavelength of $\lambda = 3.2$ Å at room temperature with a cryostat environment. The sample was rotated 0.5° after each scan, resulting in a total Ω range of 43°.

A polycrystalline sample (2x1x1 cm^3, 11.5 g) was taken to the cold-neutron TOF spectrometer IN6@ILL and measured with a Be filter and $\lambda = 5.1$ Å at 100, 200, and 300 K, also using a standard cryostat. Empty can measurements, or measurements that are made in the same sample environment but without the sample in order to account for non-sample-related scattering captured at the detectors, were taken at all three temperatures and subtracted from the sample data.

Both IN5@ILL and IN6@ILL GVDOS plots were produced using the MUPHOCOR (MUlti-PHOnon CORrection) program [7] for LAMP [8], in which the expected neutron scattering cross section and atomic mass of FeCoCrMnNi were used as starting parameters for a self-consistent multi-phonon scattering correction of the data.

2. Triple-Axis Spectroscopy

The transverse acoustic (TA) mode propagating along [$\bar{1}$00], polarized along [010] (TA$^{010}_{\bar{1}00}$), and the TA mode propagating along [$\bar{1}$10], polarized along [110] (TA$^{110}_{\bar{1}10}$) shown in Fig. 3(c,d) of the main text were taken from Triple-Axis Spectroscopy (TAS) measurements on the thermal-neutron TAS instrument 1T-1@LLB. A fixed k_f = 2.662 Å^{-1} ($\lambda = 2.36$ Å) and cryostat were used in order to take constant $\mathbf{Q}$ scans at 3, 100, and 300 K.

The TA mode and the textured band were fit using the program 'AFITV,' an analysis tool developed by B. Hennion and P. Bourges at Laboratoire Léon Brillouin [9]. It takes into account instrumental resolution by using instrumental parameters as well as sample characteristics,

in order to model the shape and size of the experimental resolution. Indeed, the instrumental resolution is energy and q dependent and is determined from the experimental setup, the phonon group velocity, and the sample mosaicity, which is a measure of the quality of a single crystal. The mosaicity measures the angular distribution of a given direction in the reciprocal space, deteriorating the resolution in q and thus in energy. The mosaicity of our single crystal was about 1°, which results in a total energy resolution between 2.2 and 1.3 meV depending on q.

AFITV makes the convolution of the scattering function and instrumental resolution function [10], therefore allowing us to decouple the intrinsic phonon measurement from the distortion caused by the spectrometer. More details on the use of this software are discussed in Appendix C.

Unfortunately, the presence of the incoherent scattering made the fitting procedure particularly challenging, so that, even if at high energy the phonon linewidth was not resolution limited, we could not reliably extract it because of the merging of the phonon with the incoherent intensity.

3. Inelastic X-ray Scattering

Inelastic X-ray scattering was used to measure the longitudinal acoustic (LA) modes propagating along the [001] and [110] directions (LA_{001} and LA_{110}) and and the transverse acoustic (TA) modes propagating along [00$\bar{1}$], polarized along [110] ($TA^{110}_{00\bar{1}}$) and propagating along [110], polarized along [001] (TA^{001}_{110}) reported in Fig. 3 of the main text. Measurements were made at the IXS ID28@ESRF beamline. The [999] reflection of the silicon monochromator was used, resulting in an incoming X-ray energy of 17.794 keV (or a wavelength of 0.697 Å) and an energy resolution of 2.8 meV. The Joule-Thomson displex was incorporated for temperature measurements at 15, 100, and 300 K.

The ID28@ESRF beamline has the advantage of being able to measure 9 points in reciprocal space simultaneously, due to the 9 analyzers mounted at fixed 2θ angular distances of 1.54° from each other. The plots in Fig. 3(a,b) from the main text and Figs. S19-S21 represent scans from all 9 of these analyzers, and therefore the intensities should not be compared directly, due to the fact that each analyzer has its own efficiency as compared to the others. All analyzers were receiving the scattered intensity through rectangular slits, with horizontal and vertical opening of 20 mm and 55 mm respectively. The horizontal opening fixes the q resolution which is $\Delta q = 0.026$ Å^{-1}. This q resolution induces an additional energy broadening as it couples to the slope of the acoustic dispersion: $\Delta E_q = v_g \Delta q$, where v_g is the group velocity. As such it plays a major role at low q, before the bending of the acoustic dispersion. As for the spectrometer energy resolution, this has been measured for each of the 9 analyzers by measuring the elastic scattering of a plexiglass sample, cooled to 14.5 K, at q values close to the maximum of the static structure factor, within the energy range ± 40 meV. Finally, the crystal used for these measurements had a very small mosaicity of only 0.1°, leading to a mosaicity contribution to the effective resolution of only 0.1 meV.

In order to extract the intrinsic phonon linewidths shown in Figs. 6,7,8 from the main text, both energy and q resolution (ΔE, Δq) have been taken into account. For this, the q distribution over the illuminated area of the analyzer has been calculated and the experimental spectrum has been fit with a superposition of phonon modes for all q's within this distribution, then convoluted with the energy instrumental resolution.

APPENDIX C: ACOUSTIC NATURE OF THE PHONON MODES

In both INS and IXS experiments we have fit our data using a delta function for the elastic line, a damped harmonic oscillator for the phonon mode, and, in the INS case, a two-part Gaussian distribution for the broad textured band. The fit was performed using AFITV for INS data and a home-made Matlab program for IXS. In both programs the theoretical model was convoluted with the instrumental resolution function prior to fitting the experimental data, allowing for the extraction of the intrinsic phonon properties (position, intensity and linewidth). Fitting the different components of the scans in this manner allows us to account for all of the intensity shown in the scans.

The result of this method of analysis is that we can track the changes in the normalized intensity of $S(\mathbf{Q},\omega,T)$, from eq. S1, of the phonon mode to determine its acoustic character. It can be shown that for an acoustic phonon, the normalized dynamic structure factor, $\mathrm{DSF}_{i,\mathbf{q}}(\mathbf{Q},\omega,T)$, is constant, where the integral is taken over the measured phonon peak [4, 11–14]. The response function, $S(\mathbf{Q},\omega,T)$, defined in Appendix B, depends on the thermal occupation factor, $n(\omega_{i,\mathbf{q}})$, the polarization of the phonon mode, $\xi_{i,\mathbf{q}}$, and the Bragg peak structure factor, F_B. This equation works in the long-wavelength limit, $|\mathbf{q}| \ll |\mathbf{Q}|$, and given that $\hbar\omega \ll k_B T$.

$$\mathrm{DSF}_{i,\mathbf{q}}(\mathbf{Q},\omega,T) = \frac{\omega_i(\mathbf{q})}{Q^2 \cdot n(\omega_{i,\mathbf{q}})} \int S_{i,\mathbf{q}}(\mathbf{Q},\omega,T)d\omega,$$
$$\text{where } \int S_{i,\mathbf{q}}(\mathbf{Q},\omega,T)d\omega \approx (\mathbf{Q}\cdot\xi_{i,\mathbf{q}})^2 |F_\mathrm{B}|^2 \frac{n(\omega_{i,\mathbf{q}})}{\omega_i(\mathbf{q})} \tag{S1}$$

In Fig. S5 we report the normalized intensity of the phonon mode across the Brillouin zone in each direction, as obtained with the fit of INS data. In order to simplify the analysis, we have imposed a constant energy position and normalized intensity for the main features of the broad band across the Brillouin zone for a given

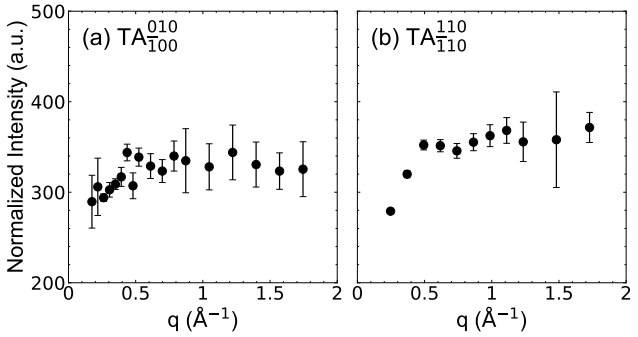

FIG. S5. Normalized intensity (see eq. S1) of the two phonon modes (see figure labels) measured by constant-**Q** inelastic neutron scattering scans on 1T@LLB at 300 K.

direction. This is justified by the fact that the broad band looks q independent, as shown in Fig. S8. Above 0.4 Å^{-1}, the normalized intensity of the phonon modes remain constant within the errorbars up to the Brillouin zone border, confirming the acoustic nature of the transverse modes throughout the Brillouin zone. A slight decrease at smaller q, below 0.4 Å^{-1}, in both directions, is in fact due to a strong entanglement of the intensities of TA and broad band with the intense elastic line, making these values more uncertain. The constant character of the phonon normalized intensity supports the conclusion that there is no interference of the phonon with the broad band. This is different from the case of other complex crystalline systems in which an intensity transfer is observed between acoustic modes and low-lying optical modes [15–20].

In Fig. S6 we report the normalized intensity of the four polarizations measured by IXS. All intensities have been normalized by the analyzer efficiencies in order to compare scans across different analyzers. If along the [110] direction in (c,d) the normalized intensity remains quite constant, along the [001] direction in (a,b) this is not so evident. Specifically, a deviation from constant clearly appears in the longitudinal polarization in (a) at $\sim$ 0.8-1 Å^{-1}, which coincides with the third regime of the longitudinal attenuation, described in Fig. 6(a) of the main text. Still, we can conclude that the acoustic character is conserved up to at least 1 Å^{-1}.

APPENDIX D: HEA DENSITY OF STATES COMPARISON

In Fig. S7, Generalized Vibrational Density of States (GVDOS) of equiatomic FeCoCrNi (FCCN) [21] at 300 K is plotted against the GVDOS of FeCoCrMnNi, replotted from Fig. 2(b) from the main text. Both measurements have been made by INS, and show close matching, including in the low energy acoustic region between 0-10 meV. These are additionally compared to elemental GVDOS measurements of Fe [22], Ni [23], and Cr [22]. The

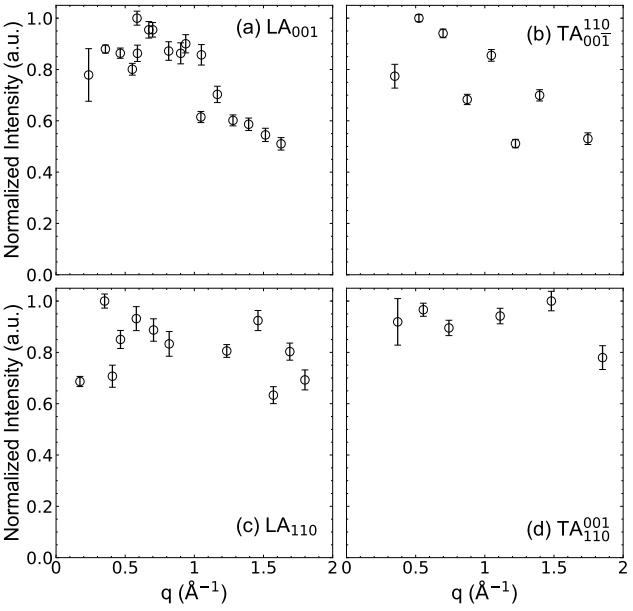

FIG. S6. Normalized intensity (see eq. S1) of the four phonon modes (see figure labels) measured by constant-**Q** inelastic X-ray scattering scans on ID28@ESRF at 300 K. All intensities have been normalized based on efficiencies of the analyzers in order to compare scans across different analyzers.

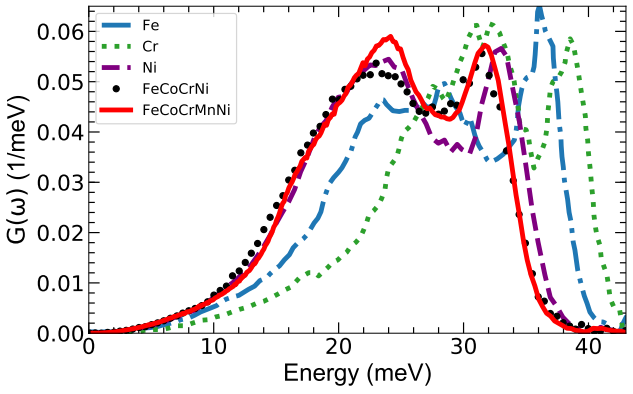

FIG. S7. The Generalized Vibrational Density of States of FeCoCrMnNi (solid red line), shown first in Fig. 2(b) from the main text, is compared to the GVDOS of FeCoCrNi (black circle markers), measured by Lucas *et al.* with Inelastic Neutron Scattering, and to several single element GVDOS, including Fe [22] (blue dash-dotted line), Ni [23] (purple dashed line), and Cr [22] (green square markers).

GVDOS of FeCoCrMnNi and FeCoCrNi appear to most closely match that of Ni.

APPENDIX E: INELASTIC SCATTERING ENERGY SCANS

All scans used to create Fig. 5 of the main text that were not already shown in Fig. 3 of the main text have been included in the following section. The scans taken during the neutron triple-axis spectroscopy experiment at 300 K are shown in Fig. S8. For the inelastic neutron scattering experiment, Figs. S9-S10 depict scans at 100 and 3 K from the $TA^{010}_{\bar{1}00}$ dispersion, respectively, and similarly for Figs. S11-S12 and the $TA^{110}_{\bar{1}10}$ dispersion.

For the inelastic X-ray scattering measurements, Figs. S13-S15 show scans from the LA_{001} polarization at 300, 100, and 15 K, respectively, and similarly for the $TA^{110}_{00\bar{1}}$ polarization in Figs. S16-S18. Scans for the LA_{110} polarization, taken at 300 K, are plotted in Fig. S19. Finally, the TA^{001}_{110} polarization measurements at 300 and 15 K are represented in Figs. S20 and S21, respectively.

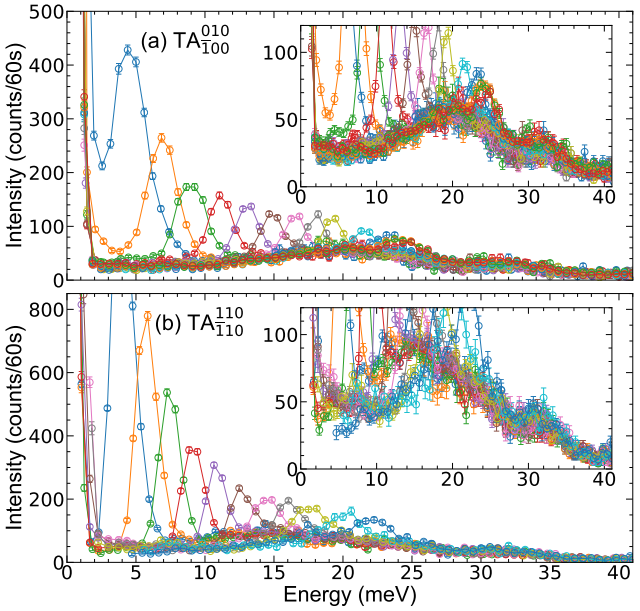

FIG. S8. Plots of the (a) $TA^{010}_{\bar{1}00}$ and (b) $TA^{110}_{\bar{1}10}$ phonon dispersions at 300 K, measured by inelastic neutron scattering, which emphasize the incoherent scattering seen in all neutron scans. The broad textured band persists through the entire Brillouin zone in both polarizations. In (a), scans cover $q = 0.1 - 0.6$ r.l.u. with a step size of 0.05 r.l.u., and $q = 0.6 - 1.0$ r.l.u. with a step size of 0.1 r.l.u. In (b), scans cover $q = 0.1 - 0.5$ r.l.u. with a step size of 0.05 r.l.u., and $q = 0.5 - 0.7$ r.l.u. with a step size of 0.1 r.l.u.

* To whom correspondence should be addressed: valentina.giordano@univ-lyon1.fr

[1] M. Feuerbacher, E. Würtz, A. Kovács, and C. Thomas, Single-crystal growth of a FeCoCrMnAl high-entropy alloy, Mater. Res. Lett. **5**, 128 (2016).

[2] S. Pailhès, V. M. Giordano, P.-F. Lory, M. D. Boissieu, and H. Euchner, *Nanostructured Semiconductors*, edited by K. Termentzidis (Pan Stanford, 2017).

[3] A. Furrer, J. Mesot, and T. Strässle, *Neutron Scattering in Condensed Matter Physics* (WORLD SCIENTIFIC, 2009).

[4] G. L. Squires, *Introduction to the Theory of Thermal Neutron Scattering* (Cambridge University Press, 2012).

[5] M. d'Astuto and M. Krisch, High resolution inelastic x-ray scattering from thermal collective excitations, in *JDN 16 – Diffusion Inélastique des Neutrons pour l'Etude des Excitations dans la Matiére Condensée* (EDP Sciences, 2010).

[6] A. Q. Baron, High-resolution inelastic x-ray scattering i: Context, spectrometers, samples, and superconductors, in *Synchrotron Light Sources and Free-Electron Lasers* (Springer International Publishing, 2016) pp. 1643–1719.

[7] W. Reichardt, *MUPHOCOR, A Fortran Program To Determine the Phonon Density of States from Neutron Scattering Experiments* (1984).

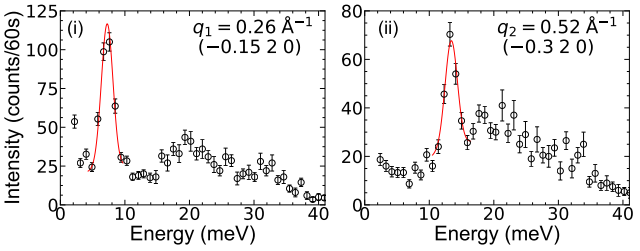

FIG. S9. Energy scans at 100 K of the transverse acoustic (TA) mode propagating along the $[\bar{1}00]$, polarized along [010] ($TA^{010}_{\bar{1}00}$), taken near the (020) Bragg peak. Experiments were made at 1T@LLB, using a fixed k_f of 2.662 Å^{-1}.

[8] D. Richard, M. Ferrand, and G. J. Kearley, Analysis and visualisation of neutron-scattering data, Journal of Neutron Research **4**, 33 (1996).

[9] B. Hennion and P. Bourges, Afitv: Refinement program for triple axis spectrometer data.

[10] G. Shirane, S. M. Shapiro, and J. M. Tranquada, *Neutron Scattering with a Triple–Axis Spectrometer* (Cambridge University Press, 2015).

[11] M. Boudard, M. de Boissieu, S. Kycia, A. I. Goldman,

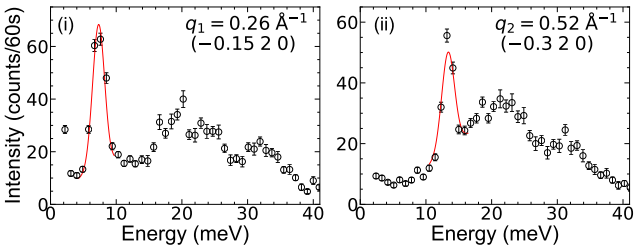

FIG. S10. Energy scans at 3 K of the transverse acoustic (TA) mode propagating along the $[\bar{1}00]$, polarized along [010] ($TA^{010}_{\bar{1}00}$), taken near the (020) Bragg peak. Experiments were made at 1T@LLB, using a fixed k_f of 2.662 Å^{-1}

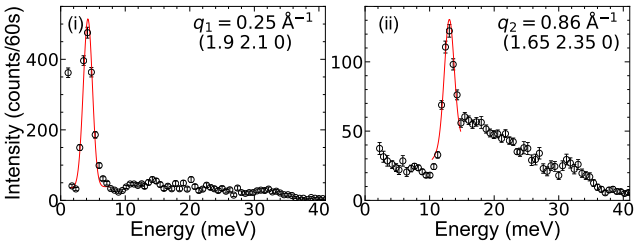

FIG. S11. Energy scans at 100 K of the transverse acoustic (TA) mode propagating along the $[\bar{1}10]$, polarized along [110] ($TA^{110}_{\bar{1}10}$), taken near the (220) Bragg peak. Experiments were made at 1T@LLB, using a fixed k_f of 2.662 Å^{-1}

B. Hennion, R. Bellissen, M. Quilichini, R. Currat, and C. Janot, Optic modes in the AlPdMn icosahedral phase, Journal of Physics: Condensed Matter **7**, 7299 (1995).

[12] P.-F. Lory, V. M. Giordano, P. Gille, H. Euchner, M. Mihalkovič, E. Pellegrini, M. Gonzalez, L.-P. Regnault, P. Bastie, H. Schober, S. Pailhes, M. R. Johnson, Y. Grin, and M. de Boissieu, Impact of structural complexity and disorder on lattice dynamics and thermal conductivity in the o-$Al_{13}Co_4$ phase, Phys. Rev. B **102**, 024303 (2020).

[13] M. de Boissieu, S. Francoual, M. Mihalkovič, K. Shibata, A. Q. R. Baron, Y. Sidis, T. Ishimasa, D. Wu, T. Lograsso, L.-P. Regnault, F. Gähler, S. Tsutsui, B. Hennion, P. Bastie, T. J. Sato, H. Takakura, R. Currat, and A.-P. Tsai, Lattice dynamics of the Zn-Mg-Sc icosahedral quasicrystal and its Zn-Sc periodic 1/1 approximant, Nat. Mater. **6**, 977 (2007).

[14] P.-F. Lory, *Dynamique de réseau et conductivité thermique dans les alliages métalliques complexes*, Ph.D. thesis, Université de Grenoble (2015).

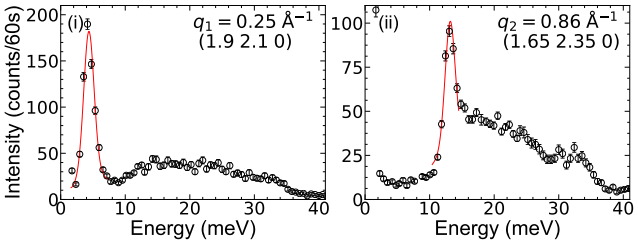

FIG. S12. Energy scans at 3 K of the transverse acoustic (TA) mode propagating along the $[\bar{1}10]$, polarized along [110] ($TA^{110}_{\bar{1}10}$), taken near the (220) Bragg peak. Experiments were made at 1T@LLB, using a fixed k_f of 2.662 Å^{-1}

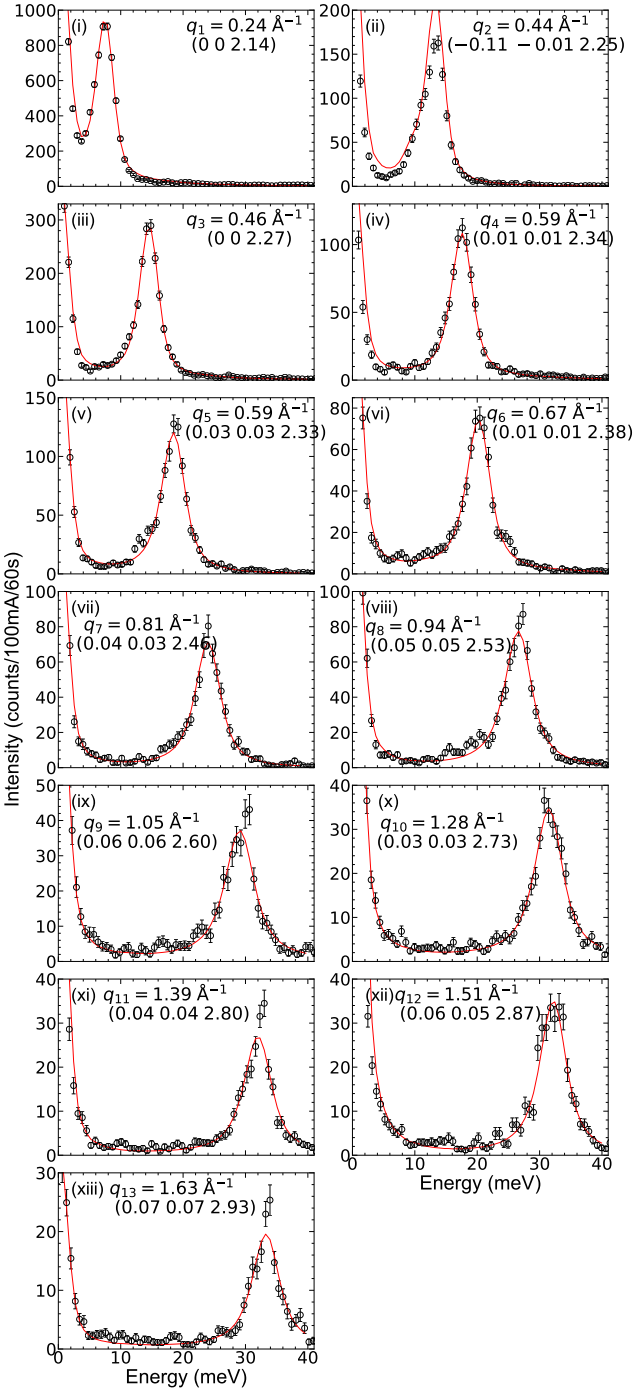

FIG. S13. Energy scans at 300 K of the longitudinal acoustic (LA) mode propagating along the [001] direction (LA_{001}), taken near the (002) Bragg peak. Experiments were made at the ID28@ESRF beamline, using the [999] reflection of the silicon monochromator.

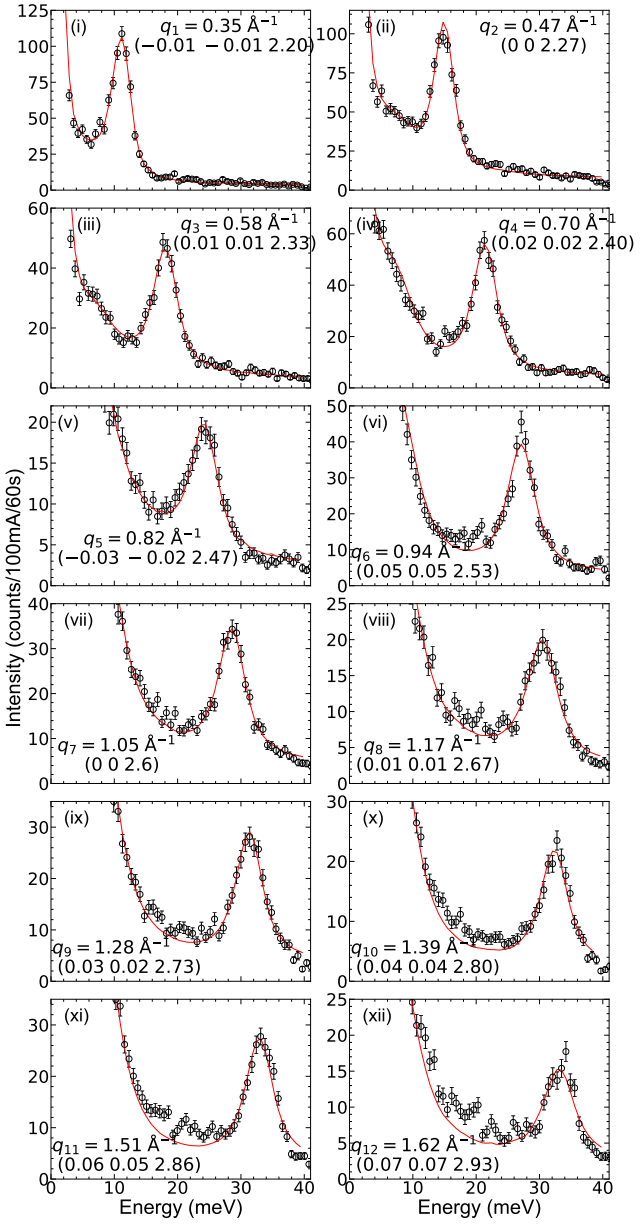

FIG. S14. Energy scans at 100 K of the longitudinal acoustic (LA) mode propagating along the [001] direction (LA_{001}), taken near the (002) Bragg peak. Experiments were made at the ID28@ESRF beamline, using the [999] reflection of the silicon monochromator.

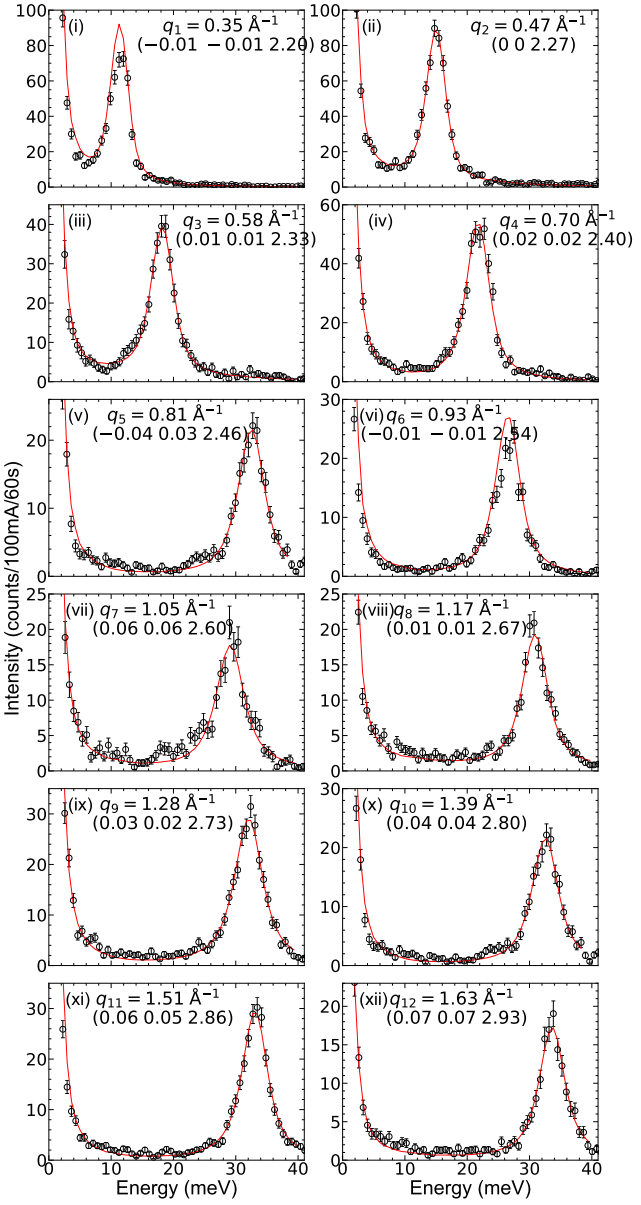

FIG. S15. Energy scans at 15 K of the longitudinal acoustic (LA) mode propagating along the [001] direction (LA_{001}), taken near the (002) Bragg peak. Experiments were made at the ID28@ESRF beamline, using the [999] reflection of the silicon monochromator.

[15] H. Euchner, S. Pailhès, L. T. K. Nguyen, W. Assmus, F. Ritter, A. Haghighirad, Y. Grin, S. Paschen, and M. de Boissieu, Phononic filter effect of rattling phonons in the thermoelectric clathrate $Ba_8Ge_{40+x}Ni_{6-x}$, Phys. Rev. B **86**, 224303 (2012).

[16] S. Pailhès, H. Euchner, V. Giordano, R. Debord, A. Assy, S. Gomès, A. Bosak, D. Machon, S. Paschen, and M. de Boissieu, Localization of propagative phonons in a perfectly crystalline solid, Phys. Rev. Lett. **113**, 025506 (2014).

[17] P.-F. Lory, S. Pailhès, V. M. Giordano, H. Euchner, H. D. Nguyen, R. Ramlau, H. Borrmann, M. Schmidt, M. Baitinger, M. Ikeda, P. Tomeš, M. Mihalkovič, C. Allio, M. R. Johnson, H. Schober, Y. Sidis, F. Bourdarot, L. P. Regnault, J. Ollivier, S. Paschen, Y. Grin, and M. de Boissieu, Direct measurement of individual phonon lifetimes in the clathrate compound $Ba_{7.81}Ge_{40.67}Au_{5.33}$, Nat. Commun. **8**, 491 (2017).

[18] H. Euchner, S. Pailhès, V. M. Giordano, and M. de Boissieu, Understanding lattice thermal conductivity in thermoelectric clathrates: A density functional theory study on binary Si-based type-I clathrates, Phys.

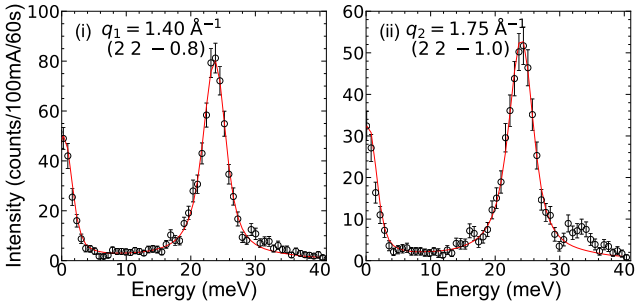

FIG. S16. Energy scans at 300 K of the transverse acoustic (TA) mode propagating along $[00\bar{1}]$, polarized along [110] ($TA^{110}_{00\bar{1}}$), taken near the (220) Bragg peak. Experiments were made at the ID28@ESRF beamline, using the [999] reflection of the silicon monochromator.

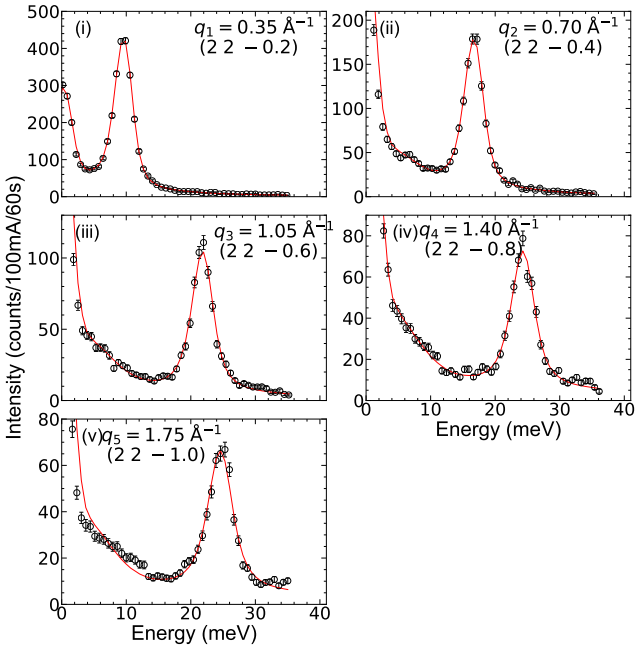

FIG. S17. Energy scans at 100 K of the transverse acoustic (TA) mode propagating along $[00\bar{1}]$, polarized along [110] ($TA^{110}_{00\bar{1}}$), taken near the (220) Bragg peak. Experiments were made at the ID28@ESRF beamline, using the [999] reflection of the silicon monochromator.

Rev. B **97**, 014304 (2018).

[19] R. Viennois, M. M. Koza, R. Debord, P. Toulemonde, H. Mutka, and S. Pailhès, Anisotropic low-energy vibrational modes as an effect of cage geometry in the binary barium silicon clathrate $Ba_{24}Si_{100}$, Phys. Rev. B **101**, 224302 (2020).

[20] S. R. Turner, S. Pailhès, F. Bourdarot, J. Ollivier, S. Raymond, T. Keller, Y. Sidis, J.-P. Castellan, P.-F. Lory, H. Euchner, M. Baitinger, Y. Grin, H. Schober, M. de Boissieu, and V. M. Giordano, Impact of temperature and mode polarization on the acoustic phonon range in complex crystalline phases: A case study on intermetallic clathrates, Phys. Rev. Research **3**, 013021 (2021).

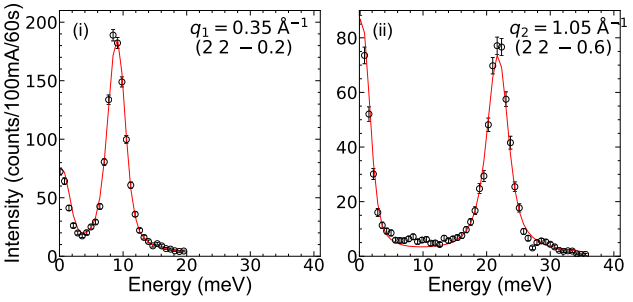

FIG. S18. Energy scans at 15 K of the transverse acoustic (TA) mode propagating along $[00\bar{1}]$, polarized along [110] ($TA^{110}_{00\bar{1}}$), taken near the (220) Bragg peak. Experiments were made at the ID28@ESRF beamline, using the [999] reflection of the silicon monochromator.

[21] M. S. Lucas, G. B. Wilks, L. Mauger, J. A. Muñoz, O. N. Senkov, E. Michel, J. Horwath, S. L. Semiatin, M. B. Stone, D. L. Abernathy, and E. Karapetrova, Absence of long-range chemical ordering in equimolar FeCoCrNi, Appl. Phys. Lett. **100**, 251907 (2012).

[22] M. S. Lucas, M. Kresch, R. Stevens, and B. Fultz, Phonon partial densities of states and entropies of Fe and Cr in bcc Fe-Cr from inelastic neutron scattering, Phys. Rev. B **77**, 184303 (2008).

[23] M. S. Lucas, L. Mauger, J. A. Muñoz, I. Halevy, J. Horwath, S. L. Semiatin, S. O. Leontsev, M. B. Stone, D. L. Abernathy, Y. Xiao, P. Chow, and B. Fultz, Phonon densities of states of face-centered-cubic Ni-Fe alloys, J. Appl. Phys. **113**, 17A308 (2013).

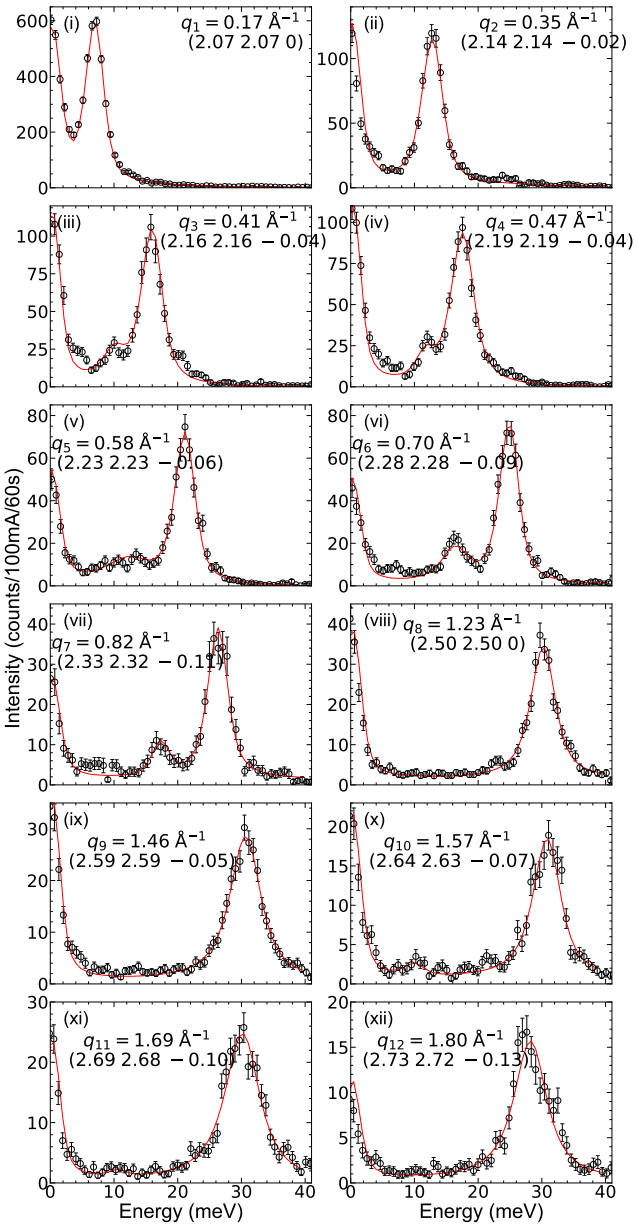

FIG. S19. Energy scans at 300 K of the longitudinal acoustic (LA) mode propagating along the [110] direction (LA_{110}), taken near the (220) Bragg peak. Experiments were made at the ID28@ESRF beamline, using the [999] reflection of the silicon monochromator.

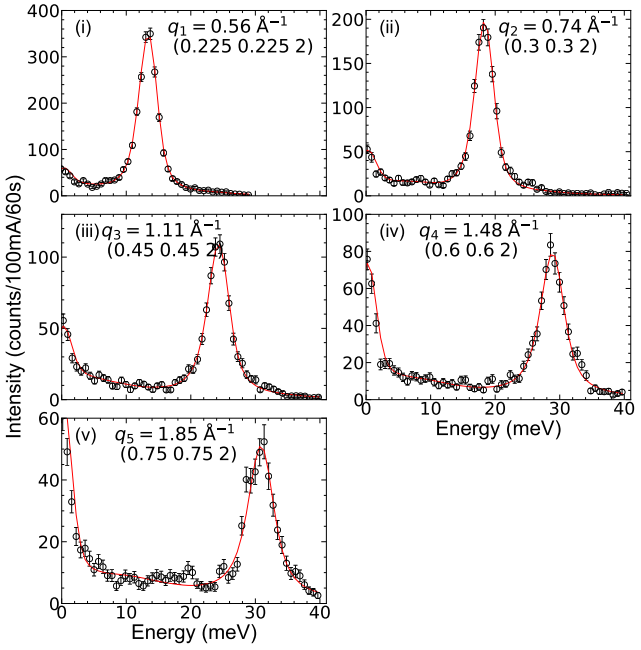

FIG. S20. Energy scans at 300 K of the transverse acoustic (TA) mode propagating along [110], polarized along [001] (TA^{001}_{110}), taken near the (002) Bragg peak. Experiments were made at the ID28@ESRF beamline, using the [999] reflection of the silicon monochromator.

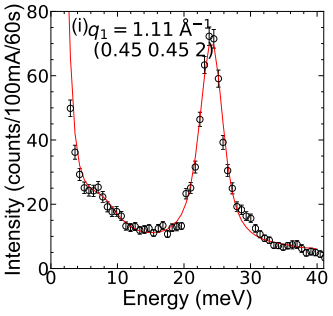

FIG. S21. Energy scan at 15 K of the transverse acoustic (TA) mode propagating along [110], polarized along [001] (TA^{001}_{110}), taken near the (002) Bragg peak. Experiment was made at the ID28@ESRF beamline, using the [999] reflection of the silicon monochromator.

4.3 Revisiting the Lattice Dynamics of Cubic Yttria-Stabilized Zirconia

State of the article: manuscript.
Authors: *Shelby R. Turner, Stéphane Pailhès, Leila Ben Mahfoud, Christian Carbogno, Marc de Boissieu, Frédéric Bourdarot, Helmut Schober, Yvan Sidis, John-Paul Castellan, Andrea Piovano, Alexandre Ivanov, Valentina M. Giordano*

Yttria-Stabilized Zirconia represents an ideal example for the study of complexity and disorder. By taking the relatively simple structure of Zirconia and doping it with various concentrations of Yttria in order to stabilize the cubic structure at room temperature, we induce disorder in the form of oxygen vacancies. An explanation of the disordered structure due to oxygen vacancies has been detailed in Section 1.3.2, and the diffuse scattering for the particular 9.5 mol.% Yttria content sample that was used to conduct the experiments in this manuscript was shown in Fig. 1.8.

As it will be stated in this Yttria-Stabilized Zirconia manuscript, the experimentally measured phonon dispersions have already been published in the 1980's. However, by working with improved instrumental resolution, we were able to uncover the intrinsic energy dependence of the acoustic phonon linewidths in this material. Through the inclusion of this manuscript I therefore reiterate one of the main themes of my thesis, which is that we lack a library of the energy and temperature dependencies of phonon linewidths in simple, complex, and disordered systems. By publishing this manuscript on the already well-studied Yttria-Stabilized Zirconia material, I add to the growing database, and emphasize the need to revisit simple materials that have already considered to be complete in their experimental findings. Yttria-Stabilized Zirconia remains a complicated material to model as well, due to the chemically disordered structure. This manuscript will hopefully reignite interest in this pursuit.

Contributions of the Ph.D Candidate:

I played a central role in preparing and conducting the neutron experiments from 1T@LLB, 4F@LLB, and IN8@ILL, and the thermal diffuse scattering experiments on the X-ray beamline ID28@ESRF. I then made the corresponding data analysis and wrote the article.

Perspectives/Further work that can be done:

The results of this manuscript highlight two fundamental needs for the understanding of phonon dynamics and thermal transport in cubic Yttria-Stabilized Zirconia: (1) the need for *ab-initio* calculations of phonon dispersions that take into account the defect and vacancy structure, and (2) the need for exhaustive investigations similar to ours at higher concentrations of Yttria, which would track the evolution of phonon scattering with vacancy content, and, by extension, the changing vacancy-induced defect structure. We give all the necessary ingredients needed in order to delve further into the extended defect phonon scattering mechanism that is at play in this material.

Towards this end, and at the time of writing, we are currently in collaboration with Christian Carbogno from the Fritz-Haber-Institut der Max-Planck-Gesellschaft in Berlin, Germany, who has begun *ab-initio* calculations on cubic Yttria-Stabilized-Zirconia. Preliminary results reveal phonon dispersions that are much different than those of the perfect cubic structure, with the appearance of a large number of optical modes, and specifically one around 9 meV, in very good agreement with our experimental findings. However, the structure is not yet stabilized, with several imaginary frequencies still being present. Once the structure is stabilized and the results

assessed, we will be able to have a more solid and extended discussion of the acoustical-optical interaction, which will then be incorporated into this Yttria-Stabilized Zirconia manuscript prior to submission.

On another note, as the thermal conductivity of Yttria-Stabilized Zirconia appears to be very dependent upon the Yttria content, I also propose that a series of similar experimental studies be made in the future that include samples that are still within the cubic phase, but with higher contents of Yttria. As the thermal conductivity at room temperature first decreases to a minimum at 10 mol.% and then increases with increasing Yttria content, we can hopefully expect to see a change in the energy dependence and/or broadening of the intrinsic linewidths across the different samples. As stated in Section 1.3.2, the oxygen vacancies evolve from being relatively isolated vacancy clusters into ordered aggregates with increasing Yttria content, and therefore creating a series of such studies would allow us to better understand the detailed phonon scattering evolution as well.

The first step towards this end is being taken: at the time of writing, we are in collaboration with Christophe Candolfi and Bertrand Lenoir from the Institut Jean Lamour at the Université de Lorraine in Nancy, France, and Petr Levinský and Jiří Hejtmánek from the Institute of Physics at the Czech Academy of Sciences in Prague, Czech Republic, who are conducting thermal conductivity measurements on our sample of Yttria-Stabilized Zirconia. With these results we hope to draw conclusions between the microscopic phonon scattering dependencies and the resulting macroscopic thermal transport in Yttria-Stabilized Zirconia.

Revisiting the Lattice Dynamics of Cubic Yttria-Stabilized Zirconia

Shelby R. Turner,[1,2,3] Stéphane Pailhès,[3] Leila Ben Mahfoud,[3] Christian Carbogno,[4] Marc de Boissieu,[2] Frédéric Bourdarot,[5] Helmut Schober,[1] Yvan Sidis,[6] John-Paul Castellan,[6,7] Andrea Piovano,[1] Alexandre Ivanov,[1] and Valentina M. Giordano[3,*]

[1] *Institut Laue-Langevin, Grenoble F-38042 Grenoble cedex, France*
[2] *Université Grenoble Alpes, CNRS, Grenoble-INP, SIMaP, F-38402 St Martin d'Hères, France*
[3] *Institute of Light and Matter, UMR5306 Université Lyon 1-CNRS, Université de Lyon F-69622 Villeurbanne cedex, France*
[4] *Fritz-Haber-Institut der Max-Planck-Gesellschaft, Faradayweg 4–6, D-14195 Berlin, Germany*
[5] *Université Grenoble Alpes, CEA, IRIG, MEM, MDN, F-38000 Grenoble cedex, France*
[6] *Laboratoire Léon Brillouin, CEA, CNRS, UMR-12, CE-Saclay, F-91191 Gif-sur-Yvette, France*
[7] *Institut für Festkörperphysik, Karlsruher Institut für Technologie, D-76021 Karlsruhe, Germany*

(Dated: August 25, 2021)

Cubic Yttria-Stabilized Zirconia has long been a ceramic material of interest for its many uses in thermal-based applications. Its low and weakly temperature dependent thermal conductivity has been ascribed to its large oxygen vacancies content, which introduces disorder and strongly scatters phonons. However, the impact of this extended defect structure, which introduces correlated disorder, on phonon dynamics is still not fully understood. In this work, we present new findings on the phonon dispersions of this material, showing, to the best of our knowledge for the first time, experimental evidence of low-energy optical branches outside of the center of the Brillouin zone, which reduce the momentum and energy phase space available for acoustic phonons. Furthermore, the observed energy dependence of the intrinsic acoustic phonon lifetimes clearly suggests the existence of competing Mie and Rayleigh scattering mechanisms. Our results allow us to uncover a new phonon dynamics scenario in cubic Yttria-Stabilized Zirconia, which will help improve our understanding in this system and, more generally, in systems where the lattice dynamics are dominated by extended defect structures.

Zirconia (ZrO_2) is one of the most studied ceramic materials due to a number of properties which make it suitable for many different applications, from a high-temperature ion conductor in solid oxide fuel cells to a material designed to be a thermal barrier coating [1–3]. Stable at room temperature in its monoclinic form [4], Zirconia then transforms to a tetragonal structure at 1440 K [5] and a cubic phase at 2640 K [6].

Its ideal resistance to fracture for a wide temperature range can be further solidified with the addition of rare-earth elements, which impacts the phase diagram and therefore changes the stability regions of the different phases. Specifically, at room temperature, Yttria-Stabilized Zirconia ($(ZrO_2)_{1-x}(Y_2O_3)_x$, YSZ) is monoclinic for $x \leq$~2 mol.%, tetragonal for ~2 $\leq x \leq$~8 mol.%, and cubic for ~8 $\leq x \leq$~20 mol.% [7]. This latter phase is characterized by a surprisingly low thermal conductivity, good thermal shock resistance, and a high melting point: a combination of properties that makes it ideal for thermal-barrier applications such as for turbine engines.

The introduction of Yttria gives rise to a highly defective crystal with a large amount of oxygen vacancies, which is proportional to the Yttria content for charge neutrality requirements [8, 9]. It follows that for large Yttria concentrations, strong disorder and large relaxations exist due to the presence of structural vacancies, leading to thermal transport properties that are much different in YSZ with respect to the ordered, pure Zirconia phase.

Indeed, while pure, monoclinic Zirconia has a room temperature thermal conductivity of 8.2 W/mK [10] which decreases with temperature, compatible with anharmonic phonon-phonon (Umklapp) processes as a dominant phonons scattering mechanism, the introduction of Yttria drastically modifies its value and behavior. Firstly, the thermal conductivity at room temperature decreases with Yttria content, *i.e.* the oxygen vacancy amount, up to x=10 mol.%, where a minimum exists which is equal to 2 W/mK. It then increases again with higher concentrations of Yttria [10, 11], which has been ascribed to a rearrangement of the vacancy clusters into locally ordered aggregates [9–15]. Moreover, at high temperature, independent of the Yttria content, the measured value is about 2 W/mK and almost temperature independent [11]. This low value corresponds to the minimum thermal conductivity calculated on the basis of the minimum phonon mean free path, like in glasses [8]. Such glass-like thermal transport properties have been ascribed to a dominant defect-induced phonon scattering mechanism above room temperature due to the extended vacancy-defect structure [12–14]. However, a full understanding of the role of oxygen vacancies and their impact on phonon propagation is still missing.

From the theoretical point of view, it is extremely difficult to calculate *ab-initio* phonon dynamics in this material due to the highly defective structure. Yet, as was proven with the molecular dynamics simulations of the quasicrystalline approximant o-$Al_{13}Co_4$ [16], the incorporation of disorder into the theoretical model is essential to our understanding of phonon propagation in disordered systems. This is especially true for cubic YSZ

with Yttria content in the 9-10 mol.% range, in which vacancies are still relatively isolated clusters: this phase is characterized by the minimum in thermal conductivity and the impact of vacancies can be thus expected to be the strongest. Only a few studies have been reported on the dynamics of this phase, mainly based on molecular dynamics simulations [17, 18] with some DFT calculations [19, 20], which mostly concentrate on phonon density of states calculations rather than on the full dispersions.

On the experimental side, the lattice dynamics of cubic YSZ have been studied by neutron and X-ray scattering and Raman spectroscopy [20–26]. Inelastic scattering studies revealed the presence of acoustic phonons dispersing up to 20 and 30 meV for transverse and longitudinal polarizations respectively, exhibiting a strong - although unanalyzed - broadening, which was ascribed to the important defect scattering and suggested as responsible for the glass-like thermal transport properties [21]. Surprisingly, no optical modes could be observed, despite the fact that they were reported in Raman studies [22, 24, 25]. As these modes are due to the out-of-phase vibrations of the two oxygen sublattices, it was argued that disorder in these latter would affect the optical modes more than the acoustic ones, such that they would not be well-defined except at the Γ point [20–22].

In order to definitively understand thermal transport in cubic YSZ, an exhaustive and high resolution measurement of its phonon dynamics is still needed which specifically addresses the quantitative measurement of acoustic phonon lifetime, the key parameter for all thermal conductivity calculations and for elucidating the dominant scattering mechanisms. This is the aim of this work. Here we present a combined inelastic neutron and X-ray scattering (INS, IXS) investigation of phonon dynamics in a single crystal YSZ with 9.5 mol.% Yttria concentration.

The higher resolution obtained with our experimental setup with respect to previous studies allows us to uncover a new understanding of the lattice dynamics in YSZ that was previously hidden by the limited resolution: here we report the first experimental evidence in the full Brillouin zone of optical modes in YSZ, which extend up to ∼35 meV. The lowest-lying optical mode, centered at 9 meV, is found to interact with the acoustic modes, marking a premature end of the pure acoustic regime. Our findings allow us to revisit the phonon dynamics in YSZ and suggests a new interpretation of the mechanisms leading to its low and temperature independent thermal conductivity.

INS measurements were made on a 1 cm^3 cube sample (CrysTec) at the Laboratoire Léon Brillouin (LLB) and the Institut Laue-Langevin (ILL), using the thermal-neutron triple-axis spectrometers (TAS) 1T@LLB and IN8@ILL and a fixed $k_f = 2.662$ $Å^{-1}$. Söller-slit collimation of 60'/20'/20'/60' was added onto the incident beam (k_i) and scattered beam (k_f) paths of 1T@LLB as well to improve the resolution (see Appendix B.1 of the Supplementary Material [27] for further explanation). From now on, 20' will be considered as shorthand for 60'/20'/20'/60' collimation, and 60' for 60'/60'/60'/60'. Further measurements were done at the cold-neutron TAS 4F2 at the LLB, using a fixed $k_f = 1.48$ $Å^{-1}$ and the Be filter. IXS measurements were made on a ∼0.001 mm^3 sample at the ID28 beamline of the European Synchrotron Radiation Facility (ESRF), using the [9 9 9] reflection of the silicon monochromator, which provides an energy resolution of 2.8 meV. More details on samples and experimental setups can be found in Appendix A and B of the Supplementary Material [27].

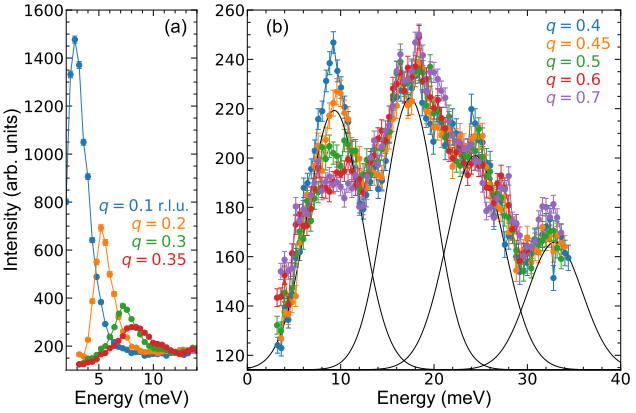

FIG. 1. High resolution energy scans, measured by Inelastic Neutron Scattering, of the transverse acoustic (TA) phonons propagating along [100], polarized along [010] are plotted. (a) shows the low-q part of the dispersion, where the clearly-defined TA mode disperses until 9 meV. In (b), we see that the TA mode is cut off by an optical branch at 9 meV. Three higher energy optical branches are also highlighted using the fit for the $q = 0.45$ r.l.u. point, plotted as a solid black line. Measurements were done on IN8@ILL.

We have performed an exhaustive investigation of phonon dynamics in YSZ, measuring transversely and longitudinally polarized modes propagating along the main symmetry directions of the cubic structure. Raw data are reported in Appendix F of the Supplementary Material [27]. In Fig. 1, we report some energy scans at constant-Q of transverse acoustic phonons propagating along [100], polarized along [010] (Δ(TA) branch), as representative for our major findings. Here, it may be seen that the TA mode disperses and broadens until $q = 0.35$ r.l.u. Above this value, it no longer disperses, remaining pinned to the 9 meV energy position and merging into a continuum of optical modes whose bands are centered at 9, 17, 27, and 32 meV in this particular polarization. We note that this is a marked difference from the TA dispersion of Argyriou *et al.* [21], whose phonons in the same polarization disperse until 20 meV, seemingly without interference.

This is not an isolated case. As can be seen in Fig. 2, which reports all of our experimentally measured dispersions, we observe a similar cut-off of the acoustic branch

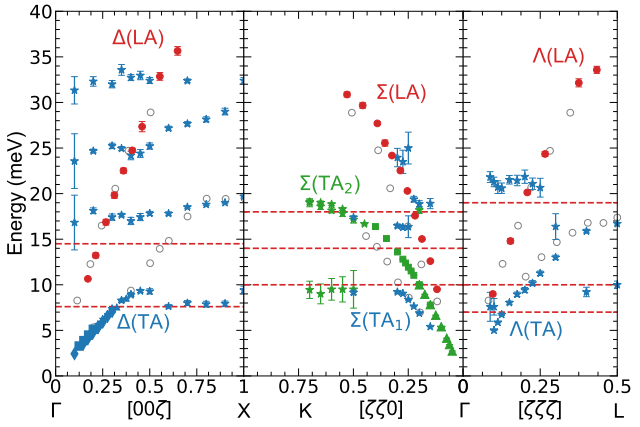

FIG. 2. Longitudinal and transverse (LA,TA) phonons have been measured in three high-symmetry directions at 300 K using a combination of inelastic neutron and X-ray scattering (INS, IXS) techniques. LA phonons (red circles) have been measured by IXS on ID28@ESRF, with horizontal lines representing the energies of the optical branches that were fixed in position during analysis. TA phonons (blue) have been measured by INS on 4F2@LLB (diamonds), 1T@LLB with 20' collimation (triangles), 1T@LLB with 60' collimation (squares), and IN8@ILL (stars). The second TA polarization in the [ζζ0] direction (green) is similarly a combination of INS setups (same marker symbols apply). Energies of those measured by Argyriou *et al.* [21] are plotted for comparison as empty gray circles. The errorbars for the left-most points of the optical branches in the [00ζ] direction depict the typical energy width of the optical mode, while for the other points they represent the error on the energy position.

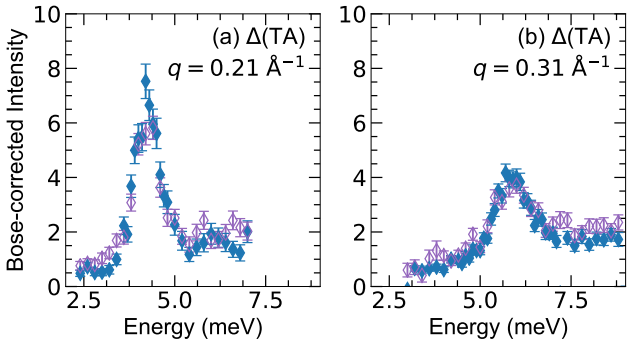

FIG. 3. Temperature dependence of representative energy scans from the Δ(TA) branch in Fig. 2. Scans have been made on 4F2@LLB at 300 K (blue) and 50 K (purple) and have had their intensities corrected according to the Bose-Einstein distribution.

$\Sigma(TA_1)$, polarized along the [001] direction and propagating along the [110] direction, while all measured LA polarizations and the $\Sigma(TA_2)$, polarized along the [110] direction and propagating along the [110] direction, appear to continue dispersing past 9 meV, crossing one or more optical branches along the way before reaching the ends of the respective Brillouin zones. The case of the Λ(TA) polarization in the [111] direction is less clear, in which the acoustic phonon possibly continues past the 9 meV optic mode and merges with the 17 meV optic mode.

Our results represent the very first experimental evidence throughout the whole Brillouin zone of optical modes for this material, which, until now, have been elusive within previous investigations. Moreover, we observe a premature end of the acoustic phase space for some transverse branches, where previous studies reported TA modes dispersing up to ∼20 meV. A very different scenario therefore arises from our data, which can be understood in terms of an improved experimental resolution. Previous INS experiments have been performed using a fixed $k_f = 4.1$ Å^{-1} [21], in which case the instrumental resolution is large, such that when the acoustic mode approaches the low-lying optical mode, they are not clearly resolved anymore, but rather appear as a single mode. The intensity transfer among the different optical bands creates the effect of a dispersive acoustic mode up to 20 meV. Such an effect of successive intensity transfer while increasing the energy between acoustic phonon branches and broad distributions of optical modes has already been evidenced in many complex crystals like quasicrystals [16, 28, 29] and clathrates [30–35]. Furthermore, we have indeed verified the consistency of our results with those of Argyriou and co-authors by repeating the measurements using the same low instrumental resolution as was used in that work: we too find that the optical mode is no longer resolved, and we find a good agreement for the dispersion of the single visible mode (See Appendix C in the Supplementary Material [27]).

It is worth underlining that the presence of a dispersionless mode at 9 meV had already been reported in previous works, specifically by Cousland *et al.* [20], who measured it along the Σ(LA) branch at three Q points. Interestingly, both in their *ab-initio* calculations of the density of states and in the ones of Tojo *et al.* [17], a small peak at 8-9 meV is present, confirming the existence of such a mode in YSZ. Still, the authors did not propose an optical nature for it but rather identified it as a soft longitudinal mode which is calculated to have an imaginary frequency in cubic ZrO_2. However, the introduction of anharmonicity stabilizes the structure, thus stabilizing the phonon branch [36].

The temperature dependence of the phonon dynamics has been investigated down to 50 K. In Fig. 3 we report data for the Δ(TA) branch at room and low temperature, after correction by the Bose factor. The good overlap confirms a negligible effect of the temperature within our experimental resolution. Indeed, we have been able to extract the intrinsic phonon linewidths, which are above the limit of our instrumental resolution, and find them to be temperature independent, confirming thus a negligible role of anharmonicity in this material, and pointing instead to a major role of defects, due to oxygen vacancies, in determining phonon attenuation.

In order to definitively shed light onto the dominant phonon scattering process and also onto the interaction between the acoustic modes and the newly evidenced optical modes, we report the extracted acoustic intrinsic linewidths and the normalized intensities in Figs. 4 and 5, respectively. Unfortunately, we could not analyze these parameters for the $\Sigma(TA_1)$ and the $\Lambda(TA)$ modes, due to resolution limitations. Details on the fitting procedures and the extraction of these quantities are given in Appendices B and D of the Supplementary Material [27].

In simple structures, it is usually expected that a dominant point defect scattering would lead to a strong dependence of the linewidth on the energy, of the type $\Gamma \propto (\hbar\omega)^4$ [37] (Rayleigh scattering). Still, extended defect structures could induce more of a Mie-type scattering, with a softer dependence such as $\Gamma \propto (\hbar\omega)^2$ [38]. Moreover, works on highly defective crystals such as random alloys [39–43] and quasicrystalline approximants [16] have reported the presence of several regimes which do not always correspond to clear power laws. In YSZ, we find quite clear power laws, but power values which span from the Mie-type to the Rayleigh-type scattering: $\Gamma = (\hbar\omega)^x$, x=2.2, 3.3, and 1.8 for the LA polarizations in subplots (a), (c), and (e) of Fig. 4, respectively, and x=5.0 and 3.9 for TA polarizations in subplots (b) and (d), respectively.

It is important to notice however, that no change in the broadening regime is resolved when approaching the low-lying optical mode for phonons which are not stopped in their dispersion, while the strong increase above 9 meV in the $\Delta(TA)$ linewidth is only due to the fact that above this energy we are in fact measuring the width of the optical band, and not the pure acoustic one anymore. Still, an interaction between optical and acoustic phonons, even when the dispersion is not stopped, can be unveiled by looking at the normalized acoustic intensity, which is found to depart from a constant value, which is associated with purely acoustic character, when approaching the energy of the optical mode, as can be seen in Fig. 5. Even if the direction of the observed departure depends on the polarization and propagation direction of the acoustic mode (for instance the normalized intensity decreases for $\Sigma(TA_2)$ in subplot (d) while it increases for all other branches), it still remains a clear signature of the end of the pure acoustic phonon regime.

As mentioned in the introduction, optical modes at the center of the Brillouin zone have already been reported by Raman spectroscopy. In these studies, it was possible to observe an optical continuum containing several distributions of optical modes, from few meV up to $\sim$ 80 meV. In a perfect cubic structure, only one Raman-active mode is authorized by the selection rules, but the presence of defects blurs the polarization of vibrational modes, thus changing their Raman activity. Specifically, a molecular dynamics study by Schelling *et al.* [18] has shown that for Yttria content larger than 4 mol.%, only phonons with energies smaller than $\sim$ 8 meV have a well-defined polarization, while at higher energy their polarization vector

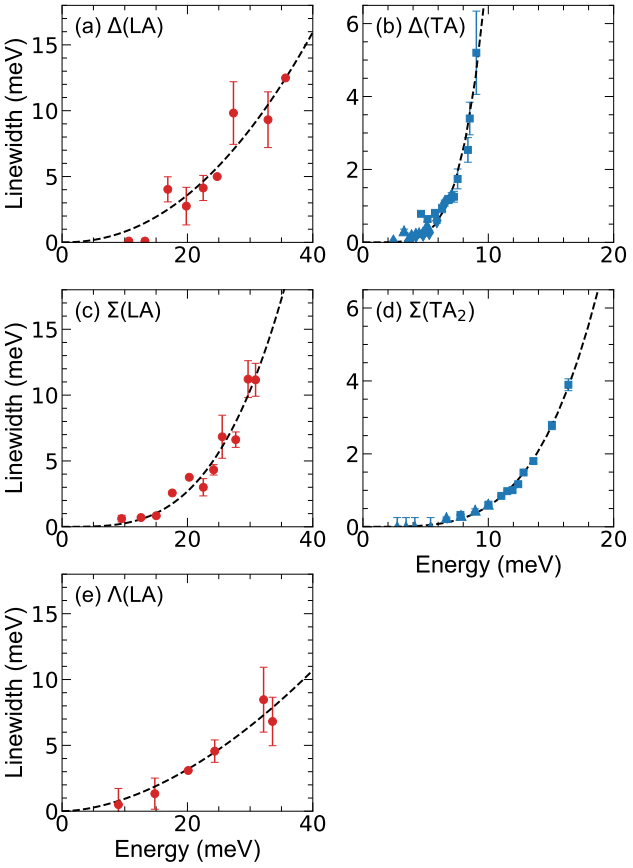

FIG. 4. When possible according to the different experimental setups, intrinsic linewidths have been extracted. Colors and symbols follow from Fig. 2. Dashed lines correspond to the fit with a power law as detailed in the text.

is less and less defined.

Thanks to this symmetry-breaking, three main bands could be identified in polarized Raman spectra for a Yttria content of x=9.5 mol.% as belonging to the A_{1g}, T_g, and E_g irreducible representations of the crystalline symmetry group O_h for the cubic fluoride-type structure [24] (see Table S3 of the Supplementary Material [27]). In all the polarizations, a well-defined peak at 9-10 meV is present, while peaks at 18 and 35 meV appear in some but not all symmetries. Our results are thus consistent with previous measurements at the Γ point.

It is interesting to comment on the different interactions observed between the lowest-lying optical mode and the acoustic branches depending upon their propagation direction and nominal polarization. As seen in Fig. 2, only the $\Delta(TA)$ and the $\Sigma(TA_1)$ are clearly stopped at 9 meV. A first attempt at understanding this can be made by looking to the nominal polarization direction of the optical mode and its relation to that of the acoustic ones. Using the irreducible representations for a perfect cubic structure, we find that only for these two transverse branches and the $\Delta(LA)$, the scalar product be-

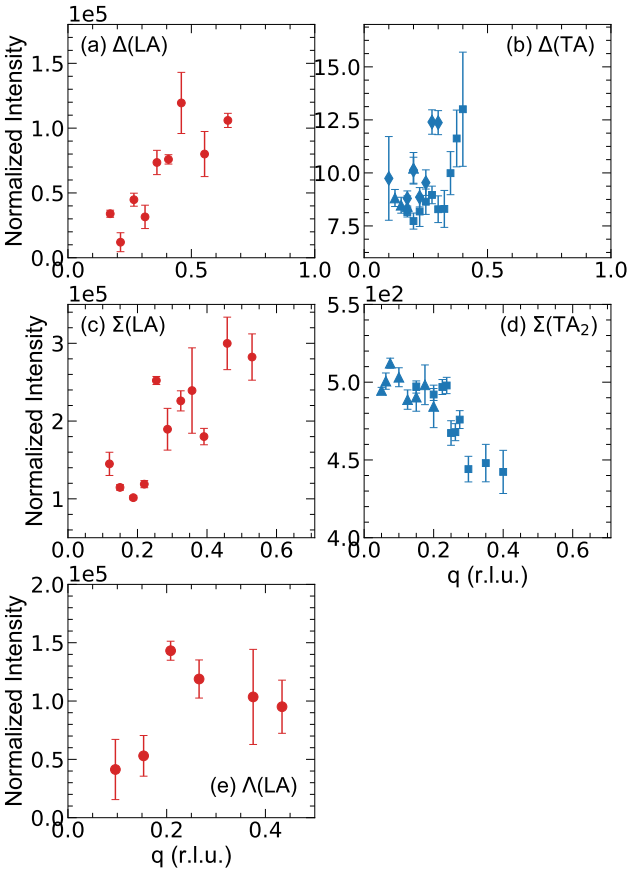

FIG. 5. The normalized intensity at 300 K is plotted in which colors and symbols follow from Fig. 2. Longitudinal acoustic (LA) modes have been measured by inelastic X-ray scattering on ID28@ESRF. All intensities have been normalized based on efficiencies of the analyzers in order to compare scans across different analyzers. Transverse acoustic (TA) modes were measured by various experimental inelastic neutron scattering setups (see text) and have been scaled to match each other in each polarization.

tween their nominal polarization and the ones of the two degenerate E_g 9 meV optical modes is non-zero, while this is not the case for all the other acoustic branches, for which the scalar product is zero with at least one of the two degenerate E_g modes.

This would indicate that the acoustic dispersion is halted only when both E_g polarizations can interact with the acoustic mode. This however does not apply to the Δ(LA), which, despite it has non-zero scalar product, is not halted in its dispersion. This can be explained by the fact that in a defective structure, polarizations and symmetry are expected to be modified, and this also depends on the position in the reciprocal lattice. As such, in order to definitively shed light onto the acoustical-optical interactions in YSZ, a calculation of the polarization and symmetry of both optical and acoustic modes throughout the Brillouin zone would be needed. This is even more true since our results clearly indicate that previously calculated phonon dispersions in YSZ, similar to the ones of pure ZrO_2, are not reliable, as they do not reproduce the early end of the acoustic phase space in some directions and polarizations, nor the existence of low-lying optical branches.

In conclusion, we have revisited the lattice dynamics of Yttria-Stabilized Zirconia (x=9.5 mol.%) with high-resolution INS and IXS measurements, giving new insight into the presence of optical branches throughout the whole Brillouin zone that interact with the acoustic phonon modes and that, in some polarizations, cause the early end of the acoustic branch. Our findings highlight the need for new *ab-initio* calculations that consider the true defect structure of YSZ and that allow us to predict the correct phonon dispersions, and, more specifically, the presence of defect-induced optical modes and the acoustical-optical interaction.

Finally, these results highlight a new understanding of the phonon spectrum in cubic Yttria-Stabilized Zirconia, suggesting that a new interpretation of its low thermal conductivity should be developed. Previously interpreted as being due to a huge disorder-induced phonon broadening [21], it now appears to be the result of two concomitant phenomena at play: not only is there an important defect-induced scattering, spanning from a Mie- to a Rayleigh- type, that is dependent upon direction and polarization, but there is also a significant reduction of the phase space in which acoustic modes are well-defined and propagative. Indeed, as we have seen, some transverse modes stop abruptly at 9 meV (instead of the previously reported 20 meV) and at wave-vectors of about half the Brillouin zone size.

To go further and to completely understand how the details of the extended defect structure, its lengthscale, and the anisotropy affect phonon dynamics and thermal transport in YSZ, a similar exhaustive investigation as a function of the Yttria content, combined with a deep defect structure study and the support of theoretical calculations, will be needed. This work represents a first important step in this direction and will undoubtedly inspire new theoretical work on this technologically relevant material.

ACKNOWLEDGMENTS

S.R.T. acknowledges financial support from the ISP program of the IDEX Université Grenoble Alpes. V.M.G. and S.P. acknowledge support from the Lyon IDEX Scientific Breakthrough program for funding of the project IPPON. V.M.G. acknowledges the ANR for funding the project MAPS-ANR-20-CE05-0046. Data from INS measurements made at the ILL are available at [44], LLB measurements correspond to proposals 405, 407 and 958, and ESRF measurements to proposal HD640.

* To whom correspondence should be addressed: valentina.giordano@univ-lyon1.fr

[1] S. M. Meier and D. K. Gupta, The evolution of thermal barrier coatings in gas turbine engine applications, J. Eng. Gas Turbines Power **116**, 250 (1994).

[2] D. R. Clarke and C. G. Levi, Materials design for the next generation thermal barrier coatings, Annual Review of Materials Research **33**, 383 (2003).

[3] N. P. Padture, M. Gell, and E. H. Jordan, Thermal barrier coatings for gas-turbine engine applications, Science **296**, 280 (2002).

[4] J. D. McCullough and K. N. Trueblood, The crystal structure of baddeleyite (monoclinic ZrO2), Acta Crystallographica **12**, 507 (1959).

[5] P. Aldebert and J.-P. Traverse, Structure and ionic mobility of zirconia at high temperature, Journal of the American Ceramic Society **68**, 34 (1985).

[6] D. K. Smith and C. F. Cline, Verification of existence of cubic zirconia at high temperature, Journal of the American Ceramic Society **45**, 249 (1962).

[7] G. Witz, V. Shklover, W. Steurer, S. Bachegowda, and H.-P. Bossmann, Phase evolution in yttria-stabilized zirconia thermal barrier coatings studied by rietveld refinement of x-ray powder diffraction patterns, Journal of the American Ceramic Society **90**, 2935 (2007).

[8] R. Mévrel, J.-C. Laizet, A. Azzopardi, B. Leclercq, M. Poulain, O. Lavigne, and D. Demange, Thermal diffusivity and conductivity of zr 1-x y x o 2-x/2 (x =0, 0.084 and 0.179) single crystals, Journal of the European Ceramic Society **24**, 3081 (2004).

[9] M. Fèvre, A. Finel, and R. Caudron, Local order and thermal conductivity in yttria-stabilized zirconia. i. microstructural investigations using neutron diffuse scattering and atomic-scale simulations, Phys. Rev. B **72**, 104117 (2005).

[10] J.-F. Bisson, D. Fournier, M. Poulain, O. Lavigne, and R. Mévrel, Thermal conductivity of yttria-zirconia single crystals, determined with spatially resolved infrared thermography, Journal of the American Ceramic Society **83**, 1993 (2004).

[11] M. Fèvre, A. Finel, R. Caudron, and R. Mévrel, Local order and thermal conductivity in yttria-stabilized zirconia. ii. numerical and experimental investigations of thermal conductivity, Phys. Rev. B **72**, 104118 (2005).

[12] T. Welberry, R. Withers, J. Thompson, and B. Butler, Diffuse scattering in yttria-stabilized cubic zirconia, Journal of Solid State Chemistry **100**, 71 (1992).

[13] T. Welberry, B. Butler, J. Thompson, and R. Withers, A 3d model for the diffuse scattering in cubic stabilized zirconias, Journal of Solid State Chemistry **106**, 461 (1993).

[14] T. R. Welberry and B. D. Butler, Interpretation of diffuse X-ray scattering *via* models of disorder, Journal of Applied Crystallography **27**, 205 (1994).

[15] J. P. Goff, W. Hayes, S. Hull, M. T. Hutchings, and K. N. Clausen, Defect structure of yttria-stabilized zirconia and its influence on the ionic conductivity at elevated temperatures, Physical Review B **59**, 14202 (1999).

[16] P.-F. Lory, V. M. Giordano, P. Gille, H. Euchner, M. Mihalkovič, E. Pellegrini, M. Gonzalez, L.-P. Regnault, P. Bastie, H. Schober, S. Pailhes, M. R. Johnson, Y. Grin, and M. de Boissieu, Impact of structural complexity and disorder on lattice dynamics and thermal conductivity in the o-$Al_{13}Co_4$ phase, Phys. Rev. B **102**, 024303 (2020).

[17] T. Tojo, T. Atake, T. Mori, and H. Yamamura, Excess heat capacity in yttria stabilized zirconia, Journal of Thermal Analysis and Calorimetry **57**, 447 (1999).

[18] P. K. Schelling and S. R. Phillpot, Mechanism of thermal transport in zirconia and yttria-stabilized zirconia by molecular-dynamics simulation, Journal of the American Ceramic Society **84**, 2997 (2001).

[19] P. Dalach, D. E. Ellis, and A. van de Walle, First-principles thermodynamic modeling of atomic ordering in yttria-stabilized zirconia, Phys. Rev. B **82**, 144117 (2010).

[20] G. P. Cousland, R. A. Mole, M. M. Elcombe, X. Y. Cui, A. E. Smith, C. M. Stampfl, and A. P. J. Stampfl, Investigation of the vibrational properties of cubic yttria-stabilized zirconia: A combined experimental and theoretical study, Journal of Physics and Chemistry of Solids **75**, 351 (2014).

[21] D. N. Argyriou and M. M. Elcombe, A neutron scattering investigation of cubic stabilised zirconia (CSZ)—II. lattice dynamics of y- and ca-CSZ, Journal of Physics and Chemistry of Solids **57**, 343 (1996).

[22] D. W. Liu, C. H. Perry, A. A. Feinberg, and R. Currat, Neutron-scattering studies of phonons in disordered cubic zirconia at elevated temperatures, Physical Review B **36**, 9212 (1987).

[23] D.-J. Kim, H.-J. Jung, and I.-S. Yang, Raman spectroscopy of tetragonal zirconia solid solutions, Journal of the American Ceramic Society **76**, 2106 (1993).

[24] M. Ishigame and E. Yoshida, Study of the defect-induced Raman spectra in cubic zirconia, Solid State Ionics **23**, 211 (1987).

[25] G. Morell, R. S. Katiyar, D. Torres, S. E. Paje, and J. Llopis, Raman scattering study of thermally reduced stabilized cubic zirconia, Journal of Applied Physics **81**, 2830 (1997).

[26] C. H. Perry, D.-W. Liu, and R. P. Ingel, Phase characterization of partially stabilized zirconia by raman spectroscopy, Journal of the American Ceramic Society **68**, C-184 (1985).

[27] See Supplemental Material (SM) at [url will be inserted by publisher] for details of the experimental conditions, data analysis, and sample characterizations.

[28] M. de Boissieu, S. Francoual, M. Mihalkovič, K. Shibata, A. Q. R. Baron, Y. Sidis, T. Ishimasa, D. Wu, T. Lograsso, L.-P. Regnault, F. Gähler, S. Tsutsui, B. Hennion, P. Bastie, T. J. Sato, H. Takakura, R. Currat, and A.-P. Tsai, Lattice dynamics of the Zn-Mg-Sc icosahedral quasicrystal and its Zn-Sc periodic 1/1 approximant, Nat. Mater. **6**, 977 (2007).

[29] H. Euchner, M. Mihalkovič, F. Gähler, M. R. Johnson, H. Schober, S. Rols, E. Suard, A. Bosak, S. Ohhashi, A.-P. Tsai, S. Lidin, C. P. Gomez, J. Custers, S. Paschen, and M. de Boissieu, Anomalous vibrational dynamics in the mg_2zn_{11} phase, Phys. Rev. B **83**, 144202 (2011).

[30] H. Euchner, S. Pailhès, L. T. K. Nguyen, W. Assmus, F. Ritter, A. Haghighirad, Y. Grin, S. Paschen, and M. de Boissieu, Phononic filter effect of rattling phonons in the thermoelectric clathrate $Ba_8Ge_{40+x}Ni_{6-x}$, Phys. Rev. B **86**, 224303 (2012).

[31] S. Pailhès, H. Euchner, V. M. Giordano, R. Debord, A. Assy, S. Gomès, A. Bosak, D. Machon, S. Paschen, and M. de Boissieu, Localization of propagative phonons in a perfectly crystalline solid, Phys. Rev. Lett. **113**, 025506 (2014).

[32] P.-F. Lory, S. Pailhès, V. M. Giordano, H. Euchner, H. D. Nguyen, R. Ramlau, H. Borrmann, M. Schmidt, M. Baitinger, M. Ikeda, P. Tomeš, M. Mihalkovič, C. Allio, M. R. Johnson, H. Schober, Y. Sidis, F. Bourdarot, L. P. Regnault, J. Ollivier, S. Paschen, Y. Grin, and M. de Boissieu, Direct measurement of individual phonon lifetimes in the clathrate compound $Ba_{7.81}Ge_{40.67}Au_{5.33}$, Nature Communications **8** (2017).

[33] H. Euchner, S. Pailhès, V. M. Giordano, and M. de Boissieu, Understanding lattice thermal conductivity in thermoelectric clathrates: A density functional theory study on binary si-based type-i clathrates, Phys. Rev. B **97**, 014304 (2018).

[34] R. Viennois, M. M. Koza, R. Debord, P. Toulemonde, H. Mutka, and S. Pailhès, Anisotropic low-energy vibrational modes as an effect of cage geometry in the binary barium silicon clathrate $Ba_{24}Si_{100}$, Phys. Rev. B **101**, 224302 (2020).

[35] S. R. Turner, S. Pailhès, F. Bourdarot, J. Ollivier, S. Raymond, T. Keller, Y. Sidis, J.-P. Castellan, P.-F. Lory, H. Euchner, M. Baitinger, Y. Grin, H. Schober, M. de Boissieu, and V. M. Giordano, Impact of temperature and mode polarization on the acoustic phonon range in complex crystalline phases: A case study on intermetallic clathrates, Phys. Rev. Research **3**, 013021 (2021).

[36] P. Souvatzis and S. P. Rudin, Dynamical stabilization of cubic ZrO_2 by phonon-phonon interactions: *Ab initio* calculations, Phys. Rev. B **78**, 184304 (2008).

[37] J. Callaway, Model for lattice thermal conductivity at low temperatures, Phys. Rev. **113**, 1046 (1959).

[38] R. Guo and S. Lee, Mie scattering of phonons by point defects in IV-VI semiconductors PbTe and GeTe, Materials Today Physics **12**, 100177 (2020).

[39] S. R. Turner, S. Pailhès, F. Bourdarot, J. Ollivier, Y. Sidis, J.-P. Castellan, J.-M. Zanotti, Q. Berrod, F. Porcher, A. Bosak, M. Feuerbacher, H. Schober, M. de Boissieu, and V. M. Giordano, Phonon behavior in a random solid solution: A lattice dynamics study on the high-entropy alloy FeCoCrMnNi, unpublished (2021).

[40] S. Mu, R. J. Olsen, B. Dutta, L. Lindsay, G. D. Samolyuk, T. Berlijn, E. D. Specht, K. Jin, H. Bei, T. Hickel, B. C. Larson, and G. M. Stocks, Unfolding the complexity of phonon quasi-particle physics in disordered materials, npj Computational Materials **6**, 4 (2020).

[41] W. A. Kamitakahara and B. N. Brockhouse, Vibrations of a mixed crystal: Neutron scattering from $ni_{55}pd_{45}$, Phys. Rev. B **10**, 1200 (1974).

[42] Y. M. Beltukov and D. A. Parshin, Theory of sparse random matrices and vibrational spectra of amorphous solids, Physics of the Solid State **53**, 151 (2011).

[43] Y. M. Beltukov and D. A. Parshin, Density of states in random lattices with translational invariance, JETP Letters **93**, 598 (2011).

[44] Shelby Rae Turner, Frédéric Bourdarot, Marc de Boissieu, Valentina Giordano, Alexandre Ivanov, Stéphane Pailhès, Andrea Piovano, Stéphane Raymond, and Helmut Schober, Disentangling anharmonic from disorder dominated thermal transport in yttria stabilized cubic zirconia (2019).

Supplementary Material for "Revisiting the Lattice Dynamics of Cubic Yttria-Stabilized Zirconia"

Shelby R. Turner,[1,2,3] Stéphane Pailhès,[3] Leila Ben Mahfoud,[3] Christian Carbogno,[4] Marc de Boissieu,[2] Frédéric Bourdarot,[5] Helmut Schober,[1] Yvan Sidis,[6] John-Paul Castellan,[6,7] Andrea Piovano,[1] Alexandre Ivanov,[1] and Valentina M. Giordano[3,*]

[1] *Institut Laue-Langevin, Grenoble F-38042 Grenoble cedex, France*
[2] *Université Grenoble Alpes, CNRS, Grenoble-INP, SIMaP, F-38402 St Martin d'Hères, France*
[3] *Institute of Light and Matter, UMR5306 Université Lyon 1-CNRS, Université de Lyon F-69622 Villeurbanne cedex, France*
[4] *Fritz-Haber-Institut der Max-Planck-Gesellschaft, Faradayweg 4–6, D-14195 Berlin, Germany*
[5] *Université Grenoble Alpes, CEA, IRIG, MEM, MDN, F-38000 Grenoble cedex, France*
[6] *Laboratoire Léon Brillouin, CEA, CNRS, UMR-12, CE-Saclay, F-91191 Gif-sur-Yvette, France*
[7] *Institut für Festkörperphysik, Karlsruher Institut für Technologie, D-76021 Karlsruhe, Germany*

(Dated: August 25, 2021)

APPENDIX A: SAMPLE CHARACTERIZATION

The samples used in the inelastic neutron and X-ray scattering experiments shown in the main text, which will be referred to as YSZ in this Supplementary Material, contain 9.5 mol.% Yttria concentration and follow the chemical formula $(ZrO_2)_{1-x}(Y_2O_3)_x$, where $x = 0.095$. Fig. S1 is an image of the sample used for the inelastic neutron scattering experiments. It is a 1 cm^3 cube manufactured by the company CrysTec with a mosaicity of 0.5°.

The sample for IXS was a single crystal of volume 0.001 m^3, with a mosaic of 0.016° along the [110] direction and 0.057° along the [001] direction.

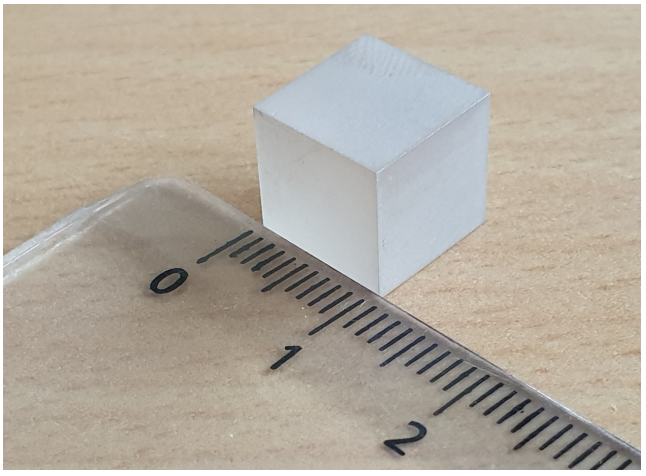

FIG. S1: Image of the Yttria-Stabilized Zirconia sample with 9.5 mol.% Yttria concentration that was used for all inelastic neutron scattering experiments. The sample measures 1x1x1 cm^3.

APPENDIX B: METHODS: INELASTIC SCATTERING MEASUREMENTS

This section will further detail the inelastic neutron and X-ray scattering (INS, IXS) experiments described in the main text. An inelastic scattering measurement involves impinging a probe particle, neutrons or photons in our case, onto a sample and measuring the change in energy caused by the interaction with the sample. More specifically, the probe particle will have initial energy and wave-vector ($|E_i, \mathbf{k}_i\rangle$) and final energy and wave-vector ($|E_f, \mathbf{k}_f\rangle$), where the wave-vector $\mathbf{k}_f$ is scattered at an angle 2θ relative to the incident wave-vector.

The measurable quantity of the experiment is the double differential cross section σ, or $\frac{d^2\sigma}{d\Omega_f dE_f}$, with dE_f the range of final energies around a certain value, and $d\Omega_f$ the solid angle within which the scattered intensity is measured around the scattering direction. In other words, scattered probe particles with energies within the range dE_f are collected in solid angle element $d\Omega_f$, and σ describes the neutrons scattered per second out of the number of incident neutrons per cm^2 per second [1, 2]. This, in turn, is related to the response function, $S(\mathbf{Q}, \omega)$,

$$\frac{d^2\sigma}{d\Omega_f dE_f} = \frac{k_f}{k_i} S(\mathbf{Q}, \omega). \tag{S1}$$

The scattering event is governed by the conservation of energy and momentum, eqs. S2-S4, with eq. S2 specifically describing the scattering triangle, which will become important in Section B 1.

$$\mathbf{Q} = \mathbf{k}_i - \mathbf{k}_f \tag{S2}$$

$$Q^2 = k_i^2 + k_f^2 - 2\mathbf{k}_i\mathbf{k}_f \cos(2\theta) \tag{S3}$$

$$\hbar\omega = E_i - E_f \tag{S4}$$

In Eq. S4 the probe energy will have a different expression depending if the probe are neutrons, with a mass, or photons.

Table S1 provides all of the polarization information for each of the modes measured in this work and plotted in the main text, allowing the reader to locate the measured dispersions in reciprocal space. The transverse acoustic (TA) modes have all been measured by INS, and

the longitudinal acoustic (LA) modes have been measured by IXS, which will be covered in the following subsections.

1. Inelastic Neutron Scattering

All INS measurements described in the main text were made using triple-axis spectrometers (TAS). Table S2 provides a summary of the several different INS setups that were used to construct the figures in the main text. The INS measurements were conducted at the Institut Laue-Langevin (ILL) and the Laboratoire Léon Brillouin (LLB) using the cold-neturon TAS 4F2@LLB and thermal-neutron TAS 1T@LLB and IN8@ILL. The "fixed k_f" refers to the experimental condition in which k_f remains fixed and k_i is adjusted in order to move in energy and create an energy scan, being, for neutrons, $\hbar\omega = E_i - E_f = \frac{\hbar^2}{2m_n}(k_i^2 - k_f^2)$.

Collimation is also listed in Table S2. This refers to Söller-slit collimation that can be placed before and after the sample onto k_i and k_f, respectively. Each neutron-absorber blade in the Söller-slit collimator has length L, and the distance between each evenly-spaced blade is d such that the resulting angular divergence, α is equal to [3]

$$\alpha = \frac{2d}{L}. \tag{S5}$$

The collimation formats listed in Table S2 have been converted into minute-of-arc. On a TAS, Söller-slit collimation is placed before and after the monochromator (still before the sample), and (after the sample) before and after the analyzer. This is usually written in a standard notation such as 60'/20'/20'/60'.

Collimation is one way to increase the resolution of the experiment since we greatly reduce the horizontal divergence of the beam. A second method of increasing resolution that was applied to these measurements was the customization of fixed k_f. By reducing the wave-vector, knowing that $k = 2\pi/\lambda$, we create a smaller scattering triangle, which is defined by eq. S2.

The instrumental resolutions of each TAS setup listed in Table S1 were modeled, taking into account instrumental parameters such as collimation and sample characteristics (dimensions and mosaicity). This was done using the analysis tool 'AFITV,' which was developed by B. Hennion and P. Bourges at Laboratoire Léon Brillouin [4]. Since the measured quantity in an INS measurement, described by eq. S1, is a convolution of the instrumental resolution and the intrinsic phonon measurement, AFITV models the instrumental resolution and then extracts the intrinsic phonon properties from the measurement.

2. Inelastic X-ray Scattering

All IXS measurements described in the main text were made using the backscattering beamline ID28 at the European Synchrotron Radiation Facility (ESRF). The incoming photon energy was 17.8 keV, resulting from the use of the [9 9 9] reflection of the silicon monochromator, giving us an energy resolution of 2.8 meV.

There are 9 analyzers on the ID28@ESRF beamline, each with its own efficiency rating. Therefore, intensities between the different analyzers should not be compared directly. Their energy resolutions have been measured on a plexiglass sample 15 K, at q points close to the maximum of the static structure factor. This procedure allows us to minimize the inelastic contribution in the measured spectra and measure essentially only the elastic line, whose shape and width reflects on the instrumental resolution. The intrinsic phonon properties of the measurement are extracted using a homemade MATLAB fitting program written by one of the authors which models the signal by convolving the theoretical signal with the experimental instrumental resolution.

APPENDIX C: LOW-RESOLUTION MEASUREMENTS AND COMPARISON WITH LITERATURE

Our results, which presented in the main text, unveil a very different phonon dynamics with respect to previous reports on YSZ, such as the one of Argyriou *et al.* [5]. In particular, Argyriou reports transverse acoustic modes dispersing up to 20 meV, and no optical modes, while, for the very same branches, we observe transverse modes halting at about 9 meV, cut off by a low-lying optical mode, along with other optical branches at higher energies. In order to understand the reasons of the disagreement, we have repeated the measurement of the Δ(TA) (halted branch) and $\Sigma(\mathrm{TA}_2)$ (non-halted branch) using the same experimental setup as Argyriou, *i.e.* with a fixed k_f of 4.1 Å^{-1}, which translates into a lower energy resolution. These energy scans are shown in Fig. S2.

As seen in Fig. S2(a), the phonon appears to continue to disperse until 20 meV with this lower resolution, in agreement with those that Argyriou and co-authors report, and in disagreement with our high-resolution results. From this comparison, we can understand that the intensity seen between 9 and 20 meV in Fig. S2 is in fact intensity from low-lying optical branches that appear to be part of the main phonon peak. Results for the non-halted $\Sigma(\mathrm{TA}_2)$ branch in (b), instead, remain consistent with our high-resolution measurements.

TABLE S1: Summary of the longitudinal and transverse acoustic (LA, TA) phonon mode polarizations that are plotted in the main text. The LA modes have been measured by IXS, and the TA modes by INS. A few of the polarizations were measured using multiple instruments/configurations. The 20' collimation nomenclature listed in the table is shorthand for 60'/20'/20'/60' collimation, or collimation placed before/after the monochromator and before/after the analyzer, respectively. Similarly, 60' collimation refers to 60'/60'/60'/60'.

Mode	Scattering plane	propagation direction	polarization direction	Bragg peak	Instrument(s)
Δ(LA)	[110][001]	[001]	[001]	(002)	ID28
Δ(TA)	[100][010]	[010]	[100]	(200)	4F2, 1T (20' and 60'), IN8
Σ(LA)	[110][001]	[110]	[110]	(220)	ID28
Σ(TA$_1$)	[110][001]	[$\bar{1}$10]	[001]	(002)	IN8
Σ(TA$_2$)	[100][010]	[$\bar{1}$10]	[110]	(220)	1T (20' and 60'), IN8
Λ(LA)	[110][001]	[111]	[111]	(111)	ID28
Λ(TA)	[110][001]	[$\bar{1}\bar{1}$1]	[111]	(222)	IN8

TABLE S2: The different instruments and experimental parameters for the inelastic neutron scattering experiments are summarized in the following table. All experiments were conducted on triple-axis spectrometers (TAS). Collimation refers to Söller-slit collimation (see text) and is given in minute-of-arc. The 20' collimation nomenclature listed in the table is shorthand for 60'/20'/20'/60' collimation, or collimation placed before/after the monochromator and before/after the analyzer, respectively. Similarly, 60' collimation refers to 60'/60'/60'/60'.

Facility	Instrument	TAS configuration	collimation
LLB	4F2	fixed $k_f = 1.48$ Å^{-1}	60'
	1T	fixed $k_f = 2.662$ Å^{-1}	60', 20'
		fixed $k_f = 4.1$ Å^{-1}	60'
ILL	IN8	fixed $k_f = 2.662$ Å^{-1}	60'

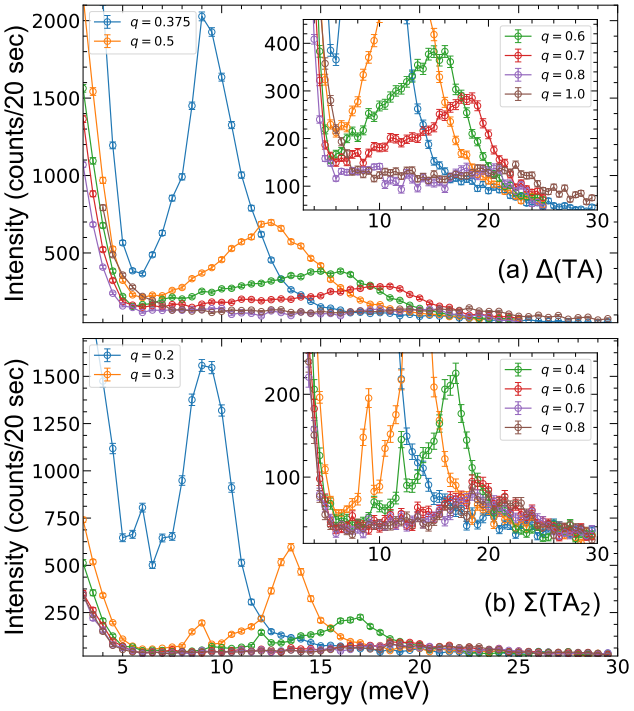

FIG. S2: Energy scans of the Δ(TA)(a) and Σ(TA$_2$)(b) branches made at 300 K on the triple-axis spectrometer 1T@LLB. A fixed k_f of 4.1 Å^{-1} was used in order to replicate the INS measurements made previously by Argyriou *et al.* [5]. The q values given in the legends are in r.l.u. Narrow, low-lying peaks in (b) are not phonons coming from the sample but rather spurions, *i.e.* artifacts of the measurement.

APPENDIX D: FITTING PROCEDURE AND ACOUSTIC NATURE OF THE PHONON MODES

In both INS and IXS experiments we have fit our data using a delta function for the elastic line, a damped harmonic oscillator for the phonon mode, and one or more Gaussian functions for the optical modes. As mentioned in Appendices B 1 and B 2, the fits were performed using AFITV for INS data and a homemade MATLAB program for IXS, which both convolute the theoretical model with the instrumental resolution function prior to fitting the experimental data, allowing thus for the extraction of the intrinsic phonon properties (position, intensity, and linewidth).

INS data from IN8 could not be fitted with the instrumental resolution due to a specific complication of using the Si monochromator feature of the beamline, and therefore we do not have intrinsic linewidths nor intensities. In the IXS data, on the other hand, the optical modes were first freely fit, and then, in a second step, and in order to simplify the procedure, their position was fixed, as it appeared quite constant with q. Such energy positions are indicated in Figure 2 of the main text as dashed red lines. Moreover, spectra were first normalized by the analyzer efficiencies in order to be able to follow the evolution of a single phonon intensity along the branch, even when said q values were measured using different analyzers.

The intrinsic intensity of the phonon mode taken from these fitting procedures allows us to track changes in the normalized intensity of the response function (see eq. S1) for each single phonon. This latter depends on the thermal occupation factor, $n(\omega_{i,\mathbf{q}})$, the polarization of the phonon mode, $\xi_{i,\mathbf{q}}$, and the Bragg peak structure factor, F_{B}. In the long-wavelength limit, $|\mathbf{q}| \ll |\mathbf{Q}|$, and given that $\hbar\omega \ll k_B T$, the normalized dynamic structure factor, $\mathrm{DSF}_{i,\mathbf{q}}(\mathbf{Q},\omega,T)$, reads [6–10]:

$$\mathrm{DSF}_{i,\mathbf{q}}(\mathbf{Q},\omega,T) = \frac{\omega_i(\mathbf{q})}{Q^2 \cdot n(\omega_{i,\mathbf{q}})} \int S_{i,\mathbf{q}}(\mathbf{Q},\omega,T)d\omega,$$
$$\text{where } \int S_{i,\mathbf{q}}(\mathbf{Q},\omega,T)d\omega \approx (\mathbf{Q}\cdot\xi_{i,\mathbf{q}})^2 |F_{\mathrm{B}}|^2 \frac{n(\omega_{i,\mathbf{q}})}{\omega_i(\mathbf{q})} \tag{S1}$$

In the long-wavelength and high-temperature limit, this should therefore be constant for a given acoustic phonon. The normalized intensity has been calculated for five polarizations and is shown in Fig. 5 of the main text. The deviations from a constant normalized intensity seen at larger q tell us that at those points, the phonons can no longer be considered as purely acoustic modes.

APPENDIX E: SYMMETRY ANALYSIS WITHIN THE O_h SPACE GROUP

The space group for cubic non-defective Zirconia is the O_h group. Looking to its character table from Silberman [11], only the mode T_{1g} should be Raman active. Still, three modes are observed in defective cubic YSZ due to the disorder-induced Raman activation (see the main text). These are the modes A_{1g},E_g and T_{1g}. Their character table with the polarization are reported in Table S3.

It is important to mention that this table holds for a perfect cubic structure at the Γ point. The symmetry of vibrational modes at a given point in the phase space in a given direction will be reduced and will therefore need to cope with the local point symmetry.

The polarization direction of our measured acoustic phonons was already reported in Table S1. It is worth noticing that by measuring the Λ(TA) branch in the [-1-11] direction starting from the (222) Bragg Peak, we did not measure a pure transverse mode, for which we should have selected the [-110] or [11-2] direction. Still it is almost fully [11-2] polarized (94%), which is the polarization that we consider for the following discussion.

By performing the scalar product between the polarization of our acoustic modes and the ones for the three irreducible representations, we find that for Σ(TA_2), Λ(TA), LA[111] and LA[110] the value is zero for at least one of the two polarizations of the double-degenerate Raman-active E_g mode. This would indicate that the acoustic dispersion is halted only when both E_g polarizations can interact with the acoustic mode. This however does not apply to LA[100], which has non-zero scalar products, but is not halted at 9 meV. Still, we have established the presence of an interaction with the optical modes in this polarization all the same through the normalized intensity (see Fig. 5(a) of the main text).

This is only a first attempt at understanding the different kind of acoustic-optical interactions. An *ab-initio* calculation of the real dispersions and their symmetry along the branch within the first Brillouin zone is needed in order to definitively understand it.

APPENDIX F: INELASTIC SCATTERING ENERGY SCANS

The INS and IXS energy scans that were used to create the figures in the main text are plotted in this section for reference.

Fig. S3 plots the scans made on the cold-neutron triple-axis spectrometer 4F2@LLB for the Δ(TA) polarization. Fig. S4 scans were made on the thermal-neutron triple-axis spectrometer 1T@LLB for the Δ(TA) polarization, with Fig. S4a having 20' collimation and Fig. S4b having 60' collimation. The final configuration for the Δ(TA) polarization was measured on the thermal-neutron triple-axis spectrometer IN8@ILL, shown in Fig. S5a.

The Σ(TA_1) polarization was measured on IN8@ILL, and scans are plotted in Fig. S5b.

The Σ(TA_2) polarization was measured on 1T@LLB with 20' and 60' collimation, and on IN8@ILL, and scans are plotted in Figs. S6a, S6b, and S7a, respectively.

The Λ(TA) polarization was measured on IN8@ILL, and scans are shown in Fig. S7b.

Finally, all LA polarizations were measured on the backscattering inelastic X-ray scattering beamline ID28@ESRF. The scans for the Δ(LA), Σ(LA), and Λ(LA) polarizations are plotted in Figs. S8a, S8b, and S9, respectively.

* To whom correspondence should be addressed: valentina.giordano@univ-lyon1.fr

[1] S. Pailhès, V. M. Giordano, P.-F. Lory, M. D. Boissieu, and H. Euchner, *Nanostructured Semiconductors*, edited by K. Termentzidis (Pan Stanford, 2017).
[2] G. Shirane, S. M. Shapiro, and J. M. Tranquada, *Neutron Scattering with a Triple–Axis Spectrometer* (Cambridge University Press, 2015).
[3] P. Z. Vitalij Pecharsky, *Fundamentals of Powder Diffraction and Structural Characterization of Materials, Second Edition* (Springer-Verlag GmbH, 2008).
[4] B. Hennion and P. Bourges, Afitv: Refinement program for triple axis spectrometer data.
[5] D. N. Argyriou and M. M. Elcombe, A neutron scattering

TABLE S3: Character table for the three irreducible representations of the group O_h corresponding to observed Raman modes. The last column gives the polarization of modes belonging to a given irreducible representation.

O_h	E	$8C_3$	$3C_2$	$6C_4$	$6C_2$	i	$8S_6$	$3\sigma_h$	$6S_4$	$6\sigma_d$	Polarization
A_{1g}	1	1	1	1	1	1	1	1	1	1	[111]
E_g	2	-1	2	0	0	2	-1	2	0	0	[11-2] or [1-10]
T_{1g}	3	0	-1	1	-1	3	0	-1	1	-1	[100] or [010] or [001]

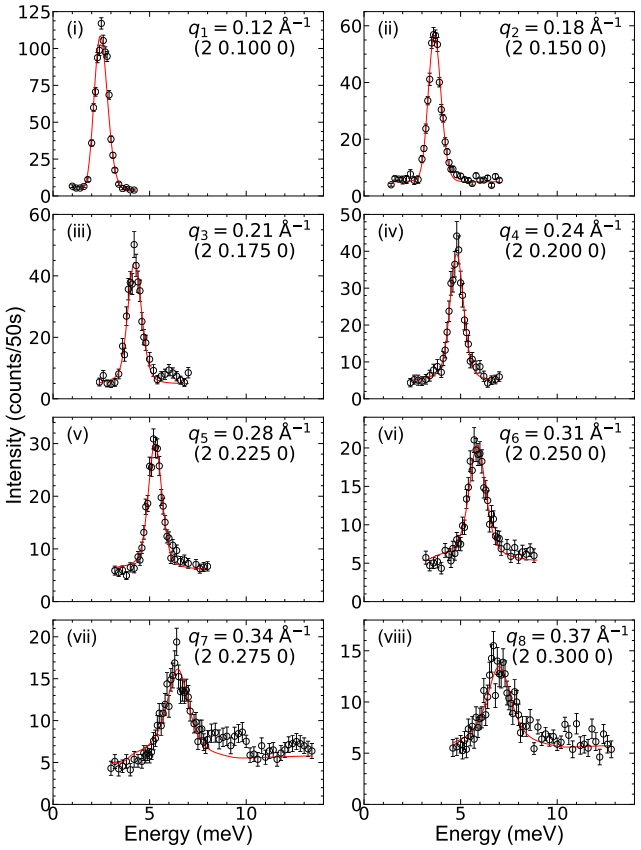

FIG. S3: Energy scans at constant Q for the Δ(TA) polarization, measured by inelastic neutron scattering on the cold-neutron triple-axis spectrometer 4F2@LLB at 300 K, are plotted as open black circles. The phonon was fit as a damped harmonic oscillator and the fit is shown in red.

investigation of cubic stabilised zirconia (CSZ)—II. lattice dynamics of y- and ca-CSZ, Journal of Physics and Chemistry of Solids **57**, 343 (1996).

[6] M. Boudard, M. de Boissieu, S. Kycia, A. I. Goldman, B. Hennion, R. Bellissen, M. Quilichini, R. Currat, and C. Janot, Optic modes in the AlPdMn icosahedral phase, Journal of Physics: Condensed Matter **7**, 7299 (1995).

[7] G. L. Squires, *Introduction to the Theory of Thermal Neutron Scattering* (Cambridge University Press, 2012).

[8] P.-F. Lory, V. M. Giordano, P. Gille, H. Euchner, M. Mihalkovič, E. Pellegrini, M. Gonzalez, L.-P. Regnault, P. Bastie, H. Schober, S. Pailhes, M. R. Johnson, Y. Grin, and M. de Boissieu, Impact of structural complexity and disorder on lattice dynamics and thermal conductivity in the o-$Al_{13}Co_4$ phase, Phys. Rev. B **102**, 024303 (2020).

[9] M. de Boissieu, S. Francoual, M. Mihalkovič, K. Shibata, A. Q. R. Baron, Y. Sidis, T. Ishimasa, D. Wu, T. Lograsso, L.-P. Regnault, F. Gähler, S. Tsutsui, B. Hennion, P. Bastie, T. J. Sato, H. Takakura, R. Currat, and A.-P. Tsai, Lattice dynamics of the Zn-Mg-Sc icosahedral quasicrystal and its Zn-Sc periodic 1/1 approximant, Nat. Mater. **6**, 977 (2007).

[10] P.-F. Lory, *Dynamique de réseau et conductivité thermique dans les alliages métalliques complexes*, Ph.D. thesis, Université de Grenoble (2015).

[11] E. Silberman and H. Morgan, *Use of group theory in the interpretation of infrared and Raman spectra*, Tech. Rep. ORNL/TM–5666 (Oak Ridge National Laboratory, 1977).

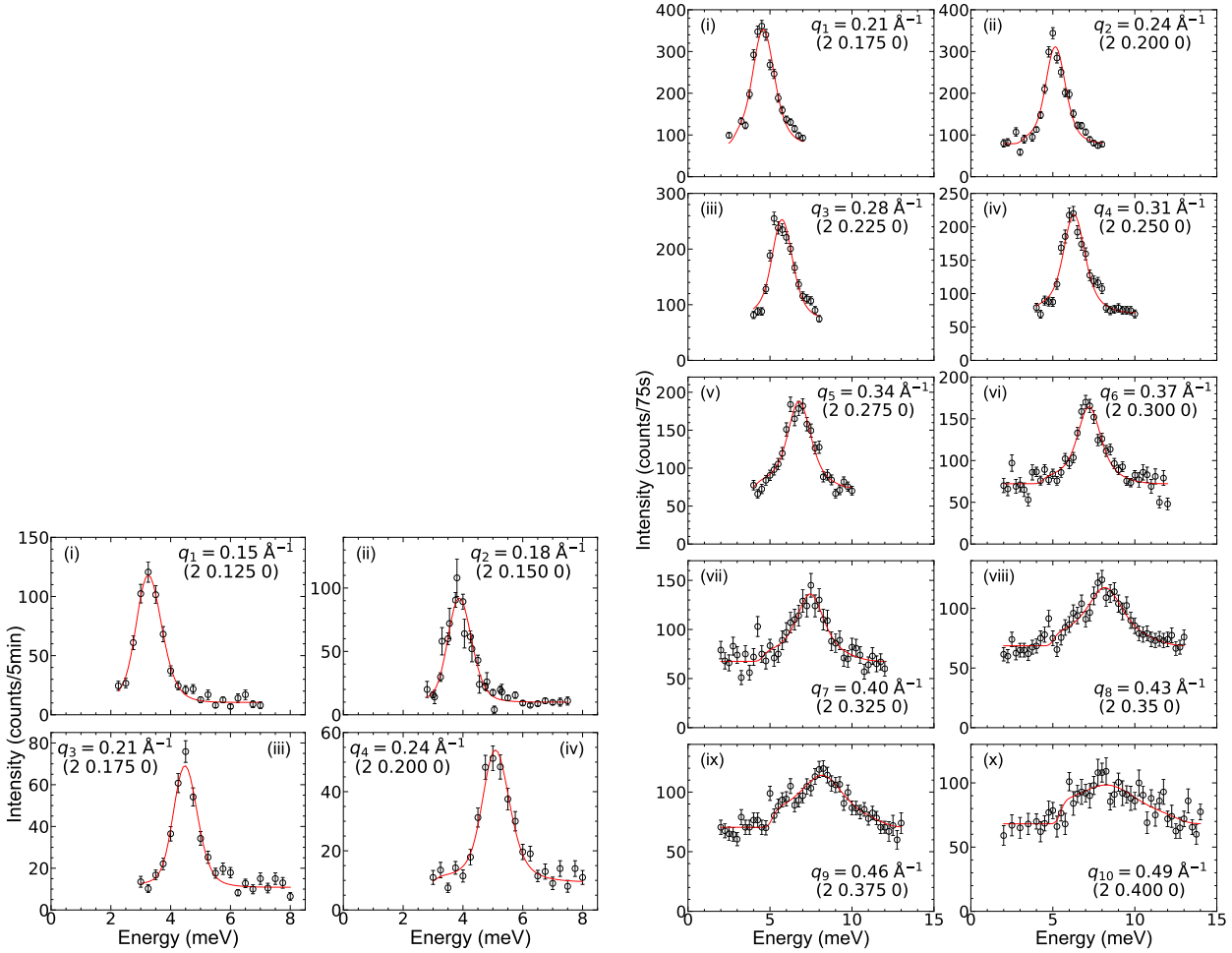

(a) Scans measured with 20' collimation.

(b) Scans measured with 60' collimation.

FIG. S4: Energy scans at constant Q for the Δ(TA) polarization, measured by inelastic neutron scattering on the thermal-neutron triple-axis spectrometer 1T@LLB at 300 K, are plotted as open black circles. The phonon was fit as a damped harmonic oscillator and the fit is shown in red.

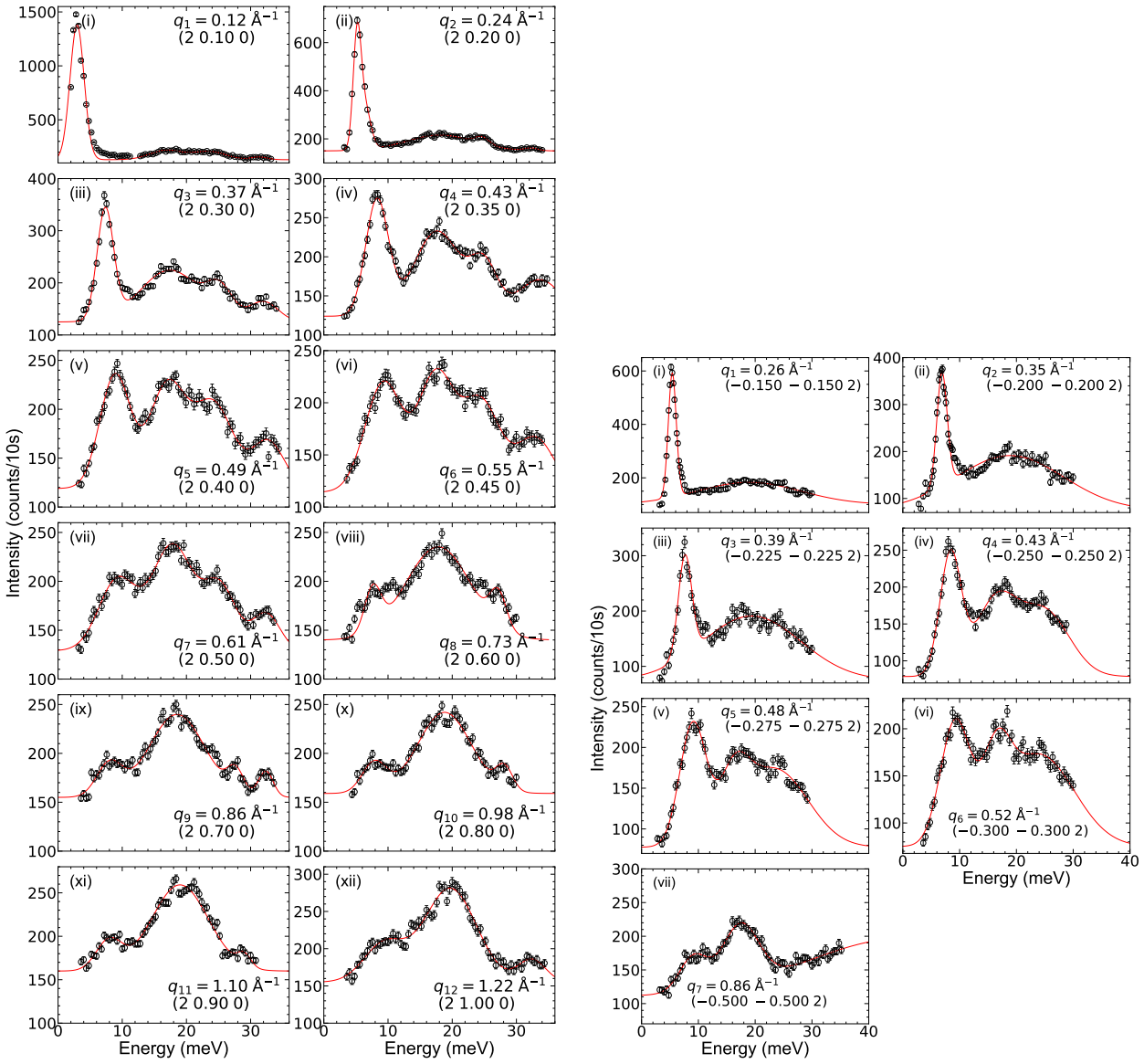

(a) Scans measured for the Δ(TA) polarization.

(b) Scans measured for the Σ(TA$_1$) polarization.

FIG. S5: Energy scans at constant Q, measured by inelastic neutron scattering on the thermal-neutron triple-axis spectrometer IN8@ILL at 300 K, are plotted as open black circles. The phonon was fit as a Gaussian peak and the fit is shown in red.

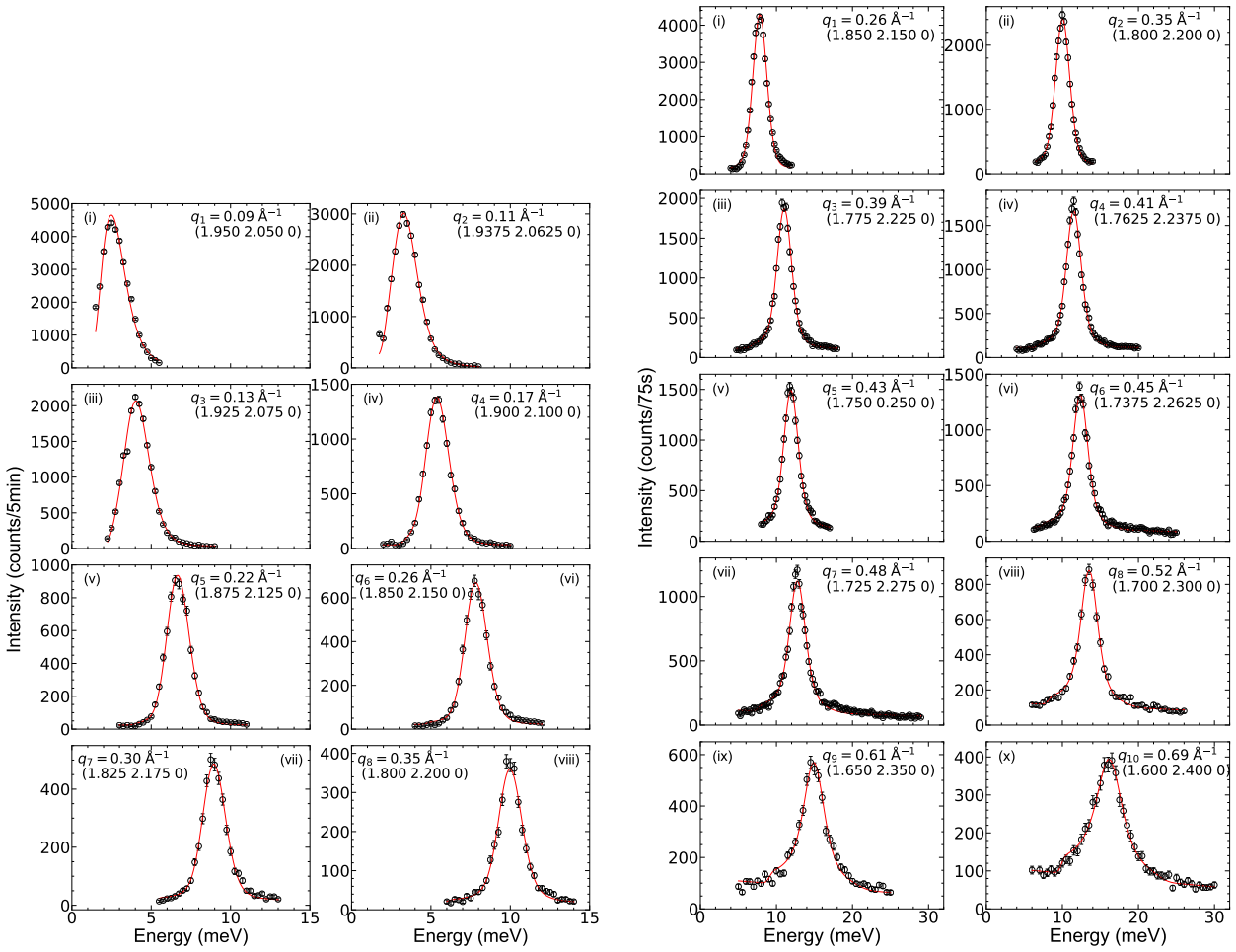

(a) Scans measured with 20' collimation.

(b) Scans measured with 60' collimation.

FIG. S6: Energy scans at constant Q for the $\Sigma(TA_2)$ polarization, measured by inelastic neutron scattering on the thermal-neutron triple-axis spectrometer 1T@LLB at 300 K, are plotted as open black circles. The phonon was fit as a damped harmonic oscillator and the fit is shown in red.

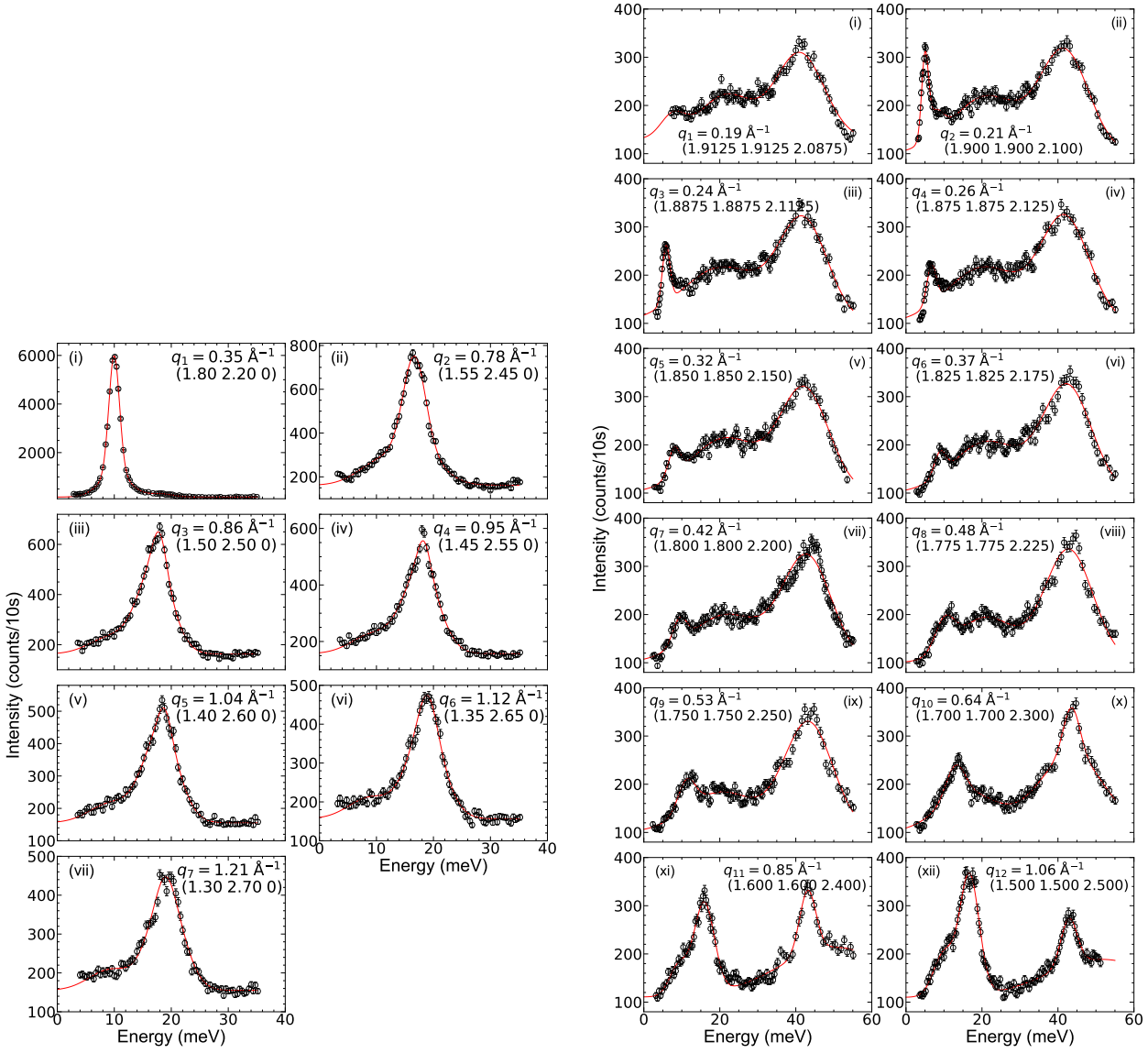

(a) Scans measured for the $\Sigma(TA_2)$ polarization.

(b) Scans measured for the $\Lambda(TA)$ polarization.

FIG. S7: Energy scans at constant Q, measured by inelastic neutron scattering on the thermal-neutron triple-axis spectrometer IN8@ILL at 300 K, are plotted as open black circles. The phonon was fit as a Gaussian peak and the fit is shown in red.

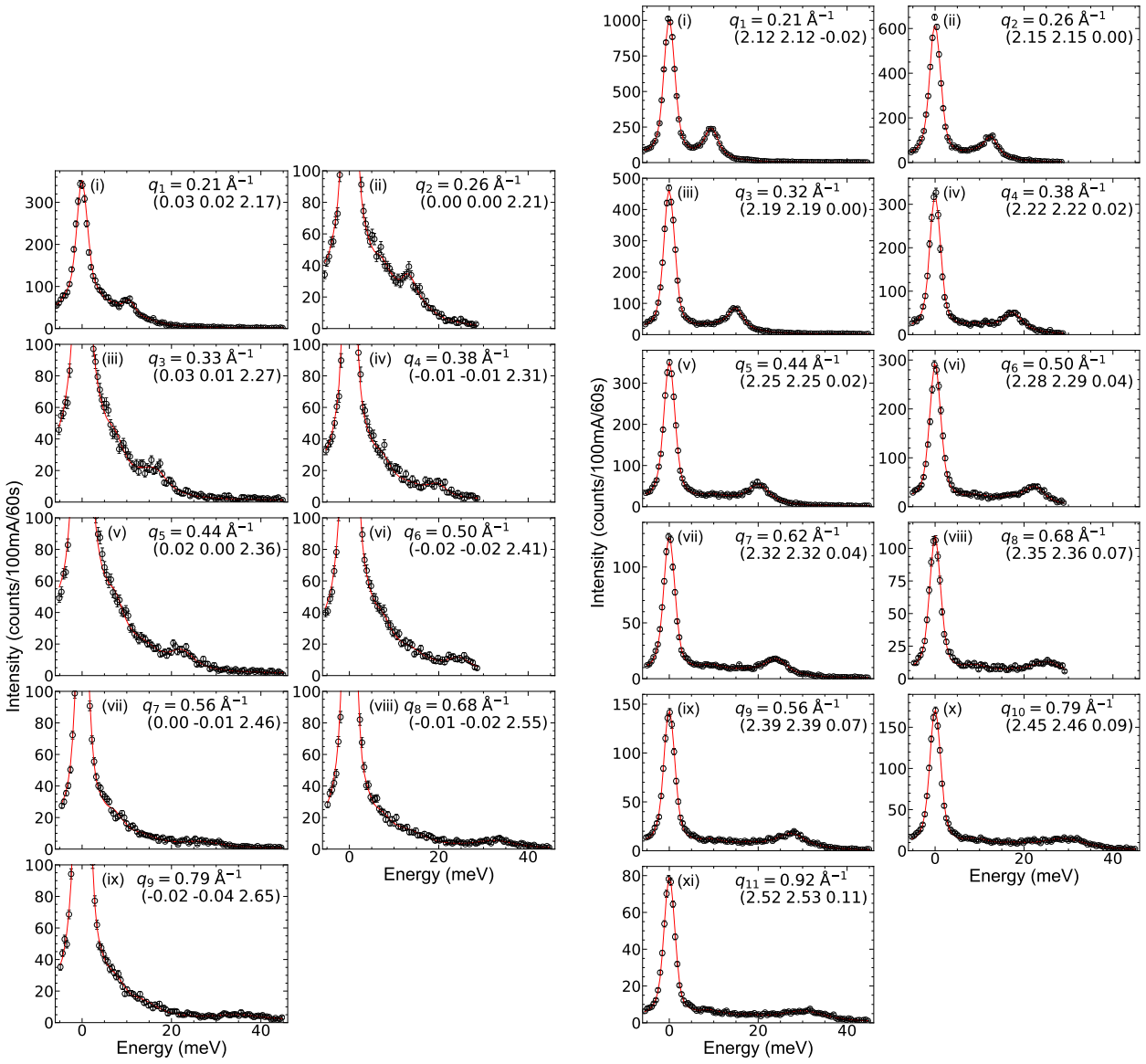

(a) Scans measured for the Δ(LA) polarization.

(b) Scans measured for the Σ(LA) polarization.

FIG. S8: Energy scans at constant Q, measured by inelastic X-ray scattering on the backscattering beamline ID28@ESRF at 300 K, are plotted as open black circles. The phonon was fit as a damped harmonic oscillator and the fit is shown in red.

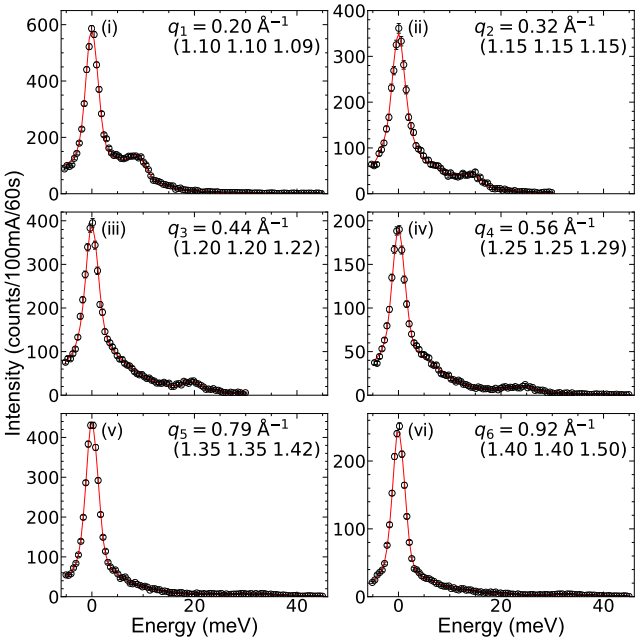

FIG. S9: Energy scans at constant Q for the Λ(LA) polarization, measured by inelastic X-ray scattering on the backscattering beamline ID28@ESRF at 300 K, are plotted as open black circles. The phonon was fit as a damped harmonic oscillator and the fit is shown in red.

General Conclusions

This thesis has included three complete case study examples of how structural and chemical disorder impact thermal conductivity through the understanding of the phonon behavior of said crystalline systems.

The three case study systems studied and discussed in this manuscript were the type-I clathrate $Ba_{7.81}Ge_{40.67}Au_{5.33}$, the high-entropy alloy (HEA) FeCoCrMnNi, and cubic Yttria-Stabilized Zirconia. While clathrates are being studied for their potential use as thermoelectric materials, HEAs are each catered to specific applications for enhanced strength, fracture resistance, temperature resistance, etc., and Yttria-Stabilized Zirconia is well known for its use as a thermal barrier coating. This proves that the concepts and phonon properties discussed in this manuscript not only apply to a wide range of thermal-based applications, but also to a wide range of goals in terms of tuning, restricting, enhancing, and engineering certain thermal properties of materials for their specific purposes. These three systems were also purposefully chosen, as, together, they run the spectrum between simple structures with induced disorder and complex structures with many atoms per unit cell.

The experimental results discussed in this manuscript have been obtained through the use of inelastic neutron and X-ray scattering (INS, IXS) techniques. INS and IXS are optimized for measuring the properties of phonons due to their high instrumental resolutions, variation and customization in terms of instrumental techniques, and their large, accessible range of energy and temperature phase space in which to measure phonon properties. The details provided in the thesis on these techniques should be seen as a guide for taking accurate phonon measurements, while also emphasizing the importance of proper data extraction and interpretation.

By focusing on INS and IXS measurements, I also solidify one of the base themes of this thesis, which is the need for full momentum and temperature ranges of phonon dispersions and linewidths in simple, complex, and disordered crystalline systems, by reminding the reader of the limitations to these techniques faced throughout this thesis. These included the need to use the neutron resonance spin echo technique in order to view a wider energy range of phonon linewidths for $Ba_{7.81}Ge_{40.67}Au_{5.33}$, and the limitations imposed by both the crystal quality and the large incoherent neutron scattering cross-section for the INS FeCoCrMnNi measurements.

Moving now to the results of each case study, firstly, through my published work on the type-I clathrate $Ba_{7.81}Ge_{40.67}Au_{5.33}$, we have shown that there is a polarization dependence at play between the low-lying optical branches in this material. As the onset of these low-lying branches represents the end of the purely acoustic and propagative phonon regime, the exact energies of these branches determine this characteristic. In particular, the rate of hardening of the lowest-lying optical branch, E_{Ba}, with temperature was confirmed to match the one simulated by the *ab initio* self-consistent phonon (SCP) theory method. The ability to pinpoint the precise energies of these modes will hopefully help us control the length of the acoustic regime in clathrates in the future. This investigation also further emphasized the importance of the quartic anharmonic phonon scattering process in the control of the plateau region of the lattice thermal conductivity in clathrates.

These results on $Ba_{7.81}Ge_{40.67}Au_{5.33}$ have also been compared in light of novel density func-

tional theory methods, including the *ab initio* harmonic calculations with the strongly constrained and appropriately normed (SCAN) meta-generalized-gradient (GGA) functional and the *ab initio* SCP method, with much success. The SCAN functional provided us with improved phonon dispersions for this Ge-based clathrate that align nicely with the experimental findings. They also helped enlighten the respective contributions of each Wyckoff position within the total phonon density of states, leading us to link the specific low-lying optical branches to their respective atomic vibrations within the cages of the unit cell. The analysis of the SCP method calculations, on the other hand, quantitatively validated the anharmonic contributions found by taking into account the cubic and quartic anharmonic terms. These comparisons not only provide vital confirmations of novel theoretical methods, but they also encourage the continued development of said methods, pointing out that the inclusion of disorder, i.e. calculations that go beyond the use of the fully ordered model, and the inclusion of anharmonic terms, lead to a closer matching of the experimentally-measured lattice thermal conductivity in clathrates.

Secondly, through the conclusions reached with the high-entropy alloy FeCoCrMnNi, we have gone one step further and analyzed not only the phonon dispersions but also the intrinsic phonon linewidths of the material. We found that the dispersions showed no change in energy dependence between the element Ni, random binary alloys such as NiFe and NiCo, and the HEA FeCoCrMnNi. The phonon linewidths, however, while exhibiting the same order of magnitude of broadening found in random binary alloys, present a stark shift from a strong to a weak phonon scattering regime in some polarizations and directions. By isolating force-constant fluctuations as the dominant phonon scattering mechanism in this material, we were able to confidently attribute the strong scattering regime and the concomitant deviation of the acoustic phonon dynamics from the Debye prediction to this specific scattering mechanism. This effect marks an important similarity to other complex and disordered systems such as glasses, quasicrystals, and clathrates, which also exhibit multiple scattering regime dependencies.

By adding intrinsic phonon linewidths of an HEA to our database of reference materials, we have unlocked a certain pattern that is seen across multiple families of disordered materials. We must continue to develop this pattern with similar case studies in the future, as it is essential to our understanding of the contributions of different phonon scattering mechanisms. The general conclusion of this case study also ended as an open invitation to continue similar studies on a wide variety of HEAs, seeing as, by cocktailing certain elements together to form specific HEAs, we should be able to promote and suppress different kinds of disorder (mass and atomic size differences, force-constant fluctuations, etc.) for experimental evaluation.

Thirdly, I reference my work on cubic Yttria-Stabilized Zirconia. This well-studied and well-applied material has been in use in industry for decades. However, through the application of improved instrumental resolution, we were able to bring a new understanding of the phonon behavior in this material to light. We were able to resolve the presence of low-lying optical branches outside of the center of the Brillouin zone for the first time, to the best of our knowledge. This in and of itself represents an important result, and to this we have added the measurement of intrinsic acoustic phonon linewidths such that we contribute to the understanding of the acoustic-optical interaction and the defect-induced scattering in this material. We can now conclude that the disorder-induced optical branches and additional phonon broadening are direct correlations to the chemical disorder caused by the doping of Zirconia with Yttria. With this particular case study and with these new understandings, we hope to stimulate new theoretical calculations based on these discoveries. Complementary simulations will help us correlate the impact that the structural disorder has on phonon linewidth using our experimental results.

In conclusion, by presenting this work, I add to the scientific community's growing library of experimental results on phonon properties, and specifically intrinsic phonon lifetimes, with the confidence that these studies have brought us closer to a unified understanding of heat transport

in complex and disordered crystalline systems. In each case, I have linked the macro and micro thermal transport scales by pinpointing the relevant phonon scattering mechanisms at play due to each system's unique structural complexity and disorder.

In terms of perspectives, we, as experimentalists, need to continue to add to this database of phonon lifetimes for simple, complex, and disordered materials alike. This will allow us to strategically draw conclusions about the ways that specific phonon scattering mechanisms affect thermal conductivity, and to predict the outcome of said mechanisms in yet unstudied materials. Only through this understanding will we be able to target certain material properties and engineer materials for their specific thermal-based applications through induced disorder and complexity. An increased volume of phonon lifetime measurements will also provide much-needed references and checkpoints for the novel theoretical methods currently being developed. In order to have confidence in the rigor and sophistication of these methods, they must be backed by strong experimental evidence. This will also allow us to trust these models as prediction methods for materials that have yet to be studied experimentally or for those materials which present difficulties in terms of high-resolution experimental measurement.

The future of phonon measurements and simulations is bright, as we learn to take full advantage of the increased computing power that has been newly made available in recent years, and to further push the boundaries of the experimental measurements that are possible. This will certainly bring about not only novel materials for thermal applications, but also an improved understanding of heat transport.

APPENDIX A

The Figure of Merit and the Efficiency of a Thermoelectric Generator

This Appendix will expand on the concepts introduced in Section 1.1, namely the derivation of the dimensionless figure of merit, ZT, which quantifies the efficiency of a thermoelectric generator. This derivation follows those provided in Refs. [264, 265].

Fig. A.1 is a sketch of a simple thermoelectric generator (TEG). This TEG consists of n-type and p-type semiconductors connected in series. For simplicity's sake within this derivation, we will assume that there are only two elements in this TEG: one n-type element and p-type element. A metal connection links these two elements to a hot junction which has temperature T_H, and we measure the thermal power absorbed into this hot junction and call it Q_H. The two elements are also linked to a cold junction which has temperature T_C, and we also measure the thermal power released from this cold junction and call it Q_C. Finally, the two elements are also linked to a resistive load, defined with resistance R_L.

We can start by making the following definitions from the figure:

$$r_{p,n} = \frac{l}{\sigma_{p,n} A}$$
$$V = S_{pn}(T_H - T_C) = S_{pn}\Delta T \tag{A.1}$$

Here, $r_{p,n}$ represents the resistance in each of the two elements which are in turn defined by their lengths l, and cross-sectional areas A, and respective electrical conductivities $\sigma_{p,n}$. Voltage generation is defined by V, where S_{pn} is the difference between the Seebeck coefficients of the two elements and ΔT is the difference in temperature between the hot and cold junctions. The Seebeck coefficients relate voltage to a temperature gradient [30].

With these definitions, we can calculate the power of this generator, where I_L, current through the load resistor, is the voltage divided by total resistance by Ohm's Law. The power is then the resistance at the load, R_L, multiplied by the square of the current.

$$I_L = \frac{S_{pn}\Delta T}{r_{p,n} + R_L}$$
$$W = I_L^2 R_L = \frac{S_{pn}^2 \Delta T^2 R_L}{(r_{p,n} + R_L)^2} \tag{A.2}$$

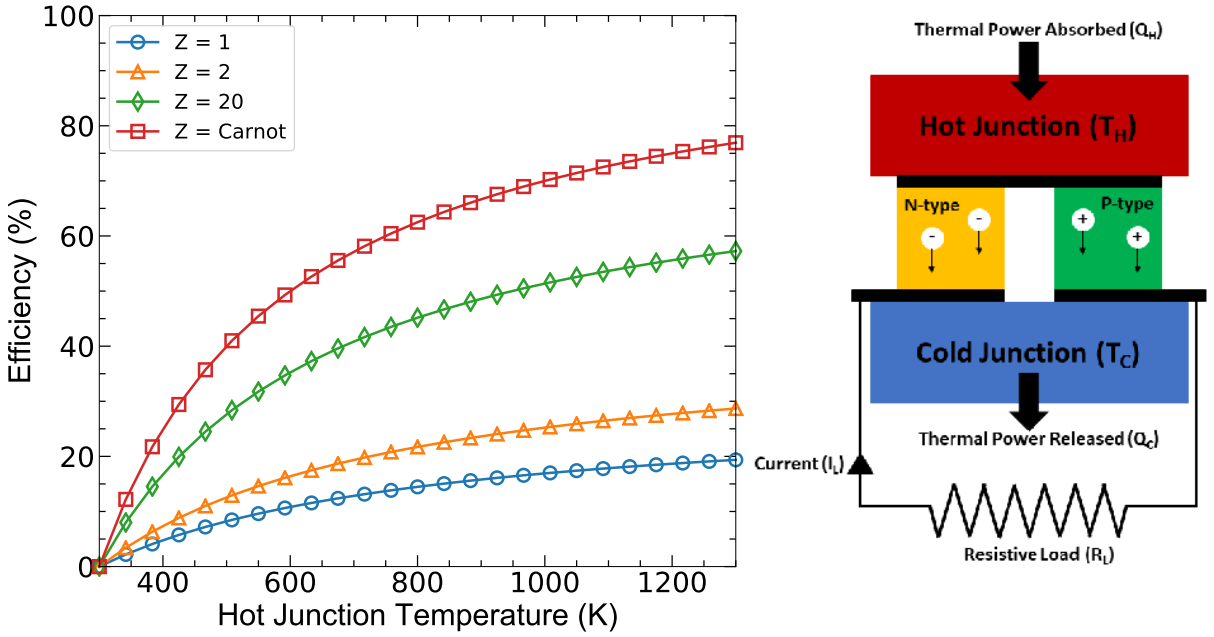

Figure A.1: A basic thermoelectric generator and its efficiency with temperature. *An example of a basic thermoelectric generator (TEG) is shown in the right panel. A hot junction with temperature T_H is separated from a cold junction with temperature T_C by n-type and p-type semiconductors. They are connected in series and create a circuit with current I_L and load resistance R_L. Thermal power absorbed at the hot junction is Q_H and thermal power released at the cold junction is Q_C. The left panel is the relationship between the temperature of the hot junction and the resulting efficiency for different values of the dimensionless figure of merit. T_C has been set to 300 K. When Z equals infinity, the Carnot efficiency, or the maximum efficiency for a TEG, is reached.*

We can analyze the efficiency of this thermoelectric generator by considering that efficiency, η, is the relationship between W and the thermal power absorbed at the hot junction, Q_H, as shown in eq. A.3.

$$\eta = W/Q_H \tag{A.3}$$

The denominator of eq. A.3, Q_H, depends on three components: the Peltier effect, Q_P, thermal conductance, Q_{TC}, and the Joule effect, Q_J. The Peltier effect is the heat energy emitted due to an electrical current going through the hot and cold junctions, and the Joule effect is the same heat energy but for a current passing through resistance [30]. The thermal conductance term depends on the thermal conductance in each of the two elements: $k_{p,n}$. Thermal conductance explains how heat flows in a given cross-section of a material. Therefore, the thermal power absorbed at the hot junction, Q_H, is the Peltier effect plus the thermal conductance of the two elements, minus the heat energy at the load resistance.

$$Q_H = Q_P + Q_{TC} - Q_J = T_H S_{pn} I_L + (k_{p,n})\Delta T - \frac{r_{p,n} I_L^2}{2} \tag{A.4}$$

Combining the formulas for Q_C and Q_H, η_{max} becomes:

$$\eta = \frac{\frac{S_{pn}^2 \Delta T^2 R_L}{(r_{p,n}+R_L)^2}}{T_H S_{pn} I_L + (k_{p,n})\Delta T - \frac{r_{p,n} I_L^2}{2}} \tag{A.5}$$

The equation for current, I_L, can be filled in to achieve our full equation:

$$\eta = \frac{\frac{S_{pn}^2 \Delta T^2 R_L}{(r_{p,n}+R_L)^2}}{\frac{T_H S_{pn}^2 \Delta T}{(r_{p,n}+R_L)} + (k_{p,n})\Delta T - \frac{S_{pn}^2 \Delta T^2 r_{p,n}}{2(r_{p,n}+R_L)^2}} \tag{A.6}$$

Next, we simplify this equation and highlight the $\Delta T/T_H$ term. It has been separated from the other variables because this describes the *Carnot efficiency*. The Carnot cycle describes a thermodynamically reversible process in which the temperatures of the hot and cold junctions are used to maximize efficiency, and the maximum amount of heat that can be converted into electrical power is known as the Carnot efficiency. The rest of the equation therefore explains the imperfections of a real system which keep η_{max} from reaching unity. We will come back to this concept at the end of the derivation.

$$\eta = \left(\frac{\Delta T}{T_H}\right) \times \frac{\frac{R_L}{(r_{p,n}+R_L)}}{1 + \frac{(k_{p,n})(r_{p,n}+R_L)}{T_H S_{pn}^2} - \frac{\Delta T r_{p,n}}{2(r_{p,n}+R_L)T_H}} \tag{A.7}$$

The following substitution, $m = \frac{R_L}{r_{p,n}}$ can be made to further simplify the equation:

$$\eta = \left(\frac{\Delta T}{T_H}\right) \times \frac{\frac{m}{m+1}}{1 + \frac{r_{p,n}(k_{p,n})(m+1)}{T_H S_{pn}^2} - \frac{\Delta T}{2T_H(m+1)}} \tag{A.8}$$

We define another new variable, the figure of merit, which is also used to simplify the equation:

$$Z = \frac{S_{pn}^2}{(r_{p,n})(k_{p,n})} \tag{A.9}$$

Combining eq. A.9 and eq. A.8, we are left with

$$\eta = \left(\frac{\Delta T}{T_H}\right) \times \frac{\frac{m}{m+1}}{1 + \frac{m+1}{ZT_H} - \frac{\Delta T}{2T_H(m+1)}}. \tag{A.10}$$

The load resistance, R_L, can be used to optimize the efficiency, which will be written as η_{max}. This occurs when $R_L = r_{p,n}\sqrt{1+ZT}$, continuing with the $m = \frac{R_L}{r_{p,n}}$ relationship. The variable $T = \frac{T_H+T_C}{2}$ is the average temperature between the two junctions in this case.

$$\eta_{max} = \left(\frac{\Delta T}{T_H}\right) \times \frac{\sqrt{1+ZT}-1}{\sqrt{1+ZT}+\frac{T_C}{T_H}} \tag{A.11}$$

Finally, we can rewrite eq. A.9 in order to view ZT in its more commonly viewed form, which depends on electrical conductivity instead of resistance, thermal conductivity, κ instead of thermal conductance, and once again the Seebeck coefficient.

$$ZT = \frac{S^2\sigma}{\kappa}T \tag{A.12}$$

The efficiency of a TEG is therefore influenced by ZT, T_H, and T_C. In the left panel of Fig. A.1, the relationship between the temperature of the hot junction and the resulting efficiency for several different values of the dimensionless figure of merit are shown for $T_C = 300$ K. As seen in the figure, for this given temperature range, efficiency is between 20 and 30% for Z values of 1-2, which is the range of values for most state-of-the-art thermoelectric materials at the time of writing (see Fig. 1.1). The Carnot efficiency, $\Delta T/T_H$, is also plotted for reference.

APPENDIX B

Raw Data from TRISP@FRM-II Neutron Resonance Spin Echo Experiment

The raw data from the Neutron Resonance Spin Echo (NRSE) measurements for the type-I clathrate $Ba_{7.81}Ge_{40.67}Au_{5.33}$, described in Section 3.1.9.5, are detailed below. Measurements were taken on the thermal-neutron triple-axis spectrometer TRISP@FRM-II at 300 K and using a fixed $\mathbf{k}_f = 2.51$ Å^{-1}. The single crystal was aligned into the [110][001] scattering plane, and the measurements focused on the transverse acoustic phonon dispersion polarized along the [001] direction, propagating along the [110] direction (TA^{001}_{110}), for phonons stemming from the intense (006) Bragg peak.

The locations of the 7 points along the TA^{001}_{110} dispersion are labeled in Fig. B.1, which has been adapted from Fig. 3(a) of Turner *et al.* [57]. Table B.1 summarizes the **q**-position, energy, group velocity, and resulting linewidth of each point.

Fig. B.2 displays the raw intensity and their respective cosine fits measured for the given spin-echo time τ_{NRSE} listed in each subplot for 'q_1' from Fig. B.1. The polarization is extracted from each fit and then plotted in Fig. B.9(i) as the uncorrected datapoints in blue. Two corrections are made to the data: the curvature correction (orange) and instrumental resolution correction (purple). (Please see Section 3.1.9 for more details.) Finally, the half-width-half-maximum of the linewidth, Γ_{HWHM}, is extracted from the corrected datapoints in green, and this value is used to plot Fig. 3.16 in Section 3.1.9. This process is repeated for Figs. B.3-B.8 and Fig. B.9(ii)-(vii), respectively.

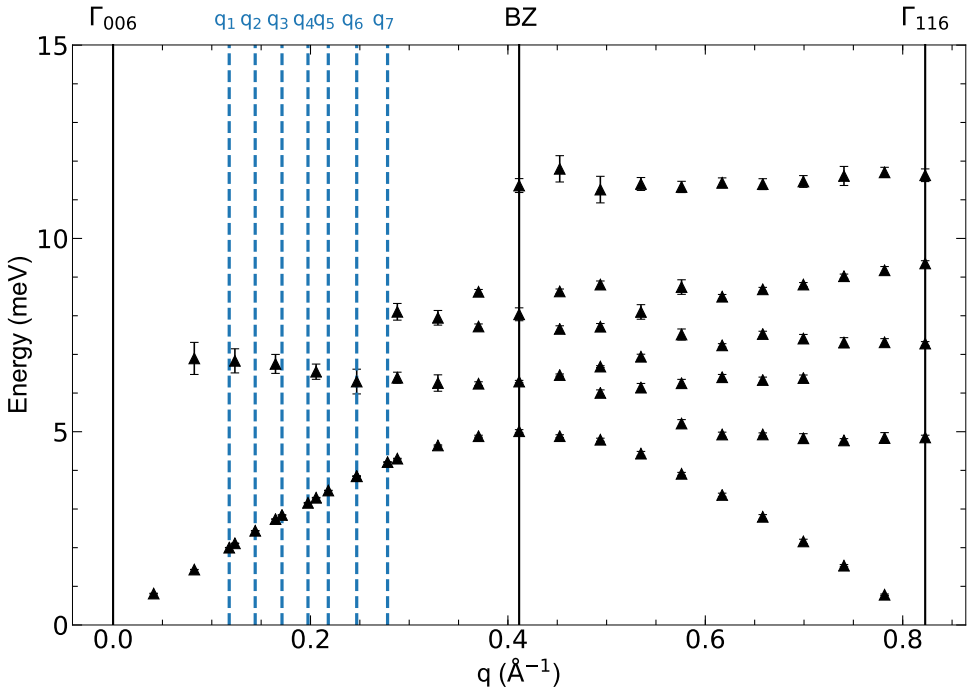

Figure B.1: Reciprocal space location of the 7 TRISP q-points. *This figure has been adapted from Fig. 3(a) of Turner et al. [57]. The transverse acoustic phonon dispersion polarized along the [001] direction, propagating along the [110] direction and similarly polarized higher-energy optical branches for the type-I clathrate $Ba_{7.81}Ge_{40.67}Au_{5.33}$ are shown. Phonons are propagating from the (006) Bragg peak, labeled Γ_{006}, towards the (116) zone center, Γ_{116}. These, and the Brillouin zone (BZ) are marked by black solid lines. The 7 q-points of interest for the Neutron Resonance Spin Echo measurement are labeled in blue by dashed lines.*

Table B.1: *Summary of experimental parameters of each q point measured from the TA^{001}_{110} phonon dispersion using the Neutron Resonance Spin Echo technique at TRISP@FRM-II. See text for more details. For each q labeled in Fig. B.1, the phonon wavevector in r.l.u. and $Å^{-1}$, along with its energy, group velocity, and resulting half-width-half-maximum linewidth. Note that the r.l.u. values are negative, reflecting the necessary defocusing condition with respect to a TAS measurement (see Fig. 3.8), while I have given the absolute value $Å^{-1}$ values in order for the reader to link these values to the q points on the dispersion shown in Fig. B.1.*

	q (ξ ξ 0) (r.l.u.)	**q (Å^{-1})**	**E (meV)**	**v_g (meV.Å)**	**Γ_{HWHM} (μeV)**
q_1	-0.143	0.118	2.000 ± 0.005	16.295 ± 0.044	13.810 ± 2.310
q_2	-0.175	0.144	2.437 ± 0.006	15.649 ± 0.165	19.919 ± 2.786
q_3	-0.208	0.171	2.846 ± 0.007	14.235 ± 0.300	36.206 ± 2.707
q_4	-0.240	0.197	3.159 ± 0.010	13.562 ± 0.049	34.377 ± 3.521
q_5	-0.265	0.218	3.478 ± 0.006	13.425 ± 0.289	30.432 ± 3.378
q_6	-0.300	0.247	3.848 ± 0.007	12.636 ± 0.277	34.884 ± 4.286
q_7	-0.338	0.278	4.214 ± 0.011	11.203 ± 0.284	47.350 ± 4.374

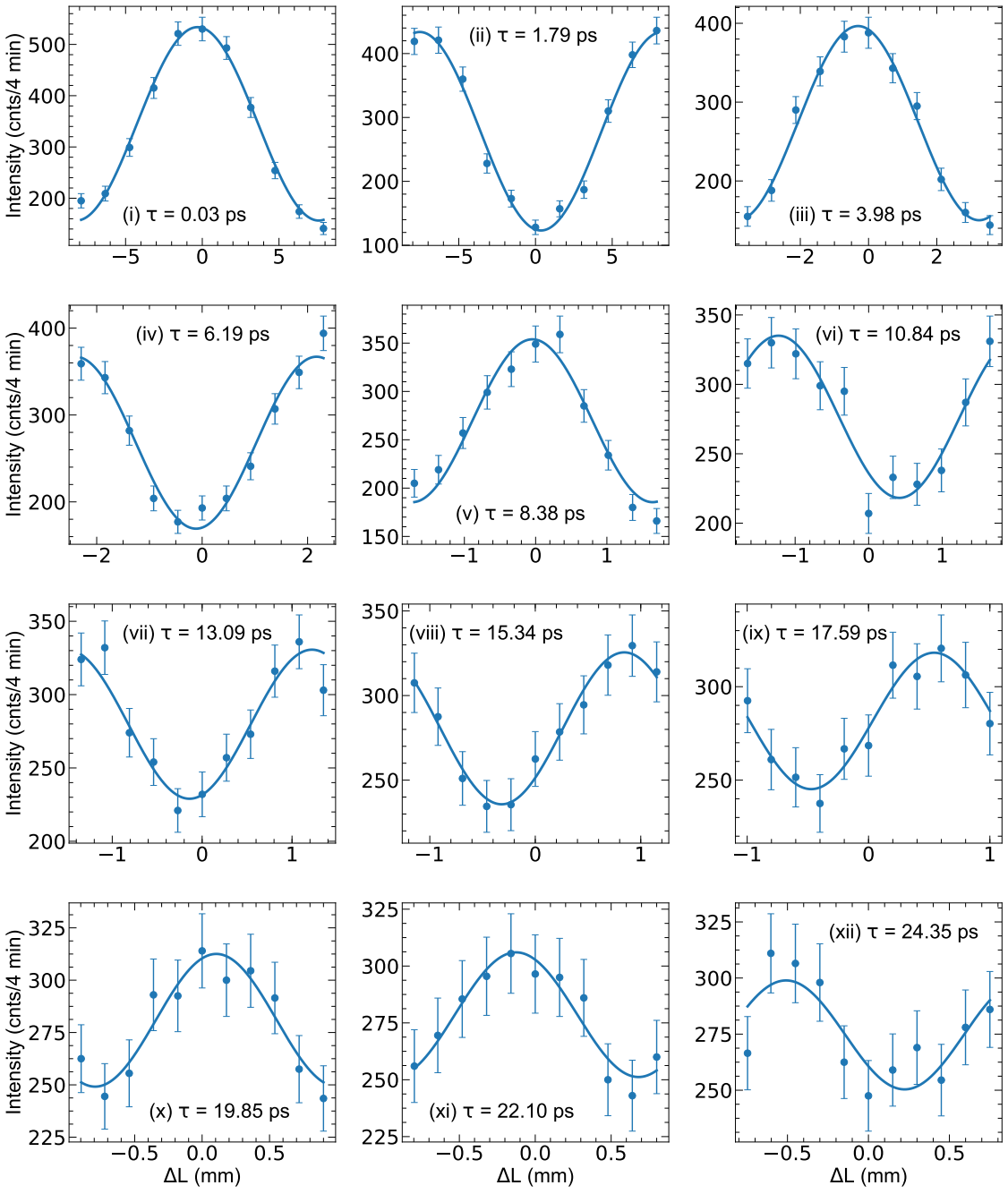

Figure B.2: *Raw intensity of a neutron resonance spin echo (NRSE) measurement for the given spin-echo times τ_{NRSE} (written simply as τ in the plots to save space), reflecting data taken for q_1 = (-0.143 -0.143 0) (see Table B.1). Data have been fit with a cosine() function and an arbitrary background set to zero in order to extract the polarization dependence. Measurement was made on the thermal-neutron triple-axis spectrometer TRISP@FRM-II for the type-I clathrate $Ba_{7.81}Ge_{40.67}Au_{5.33}$. See text for more details.*

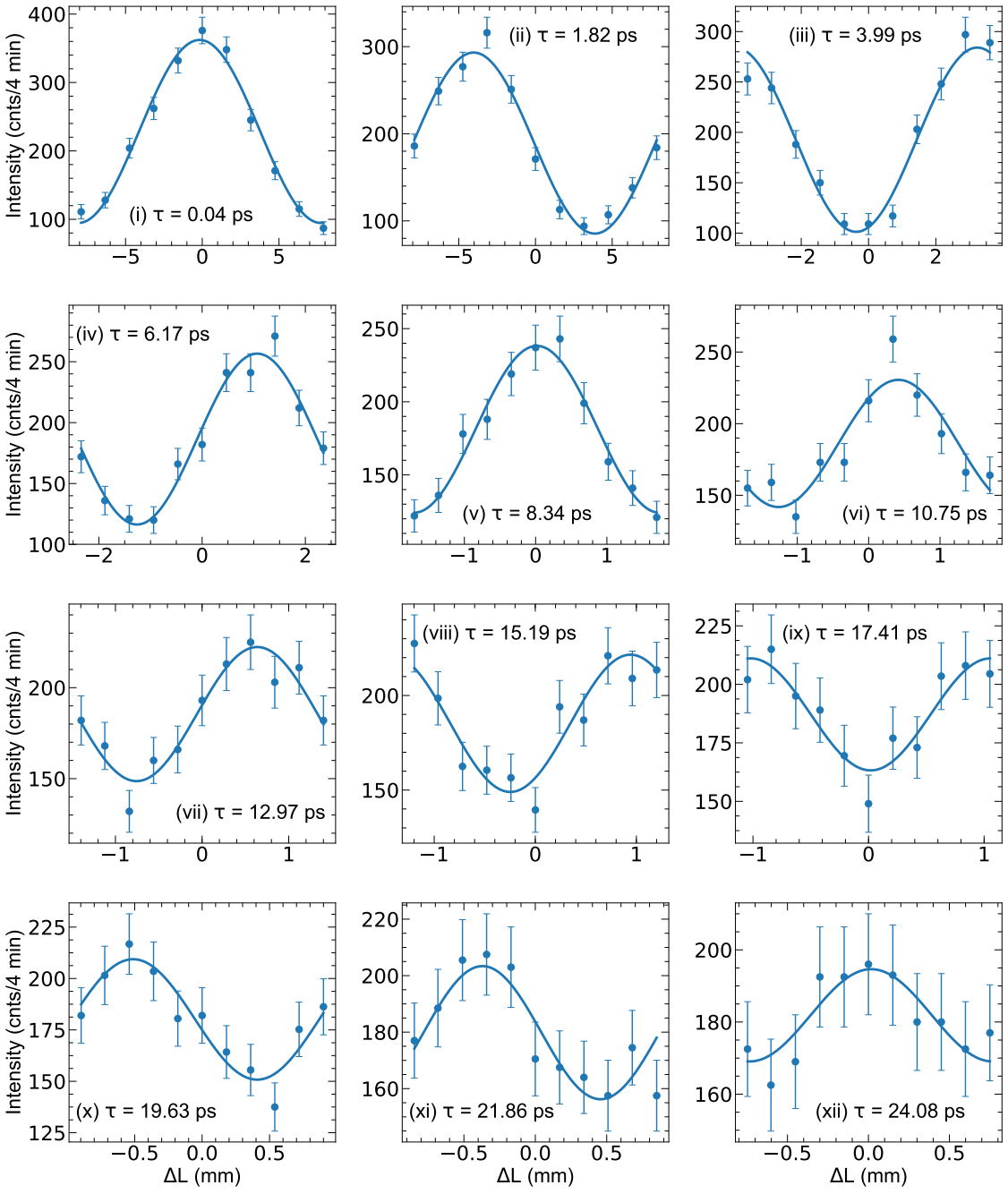

Figure B.3: *Raw intensity of a neutron resonance spin echo (NRSE) measurement for the given spin-echo times τ_{NRSE} (written simply as τ in the plots to save space), reflecting data taken for q_2 = (-0.175 -0.175 0) (see Table B.1). Data have been fit with a cosine() function and an arbitrary background set to zero in order to extract the polarization dependence. Measurement was made on the thermal-neutron triple-axis spectrometer TRISP@FRM-II for the type-I clathrate $Ba_{7.81}Ge_{40.67}Au_{5.33}$. See text for more details.*

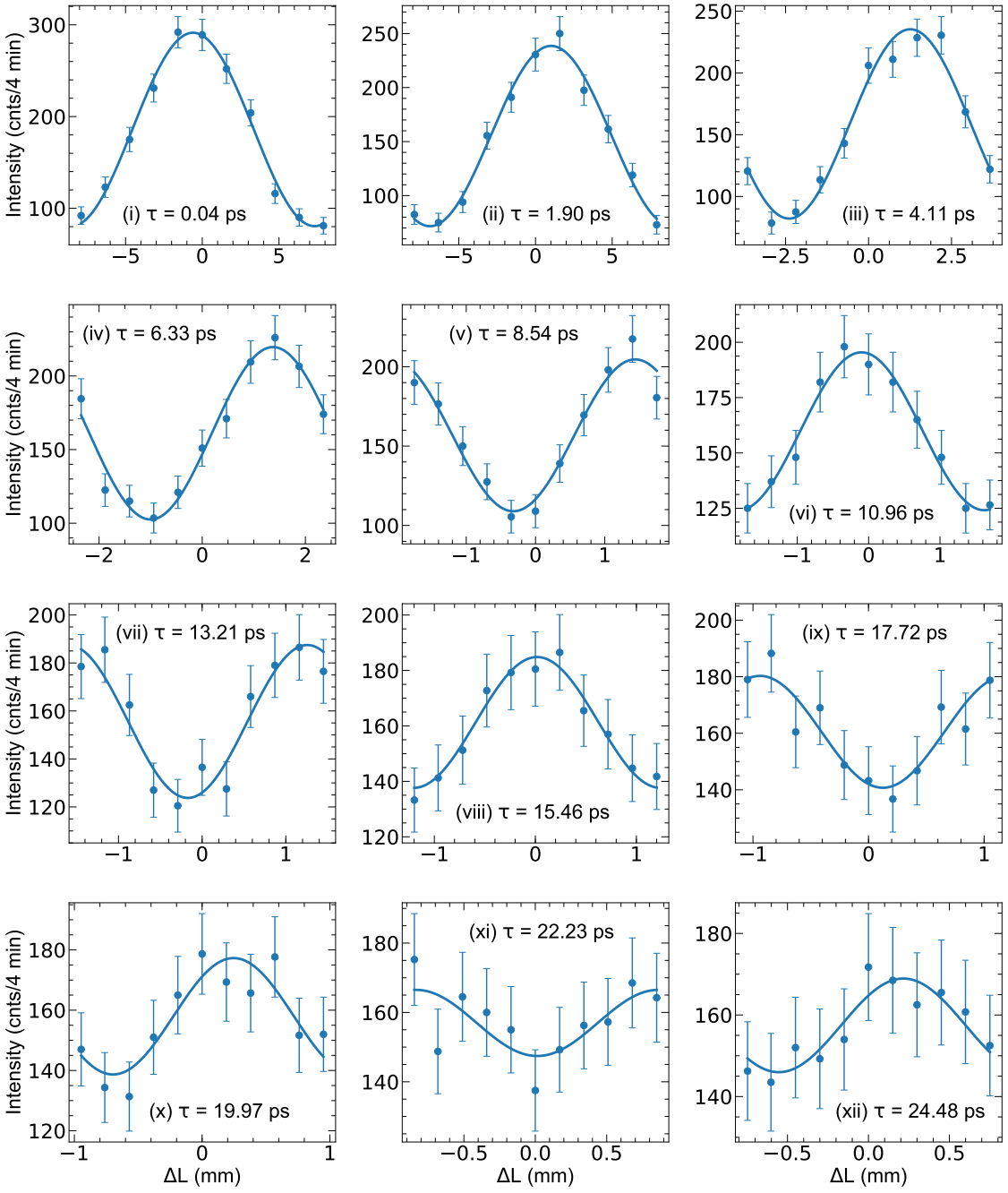

Figure B.4: *Raw intensity of a neutron resonance spin echo (NRSE) measurement for the given spin-echo times τ_{NRSE} (written simply as τ in the plots to save space), reflecting data taken for q_3 = (-0.208 -0.208 0) (see Table B.1). Data have been fit with a cosine() function and an arbitrary background set to zero in order to extract the polarization dependence. Measurement was made on the thermal-neutron triple-axis spectrometer TRISP@FRM-II for the type-I clathrate $Ba_{7.81}Ge_{40.67}Au_{5.33}$. See text for more details.*

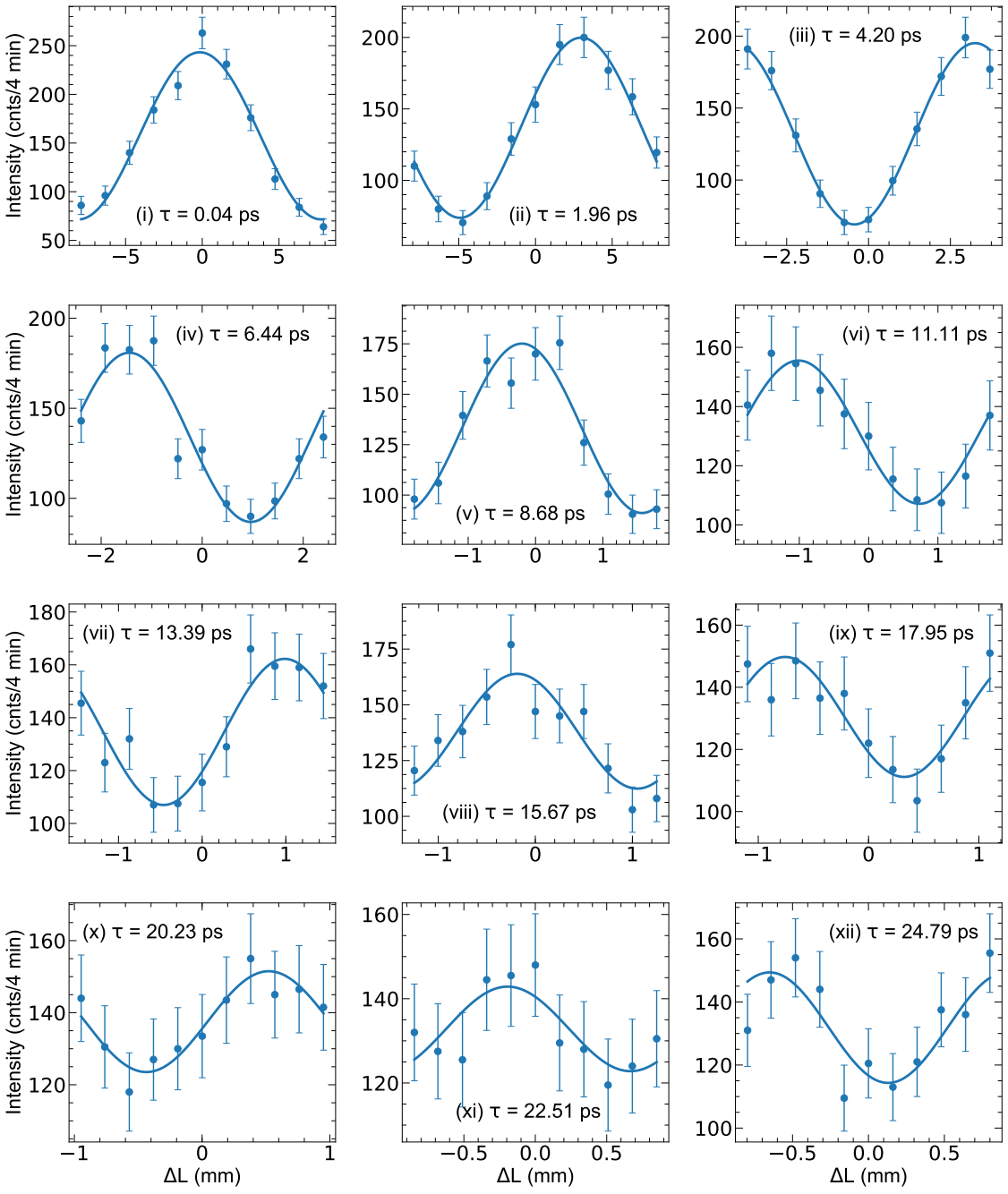

Figure B.5: *Raw intensity of a neutron resonance spin echo (NRSE) measurement for the given spin-echo times τ_{NRSE} (written simply as τ in the plots to save space), reflecting data taken for q_4 = (-0.240 -0.240 0) (see Table B.1). Data have been fit with a cosine() function and an arbitrary background set to zero in order to extract the polarization dependence. Measurement was made on the thermal-neutron triple-axis spectrometer TRISP@FRM-II for the type-I clathrate $Ba_{7.81}Ge_{40.67}Au_{5.33}$. See text for more details.*

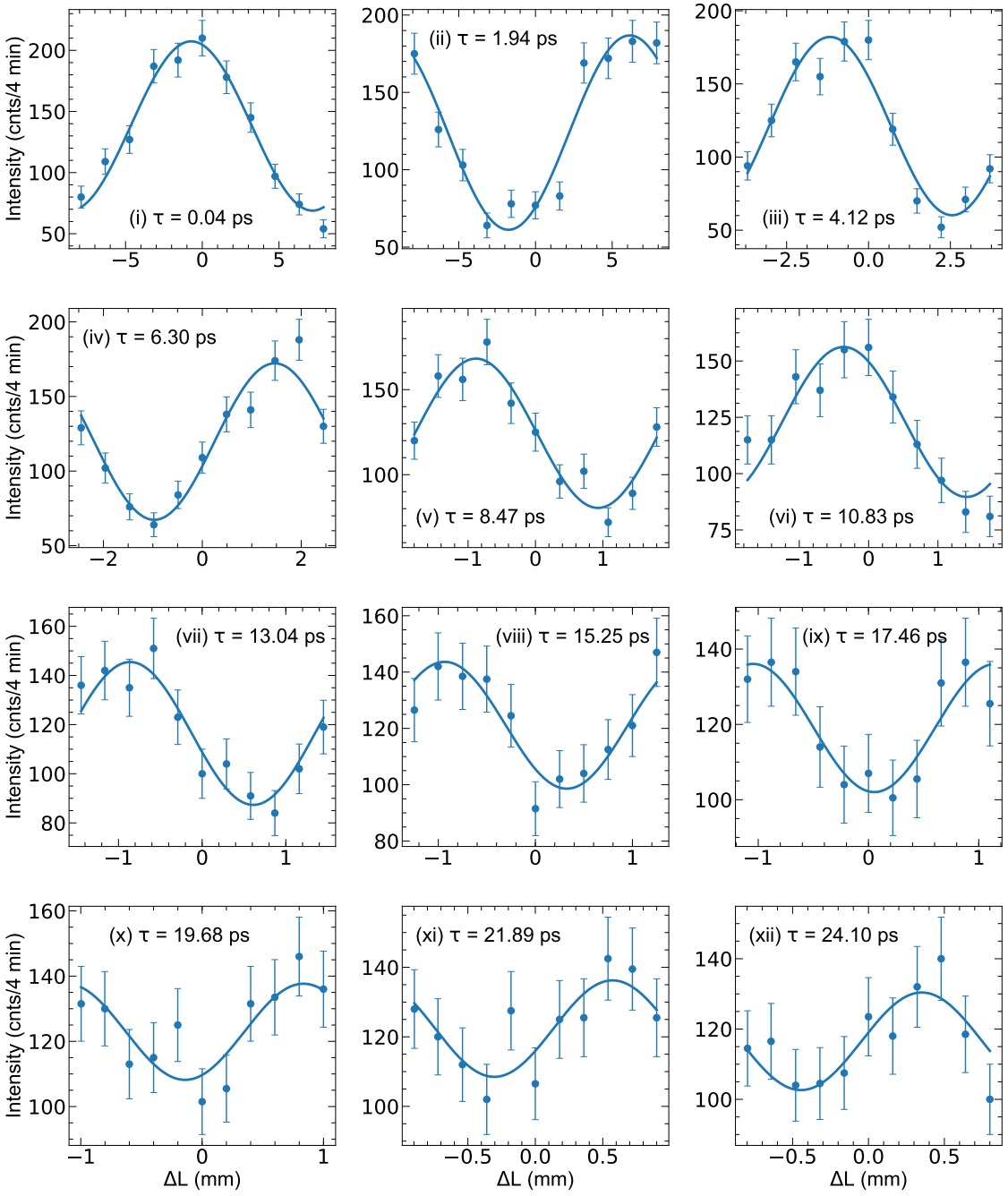

Figure B.6: *Raw intensity of a neutron resonance spin echo (NRSE) measurement for the given spin-echo times τ_{NRSE} (written simply as τ in the plots to save space), reflecting data taken for q_5 = (-0.265 -0.265 0) (see Table B.1). Data have been fit with a cosine() function and an arbitrary background set to zero in order to extract the polarization dependence. Measurement was made on the thermal-neutron triple-axis spectrometer TRISP@FRM-II for the type-I clathrate $Ba_{7.81}Ge_{40.67}Au_{5.33}$. See text for more details.*

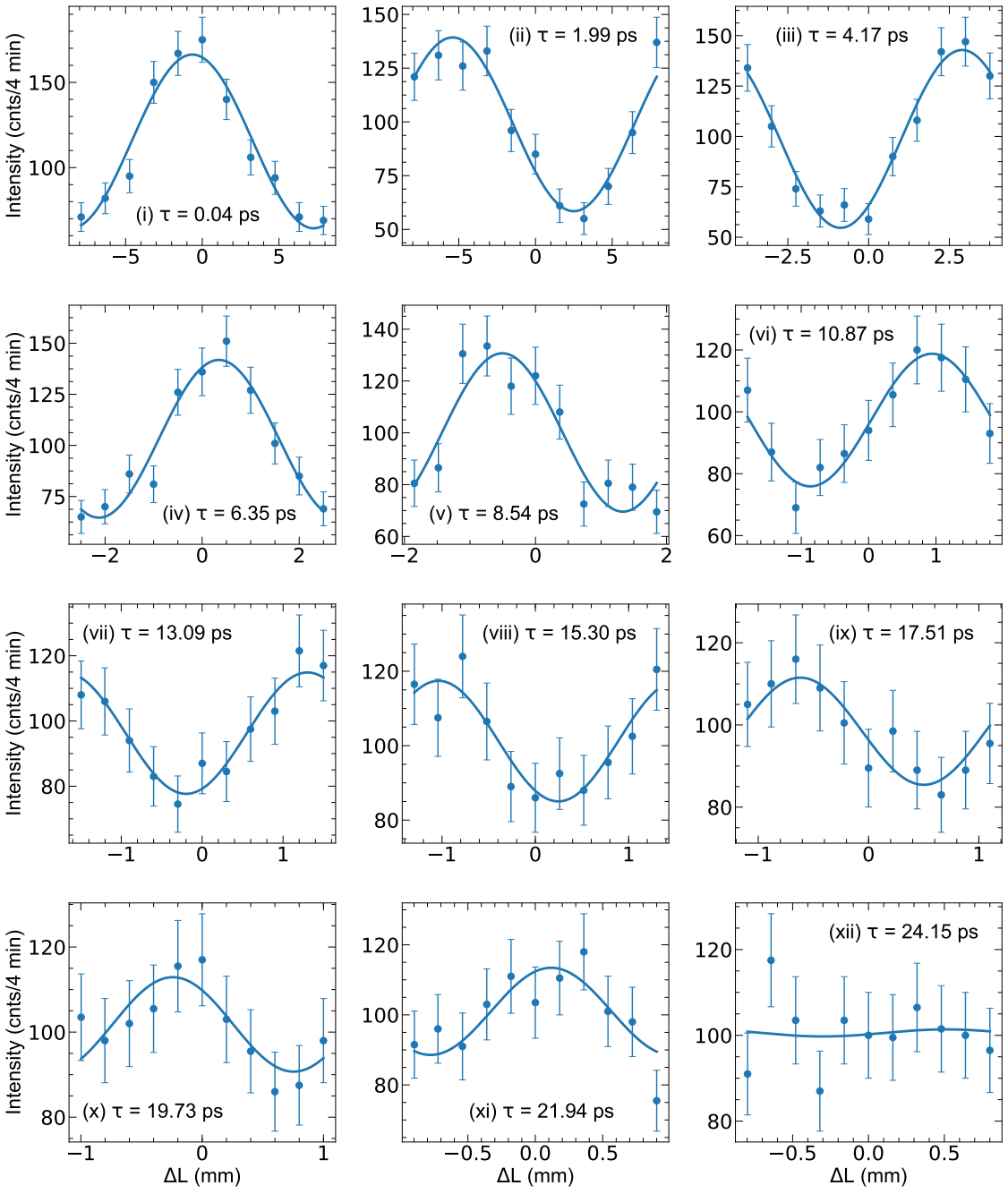

Figure B.7: *Raw intensity of a neutron resonance spin echo (NRSE) measurement for the given spin-echo times τ_{NRSE} (written simply as τ in the plots to save space), reflecting data taken for q_6 = (-0.300 -0.300 0) (see Table B.1). Data have been fit with a cosine() function and an arbitrary background set to zero in order to extract the polarization dependence. Measurement was made on the thermal-neutron triple-axis spectrometer TRISP@FRM-II for the type-I clathrate $Ba_{7.81}Ge_{40.67}Au_{5.33}$. See text for more details.*

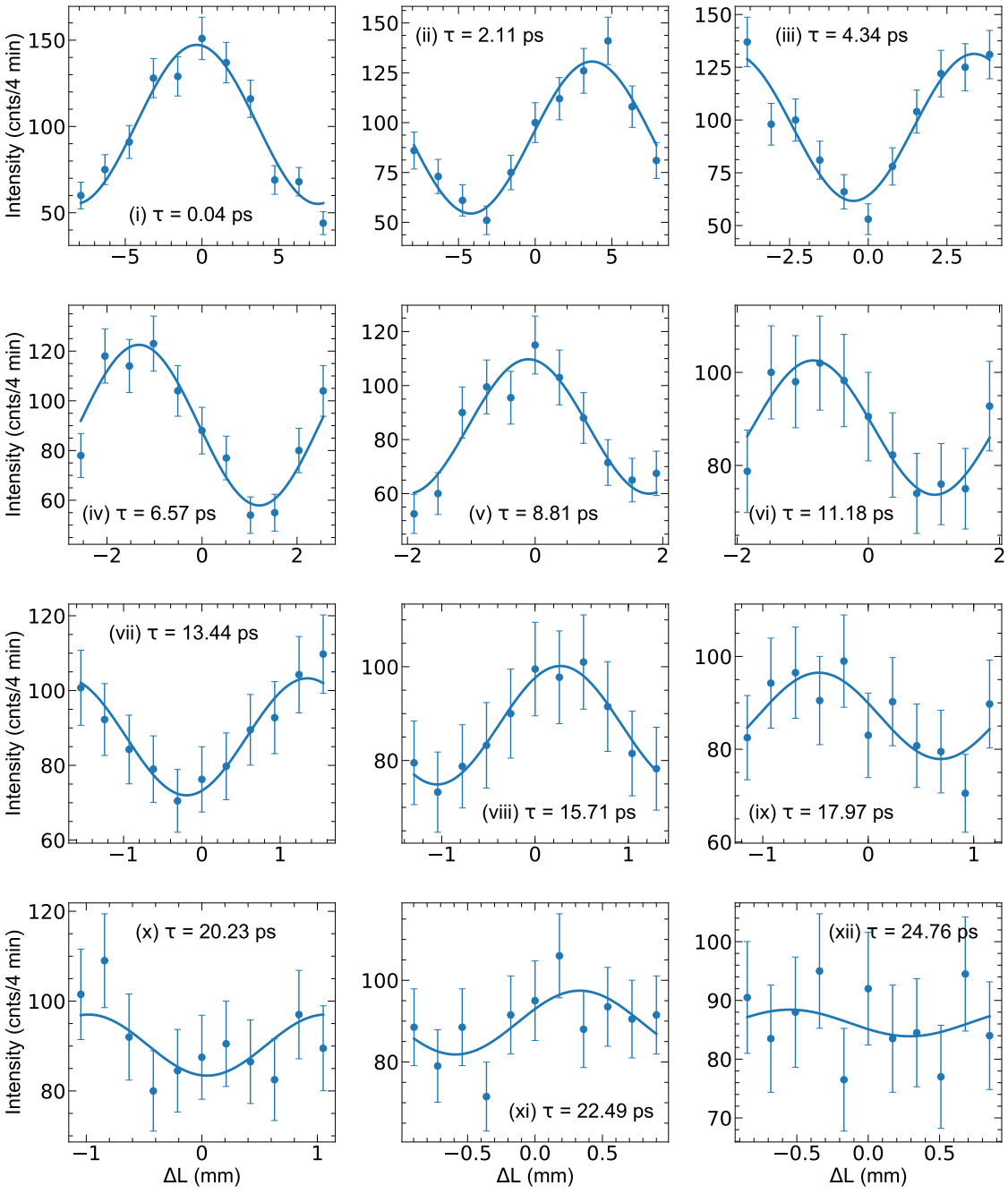

Figure B.8: *Raw intensity of a neutron resonance spin echo (NRSE) measurement for the given spin-echo times τ_{NRSE} (written simply as τ in the plots to save space), reflecting data taken for q_7 = (-0.338 -0.338 0) (see Table B.1). Data have been fit with a cosine() function and an arbitrary background set to zero in order to extract the polarization dependence. Measurement was made on the thermal-neutron triple-axis spectrometer TRISP@FRM-II for the type-I clathrate $Ba_{7.81}Ge_{40.67}Au_{5.33}$. See text for more details.*

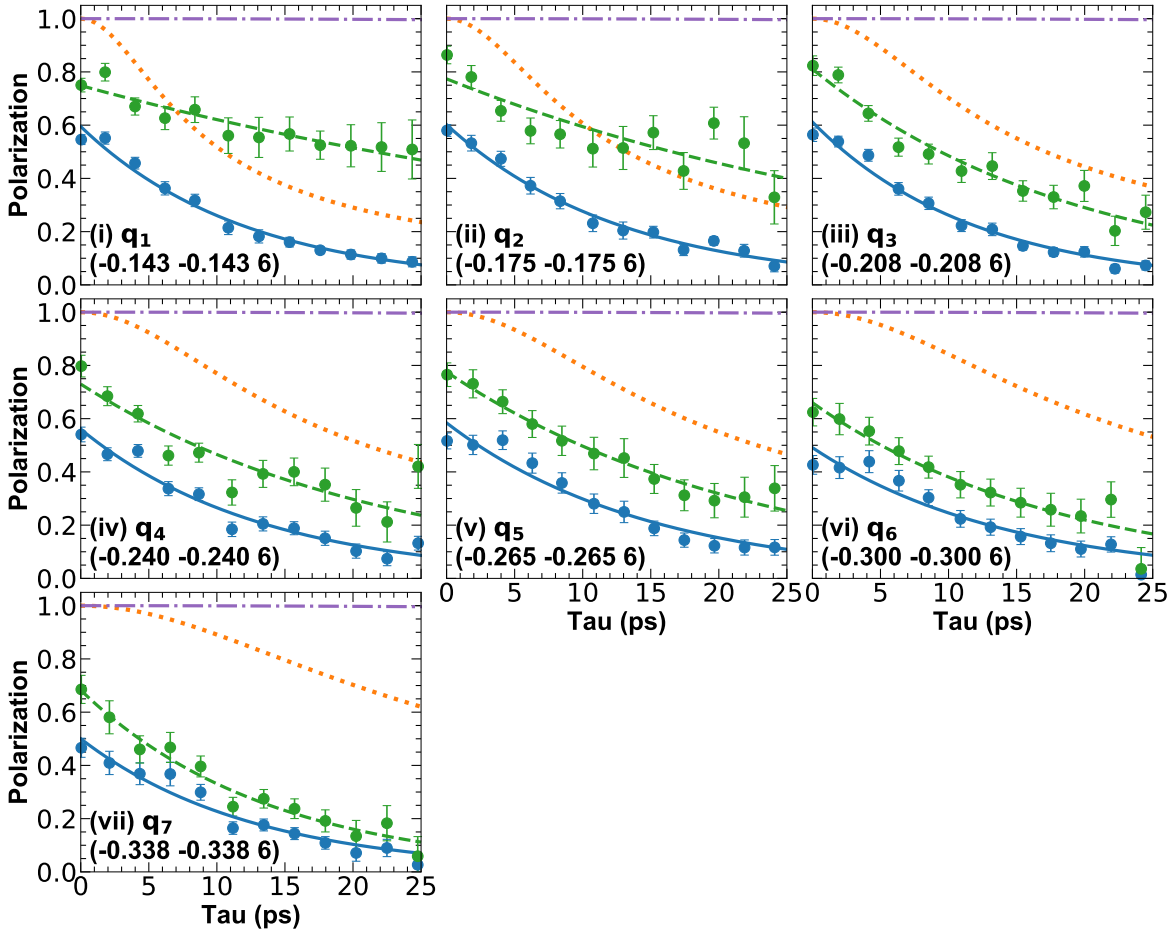

Figure B.9: *Summary of the polarization dependence vs spin-echo time of each q-point listed in Table B.1. Uncorrected datapoints (blue circles) come from the fits made in Figs. B.2-B.8. Datapoints in green reflect corrections made due to the instrumental resolution (purple dash-dotted line) and the curvature correction (orange dotted line). The uncorrected and corrected data have been fit with exponential curves, blue solid line and green dashed line, respectively, which are used to extract the half-width-half-maximum of the phonon linewidth, also given in Table B.1.*

Bibliography

[1] E. S. Toberer, A. F. May, and G. J. Snyder, Chem. Mater. **22**, 624 (2010).

[2] G. J. Snyder and E. S. Toberer, Complex thermoelectric materials, in *Materials for Sustainable Energy*, edited by V. Dusastre (Nature Publishing Group, UK, 2010) Chap. Thermoelectric Converters, pp. 101–110.

[3] A. F. Ioffe, L. S. Stil'bans, E. K. Iordanishvili, T. S. Stavitskaya, A. Gelbtuch, and G. Vineyard, Physics Today **12**, 42 (1959).

[4] M. Vedernikov and E. Iordanishvili, in *Seventeenth International Conference on Thermoelectrics. Proceedings ICT98 (Cat. No.98TH8365)* (1998) pp. 37–42.

[5] D. Champier, Energy Conversion and Management **140**, 167 (2017).

[6] P. D. Mitcheson, in *2010 Annual International Conference of the IEEE Engineering in Medicine and Biology* (2010) pp. 3432–3436.

[7] H.-S. Choi, S. Yun, and K. il Whang, Applied Thermal Engineering **27**, 2841 (2007).

[8] *Thermal Conductivity of Cage-Like Structures*, ASME/JSME Thermal Engineering Joint Conference, Vol. ASME/JSME 2011 8th Thermal Engineering Joint Conference (2011) t10039.

[9] M. Maldovan, Nature **503**, 209 (2013).

[10] J. L. Cohn, G. S. Nolas, V. Fessatidis, T. H. Metcalf, and G. A. Slack, Physical Review Letters **82**, 779 (1999).

[11] B. B. Iversen, A. E. Palmqvist, D. E. Cox, G. S. Nolas, G. D. Stucky, N. P. Blake, and H. Metiu, Journal of Solid State Chemistry **149**, 455 (2000).

[12] G. A. Slack, *CRC Handbook of Thermoelectrics*, edited by D. M. Rowe (CRC Press, 1995).

[13] M. Rull-Bravo, A. Moure, J. F. Fernández, and M. Martín-González, RSC Adv. **5**, 41653 (2015).

[14] G. J. Snyder and E. S. Toberer, Nature Materials **7**, 105 (2008).

[15] M. Beekman and D. G. Cahill, Crystal Research and Technology **52**, 1700114 (2017).

[16] H. J. Goldsmid and R. W. Douglas, British Journal of Applied Physics **5**, 386 (1954).

[17] R. P. Chasmar and R. Stratton, Journal of Electronics and Control **7**, 52 (1959).

[18] A. D. LaLonde, Y. Pei, H. Wang, and G. Jeffrey Snyder, Materials Today **14**, 526 (2011).

[19] Y. Pei, X. Shi, A. LaLonde, H. Wang, L. Chen, and G. J. Snyder, Nature **473**, 66 (2011).

[20] H.-S. Kim, N. A. Heinz, Z. M. Gibbs, Y. Tang, S. D. Kang, and G. J. Snyder, Materials Today **20**, 452 (2017).

[21] M. Hong, W. Lyu, Y. Wang, J. Zou, and Z.-G. Chen, Journal of the American Chemical Society **142**, 2672 (2020), pMID: 31940193.

[22] H. Yang, J.-H. Bahk, T. Day, A. M. S. Mohammed, G. J. Snyder, A. Shakouri, and Y. Wu, Nano Lett. **15**, 1349 (2015).

[23] Y. Bouyrie, C. Candolfi, S. Pailhès, M. M. Koza, B. Malaman, A. Dauscher, J. Tobola, O. Boisron, L. Saviot, and B. Lenoir, Phys. Chem. Chem. Phys. **17**, 19751 (2015).

[24] E. S. Toberer, A. Zevalkink, and G. J. Snyder, Journal of Materials Chemistry **21**, 15843 (2011).

[25] M. Christensen, A. B. Abrahamsen, N. B. Christensen, F. Juranyi, N. H. Andersen, K. Lefmann, J. Andreasson, C. R. H. Bahl, and B. B. Iversen, Nature Materials **7**, 811 (2008).

[26] S. Pailhès, H. Euchner, V. M. Giordano, R. Debord, A. Assy, S. Gomès, A. Bosak, D. Machon, S. Paschen, and M. de Boissieu, Phys. Rev. Lett. **113**, 025506 (2014).

[27] P.-F. Lory, S. Pailhès, V. M. Giordano, H. Euchner, H. D. Nguyen, R. Ramlau, H. Borrmann, M. Schmidt, M. Baitinger, M. Ikeda, P. Tomeš, M. Mihalkovič, C. Allio, M. R. Johnson, H. Schober, Y. Sidis, F. Bourdarot, L. P. Regnault, J. Ollivier, S. Paschen, Y. Grin, and M. de Boissieu, Nature Communications **8**, 491 (2017).

[28] V. Kuznetsov and P. Edwards, ChemSusChem **3**, 44 (2010).

[29] Z.-G. Chen, G. Han, L. Yang, L. Cheng, and J. Zou, Progress in Natural Science: Materials International **22**, 535 (2012).

[30] T. Takabatake, K. Suekuni, T. Nakayama, and E. Kaneshita, Reviews of Modern Physics **86**, 669 (2014).

[31] C. Kittel, *Introduction to Solid State Physics* (John Wiley & Sons Inc, 2004).

[32] P. G. Klemens, Proceedings of the Physical Society. Section A **68**, 1113 (1955).

[33] J. Callaway, Phys. Rev. **113**, 1046 (1959).

[34] W. A. Kamitakahara and B. N. Brockhouse, Phys. Rev. B **10**, 1200 (1974).

[35] G. M. Eliashberg, Soviet Physics JETP **11**, 696 (1960).

[36] V. V. Kabanov and A. S. Alexandrov, Phys. Rev. B **78**, 174514 (2008).

[37] C. Gadermaier, A. S. Alexandrov, V. V. Kabanov, P. Kusar, T. Mertelj, X. Yao, C. Manzoni, D. Brida, G. Cerullo, and D. Mihailovic, Physical Review Letters **105**, 257001 (2010).

[38] C. Gadermaier, V. V. Kabanov, A. S. Alexandrov, and D. Mihailovic, Journal of Applied Physics **111**, 112605 (2012).

[39] P. B. Allen, Physical Review Letters **59**, 1460 (1987).

[40] M. Kaviany, *Heat Transfer Physics* (Cambridge University Press, 2008).

[41] G. A. Slack (Academic Press, 1979) pp. 1–71.

[42] D. Shechtman, I. Blech, D. Gratias, and J. W. Cahn, Phys. Rev. Lett. **53**, 1951 (1984).

[43] D. G. Cahill and R. O. Pohl, Physical Review B **35**, 4067 (1987).

[44] R. Berman, Phys. Rev. **76**, 315 (1949).

[45] R. C. Zeller and R. O. Pohl, Phys. Rev. B **4**, 2029 (1971).

[46] R. Zorn, Physics **4**, 44 (2011).

[47] A. I. Chumakov, G. Monaco, A. Monaco, W. A. Crichton, A. Bosak, R. Rüffer, A. Meyer, F. Kargl, L. Comez, D. Fioretto, H. Giefers, S. Roitsch, G. Wortmann, M. H. Manghnani, A. Hushur, Q. Williams, J. Balogh, K. Parliński, P. Jochym, and P. Piekarz, Phys. Rev. Lett. **106**, 225501 (2011).

[48] S. N. Taraskin, Y. L. Loh, G. Natarajan, and S. R. Elliott, Phys. Rev. Lett. **86**, 1255 (2001).

[49] H. Tong, P. Tan, and N. Xu, Scientific Reports **5**, 15378 (2015).

[50] A. I. Chumakov, G. Monaco, X. Han, L. Xi, A. Bosak, L. Paolasini, D. Chernyshov, and V. Dyadkin, Philosophical Magazine **96**, 743 (2016).

[51] T. Brink, L. Koch, and K. Albe, Phys. Rev. B **94**, 224203 (2016).

[52] X. Y. Li, H. P. Zhang, S. Lan, D. L. Abernathy, T. Otomo, F. W. Wang, Y. Ren, M. Z. Li, and X.-L. Wang, Phys. Rev. Lett. **124**, 225902 (2020).

[53] W. H. Wang, Progress in Materials Science **106**, 100561 (2019).

[54] A. I. Chumakov, G. Monaco, A. Fontana, A. Bosak, R. P. Hermann, D. Bessas, B. Wehinger, W. A. Crichton, M. Krisch, R. Rüffer, G. Baldi, G. Carini Jr., G. Carini, G. D'Angelo, E. Gilioli, G. Tripodo, M. Zanatta, B. Winkler, V. Milman, K. Refson, M. T. Dove, N. Dubrovinskaia, L. Dubrovinsky, R. Keding, and Y. Z. Yue, Phys. Rev. Lett. **112**, 025502 (2014).

[55] A. S. Ahmad, X. Zhao, M. Xu, D. Zhang, J. Hu, H. J. Fecht, X. Wang, Q. Cao, and J. Z. Jiang, Journal of Low Temperature Physics **186**, 172 (2017).

[56] X. Tan, Y. Guo, D. Huang, and L. Zhang, Soft Matter **17**, 1330 (2021).

[57] S. R. Turner, S. Pailhès, F. Bourdarot, J. Ollivier, S. Raymond, T. Keller, Y. Sidis, J.-P. Castellan, P.-F. Lory, H. Euchner, M. Baitinger, Y. Grin, H. Schober, M. de Boissieu, and V. M. Giordano, Phys. Rev. Research **3**, 013021 (2021).

[58] K. Jin, B. C. Sales, G. M. Stocks, G. D. Samolyuk, M. Daene, W. J. Weber, Y. Zhang, and H. Bei, Sci. Rep. **6**, 20159 (2016).

[59] D. G. Cahill, S. K. Watson, and R. O. Pohl, Physical Review B **46**, 6131 (1992).

[60] K. W. Schlichting, N. P. Padture, and P. G. Klemens, Journal of Materials Science **36**, 3003 (2001).

[61] D. A. Ackerman, D. Moy, R. C. Potter, A. C. Anderson, and W. N. Lawless, Phys. Rev. B **23**, 3886 (1981).

[62] N. H. Andersen, K. N. Clausen, J. K. Kjems, and J. Schoonman, Journal of Physics C: Solid State Physics **19**, 2377 (1986).

[63] D. G. Cahill and R. O. Pohl, Physical Review B **39**, 10477 (1989).

[64] R. H. Nafziger and N. Riazance, Journal of the American Ceramic Society **55**, 130 (1972).

[65] B. Sobolev and N. Tkachenko, Journal of the Less Common Metals **85**, 155 (1982).

[66] A. K. Cheetham, B. E. F. Fender, and M. J. Cooper, Journal of Physics C: Solid State Physics **4**, 3107 (1971).

[67] J.-F. Bisson, D. Fournier, M. Poulain, O. Lavigne, and R. Mévrel, Journal of the American Ceramic Society **83**, 1993 (2004).

[68] D. R. Clarke and C. G. Levi, Annual Review of Materials Research **33**, 383 (2003).

[69] R. Mévrel, J.-C. Laizet, A. Azzopardi, B. Leclercq, M. Poulain, O. Lavigne, and D. Demange, Journal of the European Ceramic Society **24**, 3081 (2004).

[70] Z. Ouyang, *Deposition of Yttria-Stabilized Zirconia Thermal Barrier Coatings by Laser-Assisted Plasma Coating at Atmospheric Pressure*, Master's thesis, University of Illinois at Urbana-Champaign (2011).

[71] N. P. Padture, M. Gell, and E. H. Jordan, Science **296**, 280 (2002).

[72] G. P. Cousland, R. A. Mole, M. M. Elcombe, X. Y. Cui, A. E. Smith, C. M. Stampfl, and A. P. J. Stampfl, Journal of Physics and Chemistry of Solids **75**, 351 (2014).

[73] M. Fèvre, A. Finel, R. Caudron, and R. Mévrel, Phys. Rev. B **72**, 104118 (2005).

[74] T. Welberry, R. Withers, J. Thompson, and B. Butler, Journal of Solid State Chemistry **100**, 71 (1992).

[75] T. Welberry, B. Butler, J. Thompson, and R. Withers, Journal of Solid State Chemistry **106**, 461 (1993).

[76] T. R. Welberry and B. D. Butler, Journal of Applied Crystallography **27**, 205 (1994).

[77] J. P. Goff, W. Hayes, S. Hull, M. T. Hutchings, and K. N. Clausen, Physical Review B **59**, 14202 (1999).

[78] D. N. Argyriou and M. M. Elcombe, Journal of Physics and Chemistry of Solids **57**, 343 (1996).

[79] D. W. Liu, C. H. Perry, A. A. Feinberg, and R. Currat, Physical Review B **36**, 9212 (1987).

[80] D.-J. Kim, H.-J. Jung, and I.-S. Yang, Journal of the American Ceramic Society **76**, 2106 (1993).

[81] S. R. Turner, S. Pailhès, L. B. Mahfoud, C. Carbogno, M. de Boissieu, F. Bourdarot, H. Schober, Y. Sidis, J.-P. Castellan, A. Piovano, A. Ivanov, and V. M. Giordano (2021), Revisiting the Lattice Dynamics of Cubic Yttria-Stabilized Zirconia, unpublished.

[82] K. Suekuni, M. A. Avila, K. Umeo, and T. Takabatake, Phys. Rev. B **75**, 195210 (2007).

[83] Z. Ye, J. Y. Cho, M. M. Tessema, J. R. Salvador, R. A. Waldo, J. Yang, H. Wang, W. Cai, M. Kirkham, J. Yang, and W. Zhang, J. Alloy. Compd. **587**, 747 (2014).

[84] H. Zhang, H. Borrmann, N. Oeschler, C. Candolfi, W. Schnelle, M. Schmidt, U. Burkhardt, M. Baitinger, J.-T. Zhao, and Y. Grin, Inorg. Chem. **50**, 1250 (2011).

[85] H. Euchner, S. Pailhès, V. M. Giordano, and M. de Boissieu, Phys. Rev. B **97**, 014304 (2018).

[86] X. Shi, J. Yang, S. Bai, J. Yang, H. Wang, M. Chi, J. R. Salvador, W. Zhang, L. Chen, and W. Wong-Ng, Advanced Functional Materials **20**, 755 (2010).

[87] T. F. T. Cerqueira, S. Pailhès, R. Debord, V. M. Giordano, R. Viennois, J. Shi, S. Botti, and M. A. L. Marques, Chem. Mater. **28**, 3711 (2016).

[88] S. C. Sevov, Intermetallic Compounds - Principles and Practice: Progress, Volume 3 (John Wiley & Sons, 2002) Chap. 6. Zintl Phases, pp. 113–132.

[89] H. Kleinke, Chemistry of Materials **22**, 604 (2012).

[90] N. P. Blake, D. Bryan, S. Latturner, L. Møllnitz, G. D. Stucky, and H. Metiu, The Journal of Chemical Physics **114**, 10063 (2001).

[91] R. F. W. Herrmann, K. Tanigaki, T. Kawaguchi, S. Kuroshima, and O. Zhou, Phys. Rev. B **60**, 13245 (1999).

[92] S. Johnsen, M. Christensen, B. Thomsen, G. K. H. Madsen, and B. B. Iversen, Phys. Rev. B **82**, 184303 (2010).

[93] T. Tadano and S. Tsuneyuki, Phys. Rev. Lett. **120**, 105901 (2018).

[94] T. Tadano and S. Tsuneyuki, Phys. Rev. B **92**, 054301 (2015).

[95] T. Tadano and S. Tsuneyuki, Journal of the Physical Society of Japan **87**, 041015 (2018).

[96] W. Sano, T. Koretsune, T. Tadano, R. Akashi, and R. Arita, Phys. Rev. B **93**, 094525 (2016).

[97] Y. Oba, T. Tadano, R. Akashi, and S. Tsuneyuki, Phys. Rev. Materials **3**, 033601 (2019).

[98] Y.-N. Wu, W. A. Saidi, J. K. Wuenschell, T. Tadano, P. Ohodnicki, B. Chorpening, and Y. Duan, J. Phys. Chem. Lett. **11**, 2518 (2020).

[99] Z. Zeng, S. Li, T. Tadano, and Y. Chen, Journal of Physics: Condensed Matter **32**, 475702 (2020).

[100] J.-W. Yeh, S.-K. Chen, S.-J. Lin, J.-Y. Gan, T.-S. Chin, T.-T. Shun, C.-H. Tsau, and S.-Y. Chang, Advanced Engineering Materials **6**, 299 (2004).

[101] B. Cantor, I. Chang, P. Knight, and A. Vincent, Mat. Sci. Eng. A **375-377**, 213 (2004).

[102] J.-W. Yeh and S.-J. Lin, Journal of Materials Research **33**, 3129 (2018).

[103] M. C. Gao, J.-W. Yeh, P. K. Liaw, and Y. Zhang, eds., *High-Entropy Alloys* (Springer International Publishing, 2016).

[104] F. Granberg, K. Nordlund, M. W. Ullah, K. Jin, C. Lu, H. Bei, L. M. Wang, F. Djurabekova, W. J. Weber, and Y. Zhang, Phys. Rev. Lett. **116**, 135504 (2016).

[105] S. Sun, Y. Tian, X. An, H. Lin, J. Wang, and Z. Zhang, Mater. Today Nano **4**, 46 (2018).

[106] S. R. Turner, S. Pailhès, F. Bourdarot, J. Ollivier, Y. Sidis, J.-P. Castellan, J.-M. Zanotti, Q. Berrod, F. Porcher, A. Bosak, M. Feuerbacher, H. Schober, M. de Boissieu, and V. M. Giordano (2021), Phonon behavior in a random solid solution: A lattice dynamics study on the high-entropy alloy FeCoCrMnNi, unpublished.

[107] Y. Zhang, Y. Zhou, J. Lin, G. Chen, and P. Liaw, Advanced Engineering Materials **10**, 534 (2008).

[108] Y. Zhang, T. T. Zuo, Z. Tang, M. C. Gao, K. A. Dahmen, P. K. Liaw, and Z. P. Lu, Progress in Materials Science **61**, 1 (2014).

[109] Y. Zhang, S. Guo, C. T. Liu, and X. Yang, in *High-Entropy Alloys* (Springer International Publishing, 2016) pp. 21–49.

[110] J. He, W. Liu, H. Wang, Y. Wu, X. Liu, T. Nieh, and Z. Lu, Acta Materialia **62**, 105 (2014).

[111] A. Takeuchi and A. Inoue, Materials Transactions, JIM **41**, 1372 (2000).

[112] A. Takeuchi and A. Inoue, Materials Science and Engineering: A **304-306**, 446 (2001), rQ10, Tenth International Conference on Rapidly Quenched and Metastable Materials.

[113] X. Yang and Y. Zhang, Materials Chemistry and Physics **132**, 233 (2012).

[114] B. Ren, Z. Liu, D. Li, L. Shi, B. Cai, and M. Wang, Journal of Alloys and Compounds **493**, 148 (2010).

[115] S. Guo, C. Ng, J. Lu, and C. T. Liu, Journal of Applied Physics **109**, 103505 (2011).

[116] Y. Zhang, G. M. Stocks, K. Jin, C. Lu, H. Bei, B. C. Sales, L. Wang, L. K. Béland, R. E. Stoller, G. D. Samolyuk, M. Caro, A. Caro, and W. J. Weber, Nat. Commun. **6**, 8736 (2015).

[117] S. Mu, G. D. Samolyuk, S. Wimmer, M. C. Troparevsky, S. N. Khan, S. Mankovsky, H. Ebert, and G. M. Stocks, npj Computational Materials **5**, 1 (2019).

[118] L. Owen, E. Pickering, H. Playford, H. Stone, M. Tucker, and N. Jones, Acta Materialia **122**, 11 (2017).

[119] L. R. Owen and N. G. Jones, Journal of Materials Research **33**, 2954 (2018).

[120] M. S. Lucas, L. Mauger, J. A. Muñoz, Y. Xiao, A. O. Sheets, S. L. Semiatin, J. Horwath, and Z. Turgut, J. Appl. Phys. **109**, 07E307 (2011).

[121] M. S. Lucas, G. B. Wilks, L. Mauger, J. A. Muñoz, O. N. Senkov, E. Michel, J. Horwath, S. L. Semiatin, M. B. Stone, D. L. Abernathy, and E. Karapetrova, Appl. Phys. Lett. **100**, 251907 (2012).

[122] P.-F. Lory, V. M. Giordano, P. Gille, H. Euchner, M. Mihalkovič, E. Pellegrini, M. Gonzalez, L.-P. Regnault, P. Bastie, H. Schober, S. Pailhes, M. R. Johnson, Y. Grin, and M. de Boissieu, Phys. Rev. B **102**, 024303 (2020).

[123] I. Errea, M. Calandra, and F. Mauri, Phys. Rev. B **89**, 064302 (2014).

[124] T. Lan, C. W. Li, O. Hellman, D. S. Kim, J. A. Muñoz, H. Smith, D. L. Abernathy, and B. Fultz, Phys. Rev. B **92**, 054304 (2015).

[125] T. Nakayama and E. Kaneshita, J. Phys. Soc. Jpn. **80**, 104604 (2011).

[126] Y. Takasu, T. Hasegawa, N. Ogita, M. Udagawa, M. A. Avila, K. Suekuni, and T. Takabatake, Phys. Rev. B **82**, 134302 (2010).

[127] Q. Xi, Z. Zhang, J. Chen, J. Zhou, T. Nakayama, and B. Li, Phys. Rev. B **96**, 064306 (2017).

[128] Q. Xi, Z. Zhang, T. Nakayama, J. Chen, J. Zhou, and B. Li, Phys. Rev. B **97**, 224308 (2018).

[129] M. S. Ikeda, H. Euchner, X. Yan, P. Tomeš, A. Prokofiev, L. Prochaska, G. Lientschnig, R. Svagera, S. Hartmann, E. Gati, M. Lang, and S. Paschen, Nat. Commun. **10**, 887 (2019).

[130] M. Simoncelli, N. Marzari, and F. Mauri, Nat. Phys. **15**, 809 (2019).

[131] L. Isaeva, G. Barbalinardo, D. Donadio, and S. Baroni, Nature Communications **10**, 3853 (2019).

[132] P. B. Allen and J. L. Feldman, Phys. Rev. Lett. **62**, 645 (1989).

[133] R. Peierls, Annalen der Physik **395**, 1055 (1929).

[134] S. Mu, R. J. Olsen, B. Dutta, L. Lindsay, G. D. Samolyuk, T. Berlijn, E. D. Specht, K. Jin, H. Bei, T. Hickel, B. C. Larson, and G. M. Stocks, npj Computational Materials **6**, 4 (2020).

[135] M. Feuerbacher, E. Würtz, A. Kovács, and C. Thomas, Materials Research Letters **5**, 128 (2016).

[136] P. Brüesch, *Phonons: Theory and Experiments I* (Springer Berlin Heidelberg, 1982).

[137] R. E. Peierls, *Quantum Theory of Solids* (OUP Oxford, 2001).

[138] M. Christensen, F. Juranyi, and B. B. Iversen, Physica B: Condensed Matter **385-386**, 505 (2006).

[139] M. Born and R. Oppenheimer, Annalen der Physik **389**, 457 (1927).

[140] M. Dove, *Introduction to Lattice Dynamics*, edited by A. Putnis and R. C. Liebermann (Cambridge University Press, 2005).

[141] Dove, M.T., JDN **12**, 123 (2011).

[142] H. Schober and S. Rols, in *JDN 16 – Diffusion Inélastique des Neutrons pour l'Etude des Excitations dans la Matiére Condensée* (EDP Sciences, 2010).

[143] Y. Liu, Q. Xi, J. Zhou, T. Nakayama, and B. Li, Phys. Rev. B **93**, 214305 (2016).

[144] M. Falmbigl, G. Rogl, P. Rogl, M. Kriegisch, H. Müller, E. Bauer, M. Reinecker, and W. Schranz, Journal of Applied Physics **108**, 043529 (2010).

[145] F. Mouhat and F.-X. Coudert, Phys. Rev. B **90**, 224104 (2014).

[146] F. I. Fedorov, *Theory of Elastic Waves in Crystals* (Springer US, 1968).

[147] P. Norouzzadeh and C. W. Myles, J. Mater. Sci. **51**, 4538 (2016).

[148] T. Tojo, T. Atake, T. Mori, and H. Yamamura, Journal of Thermal Analysis and Calorimetry **57**, 447 (1999).

[149] A. Bentien, M. Christensen, J. D. Bryan, A. Sanchez, S. Paschen, F. Steglich, G. D. Stucky, and B. B. Iversen, Phys. Rev. B **69**, 045107 (2004).

[150] O. Delaire, J. Ma, K. Marty, A. F. May, M. A. McGuire, M.-H. Du, D. J. Singh, A. Podlesnyak, G. Ehlers, M. D. Lumsden, and B. C. Sales, Nature Materials **10**, 614 (2011).

[151] Z. Tian, J. Garg, K. Esfarjani, T. Shiga, J. Shiomi, and G. Chen, Phys. Rev. B **85**, 184303 (2012).

[152] T. Shiga, T. Murakami, T. Hori, O. Delaire, and J. Shiomi, Applied Physics Express **7**, 041801 (2014).

[153] O. Hellman and D. A. Broido, Phys. Rev. B **90**, 134309 (2014).

[154] C. W. Li, O. Hellman, J. Ma, A. F. May, H. B. Cao, X. Chen, A. D. Christianson, G. Ehlers, D. J. Singh, B. C. Sales, and O. Delaire, Phys. Rev. Lett. **112**, 175501 (2014).

[155] C. W. Li, J. Ma, H. B. Cao, A. F. May, D. L. Abernathy, G. Ehlers, C. Hoffmann, X. Wang, T. Hong, A. Huq, O. Gourdon, and O. Delaire, Phys. Rev. B **90**, 214303 (2014).

[156] J. Mao, J. L. Niedziela, Y. Wang, Y. Xia, B. Ge, Z. Liu, J. Zhou, Z. Ren, W. Liu, M. K. Chan, G. Chen, O. Delaire, Q. Zhang, and Z. Ren, Nano Energy **48**, 189 (2018).

[157] Y. Xia, Applied Physics Letters **113**, 073901 (2018).

[158] M. E. Manley, O. Hellman, N. Shulumba, A. F. May, P. J. Stonaha, J. W. Lynn, V. O. Garlea, A. Alatas, R. P. Hermann, J. D. Budai, H. Wang, B. C. Sales, and A. J. Minnich, Nature Communications **10**, 1928 (2019).

[159] J. Ma, O. Delaire, A. F. May, C. E. Carlton, M. A. McGuire, L. H. VanBebber, D. L. Abernathy, G. Ehlers, T. Hong, A. Huq, W. Tian, V. M. Keppens, Y. Shao-Horn, and B. C. Sales, Nature Nanotechnology **8**, 445 (2013).

[160] F. Damay, S. Petit, S. Rols, M. Braendlein, R. Daou, E. Elkaïm, F. Fauth, F. Gascoin, C. Martin, and A. Maignan, Scientific Reports **6**, 23415 (2016).

[161] J. Ding, J. L. Niedziela, D. Bansal, J. Wang, X. He, A. F. May, G. Ehlers, D. L. Abernathy, A. Said, A. Alatas, Y. Ren, G. Arya, and O. Delaire, Proceedings of the National Academy of Sciences **117**, 3930 (2020).

[162] J. Klarbring, O. Hellman, I. A. Abrikosov, and S. I. Simak, Phys. Rev. Lett. **125**, 045701 (2020).

[163] M. de Boissieu, R. Currat, S. Francoual, and E. Kats, Phys. Rev. B **69**, 054205 (2004).

[164] H. Euchner, M. Mihalkovič, F. Gähler, M. R. Johnson, H. Schober, S. Rols, E. Suard, A. Bosak, S. Ohhashi, A.-P. Tsai, S. Lidin, C. P. Gomez, J. Custers, S. Paschen, and M. de Boissieu, Phys. Rev. B **83**, 144202 (2011).

[165] H. Euchner, T. Yamada, S. Rols, T. Ishimasa, Y. Kaneko, J. Ollivier, H. Schober, M. Mihalkovic, and M. de Boissieu, Journal of Physics: Condensed Matter **25**, 115405 (2013).

[166] H. Euchner, T. Yamada, S. Rols, T. Ishimasa, J. Ollivier, H. Schober, M. Mihalkovič, and M. de Boissieu, Journal of Physics: Condensed Matter **26**, 055402 (2014).

[167] H. Euchner, S. Pailhès, L. T. K. Nguyen, W. Assmus, F. Ritter, A. Haghighirad, Y. Grin, S. Paschen, and M. de Boissieu, Phys. Rev. B **86**, 224303 (2012).

[168] D. Schopf, H. Euchner, and H.-R. Trebin, Phys. Rev. B **89**, 214306 (2014).

[169] H. Euchner and A. Groß, Chemistry of Materials **31**, 2571 (2019).

[170] X. He, D. Bansal, B. Winn, S. Chi, L. Boatner, and O. Delaire, Phys. Rev. Lett. **124**, 145901 (2020).

[171] M. Markov, J. Sjakste, N. Vast, R. Legrand, B. Perrin, and L. Paulatto, Phys. Rev. B **98**, 245201 (2018).

[172] J. Zhou, B. Liao, and G. Chen, Semiconductor Science and Technology **31**, 043001 (2016).

[173] B. Liao, B. Qiu, J. Zhou, S. Huberman, K. Esfarjani, and G. Chen, Phys. Rev. Lett. **114**, 115901 (2015).

[174] D. S. Kim, O. Hellman, N. Shulumba, C. N. Saunders, J. Y. Y. Lin, H. L. Smith, J. E. Herriman, J. L. Niedziela, D. L. Abernathy, C. W. Li, and B. Fultz, Phys. Rev. B **102**, 174311 (2020).

[175] J. Garg, N. Bonini, B. Kozinsky, and N. Marzari, Phys. Rev. Lett. **106**, 045901 (2011).

[176] K. Esfarjani, G. Chen, and H. T. Stokes, Phys. Rev. B **84**, 085204 (2011).

[177] D. A. Broido, M. Malorny, G. Birner, N. Mingo, and D. A. Stewart, Applied Physics Letters **91**, 231922 (2007).

[178] L. Chaput, Phys. Rev. Lett. **110**, 265506 (2013).

[179] T. Tadano, Y. Gohda, and S. Tsuneyuki, J. Phys.-Condens. Mat. **26**, 225402 (2014).

[180] S.-i. Tamura, Phys. Rev. B **27**, 858 (1983).

[181] B. Abeles, Phys. Rev. **131**, 1906 (1963).

[182] L. Lindsay, A. Katre, A. Cepellotti, and N. Mingo, Journal of Applied Physics **126**, 050902 (2019).

[183] A. J. H. McGaughey, A. Jain, H.-Y. Kim, and B. Fu, Journal of Applied Physics **125**, 011101 (2019).

[184] A. J. Minnich, Journal of Physics: Condensed Matter **27**, 053202 (2015).

[185] M. M. Koza, M. R. Johnson, H. Mutka, M. Rotter, N. Nasir, A. Grytsiv, and P. Rogl, Physical Review B **82**, 214301 (2010).

[186] J. Sun, A. Ruzsinszky, and J. P. Perdew, Phys. Rev. Lett. **115**, 036402 (2015).

[187] D. Bansal, A. Aref, G. Dargush, and O. Delaire, Journal of Physics: Condensed Matter **28**, 385201 (2016).

[188] C. W. Li, X. Tang, J. A. Muñoz, J. B. Keith, S. J. Tracy, D. L. Abernathy, and B. Fultz, Phys. Rev. Lett. **107**, 195504 (2011).

[189] A. A. Maradudin and A. E. Fein, Phys. Rev. **128**, 2589 (1962).

[190] M. R. Monga and K. N. Pathak, Phys. Rev. B **18**, 5859 (1978).

[191] R. S. Tripathi and K. N. Pathak, Il Nuovo Cimento B (1971-1996) **21**, 289 (1974).

[192] P. Procacci, G. Cardini, R. Righini, and S. Califano, Phys. Rev. B **45**, 2113 (1992).

[193] L. Paulatto, I. Errea, M. Calandra, and F. Mauri, Phys. Rev. B **91**, 054304 (2015).

[194] J. Sjakste, N. Vast, and V. Tyuterev, Phys. Rev. Lett. **99**, 236405 (2007).

[195] D. J. Hooton, The Philosophical Magazine: A Journal of Theoretical Experimental and Applied Physics **3**, 49 (1958).

[196] T. Tadano, Y. Gohda, and S. Tsuneyuki, Phys. Rev. Lett. **114**, 095501 (2015).

[197] A. Carreras, A. Togo, and I. Tanaka, Computer Physics Communications **221**, 221 (2017).

[198] S. Mukhopadhyay, D. Bansal, O. Delaire, D. Perrodin, E. Bourret-Courchesne, D. J. Singh, and L. Lindsay, Phys. Rev. B **96**, 100301 (2017).

[199] M. K. Gupta, R. Mittal, B. Singh, O. Delaire, S. N. Achary, S. Rols, A. K. Tyagi, and S. L. Chaplot, Phys. Rev. B **103**, 174109 (2021).

[200] T. Lanigan-Atkins, S. Yang, J. L. Niedziela, D. Bansal, A. F. May, A. A. Puretzky, J. Y. Y. Lin, D. M. Pajerowski, T. Hong, S. Chi, G. Ehlers, and O. Delaire, Nature Communications **11**, 4430 (2020).

[201] G. L. Squires, *Introduction to the Theory of Thermal Neutron Scattering* (Cambridge University Press, 2012).

[202] G. Shirane, S. M. Shapiro, and J. M. Tranquada, *Neutron Scattering with a Triple–Axis Spectrometer* (Cambridge University Press, 2015).

[203] H. Schober, Journal of Neutron Research **17**, 109 (2014).

[204] S. Pailhès, V. M. Giordano, P.-F. Lory, M. D. Boissieu, and H. Euchner, *Nanostructured Semiconductors*, edited by K. Termentzidis (Pan Stanford, 2017).

[205] S. W. Lovesey, *The Theory of Neutron Scattering from Condensed Matter* (OUP Oxford, 1986).

[206] P.-F. Lory, *Dynamique de réseau et conductivité thermique dans les alliages métalliques complexes*, Theses, Université Grenoble Alpes; Institut Max von Laue-Paul Langevin (Grenoble) (2015).

[207] M. Boudard, M. de Boissieu, S. Kycia, A. I. Goldman, B. Hennion, R. Bellissen, M. Quilichini, R. Currat, and C. Janot, Journal of Physics: Condensed Matter **7**, 7299 (1995).

[208] M. de Boissieu, S. Francoual, M. Mihalkovič, K. Shibata, A. Q. R. Baron, Y. Sidis, T. Ishimasa, D. Wu, T. Lograsso, L.-P. Regnault, F. Gähler, S. Tsutsui, B. Hennion, P. Bastie, T. J. Sato, H. Takakura, R. Currat, and A.-P. Tsai, Nat. Mater. **6**, 977 (2007).

[209] B. T. M. Willis and C. J. Carlile, *Experimental Neutron Scattering* (Oxford University Press, 2013).

[210] H. Prask, J. Rowe, J. Rush, and L. Schroder, Journal of Research of the National Institute of Standards and Technology **98**, 1 (1993).

[211] B. Dorner, *Coherent inelastic neutron scattering in lattice dynamics* (Springer-Verlag, Berlin New York, 1982).

[212] F. Hippert, E. Geissler, J. L. Hodeau, E. Lelièvre-Berna, and J.-R. Regnard, eds., *Neutron and X-ray Spectroscopy* (Springer Netherlands, 2006).

[213] A. Furrer, J. Mesot, and T. Strässle, *Neutron Scattering in Condensed Matter Physics* (WORLD SCIENTIFIC, 2009).

[214] P. Z. Vitalij Pecharsky, *Fundamentals of Powder Diffraction and Structural Characterization of Materials, Second Edition* (Springer-Verlag GmbH, 2008).

[215] N. Biniskos, *Inelastic neutron scattering on magnetocaloric compounds*, Master's thesis, RWTH Aachen University (2018).

[216] J. Voigt, Scattering methods for condensed matter research towards novel applications at future sources (Forschungszentrum Jülich, 2012) Chap. D4 Inelastic scattering: Lattice, magnetic and electronic excitations., p. D4.7, Lecture Notes of the 43rd IFF Spring ed.

[217] M. J. Cooper and R. Nathans, Acta Crystallographica **23**, 357 (1967).

[218] B. Dorner, Acta Crystallographica Section A **28**, 319 (1972).

[219] M. Popovici, Acta Crystallographica Section A **31**, 507 (1975).

[220] R. Rinaldi, L. Liang, and H. Schober, in *Neutron Applications in Earth, Energy and Environmental Sciences* (Springer US, 2009) pp. 1–14.

[221] T. Weber, R. Georgii, and P. Böni, SoftwareX **5**, 121 (2016).

[222] B. Hennion and P. Bourges, Afitv: Refinement program for triple axis spectrometer data.

[223] D. Richard, M. Ferrand, and G. J. Kearley, Journal of Neutron Research **4**, 33 (1996).

[224] O. Arnold, J. Bilheux, J. Borreguero, A. Buts, S. Campbell, L. Chapon, M. Doucet, N. Draper, R. F. Leal, M. Gigg, V. Lynch, A. Markvardsen, D. Mikkelson, R. Mikkelson, R. Miller, K. Palmen, P. Parker, G. Passos, T. Perring, P. Peterson, S. Ren, M. Reuter, A. Savici, J. Taylor, R. Taylor, R. Tolchenov, W. Zhou, and J. Zikovsky, Nucl. Instrum. Meth. A **764**, 156 (2014).

[225] R. Ewings, A. Buts, M. Le, J. van Duijn, I. Bustinduy, and T. Perring, Nucl. Instrum. Meth. A **834**, 132 (2016).

[226] G. Ehlers, A. A. Podlesnyak, J. L. Niedziela, E. B. Iverson, and P. E. Sokol, Review of Scientific Instruments **82**, 085108 (2011).

[227] N. Violini, J. Voigt, S. Pasini, and T. Brückel, Nuclear Instruments and Methods in Physics Research Section A: Accelerators, Spectrometers, Detectors and Associated Equipment **736**, 31 (2014).

[228] W. Reichardt, *MUPHOCOR, A Fortran Program To Determine the Phonon Density of States from Neutron Scattering Experiments* (1984).

[229] R. Golub and R. Gähler, Physics Letters A **123**, 43 (1987).

[230] Gähler, R. and Golub, R., J. Phys. France **49**, 1195 (1988).

[231] S. Klimko, *ZETA, A zero field spin echo method for very high resolution study of elementary excitations and first applications*, Ph.D. thesis, Technischen Universität Berlin (2003).

[232] K. Habicht, R. Golub, R. Gähler, and T. Keller, Neutron spin echo spectroscopy (Springer Berlin Heidelberg, 2002) Chap. Space-Time View of Neutron Spin Echo, Correlation Functions and Phonon Focusing, pp. 116–132.

[233] S. Prokudaylo, *Calculations for Neutron Spin Echo, Optimization of the magnetic field geometries and preparations and analysis of experiments on crystal lattice dynamics*, Ph.D. thesis, Technischen Universität München (2004).

[234] T. Keller, R. Golub, and R. Gähler, in *Scattering, Scattering and Inverse Scattering in Pure and Applied Science*, edited by R. Pike and P. Sabatier (Academic Press, London, 2002) pp. 1264–1286.

[235] N. Martin, *Etude structurale et dynamique de plusieurs systèmes magnétiques par la technique de l'écho de spin neutronique résonant*, Theses, Université de Grenoble (2012).

[236] F. Groitl, *High Resolution Spectroscopy with the Neutron Resonance Spin Echo Method*, Doctoral thesis, Technische Universität Berlin, Fakultät II - Mathematik und Naturwissenschaften, Berlin (2013).

[237] K. Habicht, R. Golub, F. Mezei, B. Keimer, and T. Keller, Phys. Rev. B **69**, 104301 (2004).

[238] T. Keller, P. Fabrykiewicz, R. Przeniosło, I. Sosnowska, and B. Keimer, Journal of Applied Crystallography **53**, 88 (2020).

[239] R. Gähler, R. Golub, and T. Keller, Physica B: Condensed Matter **180-181**, 899 (1992).

[240] N. Arend, *New Aspects of the MIEZE Technique and Verification of the Multi-level MIEZE Principle*, Ph.D. thesis, Technische Universität München (2007).

[241] K. Habicht, T. Keller, and R. Golub, Journal of Applied Crystallography **36**, 1307 (2003).

[242] M. T. Rekveldt, T. Keller, and R. Golub, Europhysics Letters (EPL) **54**, 342 (2001).

[243] T. Keller, M. T. Rekveldt, and K. Habicht, Applied Physics A **74**, s127 (2002).

[244] J. S. Tse, S. Desgreniers, Z.-q. Li, M. R. Ferguson, and Y. Kawazoe, Phys. Rev. Lett. **89**, 195507 (2002).

[245] A. Kaltzoglou, S. D. Hoffmann, and T. F. Fässler, European Journal of Inorganic Chemistry **2007**, 4162 (2007).

[246] T. Kume, H. Fukuoka, T. Koda, S. Sasaki, H. Shimizu, and S. Yamanaka, Phys. Rev. Lett. **90**, 155503 (2003).

[247] R. Debord, H. Euchner, V. Pischedda, M. Hanfland, A. San-Miguel, P. Mélinon, S. Pailhès, and D. Machon, Acta Materialia **210**, 116824 (2021).

[248] D. Li, L. Fang, S. Deng, K. Kang, L. Shen, W. Wei, and H. Ruan, Physica B: Condensed Matter **407**, 1238 (2012).

[249] Y. Saiga, K. Suekuni, B. Du, and T. Takabatake, Solid State Communications **152**, 1902 (2012).

[250] H. Shimizu, R. Oe, S. Ohno, T. Kume, S. Sasaki, K. Kishimoto, T. Koyanagi, and Y. Ohishi, Journal of Applied Physics **105**, 043522 (2009).

[251] W. Carrillo-Cabrera, S. Budnyk, Y. Prots, and Y. Grin, Zeitschrift für anorganische und allgemeine Chemie **630**, 2267 (2004).

[252] M. d'Astuto and M. Krisch, in *JDN 16 – Diffusion Inélastique des Neutrons pour l'Etude des Excitations dans la Matiére Condensée* (EDP Sciences, 2010).

[253] A. Q. Baron, in *Synchrotron Light Sources and Free-Electron Lasers* (Springer International Publishing, 2016) pp. 1643–1719.

[254] G. Margaritondo, in *Synchrotron Radiation* (Springer Berlin Heidelberg, 2014) pp. 29–63.

[255] G. Aquilanti, L. Vaccari, J. R. Plaisier, and A. Goldoni, in *Synchrotron Radiation* (Springer Berlin Heidelberg, 2014) pp. 65–104.

[256] I. Fischer, *Inelastic x-ray scattering from polycrystalline materials*, Theses, Université Joseph-Fourier - Grenoble I (2008), thèse préparée au sein du laboratoire: European Synchrotron Radiation Facility (ESRF), Grenoble.

[257] Y. Grin, Journal of Solid State Chemistry **274**, 329 (2019).

[258] K. Shibata, R. Currat, M. de Boissieu, T. J. Sato, H. Takakura, and A. P. Tsai, Journal of Physics: Condensed Matter **14**, 1847 (2002).

[259] G. Baldi, V. Giordano, G. Monaco, and B. Ruta, Journal of Non-Crystalline Solids **357**, 538 (2011), 6th International Discussion Meeting on Relaxation in Complex Systems.

[260] P. Bruna, G. Baldi, E. Pineda, J. Serrano, J. B. Suck, D. Crespo, and G. Monaco, The Journal of Chemical Physics **135**, 101101 (2011).

[261] A. Tlili, S. Pailhès, R. Debord, B. Ruta, S. Gravier, J.-J. Blandin, N. Blanchard, S. Gomès, A. Assy, A. Tanguy, and V. Giordano, Acta Materialia **136**, 425 (2017).

[262] T. Ichitsubo, W. Itaka, E. Matsubara, H. Kato, S. Biwa, S. Hosokawa, K. Matsuda, J. Saida, O. Haruyama, Y. Yokoyama, H. Uchiyama, and A. Q. R. Baron, Phys. Rev. B **81**, 172201 (2010).

[263] F. Körmann, Y. Ikeda, B. Grabowski, and M. H. F. Sluiter, npj Computational Materials **3**, 36 (2017).

[264] A. Jacquot, *Ingénierie des Matériaux et des Microgénérateurs Thermoélectriques Planaires*, Ph.D. thesis, L'Institut National Polytechnique de Lorraine (2003).

[265] D. Nemir and J. Beck, Journal of Electronic Materials **39**, 1897 (2010).